

**OPTICAL-BASED TACTILE SENSORS FOR
MINIMALLY INVASIVE SURGERIES: DESIGN,
MODELING, FABRICATION AND VALIDATION**

Naghmeh Mohammadi Bandari

A Thesis

in

The Department

of

Mechanical, Industrial and Aerospace Engineering

Presented in Partial Fulfillment of the Requirements

for the Degree of

Doctor of Philosophy (Mechanical Engineering) at

Concordia University

Montréal, Québec, Canada

January 2021

© Naghmeh Mohammadi Bandari, 2021

CONCORDIA UNIVERSITY

School of Graduate Studies

This is to certify that the thesis prepared

By: **Ms. Naghmeh Mohammadi Bandari**

Entitled: **OPTICAL-BASED TACTILE SENSORS FOR MINIMALLY INVASIVE
SURGERIES: DESIGN, MODELING, FABRICATION AND VALIDATION**

and submitted in partial fulfillment of the requirements for the degree of

Doctor of Philosophy (Mechanical Engineering)

complies with the regulations of this University and meets the accepted standards with respect to originality and quality.

Signed by the Final Examining Committee:

_____ Chair
Dr. Hovhannes Harutyunyan

_____ External Examiner
Dr. Ash M. Parameswaran

_____ External Examiner
Dr. Ashutosh Bagchi

_____ Examiner
Dr. Ramin Sedaghati

_____ Examiner
Dr. Sivakumar Narayanswamy

_____ Co-Supervisor
Dr. Muthukumaran Packirisamy

_____ Co-supervisor
Dr. Javad Dargahi

Approved by: _____
Dr. Martin D. Pugh, Chair
Department of Mechanical, Industrial and Aerospace Engineering

January, 18 2021 _____
Dr. Mourad Debbabi, Dean
Gina Cody School of Engineering

Abstract

OPTICAL-BASED TACTILE SENSORS FOR MINIMALLY INVASIVE SURGERIES: DESIGN, MODELING, FABRICATION AND VALIDATION

Naghmeh Mohammadi Bandari, Ph.D.

Concordia University, 2021

Loss of tactile perception is the most challenging limitation of state-of-the-art technology for minimally invasive surgery. In conventional open surgery, surgeons rely on their tactile sensation to perceive the tissue type, anatomical landmarks, and instrument-tissue interaction in the patient's body. To compensate for the loss of tactile feedback in minimally invasive surgery, researchers have proposed various tactile sensors based on electrical and optical sensing principles. Optical-based sensors have shown the most compatibility with the functional and physical requirements of minimally invasive surgery applications. However, the proposed tactile sensors in the literature are typically bulky, expensive, cumbersome to integrate with surgical instruments, and show nonlinearity in interaction with biological tissues. In this doctoral study, different optical tactile sensing principles were proposed, modeled, validated and various tactile sensors were fabricated, and experimentally studied to address the limitations of the state-of-the-art. The present thesis first provides a critical review of the proposed tactile sensors in the literature with a comparison of their advantages and limitations for surgical applications. Afterward, it compiles the results of the design, modeling, and validation of a hybrid optical-piezoresistive sensor, a distributed Bragg reflecting sensor, and two sensors based on the variable bending radius light intensity modulation principle. The performance of each sensor was verified experimentally for the required criteria of accuracy, resolution, range, repeatability, and hysteresis. Also, a novel image-based intensity estimation technique was proposed and its applicability for being used in surgical applications was verified experimentally. In the end, concluding remarks and recommendations for future studies are provided.

Acknowledgments

No one is able to accomplish research work without the brilliant supports of many people. I would like to thank the following people who have helped me undertake this research, without whom I would not have made it through my doctorate degree.

First of all, I would like to express my sincerest gratitude to my supervisors, Dr. Javad Dargahi and Dr. Muthukumaran Packirisamy, for their continual help, support, inspiration, encouragement, and guidance during my doctoral study.

I would also like to thank the members of my examination committee, Dr. Ash M. Parameswaran, Dr. Ashutosh Bagchi, Dr. Sivakumar Narayanswamy, and Dr. Ramin Sedaghati for their valuable advice and directions throughout my Ph.D. program.

I appreciate the financial support of the NSERC for granting me an *NSERC CREATE Fellowship in Surgical Innovation* and the FRQNT for my *FRQNT B2X Interdisciplinary Doctoral Scholarship* and the *FRQNT CCTT Award*. I would also like to express my gratitude to the School of Graduate Studies of Concordia University for granting me the *Concordia Public Scholar Award* and the Gina Cody School of Engineering of Concordia University for granting me an *International Tuition Award of Excellence*.

Moreover, I would like to thank the staff of the Mechanical, Industrial, and Aerospace Engineering (MIAE) Department for their kind and timely helps. My special thanks to Ms. Leslie Hossein, Ms. Arlene Zimmerman, and Ms. Maureen Thuringer for being always supportive, patient, and kind.

I express my sincere gratitude to Dr. Jake Barralet and Dr. Kevin Lachapelle for their kind advice and guidance during my term as a Surgical Innovation Fellow at McGill University and

McGill University Health Center (MUHC). I would also like to express my appreciation to Mr. Dan Wittenberger, Mr. Jean-Pierre Lalonde, and Mr. Nicolas Coulumbe, whose guidance, support and supervision were an invaluable source of inspiration for my research during my internship at Medtronic CryoCath, Montreal, QC. A special thanks goes to the industrial collaborator, Optech CCTT, Montreal, QC, for their support, guidance, expertise, and collaboration during my industrial internship supported by FRQNT CCTT Internship Award.

Very special thanks to all my friends and colleagues at the Robotic Surgery and Optical-Bio Microsystems Laboratories of Concordia University. I would like to particularly thank Dr. Shahram Shokouhfar, Dr. Mostapha Marzban, and Dr. Ahmad Sohrabi for their help and guidance in transferring their invaluable experiences to me throughout my doctoral study.

My heartiest warm appreciations go to my parents, Ramesh and Ali, who had continual belief in me and have been encouraging me to never give up my dreams throughout my life. Their prayers for me were what sustained me thus far. I would also like to thank my beloved sister, Dr. Narjes Bandari, from the bottom of my heart for all her support, great devotion, and dedication during my absence at home.

Last but not least, words simply can not express my profound appreciation and thankfulness to my husband, Amir. He was standing shoulder-to-shoulder with me at every single step of my doctoral study with constant support, assistance, encouragement, and motivation. Thank you, Amir, for being such a source of love and energy in every moment of this journey. I could not have achieved it without you.

To:

my beloved husband, Amir,

my mother, and my father.

Contents

| | |
|---|-------------|
| List of Figures | xii |
| List of Tables | xx |
| Nomenclature | xxii |
| 1 Introduction | 1 |
| 1.1 Minimally Invasive Surgeries | 1 |
| 1.2 Tactile Sensors for MIS | 4 |
| 1.3 Thesis Motivation | 6 |
| 1.4 Objective and Scope | 8 |
| 1.5 Contributions | 10 |
| 1.6 Publications | 12 |
| 1.7 Thesis Layout | 13 |
| | |
| 2 Tactile Sensors for Minimally Invasive Surgery: A Review of the State-of-the-Art, Applications, and Perspectives | 17 |
| 2.1 Introduction | 18 |
| 2.2 Methodology | 18 |
| 2.3 Tactile Sensors in Minimally Invasive Surgery | 19 |
| 2.3.1 Electrical-based Tactile Sensors in MIS | 19 |
| 2.3.2 Optical-based Tactile Sensors | 34 |

| | | |
|-----|-----------------------|----|
| 2.4 | Conclusions | 57 |
|-----|-----------------------|----|

3 Hybrid Piezoresistive-optical Tactile Sensor for Simultaneous Measurement of Tissue Stiffness and Detection of Tissue Discontinuity in Robot-assisted Minimally Invasive Surgery **59**

| | | |
|-------|---|----|
| 3.1 | Introduction | 60 |
| 3.2 | Sensor Design and Sensing Concept | 64 |
| 3.2.1 | Sensor Design | 64 |
| 3.2.2 | Sensing Concept | 65 |
| 3.3 | Finite Element Modeling and Simulation | 70 |
| 3.3.1 | Evaluation of Tissue Distinction (Simulation I) | 72 |
| 3.3.2 | Evaluation of Hidden Mass Detection (Simulation II) | 72 |
| 3.4 | Microfabrication and Experimental Setup | 74 |
| 3.5 | Results and Discussion | 74 |
| 3.6 | Conclusion | 80 |

4 Optomechanical Modeling and Validation of a Distributed Bragg Reflector Force Sensor with Drift and Temperature Compensation **81**

| | | |
|-------|---|-----|
| 4.1 | Introduction | 82 |
| 4.1.1 | Background | 82 |
| 4.1.2 | Rationale and Contributions | 84 |
| 4.2 | Materials and Methods | 85 |
| 4.2.1 | Sensing Principle | 85 |
| 4.2.2 | Structural Design | 88 |
| 4.2.3 | Optical Module and Experimental Setup | 90 |
| 4.2.4 | Theoretical Modeling | 92 |
| 4.2.5 | Calibration Protocol | 99 |
| 4.2.6 | Sensor Validation | 99 |
| 4.3 | Results and Discussion | 101 |

| | | |
|-------|---------------------------------|-----|
| 4.3.1 | Sensor Calibration | 101 |
| 4.3.2 | Validation | 105 |
| 4.3.3 | Sensor Specifications | 108 |
| 4.4 | Conclusion | 109 |

**5 Miniaturized Optical Force Sensor for Minimally Invasive Surgery With
Learning-Based Nonlinear Calibration 111**

| | | |
|-------|--|-----|
| 5.1 | Introduction | 112 |
| 5.1.1 | Background | 112 |
| 5.1.2 | Literature Review | 112 |
| 5.2 | Sensor Design and Modeling | 117 |
| 5.2.1 | Structural Design | 117 |
| 5.2.2 | Sensing Principle | 117 |
| 5.3 | Structural Optimization | 121 |
| 5.3.1 | Optimization Parameters | 122 |
| 5.3.2 | Feasible Range of Parameters and Constraints | 122 |
| 5.3.3 | Material Models and Finite Element Analysis | 125 |
| 5.4 | Sensor Fabrication | 127 |
| 5.5 | Calibration and Validation | 128 |
| 5.5.1 | Experimental Setup | 128 |
| 5.5.2 | Sensor Calibration | 130 |
| 5.5.3 | Experimental Validation | 132 |
| 5.6 | Performance Analysis | 133 |
| 5.7 | Conclusions | 140 |

**6 Image-based Optical-fiber Force Sensor for Minimally Invasive Surgery with
ex-vivo Validation 142**

| | | |
|-----|------------------------|-----|
| 6.1 | Introduction | 143 |
|-----|------------------------|-----|

| | | |
|---|---|------------|
| 6.2 | Material and Methods | 145 |
| 6.2.1 | Geometrical Design and Prototyping | 145 |
| 6.2.2 | Experimental Setup | 147 |
| 6.2.3 | Image-based Intensity Estimation | 148 |
| 6.2.4 | Support-Vector-Regression (SVR) Calibration | 150 |
| 6.3 | <i>Ex-vivo</i> Validation | 153 |
| 6.4 | Conclusion | 155 |
| | | |
| 7 Optical Fiber Array Sensor for Force Estimation and Localization in TAVI | | |
| Procedure: Design, Modeling, Analysis and Validation | | 157 |
| 7.1 | Introduction | 158 |
| 7.2 | Design Requirements and Structural Design | 162 |
| 7.3 | Sensor Modeling | 163 |
| 7.3.1 | Sensing Principle | 164 |
| 7.3.2 | Finite Element Simulation | 166 |
| 7.4 | Validation Study | 170 |
| 7.4.1 | Sensor Fabrication | 170 |
| 7.4.2 | Experimental Setup and Validation Test | 172 |
| 7.5 | Results and Discussion | 174 |
| 7.6 | Conclusion | 176 |
| | | |
| 8 | Conclusion | 179 |
| 8.1 | Summary and Conclusions | 179 |
| 8.2 | Future Studies | 182 |
| | | |
| | Bibliography | 184 |
| | | |
| | Appendix A | 213 |
| A.1 | Bending-based Formulation of Light Intensity Modulation for Miniaturization of Optical Tactile Sensors | 213 |

| | | |
|-------|---|-----|
| A.2 | Validation of the Variable Bending Radius Sensing Principle | 217 |
| A.3 | Fabrication and Experimental Setup Preparation for Light Intensity Measurement . | 219 |
| A.3.1 | 3D Printing Fabrication | 219 |
| A.3.2 | Experimental Setup | 220 |
| A.4 | Finite Element Analysis for Non-linear Deflection and Optimization of DBR Fiber Laser Sensor | 223 |
| A.4.1 | Finite Element Analysis | 224 |
| A.4.2 | Parametric Response Surface | 225 |
| A.4.3 | Parametric Study Results | 228 |
| A.5 | Feasibility Study of a Novel Force Sensor with Three DBR Fibers | 230 |
| A.5.1 | Finite Element Analysis | 230 |
| A.5.2 | Simulation | 231 |

List of Figures

| | |
|--|----|
| Figure 1.1 Comparison between a conventional open surgery and three main categories of MIS procedures. | 3 |
| Figure 1.2 Categories of various tactile sensors proposed in the literature for minimally invasive surgery. | 5 |
| Figure 2.1 (a) Two sensorized graspers with micro strain gauges placed at the jaws, (b) electronic feedback system with LED to display the sensor output | 21 |
| Figure 2.2 Bioinspired piezoresistive tactile sensor by Hu <i>et al.</i> | 22 |
| Figure 2.3 Placement of strain gauges on a bipolar forceps: (a) axial sensors, (b) planar sensors. | 23 |
| Figure 2.4 (a) Cross-section of the sensor structure, (b) a single sensing unit under a typical grasping force, (c) schematic of the equipped grasper with an array of sensing units. | 25 |
| Figure 2.5 (a) Schematic of the tactile sensor in interaction with soft tissue, the graph shows the relative output voltage of the sensing elements, (b) endoscope equipped with the tactile sensor, (c) submucosa of a swine stomach with an artificial tumor lump. | 26 |
| Figure 2.6 (a) Schematic of the needle embedded with piezoelectric transducer and its experimental diagram proposed by Sharma <i>et al.</i> , (b) experimental validation using a thyroid sample. | 28 |
| Figure 2.7 (a) Schematic of the orientation of electrode and flexible layered structure of the sensor, (b) prototype sensor and its data acquisition system. | 30 |

| | |
|---|----|
| Figure 2.8 (a) Structure of the capacitance cells on the substrate, (b) 3D design of the sensorized forceps, (c) micromachined prototype with an integrated sensor. | 31 |
| Figure 2.9 Typical system components of an optical sensor system based on (a) LIM principle, (b) WM and PM principles. | 35 |
| Figure 2.10 Bending loss configurations: (a) constant bending radius (CBR), (b) variable bending radius (VBR). | 36 |
| Figure 2.11 Optical fiber coupling loss configuration: (a) transmission loss, (b) reflection loss. | 38 |
| Figure 2.12 Bending loss tactile sensor proposed by Ahmadi <i>et al.</i> | 40 |
| Figure 2.13 Proposed transmissive coupling loss optical fiber sensor by Ahmadi <i>et al.</i> | 42 |
| Figure 2.14 Reflective light intensity modulation tactile sensor proposed by Yip <i>et al.</i> | 43 |
| Figure 2.15 (a) Schematic view of the sensor proposed by Noh <i>et al.</i> , (b) configuration of internal mirror and cantilever arms, (c) the image acquisition system, (d) their prototyped sensor. | 45 |
| Figure 2.16 Sensing principle of the fiber Bragg grating and wavelength shift due to an axial strain. | 47 |
| Figure 2.17 (a) Schematic of the structure of the proposed sensor by Yokoyama <i>et al.</i> , (b) reaction force on the catheter tip during the ablation procedure. | 48 |
| Figure 2.18 (a) Sensor design with three fibers in a biopsy needle developed by Park <i>et al.</i> in, and (b) graphical display showing the shape of the needle and the wavelength shift. | 49 |
| Figure 2.19 Two-DoF sensorized needle driving grasper equipped with an FPG sensor developed by Zarrin <i>et al.</i> | 50 |
| Figure 2.20 Fabry-Perot configuration: (a) extrinsic, (b) intrinsic. | 52 |
| Figure 2.21 (a) Structure and sensing principle of the FPI sensor proposed by Shang <i>et al.</i> , (b) their prototyped sensor embedded on a biopsy needle. | 54 |
| Figure 2.22 (a) Schematic of the two FPI sensor inside the needle tip and the sensorized needle proposed by Mo <i>et al.</i> , (b) temperature compensation FPI sensor for MIS needle. | 55 |

| | | |
|-------------|---|----|
| Figure 3.1 | Conceptual overview of a tactile sensor embedded in an MIS grasper. | 61 |
| Figure 3.2 | Schematic of the tissue and sensor: (a) without contact load, (b) with contact load applied from the gripping surgical tool, which leads to a deflection in both the sensor and tissue. | 64 |
| Figure 3.3 | Structural design of the hybrid sensor. | 65 |
| Figure 3.4 | Schematic view of the deformed configuration of the sensor beam and optical fibers. | 66 |
| Figure 3.5 | Mesh quality, geometric features, and dimensions of the sensor-tissue model. | 71 |
| Figure 3.6 | Force–displacement diagram of tissue phantom material made of Ecoflex [®] 00-10 silicone rubber. | 71 |
| Figure 3.7 | Schematic loading on the tissue phantom and sensor in simulation I and the tissue phantom with a hidden mass in simulation II. | 73 |
| Figure 3.8 | (a) SEM images of the V-groove on the lower surface of the sensor beam, (b) different structural components of the sensor, and (c) final assembled sensor. | 75 |
| Figure 3.9 | Schematic experimental setup for cyclic compression. | 75 |
| Figure 3.10 | Estimated force between the tissue phantoms and the sensor and the output voltage of the photodetector. | 77 |
| Figure 3.11 | (a) Variation of the force in left and right piezoresistive film with hidden mass located at $d = 5mm$, (b) variation of the ratio of forces as a function of the location of the hidden mass. | 79 |
| Figure 4.1 | (a) Narrow-band laser emission in a schematic DBR fiber laser, (b) birefringence phenomenon in a transversely loaded DBR fiber laser resulting in beating of the lasing frequency. | 86 |
| Figure 4.2 | (a) Typical structure of DBR force sensors, (b) exploded view of the typical force sensor design, (c) parametric dimensions membrane and DBR fiber. | 89 |
| Figure 4.3 | (a) Schematic diagram of the experimental setup and the system components, (b) fabricated sensor (courtesy of Optech CCTT). | 91 |

| | | |
|-------------|--|-----|
| Figure 4.4 | (a) A simplified mechanical model of the membrane and optical fiber, (b) mechanical model of the membrane shows the superpositioning contact force and external force. | 93 |
| Figure 4.5 | (a) Generalized Hertzian contact configuration between two elastic cylinders, (b) schematic of the membrane and fiber in contact, dimensions are not to-the-scale. | 95 |
| Figure 4.6 | (a) Borosilicate sample under the compression test, (b) graph of force vs. displacement to calculate the module of elasticity of the Borosilicate or membrane. | 98 |
| Figure 4.7 | (a) Variation of the beating frequency f_b and lasing wavelength λ while the ambient temperature T changed, (b) linearity of changes in the beating frequency and lasing wavelength with temperature. | 102 |
| Figure 4.8 | (a) Variation of the beating frequency f_b and lasing wavelength λ while the external force F changed, (b) insensitivity of the lasing wavelength and linearity of changes in the beating frequency to the external force. | 103 |
| Figure 4.9 | Evolution of intrinsic beating frequency over a long period of time for an Erbium-doped sample. | 104 |
| Figure 4.10 | Verification of the multi-linear calibration through comparison of the experimental data with (a) the estimated temperature, (b) the estimated external force. . . | 106 |
| Figure 4.11 | (a) Raw pressure measurement of the calibrated sensor vs. the reference Fiso pressure prob, (b) linearity of the sensor output with the reference readings with $R^2 = 0.9967$, (c) enlarged view of the recorded data by the sensor and Fiso pressure probe. | 107 |
| Figure 5.1 | Schematic MIS surgery: surgeon operates on internal organs with using long and thin MIS instruments, while a camera is used and maneuvered to have a complete vision inside the body. | 113 |
| Figure 5.2 | (a) 3D design of the sensor-embedded MIS grasper and mechanical model of an optical fiber as a beam in, (b) CBR, (c) VBR configurations. | 118 |
| Figure 5.3 | (a) Parametric geometry of the optical sensor, (b) deformation of the shell and optical fiber under a 2.0N force obtained from the finite element analysis. . . . | 122 |

| | | |
|-------------|---|-----|
| Figure 5.4 | (a) Optical fiber sample no.1 under bending test and sample no.2 after breakage, (b) force-displacement curve of the two optical fiber samples under bending tests. | 123 |
| Figure 5.5 | Stress-stretch characteristic curve of the flexible material under compression compared to the two-term Mooney-Rivlin fitting. | 126 |
| Figure 5.6 | (a) Fabricated sensor and grasper with sensorized end-effector, (b) experimental setup for sensor calibration. The laser source transmits light to the optical fiber. | 129 |
| Figure 5.7 | Force and the output voltage from the photodetector for (a) sinusoidal displacement, (b) triangular displacement, (c) response surface of SVR calibration over the working range of relative change of voltage and rate of change in voltage; black points indicate the training data used for calibration, (d) linearity of the SVR calibration. | 131 |
| Figure 5.8 | (a) Experimental setup for sensor performance assessment under cyclic triangular compression, (b) results of the force measured by the optical sensor compared to the ATI sensor. | 134 |
| Figure 5.9 | (a) Optical sensor on a mock grasper squeezing the fixture installed on the ATI Mini45 force sensor, (b) results of the force measured by optical sensor compared to the ATI sensor. | 135 |
| Figure 5.10 | (a) Force-voltage characteristic curve of the reference (blue) versus the estimated forces (red). Shaded area shows the hysteresis H , (b) drift and noise of the sensor in five hours with an exponential fit and moving average filtering. | 137 |
| Figure 6.1 | Schematic MIS procedure: the camera is used for the internal vision of the organs and grasper is used for holding and operating on the organs. | 143 |
| Figure 6.2 | (a) Prototyped force sensor embedded on the jaw of a typical MIS grasper, (b) schematic view of the transmitted light intensity on a projection plane while the optical fiber is under force. | 146 |

| | | |
|------------|--|-----|
| Figure 6.3 | (a) Experimental setup used for sensor calibration, (b) internal view of the projection chamber and camera with the top lid removed (propagation cone is overlaid on the image), (c) schematic system configuration. | 149 |
| Figure 6.4 | Variation of the light intensity of the laser spot on the projection plane captured by the camera. | 151 |
| Figure 6.5 | Training data for the SVR calibration: (a) percentage of the change in the intensity of the laser spot, (b) temporal rate of change in the intensity, (c) comparison of the SVR-estimated force with respect to the reference force, F , recorded by UTM. | 152 |
| Figure 6.6 | (a) FlexiForce sensor under calibration test, (b) force-voltage curve of FlexiForce sensor, (c) experimental setup for the <i>ex-vivo</i> validation test, (d) comparison of the force measured by the optical sensor versus the force measured by the calibrated FlexiForce sensor, (e) schematic system configuration. | 154 |
| Figure 7.1 | A schematic use-case of the proposed sensor for aortic valve localization (the figure is not to the scale) | 161 |
| Figure 7.2 | Cylindrical sensor for cardiovascular MIS applications. | 163 |
| Figure 7.3 | (a) Schematic of the constant bending radius principle, (b) schematic of the variable bending radius principle. | 165 |
| Figure 7.4 | Simplified mechanical model of optical fibers in the proposed sensor with force F applied on it from the corresponding indenter. | 166 |
| Figure 7.5 | (a) Configuration of the external force on the flexible shell, (b) internal view of the meshed model used in the simulation. | 167 |
| Figure 7.6 | Distribution of Von-Mises strain for load-case ($d = 8, \phi = 90$) in: (a) fiber-2 and indenter-2, and (b) the flexible shell. | 168 |
| Figure 7.7 | Normalized variation of the maximum deflection in each optical fiber with respect to the change in the longitudinal and circumferential positions of external force. | 169 |
| Figure 7.8 | Fabricated cylindrical optical-fiber array sensor | 171 |
| Figure 7.9 | Experimental setup, image-based DAQ, and fabricated sensor under the test | 173 |

| | | |
|-------------|---|-----|
| Figure 7.10 | Experimental results of the cylindrical array sensor under the 1 N force in longitudinal and circumferential position. | 175 |
| Figure A.1 | (a) Conceptual integration of tactile sensor on an RMIS instrument (EndoWrist™-da Vinci™ Surgical System, Intuitive Surgical Inc., Sunnyvale, CA), (b) mechanical model of an optical fiber as a beam and its shape in a single radius bending configuration. | 214 |
| Figure A.2 | (a) Structure of the proposed planar tactile sensor, (b) distribution of internal forces in the sensor (FEA). | 215 |
| Figure A.3 | Experimental setup for deflecting optical fiber under (a) CBR, (b) VBR conditions, (c) bending force, theoretical prediction and experimentally measured power loss in the proposed sensor. | 216 |
| Figure A.4 | Bending test of an optical fiber under (a) CBR, (b) VBR configuration. | 217 |
| Figure A.5 | (a) Result of the power-loss in VBR simulation, (b) theoretical prediction vs. experimentally power-loss in the for VBR and CBR. | 218 |
| Figure A.6 | Form2 3D printer working based SLA technology | 219 |
| Figure A.7 | (a) Fabricated Robotic surgery planar sensor, (b) fabricated valvuloplasty and annuloplasty cylindrical sensor, (c) 3D printed model of aortic arch and valve. | 220 |
| Figure A.8 | (a) Schematic diagram of the experimental setup, (b) experimental setup implemented for data acquisition using an Arduino embedded board and a photodetector. | 221 |
| Figure A.9 | Experimental setup implemented for data acquisition using an CCD camera | 222 |
| Figure A.10 | Maximum deflection of the membrane at connection point with the optical fiber versus the pressure. | 223 |
| Figure A.11 | (a) 3D geometrical model of the DBR sensor, (b) 2D structure of the front view of the sensor finite element analysis | 224 |
| Figure A.12 | Mesh quality, geometric features, and the max distributed transverse force per unit length on the membrane. | 225 |
| Figure A.13 | Reaction force on the optical fiber and substrate versus the pressure, membrane with 0.1 mm thickness and elastic modulus 63 GPa. | 226 |

| | |
|--|-----|
| Figure A.14 Reaction force on the optical fiber and substrate versus the pressure, membrane with 0.3 mm thickness and elastic modulus 63 GPa. | 227 |
| Figure A.15 Reaction force on the optical fiber and substrate versus the pressure, membrane with 0.5 mm thickness and elastic modulus 63 GPa. | 227 |
| Figure A.16 Reaction force on the optical fiber versus the different module of elasticity and various thicknesses. | 228 |
| Figure A.17 Beating frequency with respect to different E and t | 229 |
| Figure A.18 Sensor sensitivity with respect E and t | 229 |
| Figure A.19 Various elastic modulus versus the different thicknesses, the line shows minimum acceptable E and t to keep the system linear | 230 |
| Figure A.20 2D front view of the sensor structure with three optical fibers. | 231 |
| Figure A.21 (a) Deflected membrane while is in contact with all three fibers, (b) reaction forces versus the pressure for fibers No.1, No.2, and No.3. | 232 |

List of Tables

| | | |
|-----------|--|-----|
| Table 2.1 | Summary of the representative studies on electrical-based tactile sensors in MIS. | 33 |
| Table 2.2 | Summary of the representative studies proposing tactile sensors for MIS or RMIS based on optical sensing principles. | 56 |
| Table 3.1 | Material models used in finite element modeling of the sensor-tissue simulation. | 72 |
| Table 3.2 | Normalized maximum changes in the output voltage of photodetector and stiffness from simulation and measured in the experiment. | 77 |
| Table 4.1 | Specifications of the samples used in three-point bending tests (n=3) and material properties | 96 |
| Table 4.2 | Specifications of the proposed sensor and comparison with the requirements of various minimally invasive surgeries | 108 |
| Table 4.3 | Comparison of the specifications of the proposed sensor with representative studies. | 108 |
| Table 5.1 | Geometrical constraints and initial dimensions. | 125 |
| Table 5.2 | Material models and mechanical properties of the sensor components | 127 |
| Table 5.3 | Representative design parameters used in the RSO optimization and their corresponding goal function values. | 128 |
| Table 5.4 | Performance of SVR regression calibration. | 132 |
| Table 5.5 | Performance of the sensor in validation experiments. | 133 |
| Table 5.6 | Sensor outputs for 2 N reference force with three elliptical indenters with 2, 4, and 8 mm diameters at left, right and center of the sensor (Numbers in N). | 138 |

| | | |
|-----------|---|-----|
| Table 5.7 | Comparison of physical and functional requirements with the specifications of the proposed sensor. | 139 |
| Table 6.1 | Performance metrics for the proposed image-based force sensing technique for the <i>ex-vivo</i> test in comparison with the literature. | 155 |
| Table 7.1 | Geometric dimensions and mechanical properties of the sensor used in the finite element study. | 164 |
| Table 7.2 | Simulated geometric parameters and values used in finite element simulation. | 167 |
| Table 7.3 | Maximum deflection of optical fibers when force is applied exactly on top of their corresponding indenters. | 168 |
| Table 7.4 | Normalized intensity loss (in percentage of the maximum) in Fiber-1 with 1 N external force. | 176 |
| Table A.1 | Material properties of the sensor components and their dimensions | 225 |

Nomenclature

Symbols

| | |
|----------------|-----------------------------------|
| α | Thermal Expansion Coefficient |
| δ | Contact-induced Indentation Depth |
| δ_{FPI} | Phase Difference |
| ΔT | Temperature Variation |
| $\Delta\theta$ | Angular Misalignment |
| η | Coupling Efficiency |
| η_{eff} | Refractive Index of Core |
| ε | Mechanical Strain |
| γ | Bend Loss Coefficient |
| Λ | Period of Grating |
| λ | Wavelength |
| λ_0 | Mean of Lasing Wavelengths |
| λ_B | Bragg Wavelength |
| ν | Poisson's Ratio |
| ϕ | Phase |
| φ | Circumferential Angles |

| | |
|------------------|-------------------------------------|
| ρ | Resistivity |
| σ | Mechanical Stress |
| θ | Angular Deformations |
| τ | Time Constant |
| ξ | Thermo-optic Coefficient |
| A | Overlap Area |
| a | Radius of Core |
| B | Birefringence |
| b | Breadth of Membrane |
| C | Capacitance |
| C_{01}, C_{10} | 2MR Constitutive Constants |
| d_{eq} | Position of Center of Pressure |
| $D(L)$ | Decay Coefficient |
| E | Elastic Modulus |
| E^* | Effective Elastic Modulus |
| $E_b I_b$ | Flexural Rigidity of Beam |
| $E_c I_c$ | Flexural Rigidity of Composite Beam |
| $E_t I_t$ | Flexural Rigidity of Tissue |
| F | Force |
| F_{eq} | Total Equivalent Contact Force |
| f_b | Beating Frequency |
| $f_b S_w$ | Sensitivity of Sensor |
| I | Intensity |
| I_m | Second Moment of Area |

| | |
|------------------|--|
| k_ϵ | Axial Strain Coefficient |
| k_T | Thermal Coefficient |
| L_c | Effective Length of Fiber Laser |
| n | Refractive Index of Cavity |
| n_0 | Refractive Index of Air |
| n_1 | Refractive Index of Core |
| n_2 | Refractive Index of Cladding |
| P_0 | Input Power |
| p_{11}, p_{12} | Strain-optical Coefficient |
| p_ϵ | Strain-optic Coefficient |
| P_{in} | Input Power |
| P_{out} | Output Power |
| P_s | power at the desired length |
| Q | Electrical Charge |
| R | Resistance |
| r_b | Bending Radius |
| r_{fiber} | Radius of Fiber |
| s | Curvature Length |
| t | Thickness |
| V | Voltage |
| w | Gaussian Mode Field Radius of Optical Fibers |
| $Y_{total}(x)$ | Total Deflection |

Abbreviations

| | |
|--------|---|
| 2MR | Two-term Mooney–Rivlin |
| 3D | Three-dimensional |
| AS | Aortic Stenosis |
| AVR | Aortic Valve Replacement |
| CB-MVR | Catheter-based Mitral Valve Replacement |
| CBR | Constant Bending Radius |
| CBT | Catheter-based Techniques |
| CCD | Charged-coupled Device |
| CS | Cardiac Surgery |
| DAQ | Data-acquisition System |
| DBR | Distributed Bragg Reflector |
| DOF | Degree of Freedom |
| EDM | Electrical discharge Machining |
| EFA | Radiofrequency Ablation Surgery |
| ETO | Ethylene Oxide |
| F/T | Force/Torque |
| FBG | Fiber Bragg Grating |
| FEA | Finite Element Analysis |
| FEM | Finite Element Model |
| FPI | Fabry-Perot Interferometry |
| FSR | Force-sensing Resistor |
| GPM | Gaussian Process Models |

| | |
|------|---|
| GUI | Graphical User Interface |
| IPA | Isopropyl Alcohol |
| ISO | Isolator |
| LED | Light-emitting Diode |
| LIM | Light Intensity Modulation |
| MAE | Mean-absolute Error |
| MEMS | Micro-electromechanical Systems |
| MIS | Minimally Invasive Surgeries |
| MRI | Magnetic Resonance Imaging |
| MVR | Mitral Valve Replacement |
| OSA | Optical Spectrum Analyser |
| PD | Photodetector |
| PDMS | polydimethylsiloxane |
| PM | Phase Modulation |
| PVDF | Polyvinylidene Fluoride |
| RF | Radiofrequency |
| RHS | Right-hand-side |
| RMIS | Robot-assisted Minimally Invasive Surgery |
| RMS | Root-mean-square |
| RNN | Recurrent Neural Networks |
| ROS | Regions of Sections |
| RSO | Response Surface Optimization |
| SLA | Stereo-lithography Apparatus |
| STFN | Smart Touch Fine Needle |

| | |
|------|---|
| SVR | Support Vector Regression |
| TAVI | Transcatheter Aortic Valve Implantation |
| UTM | Universal Testing Machine |
| VBR | Variable Bending Radius |
| WDM | Wavelength Division Multiplexer |
| WM | Wavelength Modulation |

Chapter 1

Introduction

1.1 Minimally Invasive Surgeries

One of the most significant evolutions in surgery was the emergence of Minimally Invasive Surgeries (MIS). In conventional open surgery, surgeons make large incisions on the patients' body to operate on a specific organ. Open surgeries are associated with large amounts of bleeding, post-operative wound infection, trauma, pain, long anesthesia time, prolonged hospitalization, and long post-operative recovery time.

In contrast to open surgery, the MIS approach requires three to four tiny skin incisions (5-15 mm) and is performed using specially-designed long instruments. The MIS instruments and a laparoscopy camera are inserted into the patient's body, e.g., abdomen, arteries, and uterus, through the small incisions (surgical ports) [1]. The first MIS cholecystectomy was performed by Dr. Barry McKernan in 1988 [2].

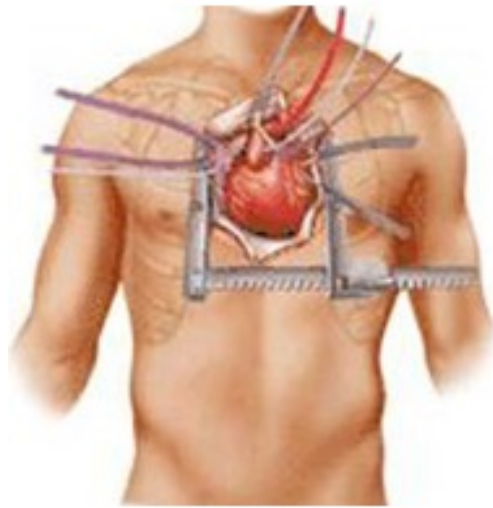
One of the most expanded areas of MIS is the trans-catheter MIS cardiovascular interventions. During MIS cardiovascular interventions, catheter-based techniques (CBT) are used to perform surgery or intervention on heart and vasculature. In this field, cardiac surgeons insert a catheter into the patient's vessels through an incision in the patient's groin or arm. Using fluoroscopy imaging technique, surgeons obtain real-time x-ray images of the catheter and the site surgery. Similar to the general surgeries (in the abdomen area), cardiac surgeries have been revolutionized by MIS CBTs, e.g., valvuloplasty, electro-physiology, and angioplasty [3].

Compared to conventional open surgeries, CBT provides more benefits to the patients, such as the reduction in anesthetic agent dosage, surgical trauma, pain, post-operative hospitalization, and scar tissue formation [4]. However, despite its advantages, MIS has several limitations for surgeons. In MIS, surgeons have compromised hand-eye coordination, tactile information, and direct access to the patient's organs[5]; therefore, the surgeon's field of view and tool movements are restricted [6]. Moreover, since the instruments are long and rigid and pass through a small surgical port, two translational degrees of freedom (DoF) of the surgeon's hands (motion to the left-right and medial-lateral) are lost. This spatial restriction imposes limitations to the working space for a surgeon and significantly affects the dexterity inside the patient's body [7]. Being exposed to the X-ray radiation is another limitation of the MIS surgeries, especially for CBT cardiovascular interventions.

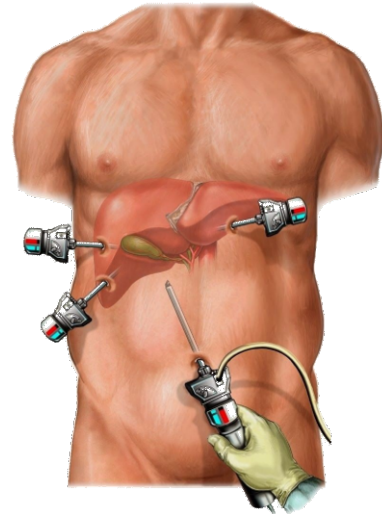
With the emergence of robots in MIS, the accuracy and dexterity of manipulation of surgical instruments in MIS were improved [8]. Furthermore, the surgeon's physical fatigue and ionizing radiation exposure were decreased via robotic-assisted minimally invasive surgery (RMIS) [9]. Robotic surgery was built upon the principles of laparoscopic MIS. The first surgical robot was Da Vinci, which was launched in the early 2000s by Intuitive Inc., CA, US. During RMIS, the surgeon sits behind a console with high-resolution 3D vision of provided by a laparoscopic stereo-camera. The system translates the surgeon's hand motions to the robot arms. The robot arms are equipped with MIS instruments. Figure 1.1 illustrates schematic comparisons between conventional surgery and three main categories of MIS procedures.

Despite the outstanding advantages of manual MIS and RMIS, several limitations persist for surgeons. Most importantly, surgeons lose their natural sense of touch, which results in limited or no haptic perception [10] during surgery.

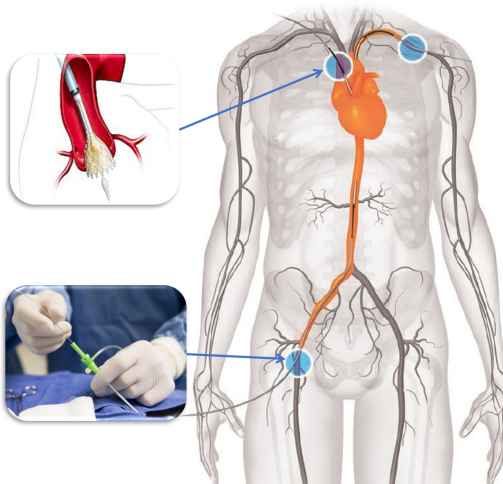
Haptic feedback includes kinesthetic (force) and cutaneous (tactile) feedback, the absence of which may adversely affect surgical efficiency and efficacy; thus, resulting in sub-optimal medical treatment [11]. Limited haptic feedback during a surgery adversely affects the ability of surgeons in tissue distinction and geometrical perception [12]. During open surgery, the kinesthetic perception of the surgeon traces the magnitude and direction of forces applied to the patient's organs, while the surgeon identifies unknown tissues through tactile perception [8]. Similarly, the surgeon can identify underlying (malignant) lump(s) through palpation of the tissues [8].



(a)



(b)



(c)



(d)

Figure 1.1: Comparison between a conventional open surgery and three main categories of MIS procedures. (a) conventional open heart surgery, (b) laparoscopy, (c) catheter-based techniques (CBT), and (d) robotic-assisted minimally invasive surgery (RMIS).

To alleviate the loss of tactile feedback during MIS and RMIS, researchers have proposed different tactile sensors to measure the important tactile cues for tissue distinction and operation, i.e., force and stiffness. The research for developing robust and accurate tactile sensors for MIS and RMIS applications has gained momentum within the last decade, thanks to the technological advancements in micro-electromechanical systems (MEMS). Within the last five years and due to the unprecedented advancements of the artificial intelligence and learning-based methods, novel calibration methods and sensor inference techniques have been developed which have pushed the boundaries of the state-of-the-art for MIS and RMIS.

1.2 Tactile Sensors for MIS

An adverse consequence of the loss of tactile perception is unintentional excessive instrument force on tissues [11]. Clinical evidence indicates that force feedback during MIS and RMIS helps surgeons to apply appropriate force to tissues to avoid tissue damage while performing surgery. For example, da Vinci surgical system, the first and one of the most commercially successful surgical robots to date [9], does not provide the force or haptic feedback. It has been reported that the grasping force would be significantly reduced by force feedback in the da Vinci-performed operations [8].

Utilization of a sensor to measure the tactile cues can ultimately increase the efficiency of the surgery by increasing the surgeon's situational awareness[8], especially for high-risk surgeries, e.g., heart and brain [13]. Such a tactile sensor shall meet specific physical and functional requirements. For example, surgical instruments like graspers and forceps have small jaws. Therefore, the sensor should be miniaturized to fit at the desired location. Also, the sensor shall be able to work under both static and dynamic conditions, specifically for moving organs like the heart [14].

Similarly, the surgeon may need to hold tissue by applying a static force continuously [15]. This static force must be constant during the holding period. Also, to avoid tissue laceration, the force must not exceed a specific range. However, due to the viscoelastic nature of the tissues, tool-tissue interaction force might diminish over time (a.k.a. stress-relaxation phenomenon), leading to tissue slippage [16]. Another example would be when the procedure is performed under magnetic

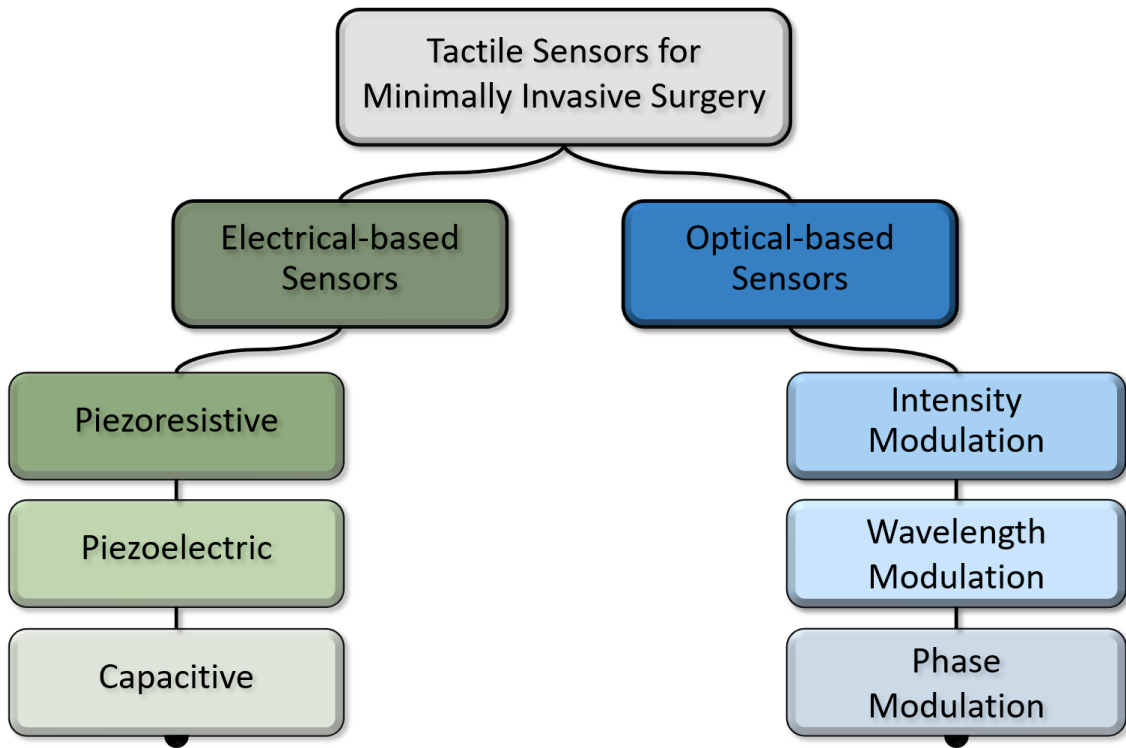


Figure 1.2: Categories of various tactile sensors proposed in the literature for minimally invasive surgery.

resonance imaging (MRI). Such a surgical procedure requires the sensor being MRI-compatible. Moreover, in some procedures like cardiovascular MIS, the sensor must be electrically-passive to avoid the interference with the electrical activity of the heart [13, 17].

Tactile sensors for the MIS applications have been mainly developed based on the electrical or optical principles. Figure 1.2 shows the categories of tactile sensors for MIS based on their sensing principles. Electrical-based tactile sensors are the most proposed sensing modality for MIS [13, 18]. Electrical sensors can be further categorized as piezoelectric, piezoresistive, and capacitive sensors. Although the electrical-based sensors address most of the requirements mentioned above, are neither MRI-compatible nor electrically-passive. Besides, the piezoelectric-based sensor can not measure the static force. High hysteresis and lack of repeatability are other disadvantages of this category of sensors. On the other hand, optical fiber-based sensors are biocompatible, lightweight, and corrosion resistance. Moreover, optical sensors are electrically passive and work appropriately in MRI environments [19]. This has led to the recent wide adoption of the optical-based sensor for

MIS and RMIS [13].

Optical sensors mainly work based on three principles: light intensity modulation (LIM), phase modulation (PM) and, wavelength modulation (WM) [13, 17]. In comparison, the LIM-based sensor provides unique advantages by being inexpensive, thermally insensitive, simple design and easily implementable, while PM-and WM-based types need a relatively expensive measurement system to calculate physical parameters like force and displacement. The downside of LIM-based sensors is that the miniaturization is still a critical issue which limits their scalability. This limitation largely affects the resolution and range of measurement [20, 21].

The design requirements (a.k.a. constraints) for the tactile sensors in MIS applications can be related to the physical and functional properties of the sensors. Physical requirements attribute mainly to the shape and size of the sensors, while the functional constraints relate to the compatibility, interaction, and performance of the sensor at the bio-environment. As an example of physical constraints, an MIS tactile sensor should be small in size and cylindrical in shape to be integrable at the body or tip of a catheter. As a functional requirement, the sensor should be capable of measuring the contact force in a range of 0-5 N with a resolution of 0.01N [22]. Furthermore, the sensor should be fairly sensitive, linear, and show a low level of hysteresis. Accordingly, the present thesis proposes the various optical-fiber-based tactile sensors for MIS/RMIS applications.

1.3 Thesis Motivation

Minimally invasive surgery has had a fast adoption within the last three decades worldwide. It is projected that in the next decade, more than 80% of all surgeries will be performed with the MIS approach. Reducing the trauma, pain, incision size, blood loss, anesthesia dosage, time of surgery, post-operative infection, and length of stay at the hospital, as well as faster recovery time, are the outstanding advantages of MIS compared to open surgery. In addition, the emergence of robot-assisted MIS (RMIS) has improved the dexterity and degrees-of-freedom of the MIS instruments, especially for precision-demanding procedures, e.g., cardiac and vascular surgery. Also, RMIS has enabled surgeons to perform remote surgery without a need to be present in the operating room. Moreover, the evolution of 3D vision systems provided surgeons with high-resolution real-time

imaging of the surgical area.

However, in conventional open surgery, the surgeon has direct access to the patient's anatomy and palpates the patient's organs and tissues for identification and diagnosis. Through palpation, the surgeon collects tactile information through fingers. For example, palpation helps to distinguish between different types of tissue and find the important anatomical landmarks. A Surgeon can detect the location of a hidden lump or abnormal tissue by touching the surrounding area and identifying the discontinuity in tissue softness. Also, tactile perception provides essential feedback to the surgeon to control the force on surgical tools, e.g., graspers or forceps, to avoid tissue damage and laceration or to prevent tissue slippage. Considering the small incisions made for MIS, limited hand-eye coordination, and rigidity of the MIS instruments, the surgeon's tactile perception is limited and not intuitive. Especially in the case of RMIS procedures, the tactile perception is lost.

In general, tactile perception includes information about the texture, shape, force, friction, temperature of tissues. Furthermore, during MIS and RMIS, surgeons have limited information (merely obtained through images) on how hard they are pulling, grasping, cutting, twisting, and/or suturing a tissue. Magnified 2D image from the camera or fluoroscopy imaging exaggerates the small movement of the surgeons' hand or organs' motions, e.g., heart beating, and exacerbates the erroneous tactile perception of surgeons.

Thanks to the advancement of micro-electromechanical systems (MEMS) technology in the last decade, the research on developing smart sensor-equipped MIS instruments for various MIS and RMIS procedures has gained momentum in the last decade. Reconstruction of the lost tactile perception and enhancing the performance of MIS and RMIS instruments through ("tactile sensors") have motivated the researchers. These tactile sensors are typically integrated at the end-effectors or the tip of the conventional MIS tools and provide surgeons with information about the force, position, tissue softness, and location of the hidden lumps. Being biocompatible, miniaturizable to fit on the limited space on the surgical tools, and performing under both static and dynamic loading condition are significant requirements of tactile sensors. In addition, since typically operation rooms have multiple electronic devices emitting strong electro-magnetic fields, tactile sensors shall be MRI-compatible and electrically-passive.

In the present thesis, initially a comprehensive critical review of the state-of-the-art, applications

and perspectives of tactile sensors for MIS applications was performed. My doctoral research was to address the clinical need for small and accurate yet robust tactile sensors for MIS and RMIS applications. Based on the literature review, miniaturization and robustness of sensor outputs has been the most important technological challenges for MIS tactile sensors. The main motivation of this doctoral research was to conceptualize, develop, and validate miniaturized tactile sensors suitable for integration with MIS instruments and compatible with the physical and functional requirements of MIS and RMIS surgical procedures.

1.4 Objective and Scope

As discussed in Chapter 1, the optical-fiber-based sensing is the most compliant principle with the requirements of MIS and RMIS procedure. Therefore, the objective of my doctoral research was to conceptualize, design, model, prototype, and validate optical-fiber-based tactile sensors for MIS and RMIS procedures. To this end, the scope of this doctoral thesis is as follows:

- (1) Developing a hybrid piezoresistive-optical tactile sensor for tissue stiffness measurements and lump detection in MIS and RMIS, which includes:
 - Conception and design of a hybrid piezoresistive-optical tactile sensor,
 - Modeling of the optical fiber coupling-loss principle and composite beam theory,
 - Mechanical modeling and characterization of a synthesized tissue phantom,
 - Finite element modeling and simulation of the mechanics of sensor-tissue interaction
 - Simulation of the stiffness measurement and lump-detection capabilities of the proposed sensor,
 - Prototyping of the sensor using MEMS techniques, and
 - Experimental validation of the sensor performance under dynamic loading conditions.
- (2) Developing a multi-physics optomechanical model for a distributed Bragg reflector force sensor based on the birefringence phenomenon, which includes:

- Structural design of the sensor and fabrication of the proposed sensor using micro-machining techniques,
 - Development of an optomechanical theoretical model for the sensing principle using theory of elasticity and optical birefringence principles,
 - Material characterization of the sensor components,
 - Multi-linear regression calibration of the developed force sensor,
 - Identification and modeling of the thermal and temporal drift in the proposed sensor,
 - Proposing compensation methods for accounting for the thermal and temporal drift of the sensor, and
 - Experimental validation of the sensor performance.
- (3) Developing a sensor-embedded surgical grasper for MIS procedures based on a novel bending-loss-based sensing principle, which includes:
- Proposition of a novel bending-loss-based force sensing principle suitable for miniaturization,
 - Parametric design of a force sensor embedded on the grasper jaw based on the proposed sensing principle,
 - Finite element modeling of the proposed sensor,
 - Miniaturization of the proposed sensor based on structural optimization,
 - Prototyping the proposed sensor and its integration at the tip of an MIS grasper,
 - Proposition of a novel rate-dependent learning-based calibration method to compensate the nonlinearities of the sensor, and
 - Experimental validation of the sensor performance under dynamic loading conditions.
- (4) Developing an accurate real-time image-based technique for optical force sensing with application in MIS tactile sensors, which includes:
- Proposition of an image-based light intensity estimation technique based on RGB-image acquisition,

- Proposition of a novel rate-dependent learning-based calibration method using the proposed image-based light intensity sensing, and
 - *ex-vivo* validation of the sensor performance under dynamic loading conditions.
- (5) Design, verification and experimental validation of a novel array optical-fiber sensor for lateral force measurement for MIS valvuloplasty, which including:
- Conceptualize and design of the sensor with the cylindrical configuration for MIS valvuloplasty,
 - Mechanical modeling of the sensor based on the bending-loss principle and beam theory,
 - Simulation of the sensor-valve interaction using the finite element method, and
 - Prototyping of the sensor using advanced 3D printing technique and experimental validation.

1.5 Contributions

The major contribution of this doctoral research is in proposing, modeling, fabricating, and validating fully-optical, miniaturized, and scalable sensors for lateral force measurement in MIS and RMIS applications. As will be discussed in Chapter 2, most of the previously proposed sensors proposed for MIS and RMIS are normal force sensors, a.k.a. tip force sensors. In fact, there is a knowledge gap in the literature about lateral force sensing in MIS and RMIS. Moreover, with the expedited global expansion of these procedures the clinical need for surgical instruments with normal and lateral force sensing capabilities is eminent and prominent. In addition, the miniaturization schema proposed and utilized throughout this research allows for adapting to various functional and physical requirements depending on the use-case applications and sensing principles used, e.g., intensity modulation, wavelength modulation.

Another contribution of this research was the development and utilization of analytical optomechanical models for the proposed sensors. Whereas, the proposed sensor structures were modeled through mechanics principles and the performance of the sensors were predicted theoretically

through coupling the mechanical models with optical models of intensity (or wavelength) modulation. Such analytical optomechanical models facilitated the structural miniaturization and accommodating the physical and functional design constraints.

Another contribution of this research was in advancing the bending-based sensing principle by the development and validation of a novel variable-bending radius (VBR) principle for light intensity modulation modality. The proposed VBR sensing principle showed high sensitivity and facilitated further miniaturization of the optical-fiber-based tactile sensors compared to existing methods. Based upon that, another contribution of this research was the development of a miniaturized, accurate, robust, and simple-structure optical force sensor which was easy to integrate at the tip of MIS graspers. The developed theoretical model for VBR was at the core of structural optimization to obtain the smallest possible structure with maximum sensitivity.

Also, to the best of my knowledge, this research was the first to utilize a nonlinear rate-dependent learning-based calibration schema for bending-based force sensors. This calibration scheme successfully captured the sensor's hysteresis and rate-dependency under both dynamic and static loading conditions. Compensating for rate-dependency and hysteresis is a major technological challenge that has limited the use of highly-flexible sensing elements in tactile sensors.

In the end, the development and integration of a robust image-based light intensity technique with a learning-based calibration method paved the way for designing array sensor configurations with multiple optical fibers. It has eliminated the need for multiple, bulky, and expensive photodetectors for tactile sensors.

For the sake of brevity, a list of other contributions of this research are as follows:

- (1) A novel hybrid tactile sensor capable of simultaneous measurement of lateral force, tissue stiffness, and mass localization,
- (2) Developing a method for the measurement of tissue stiffness using the optical fiber coupling loss and composite beam theory,
- (3) A novel aging-drift compensation model for temporal and thermal effects of drift in a distributed Bragg reflecting force sensor,

- (4) A novel catheter-tip optical-fiber array sensor to measure the lateral forces for detecting the heart aortic valve in MIS valvuloplasty,
- (5) Adapting a 3D printing technique for rapid prototyping of the miniaturized tactile sensors which is capable of using biocompatible materials.

The findings of this research have been published in the form on five journal articles and were presented in four conferences. An extensive list of the author's publications is provided in Section 1.6.

1.6 Publications

The results of this doctoral research are published (or under review) as summarized below:

- (1) Naghmeh Bandari, Javad Dargahi, and Muthukumaran Packirisamy. Optical fiber array sensor for force estimation and localization in tavi procedure: Design, modeling, analysis and validation. *IEEE Sensors*, Under-review, 2021
- (2) Naghmeh Bandari, Patrick Orsini, Corbeil Jean-simon, Érick Jarry, Marie-maude de Denus Baillargeon, Maroun Massabki, Javad Dargahi, and Muthukumaran Packirisamy. Optomechanical modeling and validation of a distributed bragg reflector force sensor with drift and temperature compensation. *IEEE Sensors Journal*, 21(3):2929–2941, 2020 [24]
- (3) Naghmeh Bandari, Javad Dargahi, and Muthukumaran Packirisamy. Image-based optical-fiber force sensor for minimally invasive surgery with ex-vivo validation. *Journal of the Electrochemical Society*, 167(12):127504, 2020 [25]
- (4) Naghmeh Bandari, Javad Dargahi, and M Packirisamy. Camera-based optical-fiber tactile sensor for intraoperative grasping force measurement. In *237th ECS Meeting with the 18th International Meeting on Chemical Sensors (IMCS 2020)*. ECS, 2020 [26]
- (5) Naghmeh Bandari, Javad Dargahi, and Muthukumaran Packirisamy. Tactile sensors for minimally invasive surgery: a review of the state-of-the-art, applications, and perspectives. *IEEE Access*, 8:7682–7708, 2020 [27]

- (6) Naghmeh Bandari, Javad Dargahi, and Muthukumaran Packirisamy. Miniaturized optical force sensor for minimally invasive surgery with learning-based nonlinear calibration. *IEEE Sensors Journal*, 20(7):3579–3592, 2020 [21]
- (7) Naghmeh Bandari, Javad Dargahi, and Muthukumaran Packirisamy. Validation of a variable bending radius sensing principle for optical-fiber tactile sensors. In *2019 Photonics North (PN)*, pages 1–1. IEEE, 2019 [28]
- (8) Naghmeh M Bandari, Amir Hooshair, Muthukumaran Packirisamy, and Javad Dargahi. Bending-based formulation of light intensity modulation for miniaturization of optical tactile sensors. In *Optical Sensors*, pages SeM2E–3. Optical Society of America, 2018 [20]
- (9) Naghmeh M Bandari, Roozbeh Ahmadi, Amir Hooshair, Javad Dargahi, and Muthukumaran Packirisamy. Hybrid piezoresistive-optical tactile sensor for simultaneous measurement of tissue stiffness and detection of tissue discontinuity in robot-assisted minimally invasive surgery. *Journal of biomedical optics*, 22(7):077002, 2017 [29]
- (10) Naghmeh M Bandari, Amir Hooshair, Muthukumaran Packirisamy, and Javad Dargahi. Optical fiber array sensor for lateral and circumferential force measurement suitable for minimally invasive surgery: Design, modeling and analysis. In *Specialty Optical Fibers*, pages JT4A–44. Optical Society of America, 2016 [30]

1.7 Thesis Layout

This thesis is prepared in manuscript-based style as per "*Thesis Preparation and Thesis Examination Regulations (version-2020) for manuscript-based Thesis*" guideline of the School of Graduate Studies at Concordia University. This thesis is prepared in eight chapters based on the contents of five published journal articles, four published conference papers, one journal article under review and two under-preparation manuscripts. In order to avoid redundant contents and the fact that two of the conference papers reflected the preliminary results of Chapter 5, they are included in Appendices (A.1 and A.2). In the following, the layout of the chapter are presented:

Chapter 2 presents a critical literature review of the state-of-the-art, applications, and future perspectives of MIS tactile sensors published in *IEEE Access* journal. The contents of this chapter are duplicated from:

- (1) Naghmeh Bandari, Javad Dargahi, and Muthukumaran Packirisamy. Tactile sensors for minimally invasive surgery: a review of the state-of-the-art, applications, and perspectives. *IEEE Access*, 8:7682–7708, 2020 [27]

Chapter 3 presents the novel hybrid tactile sensor based on the published journal article in the *Journal of Biomedical Optics*. The contents of this chapter are duplicated from:

- (1) Naghmeh M Bandari, Roozbeh Ahmadi, Amir Hooshier, Javad Dargahi, and Muthukumaran Packirisamy. Hybrid piezoresistive-optical tactile sensor for simultaneous measurement of tissue stiffness and detection of tissue discontinuity in robot-assisted minimally invasive surgery. *Journal of biomedical optics*, 22(7):077002, 2017 [29]

The contribution of R. Ahmadi was in design, prototyping, and experimental data collection. The contribution of A. Hooshier was in material characterization and model fitting.

Chapter 4 presents a novel optomechanical model for a distributed Bragg reflecting force sensor with drift and temperature compensation based on a published journal article at *IEEE Sensors Journal*. The contents of this chapter are duplicated from:

- (1) Naghmeh Bandari, Patrick Orsini, Corbeil Jean-simon, Érick Jarry, Marie-maude de Denus Baillargeon, Maroun Massabki, Javad Dargahi, and Muthukumaran Packirisamy. Optomechanical modeling and validation of a distributed bragg reflector force sensor with drift and temperature compensation. *IEEE Sensors Journal*, 21(3):2929–2941, 2020 [24]

The second to the sixth co-authors in [24] were industrial collaborators and contributed in design of the sensor, prototyping of the device, preparation of the test setup, and data collection of the study.

Chapter 5 presents a miniaturized optical tactile sensor based on VBR sensing principle. The contents of this chapter are collated from one journal article, published in the *IEEE Sensors Journal* and two conference papers presented by the author at *Advanced Photonics Congress 2018*, Zurich, Switzerland, and *Photonics North Conference 2019*, Quebec City, QC, Canada:

- (1) Naghmeh Bandari, Javad Dargahi, and Muthukumaran Packirisamy. Miniaturized optical force sensor for minimally invasive surgery with learning-based nonlinear calibration. *IEEE Sensors Journal*, 20(7):3579–3592, 2020 [21]
- (2) Naghmeh Bandari, Javad Dargahi, and Muthukumaran Packirisamy. Validation of a variable bending radius sensing principle for optical-fiber tactile sensors. In *2019 Photonics North (PN)*, pages 1–1. IEEE, 2019 [28]
- (3) Naghmeh M Bandari, Amir Hooshair, Muthukumaran Packirisamy, and Javad Dargahi. Bending-based formulation of light intensity modulation for miniaturization of optical tactile sensors. In *Optical Sensors*, pages SeM2E–3. Optical Society of America, 2018 [20].

The contribution of A. Hooshair in [20] was in material characterization and model fitting.

Chapter 6 introduces a novel image-based light intensity measurement system and calibration methods for force sensing in MIS applications based on a published journal article in *Journal of the Electrochemical Society* and a conference article at *237th ECS Meeting with the 18th International Meeting on Chemical Sensors 2020*, Montreal, Canada, May 2020. The contents of this chapter were collated from:

- (1) Naghmeh Bandari, Javad Dargahi, and Muthukumaran Packirisamy. Image-based optical-fiber force sensor for minimally invasive surgery with ex-vivo validation. *Journal of the Electrochemical Society*, 167(12):127504, 2020 [25]
- (2) Naghmeh Bandari, Javad Dargahi, and M Packirisamy. Camera-based optical-fiber tactile sensor for intraoperative grasping force measurement. In *237th ECS Meeting with the 18th International Meeting on Chemical Sensors (IMCS 2020)*. ECS, 2020 [26]

Chapter 7 presents a novel array optical-fiber-based sensor for MIS valvuloplasty applications based on a conference paper presented by the author at *Advanced Photonics Congress 2016*, Vancouver, BC, Canada and a journal article under review at the *IEEE Sensors Journal* including the prototyping and experimental validation of the proposed array sensor. The contents of this chapter are composed of:

- (1) Naghmeh M Bandari, Amir Hooshier, Muthukumaran Packirisamy, and Javad Dargahi. Optical fiber array sensor for lateral and circumferential force measurement suitable for minimally invasive surgery: Design, modeling and analysis. In *Specialty Optical Fibers*, pages JT4A–44. Optical Society of America, 2016 [30]

The contribution of A. Hooshier was in the manuscript preparation.

- (2) Naghmeh Bandari, Javad Dargahi, Muthukumaran Packirisamy. Optical Fiber Array Sensor for Force Estimation and Localization in TAVI Procedure: Design, Modeling, Analysis and Validation, *IEEE Sensors Journal*. (*under review*).

Chapter 8 provides a summary of the research with concluding remarks and recommendations for future studies.

In addition, an appendix is provided at the end of this thesis, which is comprised of five parts. Section A.1 and A.2 of the appendix is duplicated of two conference papers, i.e., [20] and [28], respectively.

Section A.3 of the appendix provides a summary of the methods for fabrication of the tactile sensors and experimental setup for data acquisition for future researchers. Accordingly, a comprehensive study regarding the advanced fabrication technique for tactile sensors is under preparation to be submitted as a journal article, as below:

- (1) Naghmeh Bandari, Javad Dargahi, and Muthukumaran Packirisamy. 3D printing of Optical Sensing Elements: Challenges and Solutions. *Under preparation*.

Section A.4 and A.5 of the appendix present the results of structural and material optimization and two preliminary studies for alternative designs of the sensor introduced in Chapter 4. These studies are under preparation to be submitted as a journal article, as below:

- (1) Naghmeh Bandari, et al. Optomechanical Modeling and Validation of a nonlinear bi-variable DBR fiber laser force sensor, *Under preparation*.

Chapter 2

Tactile Sensors for Minimally Invasive Surgery: A Review of the State-of-the-Art, Applications, and Perspectives

Minimally invasive surgery has been one of the most significant evolutions in medicine. In this approach, the surgeon inserts specially-designed instruments through a small incision on the patient's skin into the body cavities, abdomen, veins or, arteries and performs the surgery on organs. As a major limitation, surgeons lose their natural tactile perception due to indirect touch on the organs. Since the loss of tactile perception compromises the ability of surgeons in tissue distinction and maneuvers, researchers have proposed different tactile sensors. This review is to provide researchers with a literature map for the state-of-the-art of tactile sensors in minimally invasive surgery, e.g. in robotic, laparoscopic, palpation, biopsy, heart ablation, and valvuloplasty. In this regard, the pertinent literature from the year 2000 on sensing principles, design requirements, and specifications were reviewed in this study. The survey showed that size, range, resolution, variation, electrical passivity, and magnetic-resonance-compatibility were the most critical specification to study for tactile sensors. Based on the results, some of the requirements, e.g., magnetic-resonance-compatibility and

electrical passivity are of less generality and more application-dependent; however, size, resolution, and range specifications differ for various applications and are of utmost importance.

2.1 Introduction

Minimally invasive surgery (MIS) has been the preferred surgical approach over the conventional open surgery due to various advantages. MIS approach allows the surgeon to reach the internal anatomy through small skin incision using specifically-designed low-profile surgical instruments or flexible catheters [1]. As a result, MIS reduces the anesthesia time, incision size, intraoperative blood loss, postoperative infection, trauma, and hospitalization time [8].

This review aims to provide an overview of the state-of-the-art of the proposed tactile sensors integrated with the MIS and RMIS surgical instruments. Previous reviews in the literature have mainly focused on either optical or electrical sensors, e.g., [31]. Also, the reviews which covered both principles were not specifically focused on the MIS/RMIS applications, e.g., [32]. To this end, in this review, various types of tactile sensors, the sensing principles, surgical applications, advantages, and limitations were discussed. Also, the theoretical background of the sensing principles and design requirements of the sensors were critically described and compared. Different physical, engineering, and biologic requirements of the tactile sensors, i.e., size, range, resolution, variation, electrical passivity, and MRI-compatibility, were highlighted. In the end, the concluding remarks summarized the current technological obstacles and perspectives for future research and development.

2.2 Methodology

Researchers have investigated the physical and functional requirements of tactile sensors for surgical applications from various points of view, e.g., geometrical, mechanical, electrical, and medical specifications. Therefore, the available literature is broad and multi-disciplinary. This review is based on surveying the literature on *Google Scholar*, *Scopus*, *Engineering Village*, and *PubMed*. The period was limited to articles published from the year 2000 to 2020. Keywords used in the searches were logical ('.AND.'-'OR.') combinations of 'tactile sensor', 'force sensor', 'pressure

sensor', '*optical sensor*', '*fiber optic sensor*', '*MIS sensor*', '*RMIS sensor*'. The duplicate findings were discarded and the remaining papers were reviewed according to their sensing principles with application in MIS/RMIS procedures, e.g., robotic surgery, laparoscopy, palpation probing, biopsy needling, heart ablation, valvuloplasty. The summary of the literature review is provided in Section 2.3.

2.3 Tactile Sensors in Minimally Invasive Surgery

2.3.1 Electrical-based Tactile Sensors in MIS

In the last decade, many tactile sensors have been developed and investigated for MIS/RMIS applications. Although they were mostly research prototypes, a few were commercialized. The application of the sensor is a major factor that imposes physical and functional requirements. Therefore, in choosing a sensing principle, the application factor must be carefully taken into account. Researchers must first define the use-case of the sensor before adopting a sensing principle and developing a sensor upon that.

The most adopted sensing principles for MIS and RMIS tactile sensors are electrical-based sensors [13, 18]. These tactile sensors are further categorized into piezoresistive, piezoelectric, and capacitive sensors. In the following, the electrical-based tactile sensors are summarized. In the end, a summary of verified and validated electrical-based MIS and RMIS sensors are tabulated.

Piezoresistive Tactile Sensors

The piezoresistive sensing principle is based on the change in the resistivity of the material caused by a mechanical strain in response to a physical stress, e.g., compressive, shear, thermal stress. The change in the resistance of a (semi-)conductor is a function of its physical dimensions and the material resistivity. The change in the dimensions is exploited mainly in the metallic conductors. For example, strain-gauges have been developed based on the geometrical deformation of strain-sensor-embedded structures. For semiconductors, however, the change in (specific) resistivity is employed [33].

Strain gauges are a popular type of piezoresistive sensors, which are normally thin, long, and

zig-zag-patterned conductors. When a conductive material is deformed, its dimension vary in the x, y, and z directions due to its Poisson's ratio. The spatial strains caused by the deformation regulates the variation of the resistance [33, 34] according to Eq. 1.

$$\frac{\Delta R}{R} = (1 + 2\nu) \frac{\Delta L}{L} + \frac{\Delta \rho}{\rho}, \quad (1)$$

where, R , ν , and ρ are the resistance of the piezoresistor, Poisson's ratio, and resistivity, respectively. While $\Delta \rho / \rho$ is negligible in metals and strain gauges, it is noticeable in semiconductors. The change in the resistance can be expressed in terms of the applied pressure, force, temperature or deformation. The applied stress can be further written in terms of the observed strain using a constitutive equation, e.g., linear Hooke's law for springs.

In an early study, Tanimoto *et al.* [35] proposed a micro piezoresistive force sensor for intravascular neurosurgery to measure the interaction force between the catheter with 1.65 mm of diameter and blood vessels. For the first time in the world, they evaluated their tactile sensor in a canine animal model. The sensor was comprised of a set of piezoresistive strain gauge on a silicon diaphragm. The silicon diaphragm would deflect due to the applied pressure, and the resistance of the strain gauges would change. The validation was performed for the range of force caused by the blood pressure in healthy circulation, i.e., 60-130 mmHg. Their sensor was capable measuring at a rate of over 2 kHz and successfully captured the fluctuation of blood pressure.

Similarly, Dargahi *et al.* [36] mounted two micro-strain-gauge sensors at the back-face of a custom-designed endoscopic grasper. Two different types of the proposed grasper and their associated electronic feedback system is shown in Figure 2.1(a). The magnitude of the applied force on the grasper was displayed on a light-emitting diode (LED) display (Figure 2.1(b)). Their force sensor was working linearly in the range of 0.5 to 10 N with 0.5 N precision. The sensor had high sensitivity and a wide range of measurement suited for the endoscopic surgery. Since endoscopic grasper was to work safely in the liquid-present human body, they encapsulated the sensor with a silicon rubber wrap that sealed the tactile sensor. King *et al.* [37, 38] integrated a FlexiForceTM piezoresistive force sensor on a surgical tool of the da Vinci system and transmitted the grasping force to the surgeons. Their study revealed that the force feedback could enhance the safety in

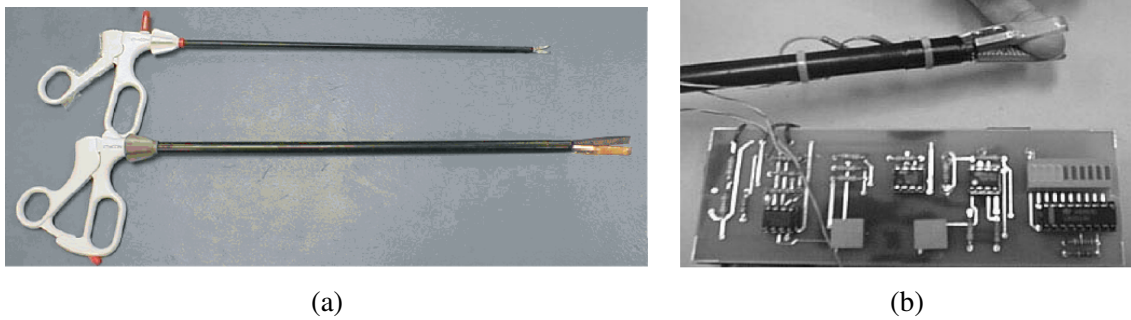


Figure 2.1: (a) Two sensorized graspers with micro strain gauges placed at the jaws, (b) electronic feedback system with LED to display the sensor output [36].

robotic surgery by reducing the grasping forces during the procedures significantly.

In another effort, Hu *et al.* [39], developed a tactile sensor inspired by the biological hair cells. The hair cells consist of a cilium and a neuron. When an external force or local fluid flow deforms the cilium, the mechanical deformation is conveyed through the neuron attached to the bottom of the cilium and generates the action. This bioinspired tactile sensor was proposed for robotic end-effector. It was composed of a central silicon post and a bottom polyamide diaphragm with four integrated piezoresistors. Figure 2.2(a) illustrates the 3D design, and the view of the bottom surface included the resistors. Bending the silicon post would deform the diaphragm on which piezoresistors were located. As a result, three components of the mechanical forces were captured by four piezoresistors. Having the high aspect-ratio silicon post surrounded by a cylindrical cavity increased the sensitivity of the sensor as well as the measurement range.

To have a structure and size suited for the MIS instrument, a deep reactive-ion etching process was used for the fabrication of their sensor. The micro-needle pushing experiment was done in three directions of X, Y, and Z, while the differential voltages of resistors were recorded for calibration. The experimental results showed the shear and normal force sensitivity of 10.8 V/N and 3.5 V/N , respectively. This bio-inspired tactile sensor was a promising device for MIS applications due to its high sensitivity, durability, and simplicity. However, due to the limited lateral displacement of the silicon post, the sensor output would saturate in a shear force greater than 0.05 N . The schematic of their tactile sensor on a printed circuit board mounted on a robotic end-effector and the fabricated sensor with its wire-bonding are shown in Figure 2.2(b).

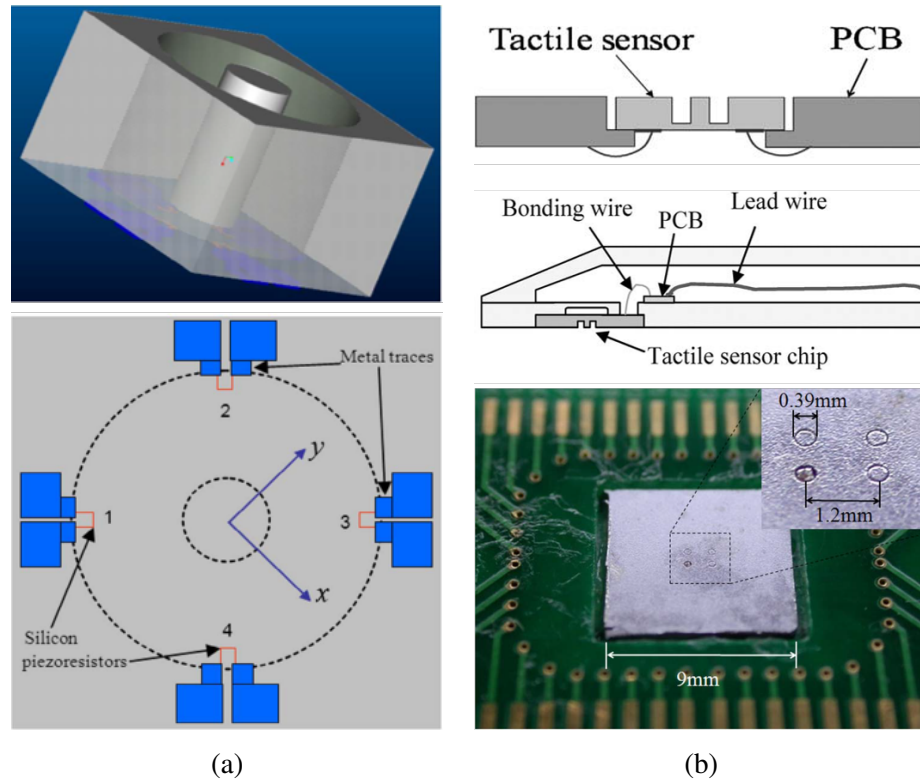


Figure 2.2: Bioinspired piezoresistive tactile sensor by Hu *et al.*[39]: (a) 3D design and the bottom-view of the embedded resistors, (b) microscopic view of the assembled tactile sensor and its associated circuitry.

In another study, Zarenia *et al.* [40] sensorized a bipolar forceps to measure tool-tissue interaction force during the neurosurgical procedure. They installed strain gauge sensors to a commercially available bipolar forceps. When the surgeon opens and closes the prongs of the forceps, forces would be applied perpendicular to the longitudinal axis of the prongs. These forces would cause deformation in strain gauges and subsequently change their electrical resistance. They proposed two configurations for the strain gauges. In the first design, for axial measurement, a set of strain gauges were installed on the lateral side of the forceps along the X-axis, as shown in Figure 2.3(a). Since in reality, in addition to the axial strain, a lateral strain is occurred by the axial shortening in forceps prongs, a planar configuration with two sets of strain gauges in both X- and Y- axes were developed. Figure 2.3(b) depicts the planar configuration. To increase the sensitivity, Zarenia *et al.* used finite-element analysis to optimize the location of the strain gauges on the forceps.

They tested the axial and planar bipolar forceps in five different neurosurgical tasks on two

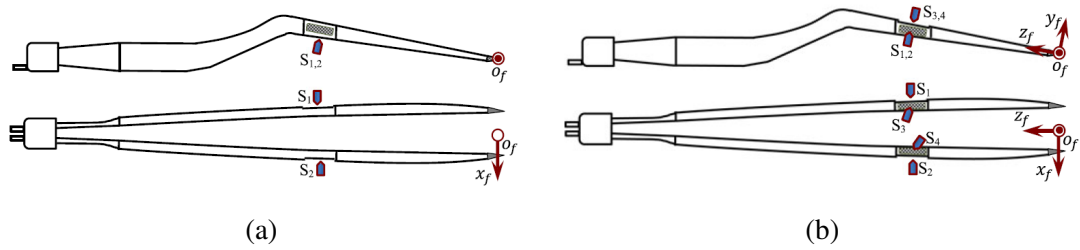


Figure 2.3: Placement of strain gauges on a bipolar forceps: (a) axial sensors, (b) planar sensors [40].

cadaveric brains. In all tasks, the axial forces were less than the planar force. Moreover, their sensorized forceps showed the efficiency of measuring the real-time intraoperative tool-tissue interaction force. Such information would be invaluable for training and evaluating the performance of inexperienced surgeons with sensor-equipped surgical robots and virtual reality simulators.

Although piezoresistive tactile sensors exhibit high dynamic range of measurement, high spatial resolution, simple manufacturing process, and durability, their major limitation is hysteresis [32]. Unless compensated, hysteresis decreases the reliability of the system by reducing the sensitivity and repeatability of the tactile sensors [13, 32]. As an option, embedding the piezoresistors in a flexible self-recoverable structure is an option [41]. However, a secondary hysteresis might occur due to the viscoelastic properties of such a structure. Another possibility would be to compensate for the hysteresis through proper nonlinear calibration [21]. A summary of the state-of-the-art piezoresistive tactile sensors postulated for MIS are mentioned in Table 2.1.

Piezoelectric Tactile Sensors

Since 1880, the discovery of the piezoelectric effect led to the most significant revolution in developing transducers and sensors. Also, with the discovery of the piezoelectricity in Polyvinylidene Fluoride (PVDF), it has emerged in the electrical-base sensors in the 60s. Piezoelectricity is the phenomenon of accumulation of electric charge on the surface of a solid due to physical stress. Such accumulation of charge on one surface of a solid produces electrical potential difference across the solid. Consequently, the deformed solid acts as a capacitor. However, since the electric charges tend to migrate from high potential to low potential, and in the absence of a physical barrier, e.g.,

di-electric, the charges move toward the low potential locations. This makes the piezoelectric phenomenon temporary under constant mechanical stress (static loading). Equation 2 shows the simple mathematical relationships between the electromechanical effects used in the design of piezoelectric sensors [42].

$$\bar{V} = f\sigma, \quad (2)$$

where V is the generated electric field in volts per meter and σ , is the induced stress by physical loading. The coefficient f is a constant. The produced mechanical strain is defined by Eq. 3:

$$\varepsilon = Vd, \quad (3)$$

d is the piezoelectric coefficient and has the following relationship with f and E Young's modulus of the piezoelectric material.

$$\frac{1}{fd} = E. \quad (4)$$

Equations 3 and Eq. 4, are the fundamental expressions to correlate the electrical voltage and physical loading. Similar to the piezoresistive theoretical framework, proper constitutive assumptions can be employed to relate the physical stress to the piezoelectric voltage.

In the last decade, many tactile sensors have been proposed based on the piezoelectric principle. For example, Elkund *et al.* [43] developed a piezoelectric tactile sensor for measuring the tissue stiffness at the tip of a surgical catheter. Their sensor was tested in both silicon and a human prostate model. It was intended to be used for diagnosing prostate cancer. In continuation, Sokhanvar *et al.* [44] proposed piezoelectric-based sensors for application in minimally invasive endoscopic instruments. They utilized the microelectromechanical system (MEMS) technology to fabricate a miniaturized tactile sensor for MIS graspers. To have a sensitive and linear system, they used PVDF film as the transducer to measure the force, force position, and softness of the grasped object. Estimating the relative softness of the object necessitated at least two independent sensors to quantify the applied force on the object and its total deflection. Figure 2.4(a) illustrates the cross-section of the sensor structure proposed in [44]. Also, Figure 2.4(b) and (c) show a single sensing

unit under applied force during a grasping task, and a schematic of the sensor on the grasper, respectively. When the object was grasped, the middle PVDF film would deform and change the sensor's voltage. The voltage was calibrated versus the softness of the object.

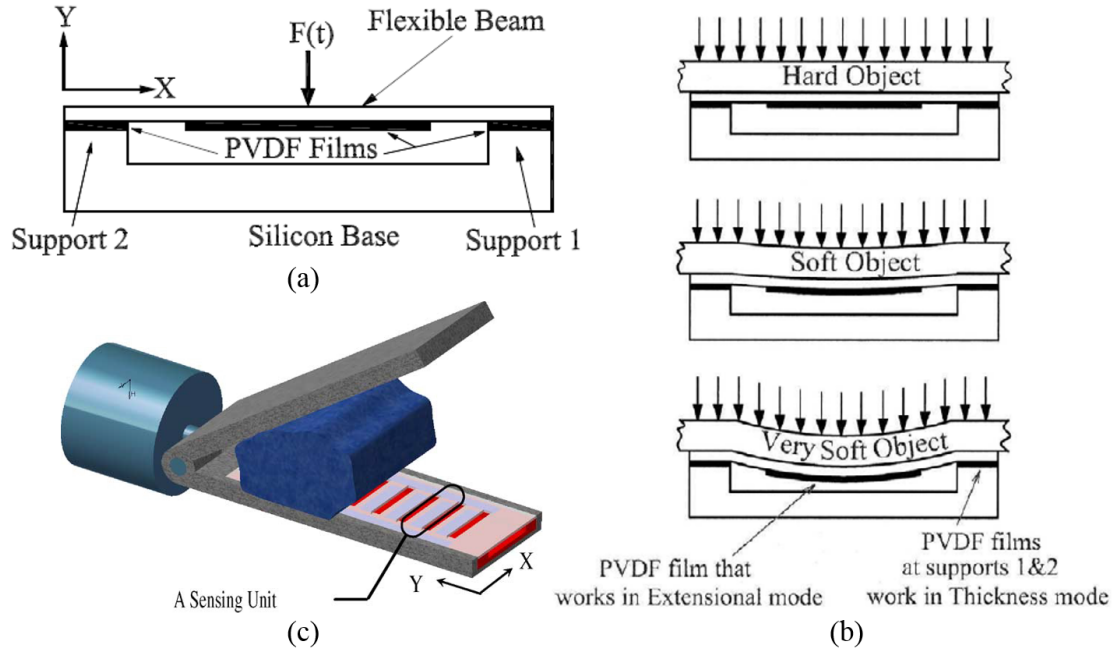


Figure 2.4: (a) Cross-section of the sensor structure, (b) a single sensing unit under a typical grasping force, (c) schematic of the equipped grasper with an array of sensing units [44].

Also, the PVDF on support-1 would show the grasping force when the tissue was grasped, while support-2 was used to determine the position of the point load. To validate the sensor performance, firstly, they selected four samples of the materials with known durometers and calculated their compressive Young's modulus, which was in the range of 50 to 280 kPa and hard material with 6 MPa. In fact, each material was a representative of human tissue. Due to the favorable results of their sensor in material distinction and contact point detection, they postulated to use the sensor in an array configuration. However, because of the intrinsic decay of voltage in the piezoelectric sensing element, their sensor was not able to meet the use-case requirements for static loading conditions, e.g., in the constant grasping of tissues.

In a similar study, Chuang *et al.* [45] fabricated a miniature piezoelectric tactile sensor to detect submucosal tumors in endoscopic procedures. The sensor was made of a PVDF sensing film

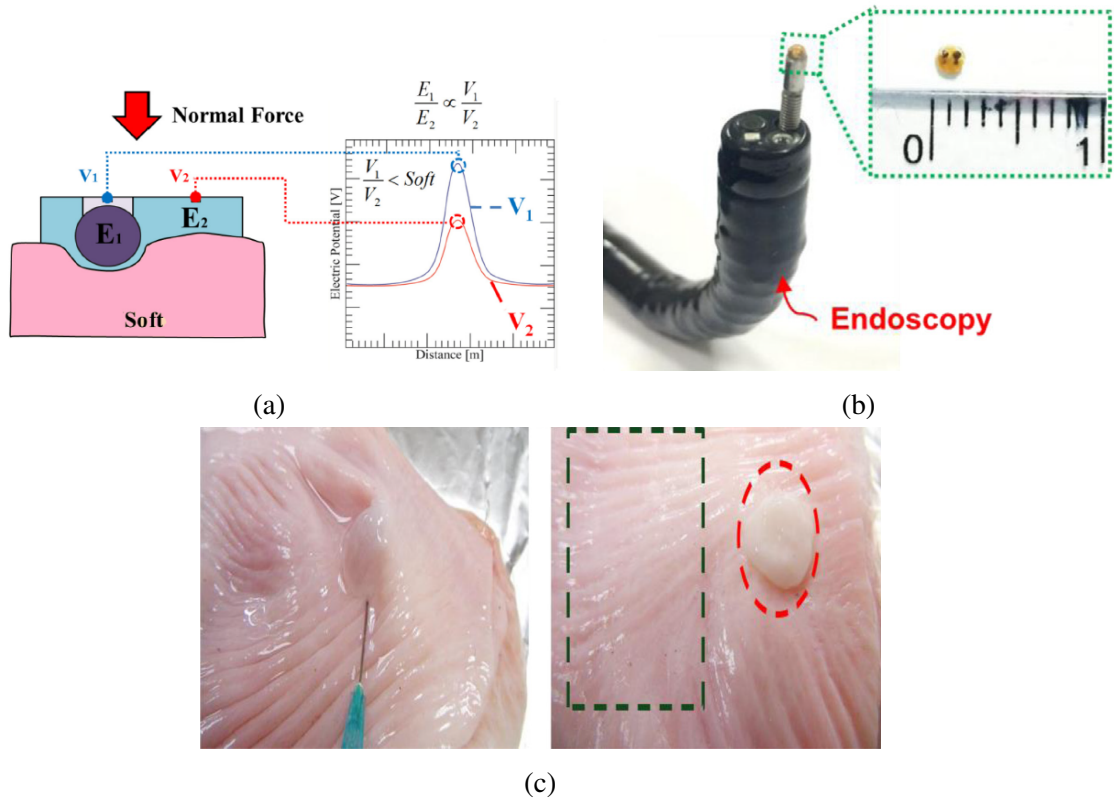


Figure 2.5: (a) Schematic of the tactile sensor in interaction with soft tissue, the graph shows the relative output voltage of the sensing elements, (b) endoscope equipped with the tactile sensor, (c) submucosa of a swine stomach with an artificial tumor lump [45].

and two components consisted of a hard copper ball and polydimethylsiloxane (PDMS) soft outer packaging, as shown in Figure 2.5(a). Since these two components had different stiffness, they would sense different deformations under an external force. Therefore, when the sensor touched an object, the piezoelectric film under the two components would generate different voltages. The ratio of these two voltage outputs was used to calibrated versus the elasticity of the tested objects. This sensor could be integrated on the endoscope to distinct the hidden tumor from healthy tissues. Their results suggested the feasibility of a sensorized endoscope be used as a diagnostic instrument for faster and more precise treatment. The equipped endoscope with this tactile sensor is illustrated in Figure 2.5(b). They proposed an analytical model based on the tandem spring model and change in voltage output of piezoelectric components.

To validate the sensor performance, five different elastomers with known moduli of elasticity

were injected into the normal tissue of the pig stomach submucosa. Figure 2.5(c) depicts the submucosa of the pig stomach included an artificial tumor. The sensor was able to estimate the elastic moduli of the samples between 1.01 and 3.51 MPa. Their results verified their postulation and were in fair agreement with the theoretical predictions.

In a recent study, Sharma *et al.* [46] introduced a biopsy needle equipped with a piezoelectric sensor. Their system, named as the Smart Touch Fine Needle (STFN) was capable of detecting the variation in tissue stiffness. It was utilized to characterize the thyroid tumor based on its mechanical properties. Studies have shown that malignant thyroid nodule is stiffer than the healthy nodules [47]. Therefore, real-time mechanical characterization of the thyroid nodules would help in the early detection of malignancies.

In [46], the sensor was fabricated using additive manufacturing technology to have a precise and low-cost manufacturing process. A piezo-cylinder was used as a force transducer attached to the fine needle. The electric current induced by the mechanical force on the piezoelectric component was recorded in time. The schematic of the needle embedded with piezoelectric transducer and its experimental diagram is depicted in Figure 2.6(a). To calibrate their sensorized needle, they tested it on a series of known stiffness biomaterials. Also, they performed *ex-vivo* experiments on a series of extracted porcine kidneys. The force data during the insertion into the samples were recorded to characterize the tissue stiffness, as shown in Figure 2.6 (b).

To evaluate the sensor performance, different malignant thyroid samples of patients were tested and compared with the normal thyroid tissue. Results revealed that the stiffness of normal tissue was 0.06 ± 0.02 mN/mm, while the stiffness for the malignant tissue varied from 0.02 ± 0.00 to 0.41 ± 0.03 mN/mm.

Piezoelectric tactile sensors exhibit high sensitivity and accuracy. In addition, PVDF film transducers are fairly linear and respond at high frequency. However, piezoelectric sensors can not detect static loads. This constitutes their major limitation for surgical applications. Furthermore, piezoelectric sensors are thermal-sensitive, which means their characteristic equation changes by varying temperatures. In a surgical setup, the sensor is exposed to various temperatures, i.e., from $18 - 20^\circ C$ (operation room temperature) to $37^\circ C$ (core-body temperature). Therefore, thermal sensitivity also hinders its application in MIS and RMIS. A summary of the representative studies on piezoelectric

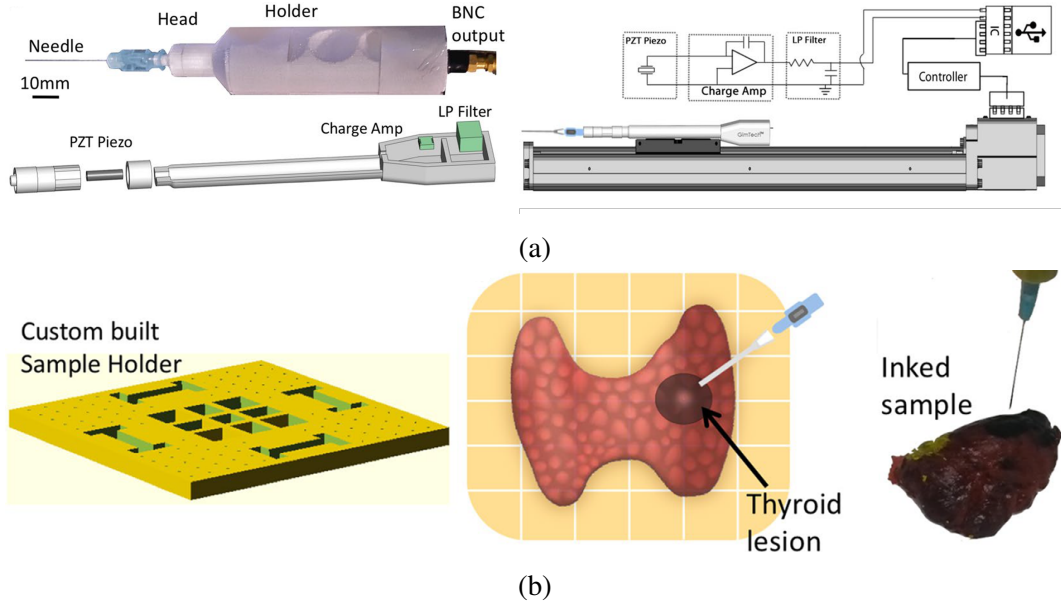


Figure 2.6: (a) Schematic of the needle embedded with piezoelectric transducer and its experimental diagram proposed by Sharma *et al.* [46], (b) experimental validation using a thyroid sample.

tactile sensors for MIS applications is presented in Table 2.1.

Capacitive Tactile Sensors

Capacitive tactile sensors are the next widely used electrical-based sensors in MIS and RMIS. Essentially a capacitor is made of two facing conductive plates with a relatively small gap in between. If an electric potential difference is applied on the two plates, equal and opposite electrical charges are accumulated on both surfaces. An insulator slab (dielectric) might be placed in the gap space to increase the capacitance. The capacitance for two parallel plates, C , is defined by Eq. 5, in which Q is the stored charge and V is electrostatic potential. Also, the capacitance can be estimated by employing Eq. 6, where A is to perpendicular projected overlap area of the plates, ϵ is the permittivity, and d is the distance between two plates.

$$C = \frac{Q}{V}, \quad (5)$$

$$C = \frac{\epsilon A}{d}. \quad (6)$$

The capacitive sensors work based on relating the change in the voltage of a capacitor to physical variables, e.g., force, pressure, displacement, temperature, or humidity. The way each of the variables changes, i.e., A or d , is usually obtained through the mechanical modeling of the sensor. Afterward, the obtained equation is substituted in Eq. 5 and Eq. 6 to find the relationship between the physical variable and voltage. For example, normal force and pressure on the plates can change the distance between the plates. Equation 7 shows the relationship between the normal force, F , on the parallel plates and the output voltage of the capacitor.

$$F = \frac{\epsilon AV^2}{2d^2} = \frac{CV^2}{2d}. \quad (7)$$

Researchers have proposed various capacitive tactile sensors for MIS applications. In an early study, Eltaib and Hewit [48] recommended a micromachined capacitive pressure sensor integrated at the end of a tactile probe. The probe was sinusoidally vibrated into the examined tissue. This displacement caused a sinusoidal force on the capacitive sensor. Therefore, the change in capacitance was measured and transformed into the output voltage. The stiffness map of the probed tissue was displayed on a digital graphical contour to inform the surgeon of the difference between soft and hard tissue as a cue for finding abnormalities.

Also, Peng *et al.* [49] proposed a flexible tactile sensor using PDMS as the sensor structural element. PDMS is well-known for having flexibility, ductility, durability, and biocompatibility. Furthermore, PDMS is easy to micro-fabrication for integration with the existing endoscopic instruments. Their sensor was capable of measuring the tissue elasticity and contact force, simultaneously. Figure 2.7(a) shows two different sensing elements composed of a flexible membrane within an array of capacitors in the top and bottom of PDMS layers. Upon the contact between the sensor and tissue, the relative deflection of two sensing elements would be measured by the embedded capacitors. Figure 2.7(b) depicts a fabricated PDMS tactile sensor in [49]. The sensor calibration was performed by using the sensor on rubber samples with various known hardness. Results verified that the sensor could measure elasticity range from 0.1 to 0.5 MPa with a resolution of 0.1 MPa.

Paydar *et al.* [50] proposed a miniaturized and low-profile thin-film capacitive force sensor array to integrate with a tactile feedback system for MIS. The sensor was comprised of a dielectric

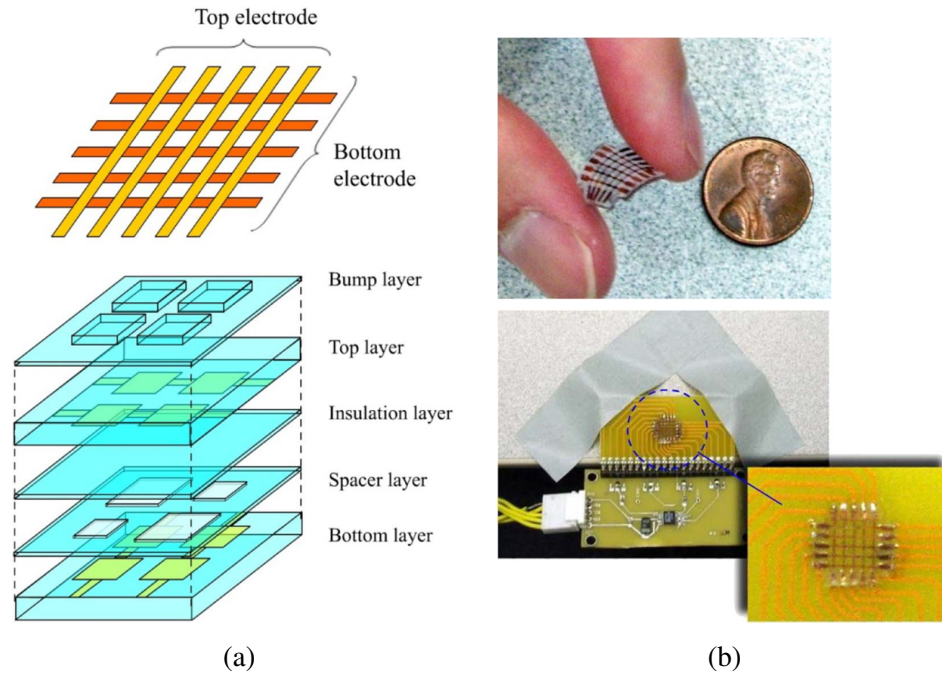


Figure 2.7: (a) Schematic of the orientation of electrode and flexible layered structure of the sensor, (b) prototype sensor and its data acquisition system [49].

sandwiched between two metal plates. When a load was applied to the sensor, it would deflect the dielectric and change the distance between two plates. They calibrated the change in capacitance to the applied force. For better results, they fabricated the sensor with gold plates and parylene-C as the insulating material to address the biocompatibility and electrical properties like permittivity and resistivity. Using the MEMS technology, they miniaturized the sensor to fit in the small surface of a da Vinci Cadier™ grasper. Their results showed that the proposed capacitive force sensor could measure the dynamic and static force in the range of 0 to 40 N with a base capacitance of 16.3 pF for 1 mm² and 146 pF for 9 mm² capacitive area.

Recently, Kim *et al.* [51] proposed a novel sensorized surgical forceps comprised of two compact capacitive sensors on both jaws of the forceps. During a surgical procedure, forceps would undergo three manipulation forces in three directions due to pitching, yawing, and sliding. Also, rotational torque and grasping force are applied to the forceps by rolling and grasping motions, respectively [52]. In addition to that, the other surfaces were used to palpate the tissue by the surgeon to move or check tissue condition. To this end, two three-axis force sensors were designed to be installed at each jaw of the forceps to provide surgeons with all the forces and torque information.

Each force sensor was composed of three perpendicular and parallel configuration of capacitance cells, a movable ground plate to convey the forces, and a triangular substrate. Figure 2.8(a) shows the structure of each 3-DOF sensors under the load. The 3D design of the sensorized forceps and the prototype, manufactured by the machining process, are shown in Figure 2.8(b) and Figure 2.8(c), respectively.

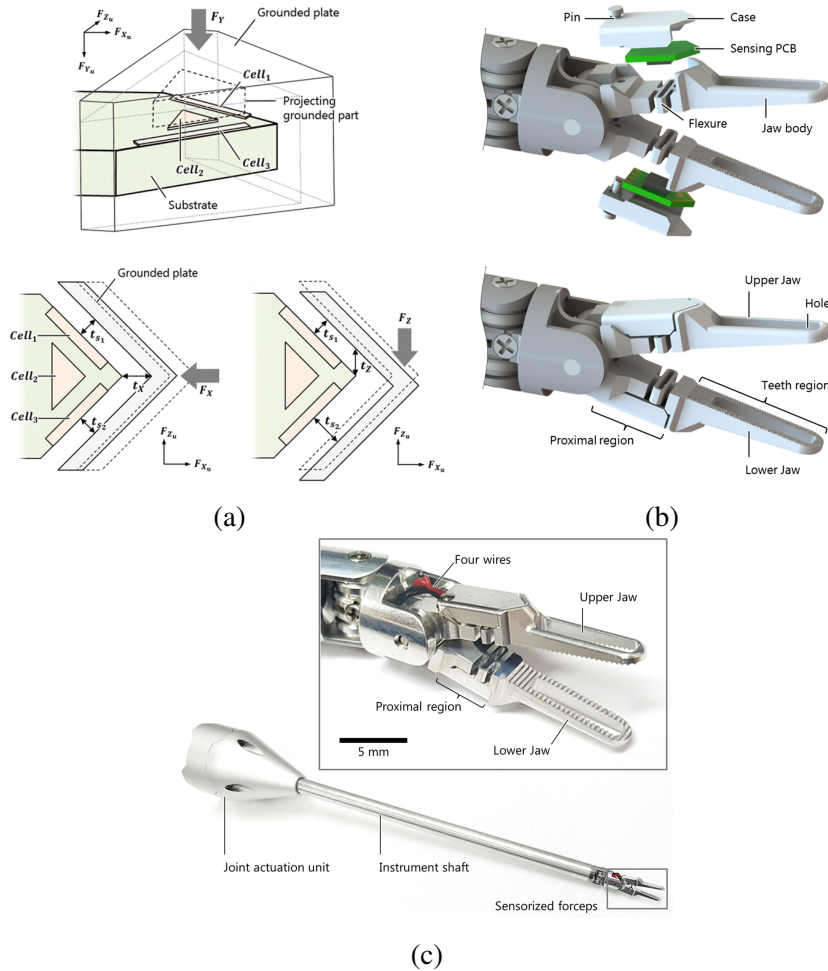


Figure 2.8: (a) Structure of the capacitance cells on the substrate, (b) 3D design of the sensorized forceps, (c) micromachined prototype with an integrated sensor [51].

Utilizing a precise mobile platform and a pre-calibrated ATI-nano17 force sensor, they calibrated their 6-DOF sensors to 6-DOF external forces and torques on the grasper. The mapping equation was:

$$\begin{pmatrix} F_{grasping} \\ F_{palpation} \\ T_{rotation} \\ F_{manipulation-x} \\ F_{manipulation-y} \\ F_{manipulation-z} \end{pmatrix} = \begin{bmatrix} a_{11} & a_{12} & \cdots & & & \\ & \cdot & & & & \\ & & \cdot & & & \\ & & & \cdot & & \\ & & & & \cdot & \\ \cdots & & a_{56} & a_{66} & & \end{bmatrix} \begin{pmatrix} \Delta V_{cell-1} \\ \Delta V_{cell-2} \\ \Delta V_{cell-3} \\ \Delta V_{cell-4} \\ \Delta V_{cell-5} \\ \Delta V_{cell-6} \end{pmatrix}, \quad (8)$$

where, a_{ij} were the calibration constants and V_{cell-i} were the change in voltage of the i -th capacitive sensor (named as a sensing cell). The calibration constants were identified with applying known uni-axial forces on the grasper and performing a least square error fitting on Eq. 8. The verification experiments showed 3.2, 0.51, and 1.53 N for maximum manipulating forces in X, Y, and Z directions, respectively. Also, the maximum torque was measured 0.42 mNm. For this sensor, packaging the electronic components for sterilization was mentioned as a future development.

Capacitive tactile sensors are generally highly sensitive and precise. Such sensors typically have a force range of 0 – 20 N with capacitance less than 1 pF. Also, relatively easy integration with MEMS technology to design thinner dielectric layers and having high resolution and temperature independence are the remarked advantages. These advantages make the capacitive tactile sensors favorable options for surgical tactile sensors [31, 50].

On the other hand, compromised repeatability due to the hysteresis and cross-talk has limited the use of the capacitive sensors for very high-precision applications. Also, electromagnetic interference with neural or cardiac activity has limited their use in the heart and brain surgery [13]. A summary of the most investigated capacitive tactile sensors in MIS is presented in Table 2.1.

Table 2.1: Summary of the representative studies on electrical-based tactile sensors in MIS.

| Authors | Year | Principle | Application | Measurands | Range | Characteristics |
|-------------------------------|------|----------------|-----------------|-----------------|--|--|
| Dargahi <i>et al.</i> [53] | 2000 | Piezoelectric | Endoscopy | Force | 2 N | Error: 0.2 N |
| Eltaib <i>et al.</i> [48] | 2000 | Capacitive | Laparoscopy | Force | 0-75 mV | Capacitance < 60 pF |
| Kattanaset <i>et al.</i> [54] | 2004 | Piezoresistive | MIS | Pressure | 245-1080 kPa | N/A |
| Ottermo <i>et al.</i> [55] | 2004 | Piezoelectric | MIS | Force | 10 N | $A_{profile}=24 \times 8$ mm |
| Qasameh <i>et al.</i> [56] | 2008 | Piezoelectric | MIS | Force | 0.01-4 N | Not Reported |
| Trejos <i>et al.</i> [57] | 2009 | Piezoresistive | MIS | Force/Torques | $F_{lateral} = \pm 5$ N $F_{axial} = \pm 25$ N $T_{rotation} = \pm 80$ Nmm | RMSE _{force} : 0.35 N RMSE _{torque} : 1.5 Nmm |
| Golpaygani <i>et al.</i> [58] | 2009 | Capacitive | RMIS | Force | 0.1-0.7 N | Sensitivity: 0.83 kHz/N |
| Jalkanen <i>et al.</i> [59] | 2010 | Piezoelectric | Palpation | Stiffness | 2-10 kPa | $R^2 = 0.94$, $p < 0.05$ |
| Kalantari <i>et al.</i> [60] | 2011 | Piezoresistive | Catheterization | Force | 0.1-2.5 N | RMSE: 0.611 N |
| Baki <i>et al.</i> [61] | 2012 | Piezoresistive | MIS | Force | 2 N | Res _F : 5 mN |
| Talasz <i>et al.</i> [62] | 2012 | Capacitive | Profilometry | Force | $F_{palpation}=4-5$ N $F_{gripping} = \pm 0.5$ N | N/A |
| Hwang <i>et al.</i> [63] | 2013 | Piezoresistive | RMIS | Force | 0.0-3 N | Linearity > 99.6% |
| Lee <i>et al.</i> [64] | 2014 | Piezoelectric | Palpation | Force/Pressure | 3-30 kPa | Sensitivity: 0.38 mV/kPa |
| Li <i>et al.</i> [65] | 2015 | Piezoresistive | MIS | Force | $F_{axial} = \pm 3.0$ N $F_{radial} = \pm 1.5$ N | Res _{axial} =0.15 N Res _{radial} =0.015 N |
| Kim <i>et al.</i> [66] | 2015 | Capacitive | MIS | Force | $F_x = \pm 2.5$ N, $F_y = \pm 5$ N $F_z = \pm 2.5$ N, $F_{grasping} = 5$ N | RMSE _x =0.0837 N, RMSE _y =0.0732 N RMSE _z =0.114 N, RMSE _{grasping} =0.0957 N |
| Hessinger <i>et al.</i> [67] | 2016 | Piezoresistive | MIS | Forces/Torques | 10 N 1 Nm | Error _{axial} = 4.92% Error _{rotation} = 1.13% |
| Zhang <i>et al.</i> [68] | 2017 | Piezoelectric | MIS | Tissue Hardness | 500 kPa | N/A |
| Kim <i>et al.</i> [69] | 2017 | Capacitive | RMIS | Force/Torque | Force= ± 1.5 N Torque _z = ± 20 Nmm Torque _{x,y} = ± 10 Nmm | Res _F =0.21 mN Res _T =0.35 Nmm |
| Rado <i>et al.</i> [70] | 2018 | Piezoresistive | MIS | Force | Gripping Force: 1-20 N Tactile Sensing: 0.01-2 N | N/A |
| Ju <i>et al.</i> [71] | 2019 | Piezoelectric | Catheterization | Tissue Hardness | 0-1.7 MPa | Errors < 3.5% |
| Kim <i>et al.</i> [72] | 2020 | Capacitive | RMIS | Force/Torque | $F_x = \pm 0.3$ N, $F_y = 0-0.5$ N $F_z = 0-0.9$ N, $F_{gripping,y} = 0-0.9$ N | Average Elastic Modulus, E = 581 kPa Accuracy=98.1% |

RMSE: root mean square error, R^2 : goodness of fit, Res_F: force resolution, Res_T: torque resolution.

2.3.2 Optical-based Tactile Sensors

The contributions of optical tactile sensors in the MIS and RMIS applications are described in this section. The emphasis was on the sensors prototyped and validated in at least one physical or functional requirement for a tactile sensor in *in-vivo*, *in-vitro*, or *ex-vivo* experiments.

The first literature reporting development of an optical sensor for medical applications dates back to 1953s. The first application of such a sensor was intravascular and cardiac diagnostic measurements [73–75]. In 1960, Polanyi *et al.* [76] presented an optical system for the measurement of the *in-vivo* oxygen concentration in the blood. In an early study, Frommer *et al.* [77] proposed a fiber-optic catheter system that could record intracardiac oxygen saturation continuously up to 3 hours in the patients with valvular heart disease. Their instrument provided a novel and valuable tool both for cardiovascular diagnosis and clinical investigations.

During the years, numerous optical tactile sensors have been designed and introduced to be used in the medical approach, especially in MIS procedures. The main characteristics of the optical sensors, that led to their wide adoption in MIS were intrinsic small size, biocompatibility, magnetic, and electrical passivity. Thanks to these specifics, the development of optical tactile sensors for the MIS has gained momentum over the electrical-based sensors. Especially for MRI-guided surgeries such as the brain and cardiac interventions, the optical-based sensors have been the only MRI and electrically passive sensing modalities. The basic sensing element of optical tactile sensors is an optical fiber. The optical-fiber-based sensors mainly work based on three principles: wavelength (WM), phase (PM), and light intensity modulation (LIM) [13, 78, 79].

As depicted in Figure 2.9(a), an optical fiber sensor system generally consists of a light source, to which an optical fiber is connected and the light is transmitted from the source into the optical fiber. The optical fiber is passed through the sensor structure, where the intensity, phase, or wavelength modulation happens. Afterward, the modulated light goes to an optical detector. The choice of the optical detector depends on the sensing principle, whereas, for intensity modulation, the detector could be a photodetector or a camera to measure the intensity of the passed (or reflected) light in the fiber. Also, the detector could be an optical spectrum analyzer (OSA) for obtaining the wavelength spectrum of the light, or a fringe-pattern display to quantify the phase modulation (Figure

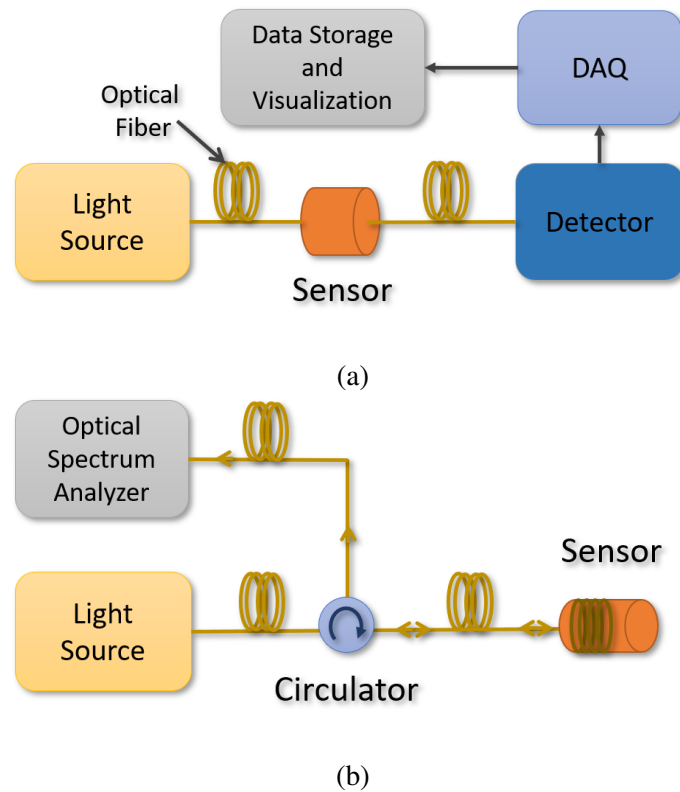


Figure 2.9: Typical system components of an optical sensor system based on (a) LIM principle, (b) WM and PM principles.

2.9(b)). A post-processing step is also required to obtain the calibration parameters after recording the output light.

Light Intensity Modulation Optical Tactile Sensor

The first generation of the optical sensors was designed based on the intensity-modulation principle. This sensing principle relies on the variation in light power due to an external modulator parameters like force, pressure, displacement, temperature, etc. LIM sensing principle provides the unique advantages of being inexpensive, thermally insensitive, simple in design, and easily implementable. Thanks to these features, intensity-modulated sensors are favorable for making array sensors and multiple DoF sensors. The main modulation modes in the LIM sensing principle are bending loss and coupling loss. In continuation, these principles will be described and exemplified.

(1) Bending Loss Principle

When an optical fiber is bent along its length, the change in the incidence angle of the light beam causes intensity loss [80]. Theoretically, there is a critical bending radius for any fiber. When the bending radius is larger than the critical bend radius, there is no intensity loss, and when it is smaller than the critical bending radius, the intensity loss occurs. The critical bending radius is an essential factor for the sensor design. Figure 2.10(a) schematically represented an optical fiber under a single-radius bending deformation induced by force, F .

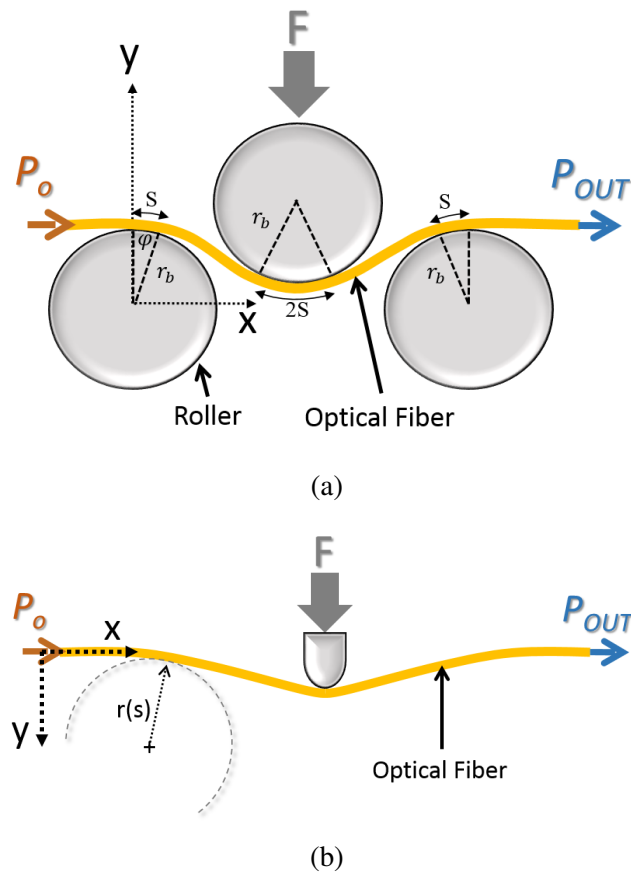


Figure 2.10: Bending loss configurations: (a) constant bending radius (CBR), (b) variable bending radius (VBR).

One of the most adopted theoretical models for the intensity modulation is presented in Figure 2.10(a), which was first formulated by Gauthier, R.C. and Ross C. [80]. In their analysis, it was assumed that the fiber undergoes constant bending radius (CBR) deformation by passing through a mobile and two fixed cylindrical indenters (rollers). Applying the force on the upper mobile indenter bends the fiber and causes a light leakage from the body of fiber and

intensity decay in the light output. The power decay model shows the correlation between the displacement of the mobile roller with the output power of the optical fiber. It has been used for calibration of the bending-based intensity modulation optical fiber tactile sensors. Equations 9–11 express the relationship between the power loss and central curvature angle of in a constant bending radius deformation [80].

$$P(s) = P_0 e^{-\gamma s}, \quad (9)$$

$$s = r_b \varphi, \quad (10)$$

$$\gamma = c_0 r(s)^{-\frac{1}{2}} e^{-c_1 r(s)}, \quad (11)$$

where, P_0 is the input power to a fiber with a constant bending radius of r_b and a curvature length of s ; whereas $P(s)$ is the power at the desired length, s , on the fiber bent arc, and γ is the constant known as the bend loss coefficient. γ is an intrinsic constant dependent on the wavelength of the transmitting light, geometry, and optical characteristics of the fiber, e.g., critical angle, the refractive index of core and cladding.

Also, $r(s)$ is the local radius of curvature as a function of arc length of s and c_0 and c_1 are intrinsic optical properties of the fiber. Using two corrugated moving plates to apply a series of micro bending along the fiber length sandwiched between the plates, is another common type of bending loss optical sensors. In this configuration, multiple bendings cause more intensity loss and improve the sensitivity of the sensor [81].

The use of cylindrical rollers made the physics underlying the intensity modulation simple by enforcing a constant bending radius (CBR) configuration. However, it made the sensor structure bulky and was a limitation for the miniaturization. To cope with this limitation, Bandari *et al.* [20, 28] introduced a new sensing principle based on a variable bending radius (VBR). The VBR principle was based on utilizing only a single arbitrary shape indenter with a significantly small size. Figure 2.10(b) depicts the VBR configuration. They formulated the VBR principle by differentiating Eq. 9 with respect to s . Their proposed formulation was

based on integrating the infinitesimally small change in the power employing $d\gamma$ as:

$$dP(s) = (-\gamma P_0 e^{-\gamma s} - s P_0 e^{-\gamma s} (-\frac{1}{2} c_o r(s))^{-\frac{3}{2}} \times e^{-c_1 r(s)} - c_o c_1 r(s)^{-\frac{1}{2}} e^{-c_1 r(s)} \frac{dr(s)}{ds}) ds. \quad (12)$$

By integrating the $dP(s)$ over the length of the fiber, the power-loss was obtained as a function of the radius of curvature function, $r(s)$, as Eq. 13.

$$\int_0^s dP = P(s) - P_0. \quad (13)$$

(2) Coupling Loss Principle

Coupling loss-based optical sensors work with two modalities: transmission loss and reflection loss. In both modalities, the light intensity is changed while it transfers between two coupled optical fibers. In the transmissive LIM sensors, typically, a gap between the fibers results in a predictable initial coupling power loss, which would change with the transverse, longitudinal, and angular misalignments between the fibers. Figure 2.11(a) illustrates a schematic of transmission loss due to distance d , between two optical fibers.

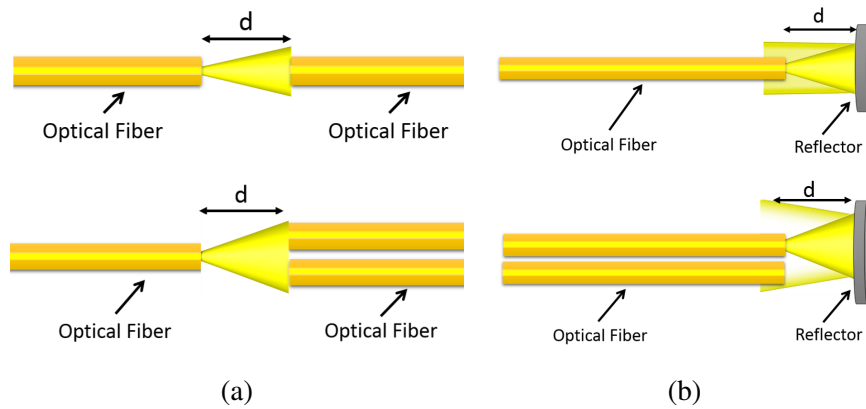


Figure 2.11: Optical fiber coupling loss configuration: (a) transmission loss, (b) reflection loss.

Equation 14 states the fundamental model relating the coupling efficiency, η (the ratio of the transmitted power to the initial power) to the angular misalignment between the fibers, and

the gap length [74].

$$\eta = \frac{P_{out}}{P_{in}} = 4 \frac{D}{B} \exp\left(-A \frac{C}{B}\right), \quad (14)$$

where A, B, C, and D are intrinsic properties of the fibers, structural design parameters, gap medium between the fibers and the angular misalignment caused by the physical load, respectively. Comparing the output (measured) and input powers (set at the source), the coupling efficiency, η is calculated, and the unknown parameters in Eq. 14, are estimated.

The second coupling loss principle is the reflective LIM, as shown in Figure 2.11(b). In this configuration, a movable reflecting surface is placed in distance d in front of the fibers perpendicular to their central axes. Most of such sensors have been proposed based on using a pair of straight parallel optical fibers, whereas one is the emitting fiber projecting light to the reflector, and one fiber receiving the back-scattered light. The intensity of the received light is proportional to d . For further simplification of the design, researchers have used a fiber-optic coupler to couple the reflective light to a single fiber, i.e., known as retro-reflective fiber.

Faria *et al.* [82] presented a theoretical analysis of a reflective sensor with a pair of straight parallel optical fiber. In [82] geometrical approach and electromagnetic theory of the paraxial Gaussian beam approach revealed that the increase of the distance would initially increase the reflective light intensity while more distance would decrease the intensity. Polygerinos *et al.* [83] described a mathematical model for the fiber-optic reflective LIM sensor using an optical coupler. They used the Gaussian light-intensity distribution and modeled the transmitted light in two configurations, i.e., axially moving reflector and tilted reflector along the axis perpendicular to the optical fiber axis. They experimentally proved that the collected light was a function of the distance d .

There are several examples of LIM optical tactile sensor in the literature. For example, Ahmadi *et al.* [84] developed a bending loss optical tactile sensors composed of three single-mode optical fibers where each fiber passed through three perpendicular rods. Each fiber was sandwiched between one short movable rod and two fixed rods. Three upper movable rods were attached to a flexible beam in certain different lengths. Figure 2.12(a) shows the configuration of the rods and fibers in this sensor. The beam was glued in two sides to the sensor substrate. The applied force would deflect the beam, and the rod would bend the connected optical fiber. The bending caused intensity decay

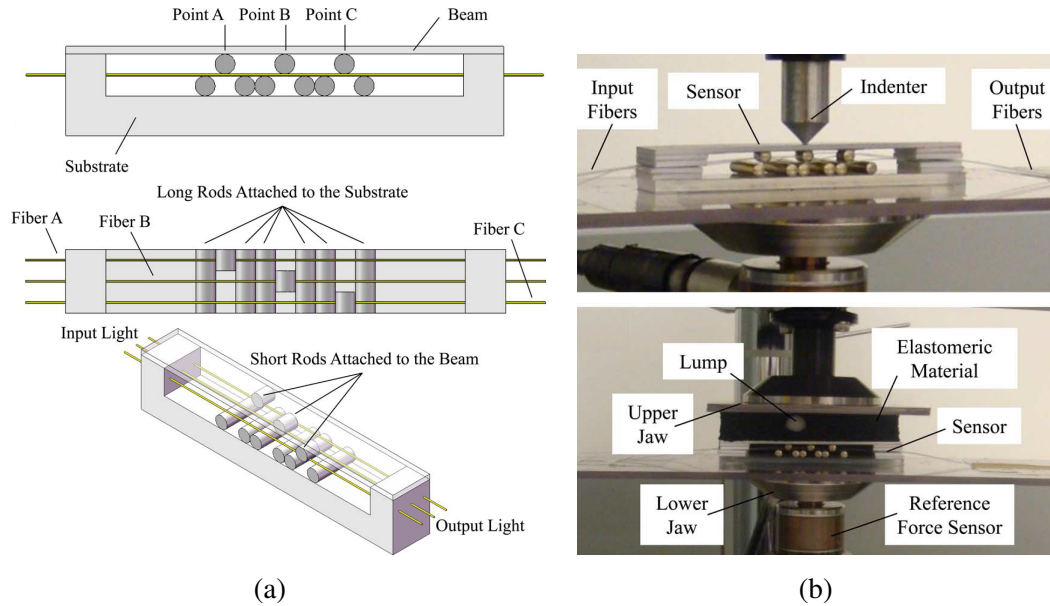


Figure 2.12: Bending loss tactile sensor proposed by Ahmadi *et al.* [84]: (a) structural design, (b) fabricated sensor under the point load and interaction with the tissue phantom.

in the deformed optical fiber. Therefore, measuring the relative deflection of the beam resulted in estimating the unknown force.

They used silica sheets to fabricate the substrate sensor to achieve the biocompatibility and electrical passivity requirements. The beam was made of hi-impact polystyrene to have sufficient flexibility. The point load was applied on different locations on the beam while the intensity output was being recorded as the output voltage of the photodetectors.

The validation experiment was done by considering the interaction between an elastomeric tissue phantom consist of a rigid artificial spherical tumor. The fabricated sensor under the point load and interaction with the tissue phantom is depicted in Figure 2.12(b). Results verified that the sensor was able to identify the location of the concentrated force caused by a rigid tumor. The range of measurement was demonstrated in 0-4 N. Furthermore, the sensor worked under both static and dynamic loading conditions. Also, they recommended using the MEMS technology to miniaturize the sensor structure and utilizing the micromirror to reflect the output light.

In continuation, Bandari *et al.* [30] proposed an array optical sensor to measure the lateral and circumferential force for valvuloplasty cardiac surgery. The proposed sensor was composed of four single VBR optical sensors that were configured cylindrically. Four semi-cylindrical indenter

were attached to the inner surface of the flexible shell in different longitudinal locations. This configuration made the sensor integrable at the tip of a valvuloplasty catheter. A parametric finite element analysis was done to model the sensor. The analytical and numerical validation of the sensor provided the feasibility of using this sensor to consider the heart valves condition and location.

In another study [85], a novel sensing mechanism was proposed, fabricated, tested, and shown to be feasible for MIS procedures (Figure 2.13). The working principle of the proposed sensor was based on calculating the deformation of contacting tissue through measuring the transmissive coupling loss through a fiber attached to the top beam. Similarly, the total contact force was estimated by measuring the coupling loss through two receiving fibers. Quantitative estimation of the stiffness of the tissue was shown to be correlated to the ratio of force to the deflection. The coupling loss between the left and right portion of fiber A was due to the gap and angular misalignment. Deformation of tissue produced the angular misalignment of left and right portions of fiber A; while, the power loss at fibers B and C was due to both the gap and lateral misalignment. The lateral misalignments of left and right portions of fibers B and C were produced due to the deformation of the elastic foundation. In this study [85], an N-Type $< 100 >$ silicon wafer was used to make the beams, substrate, and supports while a PDMS film was used to make the elastic foundation. Three single-mode optical fibers were utilized and connected to three photodetectors to measure the transmitted light intensity. Also, an ElectroForce testing machine was used to apply the force on the tissue in two modes: a dynamic concentrated force to examine the response of the sensor under dynamic loads and a test with a distributed force to examine the ability of the sensor in lump location.

To verify the ability of the sensor in measuring the relative softness of different tissues, three silicon rubbers with different shore hardnesses were used. During the experiments, a force with a triangular function was applied at a frequency of 0.1 Hz. The results verified that the proposed sensor was capable of distinguishing three distinct materials. Moreover, the results demonstrated equal outputs from both fibers B and C, which indicated a homogeneous distribution of force on the sensor. However, shape optimization was needed to address the miniaturization and waterproof requirements. In addition, a more detailed mechanical model (analytic or FEA) should be provided to investigate the sensitivity of the sensor to the size, depth, and material properties of the lump in

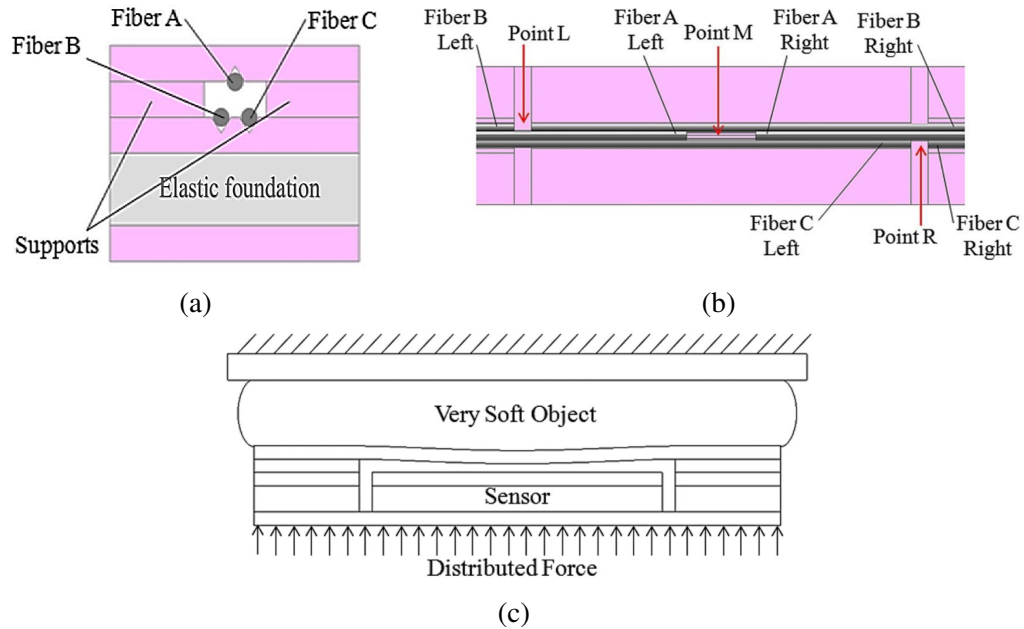


Figure 2.13: Proposed transmissive coupling loss optical fiber sensor by Ahmadi *et al.*[85]: (a) cross-sectional view of the structure of the sensor, (b) top view of the configuration of fibers and gaps, (c) illustrative presentation of typical deflection of sensor and soft tissue under distributed force.

the tissue during lump location applications.

As an emerging MIS approach in the last decade, cardiac surgery on a beating heart has been expanded significantly, i.e., the off-pump technique. MIS techniques have played a key role in this expansion. For example, mitral valve replacement (MVR) (and annuloplasty) was one of the first major cardiac surgeries which were revolutionized by catheter-based techniques (CBT). During a CB-MVR an artificial mitral valve is deployed on the defective natural valve using a metallic expandable anchorage device. To secure the prosthetic valve in place, on the annulus (peripheral ring of the valve), a minimum anchorage force of 1.5 – 4 N is reported to be necessary upon deployment [86]. Conventionally, anchorage of the valve is examined manually and qualitatively by the surgeon; however, due to beating movement of the heart and valve motion, the tactile perception of the surgeon from the anchorage force is polluted.

Therefore, to address the need for a sensor capable of precise force measurement in the highly dynamic intracardiac environment, Yip *et al.* [87] developed an optical tactile sensor based on the reflective light intensity modulation principle. The proposed sensor was comprised of three pairs

of optical fibers placed in a triangular configuration. Each pair of fibers included an emitting fiber, coupled to a light source, and a receiving fiber connected to a phototransistor circuit. A reflecting plate was located at a distance of 4 mm against the fibers. The external diameter and the length of the sensor were $\phi 5.5$ mm and 12 mm, respectively.

To avoid the interfering with the intra-operative ultrasonic imaging, the rigid components were made of acetal material. A silicon sealer provided fluid sealing of the sensor. An elastic component (Silicon rubber, Polysiloxane, with a shore hardness of 35) was used to join two parts of the sensor with flexibility. Upon applying a force on the tip of the sensor, it would press the elastic element and subsequently changed the orientation of the reflective plate. The change in the spatial orientation of the plate would cause depreciation of the light intensity in the receiving fiber. Figure 2.14 illustrates the sensing principle, geometric design, and final prototype of the proposed sensor.

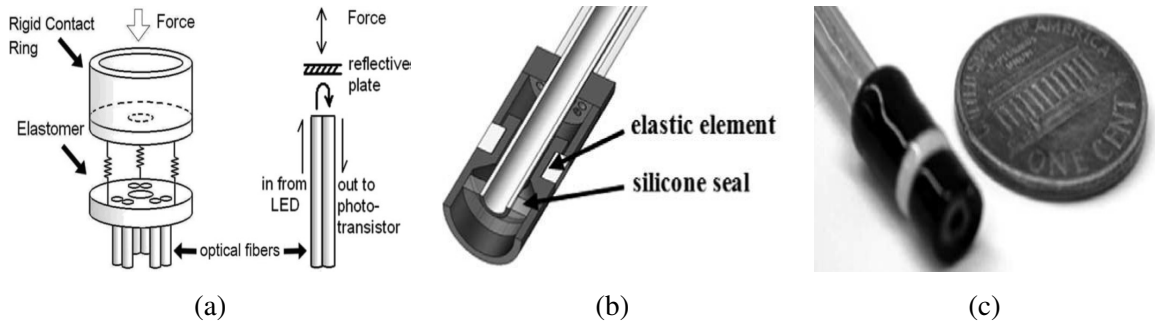


Figure 2.14: Reflective light intensity modulation tactile sensor proposed by Yip *et al.* [87]: (a) sensing principle of the sensor, (b) cross-sectional view of the sensor, (c) fabricated prototype of the sensor.

Since Silicon rubbers exhibit a nonlinear force-deflection behavior with hysteresis; therefore, the quadratic viscoelastic function was used for calibration. The calibration was performed by applying a sinusoidal chirp force to the sensor, with an amplitude of 4 N and a terminal frequency of 6 Hz. To simulate the immersion of the sensor in blood, the calibration tests were performed in the water while its temperature was maintained at 37°C . In order to assess the generality of the obtained coefficients, the input loads of chirp waveform and triangular waveform were reconstructed from the voltage signals. The correlation coefficient of reconstruction and chirp input was $R^2 = 0.9889$ and for triangular input was $R^2 = 0.9867$. *In-vivo* experimentation on the sensor was performed on Yorkshire pigs. The sensor was integrated on a 14-gauge needle and inserted into the left atrium of

the animals. The tests were conducted under 3D ultrasound navigation.

During the surgery, surgeons had real-time visual force feedback and tried not to exceed the force magnitude of 1.5 N. Post-mortem examinations show that the anchor was deployed correctly in place with a force of less than 2 N. However, due to the integration of the sensor on a rigid surgical instrument, surgeons could perceive the force during the operation to control the required force magnitude, while in the case of robotic surgeries or flexible instruments, the transmitted light can be sensitive to optical fiber bending. Furthermore, the elastic component material properties should be considered due to hysteresis in higher frequency signals.

Another emerging field of MIS application is cardiac ablation. A common cardiovascular disease is the abnormal heart rhythm or cardiac arrhythmia [88]. During the years, different medication courses have been investigated for arrhythmias, yet the most effective treatment is the radiofrequency ablation surgery (RFA). During RFA, a long, thin, and flexible catheter is subcutaneously steered to the right atrium. By tracking the catheter tip via real-time fluoroscopic imaging, the surgeon confirms the secure contact between the RF electrode and the atrial wall and initiates the ablation process [17]. Studies have revealed that the electrode-tissue contact force is a major factor affecting the success of an RFA procedure. A large contact force, i.e., beyond 0.3 N, would tear or perforate the tissue, while an insufficient force leads to a suboptimal contact area and fail the procedure [22]. To satisfy these requirements during the ablation procedure, sensors are designed to be integrated at the tip of the catheter.

In this regard, Noh *et al.* [89] proposed a new miniature three-axis force sensor, which is integrable at the tip of the ablation catheter to measure the contact force. In their study, a novel sensing mechanism based on reflective coupling loss LIM principle and an unprecedented intensity estimation mechanism based on a charged-coupled device (CCD) camera utilization was proposed. As depicted in Figure 2.15(a), the sensor consisted of a flexible cylindrical casing with a mounted mirror inside, a four-core bundle optical fiber, an LED light source, and a CCD camera (resolution 640×480 , at 30 fps). The mirror was fixed on three cantilever arms at a $3 \times 120^\circ$ circular configuration. Upon application of external force to the sensor, the flexible tip of the sensor would deflect and so would each of three cantilever beams. The deflections would move the white plate to a new orientation.

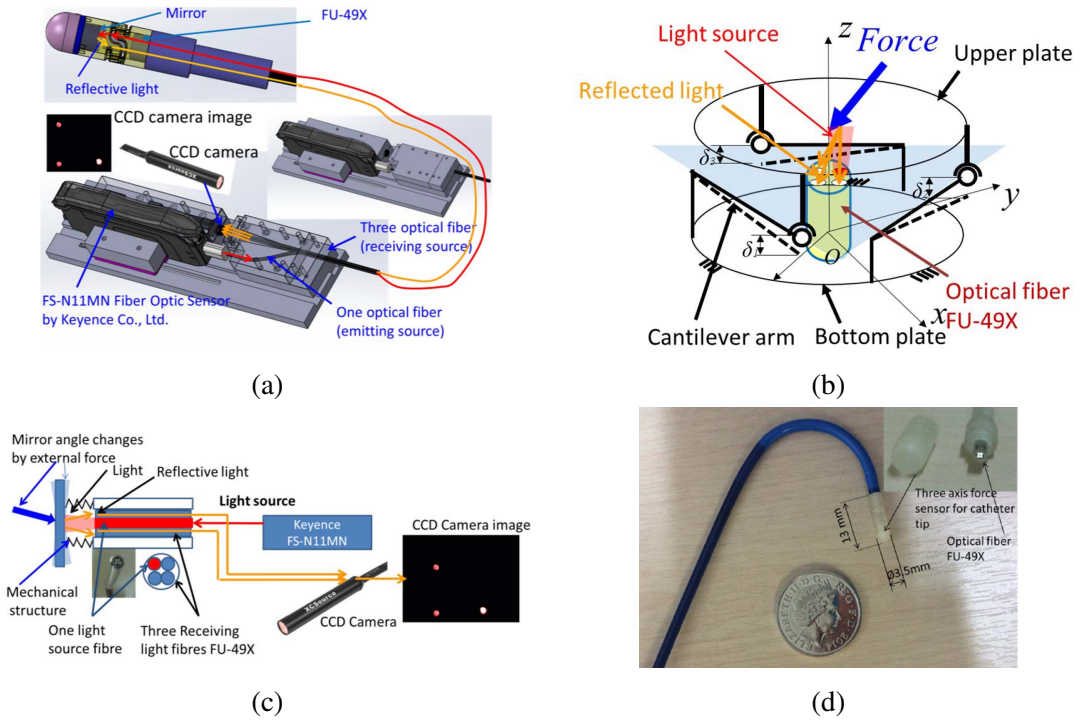


Figure 2.15: (a) Schematic view of the sensor proposed by Noh *et al.* [89], (b) configuration of internal mirror and cantilever arms, (c) the image acquisition system, (d) their prototyped sensor.

As illustrated in Figure 2.15(b), the light source illuminates the tip of the sensor through one of the fibers. The reflected light from the interior mirror was transmitted back to the CCD camera through three optical fibers. An image processing software was developed to estimate the light intensity in each of the three receiving optical fibers. The reflected light intensity is a function of the orientation of the mirror, and the deflection of beams governs the orientation. Since the deflection of a beam is linearly proportional to the force, the intensities of reflected lights recorded by CCD camera were mapped to the external calibration forces. To do so, a multi-linear regression model with nine-regression coefficients was used. As depicted in Figure 2.15(c), each frame was divided into three regions of sections (ROS), which were corresponding to each fiber. The intensity value was calculated as the mean value of pixels in each ROS at a given time. The first prototype of the sensor consisted of a 3D printed deformable structure is shown in Figure 2.15(d).

To perform the calibrations, a device equipped with a force sensor was used. The fabricated sensor was subjected to a compressive axial load of $F_z = 0$ to 1.5 N, and lateral push-pull forces of $F_x = F_y = -0.5$ to 0.5 N. Results showed a linear relationship between the light intensity values

of three receiving fibers and the force applied to the sensor. However, this study could be further improved by increasing the resolution of the camera, implementing an edge detector over each ROS to discard the contribution of black pixels to improve sensitivity, studying the effects of filtering parameters on the accuracy, and re-configuring the bundle to be more symmetrical.

Intensity modulation optical sensors are popular for their inexpensive and simple sensing structure and processing system. They are not sensitive to temperature variation, thus, eliminates the need for a thermal compensation schema. On the other side, because of the light source fluctuation, fiber deflection in the bending model or fiber misalignment in the coupling loss model, there is undesired drift in the intensity data reading. A summary of the state-of-the-art of LIM optical tactile sensors proposed for MIS is tabulated in Table 2.2.

Wavelength Modulation Optical Tactile Sensor

Wavelength modulation optical sensors were proposed to achieve higher resolution measurements in comparison with the LIM-sensors. For the first time, in 1978, Hill *et al.* [90] made a periodic change in the refractive index of the core of the optical fibers via electromagnetic waves and developed the Fiber Bragg Grating. Afterward, Meltz *et al.* [91] demonstrated a new method to develop Bragg grating in the fiber by exposure to coherent two-beam UV interference. An FGB-based sensor works based on the radiation reflection of a narrow range of wavelengths in the Bragg area on the core. The central wavelength of this range is called a Bragg wavelength, λ_B . Bragg wavelength is a function of the refractive index of the core, η_{eff} and the period of the grating, Λ , as expressed in Eq. 15:

$$\lambda_B = 2\Lambda\eta_{eff}, \quad (15)$$

Axial strain induced by physical loads like force, pressure, displacement, vibration, or temperature changes influences Λ and η_{eff} ; thus, subsequently causes a reflected wavelength shift. The wavelength shift is defined as $\Delta\lambda_B$ and is calculated by Eq. 16:

$$\frac{\Delta\lambda_B}{\lambda_B} = k_\epsilon \cdot \epsilon + k_T \Delta T, \quad (16)$$

where, k_ϵ is the coefficient for axial strain, ϵ and k_T is the coefficient for the temperature change, ΔT [92]. Depending on the application, a sensor structure is designed to translate the physical stimulus, i.e., force, pressure, thermal strain to FBG fiber. Afterward, calibration of the wavelength change with respect to the physical stimulus is performed the least square fitting. Figure 2.16 schematically shows the input and output light spectra happening in a fiber Bragg grating due to an axial strain.

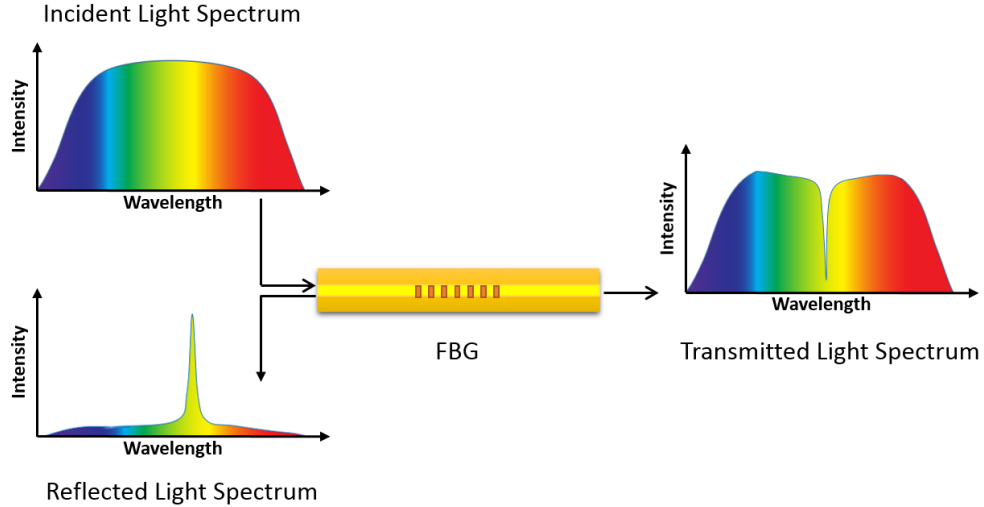


Figure 2.16: Sensing principle of the fiber Bragg grating and wavelength shift due to an axial strain.

As a commercialized example, Yokoyama *et al.* [22] developed an FBG force sensor to be integrated at the tip of the RF ablation catheter. The sensor consisted of three FBGs embedded in a compliant tip of the catheter. During the ablation procedure, the contact force between the cardiac wall and the tip of the catheter caused axial strains and shifts on the reflected spectra of the three FBGs. Depending on the level of axial and lateral components of the tip force, each fiber would exhibit different spectrum changes. To validate the sensor, the researchers performed a total of 1409 measurements on two catheters in perpendicular, parallel, and 45° directions. Calibration was performed using a least-square error fitting. Afterward, the sensor was embedded in an RF ablation catheter and was used in 10 anesthetized canine animal models. The results confirmed the measurement linearity of the sensor with $R^2 = 0.988$. The mean error of readings was less than 1.0%, and the range of measurement was 0 – 0.5 N with a resolution 10 mN. This sensor was later commercialized as a part of the ablation catheter TactiCathTM Quartz ablation catheter (formerly

Endosense SA, Switzerland, acquired by Abbott Laboratories, Illinois, USA.) Figure 2.17 shows the schematic of this sensor and the tip contact force during the ablation procedure.

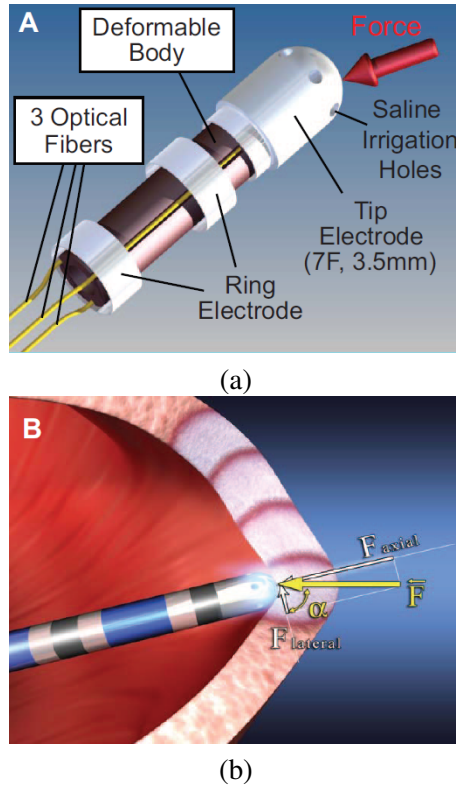


Figure 2.17: (a) Schematic of the structure of the proposed sensor by [22], (b) reaction force on the catheter tip during the ablation procedure.

In another representative study, Park *et al.* [92] proposed an MRI-compatible biopsy needle equipped with tactile sensors to measure the needle deflection profile while inserted into a tissue. In diagnostic biopsy and localized treatment monitoring, the tip of the needle is important to end up at the pre-planned location for taking biopsy samples. To this end, three optical fibers were attached to the inner part of the biopsy needle. The three FBG fibers were embedded in a circular pattern with 120° angular separations. Electrical discharge machining (EDM) was used to manufacture the fiber holder grooves in the needle. It helped to make accurate details in the metal without ferromagnetic extra parts to save MRI-compatibility. Figure 2.18(a) illustrates the sensor designed with three fibers configuration in the biopsy needle and FBG locations.

The prototype was calibrated using two orthogonal digital cameras. The cameras were used to capture the 3D shape of the needle in bench tests. Calibration was done while needle deformed

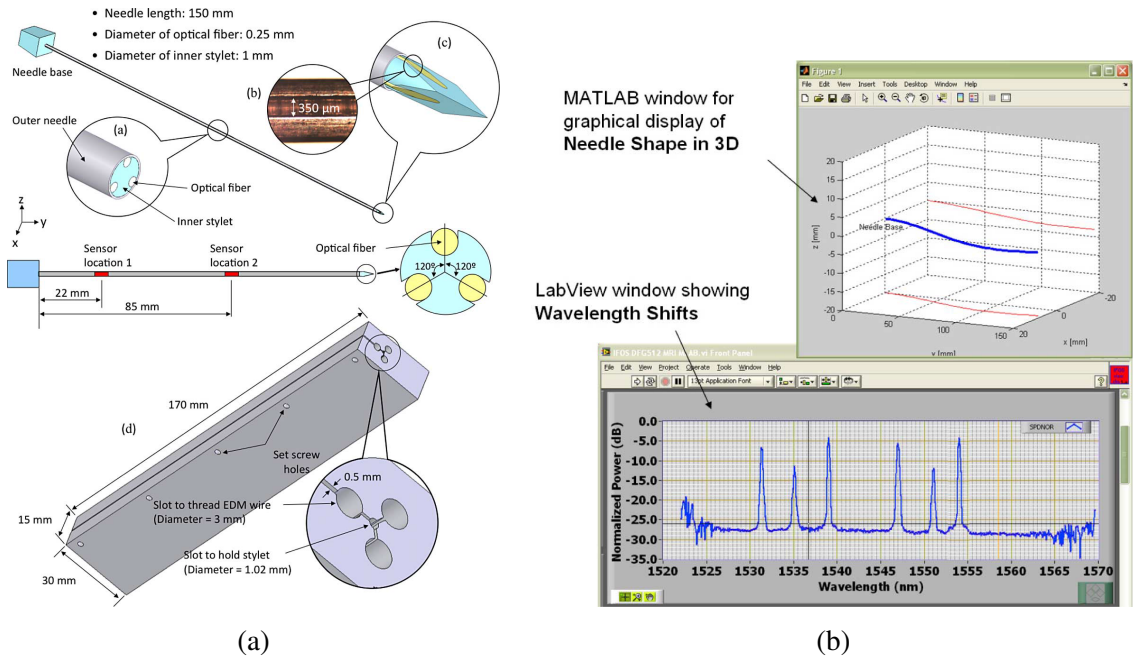


Figure 2.18: (a) Sensor design with three fibers in a biopsy needle developed by Park *et al.* in [92], (b) graphical display showing the shape of the needle and the wavelength shift.

vertically and horizontally in lateral axes. Also, the needle was exposed to various temperatures in the range of 20°C to 55°C in the absence of any mechanical force. The researchers successfully mapped a linear transformation between the needle curvatures in two lateral axes and temperature change to the FBG wavelength shift. Figure 2.18(b) shows a representative shape of the needle and its corresponding wavelength spectrum in bench tests.

Also, the needle was used under MRI imaging. Results showed fair agreement and verified accurate sensor performance in the MR environment. Using three or more fibers have been recommended to improve the system accuracy as well as using the sensors as force gauges to fine the tissue deformation model. This study shows a good example of sensor embedded medical devices for shape sensing flexible interventional instruments. Further development on this sensor could possibly be applicable for prostate and breast robot-assisted brachytherapy research [93, 94].

Zarrin *et al.* [95] developed two sterilizable sensorized needle driver graspers for laparoscopic instruments. Two FBG sensors were mounted in the custom-designed jaws of a grasper to measure axial and grasping force intraoperatively. The first prototype was designed with a T-shaped movable component contained an FBG to measure the axial force due to generated axial strain. A second

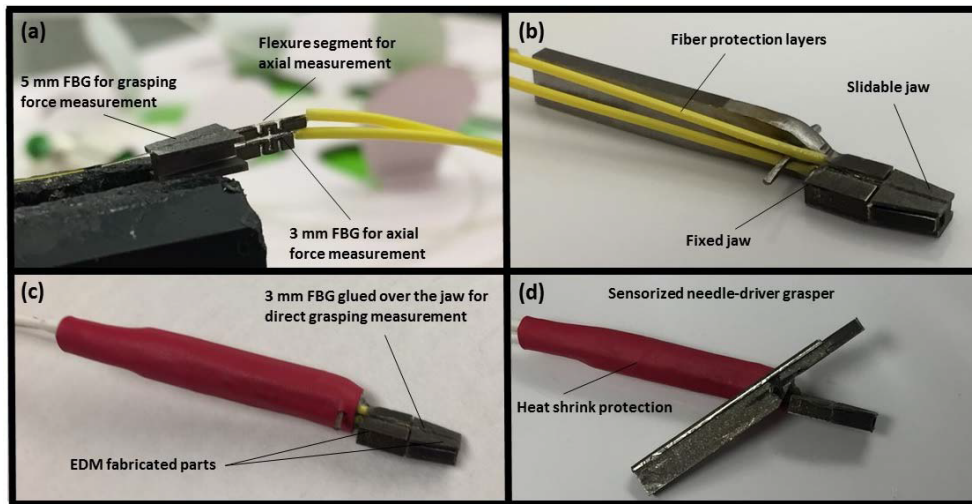


Figure 2.19: Two-DoF sensorized needle driving grasper equipped with an FPG sensor developed by Zarrin *et al.* in [95].

FBG was attached to the working part of the jaw to capture the grasping force directly. Calibration was done to find the relationship between the reference force from an ATI-nano commercial force/torque (F/T) sensor and wavelength shifts of the FBGs. However, the first design was not reliable enough to measure the axial force because of the outward bending of the jaws while grasping an object. Also, the sensor was not capable of measuring the accurate force values in different locations on the jaw. Nevertheless, the sterilization and resolution requirements were not addressed [96].

To cope with the limitations, a new prototype was developed to improve the sensing ability. Due to achieve biocompatibility and sterilizability, stainless steel was used to manufacture the sensor structure. The jaw was fabricated using a wire EDM machine to have a high-quality surface finishing and resulted in less friction between the sliding parts, thus more accuracy of axial force measurement. An I-beam component was embedded in the second prototype, and two FBGs were attached to measure the axial and grasping force. To alleviate the undesired outward bending of the axial sensor, it was located at the neutral axes of the cross-section of the jaw for better reinforcement. In addition, an I-beam was attached at the tip of the instrument to reduce the axial strain. Figure 2.19 depicts the sensor-embedded needle-driver grasper. Researchers utilized finite element analysis to predict the results deformation under working loads which were reported in acceptable

axial strain and out-of-plane warping.

An optical interrogator was used to record the FBG wavelength, while the applied grasping and axial force were recorded by ATI-nano F/T sensor. Furthermore, the location of the force was changed to evaluate the sensor response versus the location. The relationship between the recorded force data and FBG wavelength shift was calibrated using the linear regression. With the applied force in the range of 0 – 10 N, the demonstrated measurement range of the sensor was 0 – 6 N for grasping and 0.27 and 0.3 for loading along the x - and y - directions, respectively. The sensitivity for the grasping and axial sensors were 64.38 and 166.5 N/mm , respectively. The results were acceptable to present this sensorized needle-driver grasper for MIS applications. However, temperature compensation was still unmet.

In summary, the FBG-based sensors are bio- and MRI-compatible, which are the most limiting factor for non-optical sensing principles. Depending on the structural design and manufacturing material, the sensor could be sterilizable and physically robust. In addition, multiple FBG portion with various bragg-lengths can be created along a single optical fiber and be calibrated to measure various parameters, simultaneously. Furthermore, due to their small size and flexibility, an FBG-based sensor can fit on the typically confined structures of surgical instruments used for MIS and RMIS applications. These sensors are sensitive enough to capture the small strain in the micro-scale. However, relatively expensive and sophisticated optical source and optical interrogator are needed for the FBG signal processing system.

Also, a major drawback of the FBG sensors is that such sensors are intrinsically temperature-sensitive and require temperature compensation to preserve their sensitivity and accuracy. Nevertheless, FBG-sensors make favorable options for accurate temperature monitoring applications. Some MIS and RMIS application such as cryosurgery and radiofrequency tissue ablation [97] are associated with intraoperative high-temperature changes, e.g., from -80°C to $+60^{\circ}\text{C}$. Therefore, there is a compromise between the reliable range of working temperature and force sensing capabilities of FBG-sensors. Representative FBG sensors for MIS applications are summarized in Table 2.2.

Phase Modulation Optical Tactile Sensor

Another optical phenomenon based on which sensors have been proposed is the phase modulation principle. Such sensors basically, work based on Fabry-Perot interferometry (FPI). The FPI-based sensors are comprised of a semi-reflective surface at the end of an emitting optical fiber and another reflective surface placed at a certain distance in front of it (Figure 2.20). Such configuration is known as the Fabry-Perot cavity.

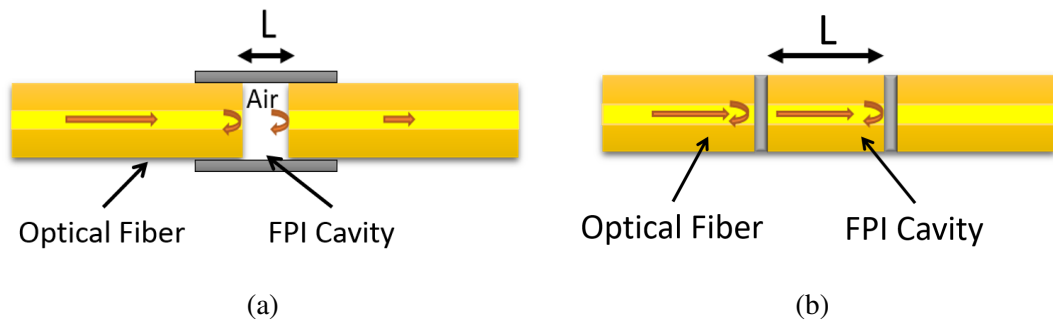


Figure 2.20: Fabry-Perot configuration: (a) extrinsic, (b) intrinsic.

In a Fabry-Perot cavity, light reflects back partially to the emitting fiber, while another retro-reflection happens at the surface of the reflective surface at a distance. By visualizing the superposed light-emitting back from the fiber, circular interference patterns form as a result of the phase difference between the two retro-reflections (one from the semi-reflective end of the fiber and one from the reflective surface in the cavity). By analyzing the width of dark and bright bands in the interference pattern, a precise estimation of the distance (cavity length) is obtained. The band thickness and their intensity is a function of the Fabry-Perot cavity length; therefore, external force, pressure, and displacement causing the change in cavity distance can be calibrated with respect to the phase shift or change in the intensity of the fringes [98].

Depending on whether the light leaves the emitting Fabry-Perot fiber or reflects internally, this sensing principle is categorized as extrinsic and intrinsic, respectively. Figure 2.20 depicts these two categories schematically. Also, a comprehensive review of the physics and application of FPI sensors is provided in [99]. The phase difference of the interference signal, δ_{FPI} is expressed as

Eq. 17), [100]:

$$\delta_{FPI} = \frac{2\pi n^2}{\lambda} L_{cavity}, \quad (17)$$

where, λ is the wavelength of the incident light, n is the refractive index of the cavity main and L_{cavity} is the length of the FP cavity. In addition, the reflected intensity can be calculated through the summation of two reflected light intensity, I_1, I_2 with two different phases, ϕ_1, ϕ_2 and applying Euler's identity, Eq. 18), [101]:

$$I = I_1 + I_2 + 2I_1 I_2 \cos(\phi_1 - \phi_2). \quad (18)$$

Shang *et al.* [102] proposed an MRI-compatible FPI optical sensor to measure needle insertion force for prostate cancer brachytherapy. They designed a mechanical fixture to keep the FPI sensor and embedded it into an MRI-compatible prostate needle insertion robot [103]. The sensing principle of the sensor and its structure are shown in Figure 2.21(a). As illustrated, the fringes generated by red beams would be different from those created by black beams when the cavity length was changed by applying the load. Therefore, the change in fringe intensity was calibrated versus the magnitude of the applied force.

Also, a finite element analysis was performed for structural optimization to keep the sensor structure intact under the working force range. Calibration was done by putting standard weights on the sensor prototype. Figure 2.21(b) illustrate the FPI sensor in the biopsy needle. A photodetector converted the reflected light signal into a voltage signal, and force-voltage data were recorded for post-processing. The sensor worked accurately in the range of 0 – 10 N with the 0.318 N root-mean-square (RMS-) error.

In another effort, Mo *et al.* [104] presented an FPI force sensing system to use in the needle insertion application. Two FPI sensors were mounted in parallel at the tip of a puncture needle with 1.54 mm internal diameter. The two sensors worked based on the interferometric intensity-phase modulation. One of the FPI sensors was designed to measure the axial force at the tip and temperature, while the second FPI sensor was utilized as the reference temperature sensor. The schematic figure of the two FPI sensors inside the needle tip and the sensor-embedded needle is shown in Figure 2.22(a). A laser source with the wavelength 1550 nm transmitted the light and a

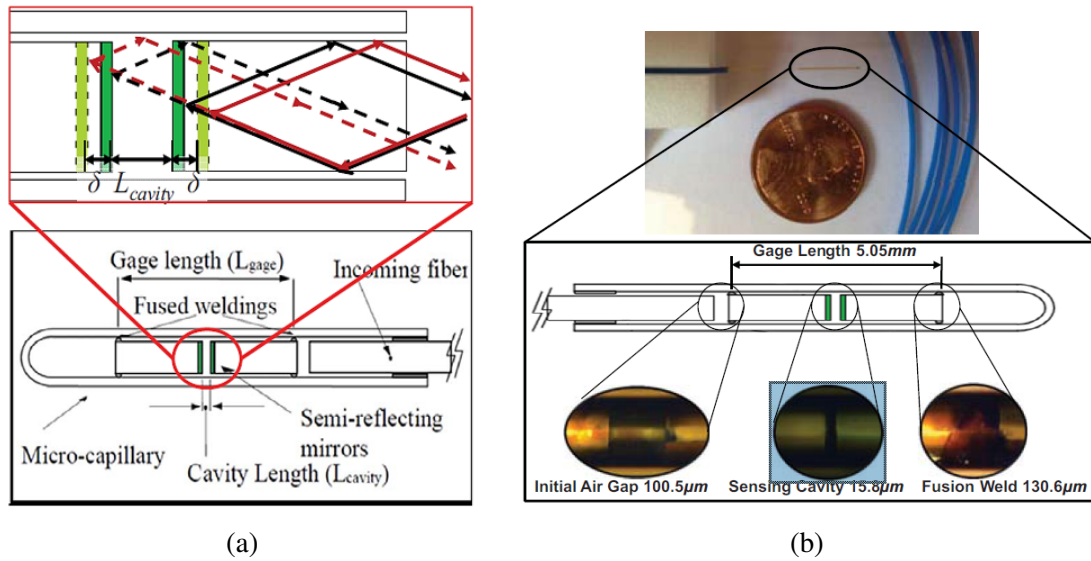


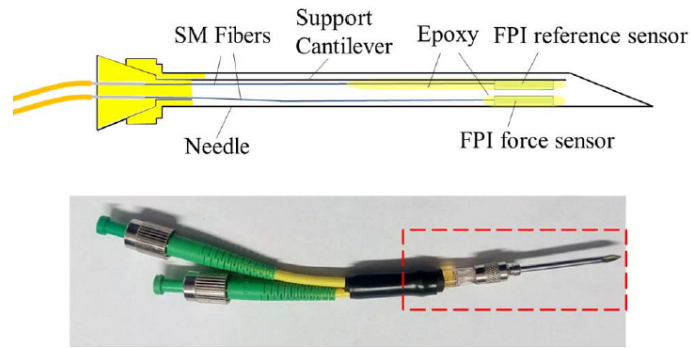
Figure 2.21: (a) Structure and sensing principle of the FPI sensor proposed by Shang *et al.* in [102], (b) their prototyped sensor embedded on a biopsy needle.

splitter, which divided the light into two fibers. The interfered pattern of two sensors was measured by photodiodes, and the force and temperature estimation was performed in a computer workstation. Figure 2.22(b) illustrates the temperature FPI sensor embedded on the needle.

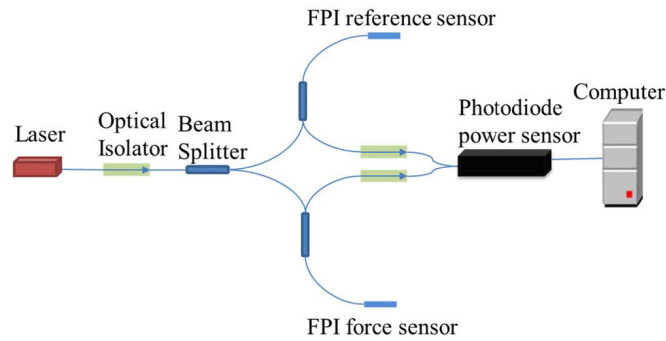
The system was calibrated with a commercial dynamic force sensor and a linear model was obtained between the dynamic force and temperature compensated intensity phase of the FPI force sensor. The result showed that the system performance was accurate in the range of 0 – 8 N and the temperature range of 23 – 37.5 °C. The system performance was verified with an insertion experiment inside a skin phantom at various temperatures and different insertion depths. Analyzing the tip force and insertion speed was recommended to detect the tissue type and its abnormality in the future investigation.

FPI sensors are highly sensitive with a tunable range of measurements. Structural optimization has become a scheme in fine-tuning FPI sensors for the mechanical requirements of MIS applications. Furthermore, FPI sensors can be integrated into the small space of the surgical instruments. Also, they are biocompatible and work in magnetic field environments properly. In comparison with the expensive optical analyzer of FBG sensors, signal processing of the FPI sensors is fairly simpler and does not require intense signal processing algorithms.

In addition, FPI sensors are sterilizable with both ethylene oxide and steam. However, care



(a)



(b)

Figure 2.22: (a) Schematic of the two FPI sensor inside the needle tip and the sensorized needle proposed in [104], (b) temperature compensation FPI sensor for MIS needle.

must be taken in handling these sensors, since the precise alignment and packaging of the fibers are crucial for maintaining the calibration. Another limitation of FPI sensors is that FPI cavities are intrinsically open structures, which firstly makes the whole structure of the sensor compliant and prone to fracture, and secondly makes it open to biological fluids. The latter would compromise the whole sensor performance by altering the light path, if not blocking. Also, the open cavity structure makes the sterilization validation process cumbersome due to providing a space for the micro-organisms to grow and not reachable by sterilizing agents [105–107]. Another limitation of the FPI sensors is manufacturability. Table 2.2 presents a summary of various FPI sensors developed for MIS applications.

Table 2.2: Summary of the representative studies proposing tactile sensors for MIS or RMIS based on optical sensing principles.

| Authors | Year | Principle | Application | Measurands | Range | Characteristics |
|-----------------------------------|------|-----------|------------------|-------------|--|---|
| Webb <i>et al.</i> [108] | 2000 | FBG | MIS | Temperature | 0-55 C | Res= 0.2°C Error _{max} = 3°C |
| Tada <i>et al.</i> [109] | 2002 | LIM | MIS | Force | 0-16 N | Res= 0.5 N Error= ±0.3 N |
| Chapuist <i>et al.</i> [110] | 2004 | LIM | Neuroscience | Torque | ±5 Nm | Res= 0.07 Nm S = 7.21 \sqrt{Nm} |
| Su <i>et al.</i> [111] | 2009 | LIM | Biopsy | Force | 0-20 N | Res= 0.2 N Linearity= 96.7% |
| Muller <i>et al.</i> [112] | 2009 | FBG | RMIS | Force | $F_x=0-10$ N $F_y=0-10$ N $F_z=0-20$ N | Res _{x,y,z} = 100 mN SD= 4 mN |
| Polygerinos <i>et al.</i> [113] | 2009 | LIM | Cardiac ablation | Force | 0-1.10N | Res= 0.04 N Variation \downarrow 0.2 N |
| Kesner <i>et al.</i> [114] | 2011 | LIM | MIS | Force | 0-10N | Res= 0.2 N RMSE <0.2 |
| Su <i>et al.</i> [98] | 2011 | FPI | Needle steering | Force | 10 N | Res= 1 mN SNR = 98% |
| Liu <i>et al.</i> [115] | 2012 | FPI | Eye surgery | Force | 6 mN | Res= 0.25 mN S= 40 $\mu\text{m}/\text{mN}$ |
| Polygerinos <i>et al.</i> [116] | 2013 | LIM | Cardiac ablation | Force | 0-0.50 N | Res < 0.01 N Accuracy= 94% Linearity= 96% Hysteresis= 6% |
| Elayaperumalu <i>et al.</i> [117] | 2014 | FBG | Biopsy | Force | ±0.5 N | Res= 0.043 N Error _x = 1.1 mN Error _y = 0.4 mN Error _z = 1.2 mN |
| Ahmadi <i>et al.</i> [118] | 2015 | LIM | MIS | Force | 0-2N | Error=3% |
| Mo <i>et al.</i> [119] | 2015 | FPI | MIS | Force | 0-5 N | Res= 0.1 mN |
| Qiu <i>et al.</i> [120] | 2016 | FPI | OCT | Force | 1.2 N | Res= 0.25 mN |
| Li <i>et al.</i> [121] | 2018 | FBG | Palpation | Force | 0-5 N | Res= 93 mN Error < 8.22% Location \downarrow 8 mm |
| Bandari <i>et al.</i> [28] | 2019 | LIM | MIS | Grasping | 0-2N | Res=0.02 N Linearity=94% RMSE=0.11 N SD=0.07N |
| Wanninayake <i>et al.</i> [122] | 2019 | LIM | MIS | Indentation | 1-3 mm | N/A |

S: Sensitivity, SD: Standard Deviation, Res: Resolution, SNR: Signal-to-Noise Ratio
OCT: Optical Coherence Tomography

2.4 Conclusions

In this paper, articles proposing novel tactile sensors for MIS or RMIS application were reviewed. The main motivation for this paper was the lack of a multi-disciplinary review with the focus on tactile sensors with MIS/RMIS application. Most of the reviews in the literature are centered on the sensing principles, while some focus merely on artificial skin and artificial sense of touch for robots. Therefore, initially, a systematic categorization of the available sensors in the literature was provided, i.e., electrical-based and optical-based sensors. Afterward, the sensing principles and theoretical backgrounds, as well as the methodological details and technical advancements adopted by researchers in each category, were reviewed. At the end of each sensing principle, the representative studies were reviewed critically, and at last, the advantages and limitations of each were discussed.

An emerging research and development trend in the literature is the evolution of *hybrid* sensors. Hybrid sensors are basically, the sensors which employ more than merely one sensing principle to measure one or multiple physical stimuli, e.g., force, displacement, stiffness, etc. In fact researchers have proposed the use of hybrid sensors on two grounds: 1) for obtaining more robust measurements of physical stimuli, e.g., common noise cancellation, temperature compensation, and 2) for covering wider working environments, e.g., using a sensor under static forces and another under dynamic forces, or using a sensor when the magnetic field is present and another when the magnetic field is negligible.

There is a relatively small number of recent developments of hybrid sensors for MIS and RMIS, e.g., [29, 123–129]. However, thanks to the adoption of the recently developed concepts of sensor fusion and machine learning, this field of research has gained momentum. There are still technical and methodological challenges such as multi-sensor cross-talk, noise amplification, heterogeneous refresh-rate, asynchrony of sensor readings, and increased the complexity of the system. Therefore, new research efforts are yet expected to overcome the impediment of the technological limitations for hybrid tactile sensors.

Although the majority of the current literature has used a linear uni- or multi-variable regression calibration schema, new non-linear technique is emerging. Some of the recent developments have

adopted more complex phenomena or structures such as variable bending radius (VBR) intensity modulation [20, 21] and viscoelastic structures [89] to achieve more precision and less hysteresis. Such phenomena or structures are intrinsically non-linear, thus need non-linear regression models. The models proposed include both analytical and heuristic models. While for analytical models, power-law and polynomial expressions have been the most popular, the heuristic models have adopted neural network [130], deep-learning [131], and support vector regression methods [13, 21].

In addition, the future works might include chamberless light modulation, rigorous modeling of the light modulation, rate-dependent calibration law, power spectral density analysis to quantize dynamics of the problem, camera-based intensity quantization, and miniaturization by using pre-bundled multi-core optical fibers. Also, as the shape-sensing of the soft-robots, e.g., catheters, for MIS and RMIS, has gained momentum in the field of robotics [14, 130–133], the need for the body-embedded sensor for shape sensing is eminent and prominent.

Chapter 3

Hybrid Piezoresistive-optical Tactile Sensor for Simultaneous Measurement of Tissue Stiffness and Detection of Tissue Discontinuity in Robot-assisted Minimally Invasive Surgery

To compensate for the lack of touch during minimally invasive and robotic surgeries, tactile sensors are integrated with surgical instruments. Surgical tools with tactile sensors have been used mainly for distinguishing among different tissues and detecting malignant tissues or tumors. Studies have revealed that malignant tissue is most likely stiffer than normal. This would lead to the formation of a sharp discontinuity in tissue mechanical properties. A hybrid piezoresistive-optical-fiber sensor is proposed. This sensor is investigated for its capabilities in tissue distinction and detection of a sharp discontinuity. The dynamic interaction of the sensor and tissue is studied using finite element method. The tissue is modeled as a two-term Mooney–Rivlin hyperelastic material. For experimental verification, the sensor was microfabricated and tested under the same conditions as of the simulations. The simulation and experimental results are in a fair agreement. The sensor exhibits

an acceptable linearity, repeatability, and sensitivity in characterizing the stiffness of different tissue phantoms. Also, it is capable of locating the position of a sharp discontinuity in the tissue. Due to the simplicity of its sensing principle, the proposed hybrid sensor could also be used for industrial applications.

3.1 Introduction

During the last decade, robot-assisted minimal invasive surgeries (RMIS) have been introduced as an alternative to the surgeon-operated minimally invasive surgeries (MIS) to enhance the precision and dexterity of tool maneuvering. RMIS could open a new horizon to health care providers seeking a reliable solution for remote surgeries. Despite the advantages of RMIS to both surgeon and patient, losing the sense of touch is a major shortcoming [11, 134]. The first generation of the da VinciTM surgical system (Intuitive Surgical, Inc., Sunnyvale, California), with > 3400 units sold worldwide, did not provide surgeons with haptic feedback during tissue manipulation [134]. Surgeons usually palpate the tissues to have a perception of its stiffness to identify if it is a malignant mass, an artery, or a nerve.

To compensate for the lack of haptic and tactile information, haptic feedback systems, using tactile sensors and actuators, were introduced as a part of RMIS surgical units [11, 134]. Furthermore, the haptic feedback systems prevented tissue laceration by limiting the holding force that surgeons were able to apply [134–137]. It has been experimentally shown that providing tactile feedback would lead to less grasping force in the da VinciTM system [37, 38]. In this regard, King *et al.* [37, 38] integrated a FlexiForceTM force sensor on the surgical tool of the da VinciTM system and transmitted the grasping force to the surgeons. Their study revealed that the force feedback could reduce the grasping forces during the operations significantly. Also, other researchers have equipped surgical graspers with tactile sensors to assess the stiffness of the tissue [138–141]. Figure 3.1 shows a typical setup for robotic surgery in an operation room as well as a conceptual integration of a force sensor on a grasper of the da VinciTM system.

Constitutively, most living tissues show a viscoelastic mechanical behavior [142, 143]. A major phenomenon associated with the viscoelasticity of these tissues is the stress relaxation under

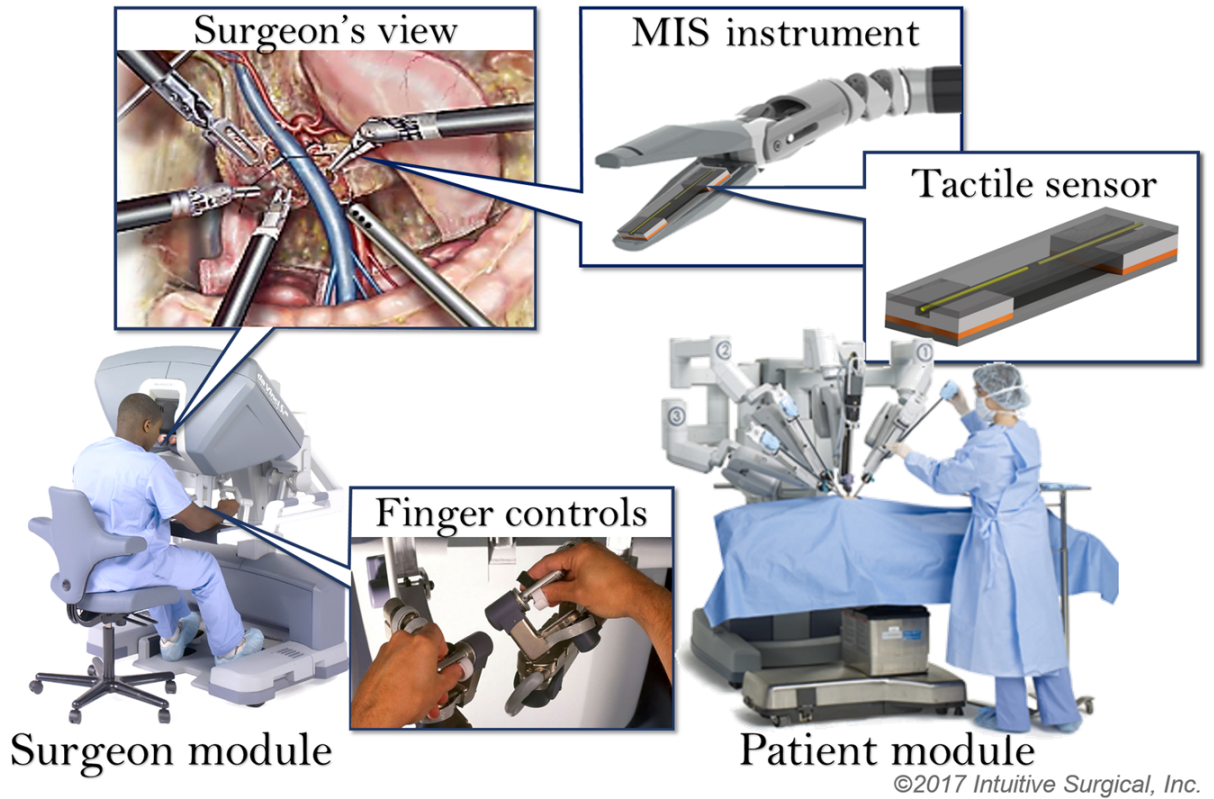


Figure 3.1: Conceptual overview of a tactile sensor embedded in an MIS grasper. A surgeon uses the finger controls of the surgeon module to perform surgery. MIS instruments, equipped with tactile sensors, can help surgeons in tissue distinction. [Reproduced with permission, courtesy of (Intuitive Surgical Inc., California)].

sustained grasping pinch [142], which results in an exponential depreciation in the contact force between the surgical tool and the tissue. Depending on the microstructure of tissue, the time constant of this stress relaxation can range anywhere between one-tenth of a second and several minutes [143]. This phenomenon leads to a dynamic interaction force between the surgical tool and tissue. The major limitations in developing a tactile sensor for minimally invasive surgical applications are size, biocompatibility, electro-passivity, magnetic resonance (MR) compatibility, and x-ray opacity [144].

The tactile sensors proposed in the literature are designed based on electrical or optical sensing principles [16]. Electric tactile sensors mainly employ variable capacitance, piezoelectricity, and piezoresistivity phenomena, and therefore, they are not MR-compatible and electro-passive [145]. However, electric sensors possess simple sensing principles and are capable of direct force measurement. Also, electrical sensors are scalable to different length scales. These properties have led researchers to use such sensors in the minimally invasive surgical applications where MR compatibility and x-ray opacity are not a clinical priority [44], for example, gastrointestinal surgeries.

On the other hand, optical-based sensors satisfy MR compatibility, electro-passivity, and size conditions; therefore, they make a good choice in minimally invasive surgical applications [17, 44, 144, 146, 147]. In addition to that, possibilities for miniaturization and low-cost production are of remarkable advantages of optical-based sensors; [78, 148], however, optical-based sensors are not capable of direct force measurement. On the other hand, because of the nonlinear mechanical properties of the biological tissues, establishing a simple and valid force estimation scheme from the measured deformation is cumbersome.

Researchers have developed optical tactile sensors based on three sensing principles of fiber bragg grating (FBG), Fabry–Perot interferometry (FPI), and light-intensity modulation (LIM) [78, 148]. In an early study, Polygerinos *et al.* [17] proposed a miniaturized optical fiber sensor for measuring the point loads at the tips of angiographic catheters; however, the proposed sensor was unable to measure the actual lateral forces acting on the tip of the catheter. In another study, Yip *et al.* [87] developed an LIM force sensor for surgical application based on the deformation-induced intensity modulation in a set of optical fibers.

Elayaperumal *et al.* [117] demonstrated a triaxial tip-force sensing needle to provide the real-time haptic feedback during surgery. In their study, an FBG sensor was attached to a biopsy needle for strain measurement. Recently, Qiu *et al.* [120] developed an FPI force sensor equipped with a miniaturized quantitative optical coherence elastography. Their sensor was capable of in situ estimation of the elastic modulus of a biological tissue based on the simultaneous measurement of force and deflection in it. Similarly, Noh *et al.* [89] proposed a miniaturized triaxial LIM force sensor, mounted at the tip of a cardiac ablation catheter to measure the contact force. In their study, the deflection-induced change in the light intensity carried by three optical fibers was measured using a CCD camera and a multilinear calibration scheme was used for force estimation.

In an early effort, researchers of this study developed an optical sensor working based on the bending intensity-modulation sensing principle. That sensor was capable of estimating the external force and locating a hidden mass inside a tissue phantom discretely in four regions [84]. However, it was neither miniaturized nor capable of estimating the stiffness of tissue. In continuation, highly sensitive sensors based on the intensity loss in a coupling gap were developed [19, 85, 118, 149]. This could significantly improve the sensitivity of sensors and simplify the designs. Despite the improvements, accurate force estimation and hidden mass location were yet to be addressed.

To address the common problem of precise force measurement in RMIS applications, a hybrid force sensor was designed, modeled, simulated, fabricated, and experimentally verified in this study. This hybrid sensor uses sensing principle of piezoresistivity, to directly measure the contact force and intensity modulation in optical fibers, also to estimate the deformation in the tissue (Figure 3.2). The idea of hybrid sensing is to increase the accuracy of the sensor by replacing “force estimation” with “direct force measurement.” In addition, piezoresistive sensors exhibit scalability, linearity, low hysteresis, and low noise. Also, such sensors can work under both static and dynamic conditions while maintaining acceptable repeatability [60]. By this design, the sensor is capable of estimating the stiffness of the tissue being contacted and can also measure the ratio of force in two separate piezoresistive sensing elements and detect the position of a hidden mass in tissue. Detecting stiffened tissues or masses is a routine exercise performed by surgeons through palpation in open surgeries [150]. Various studies have shown that it is very likely that malignant masses or tumors have a higher stiffness than the surrounding tissue [151–153].

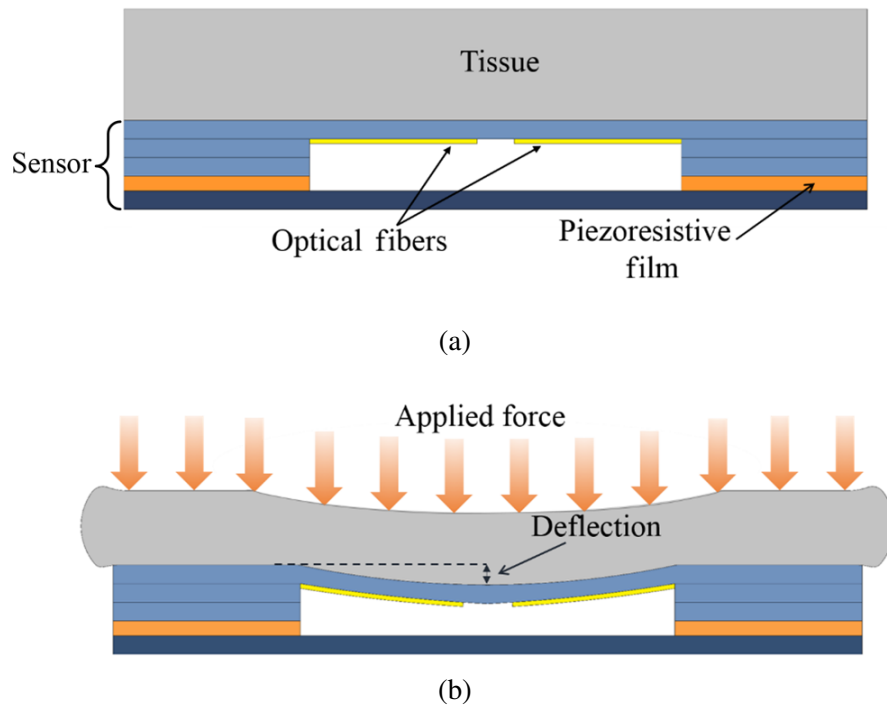


Figure 3.2: Schematic of the tissue and sensor: (a) without contact load, (b) with contact load applied from the gripping surgical tool, which leads to a deflection in both the sensor and tissue.

3.2 Sensor Design and Sensing Concept

3.2.1 Sensor Design

A schematic of the three-dimensional (3-D) hybrid force sensor proposed in this study is shown in Figure 3.3. The sensor incorporates two piezoresistive force sensing elements, two separate optical fibers, and eight silicon structural elements. A V-groove is bulk micromachined on the bottom surface of the beam on which two optical fibers were placed with a fixed gap (Figure 3.3(a)). The beam is fixed on the supports. The substrate, piezoresistive elements, and the chips form a sandwich configuration to transfer the interaction force from the beam to the substrate (Figure 3.3(c)). Each piezoresistive element consists of a piezoresistive film and two copper shell electrodes. One of the optical fibers was connected to a light source while the other was connected to a photodetector.

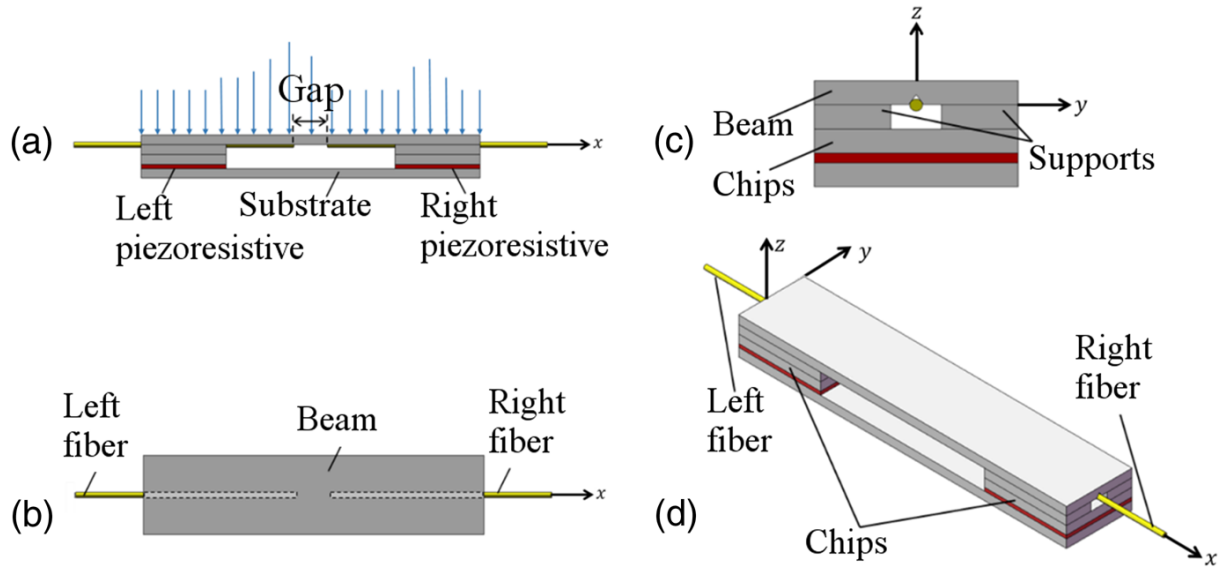


Figure 3.3: Structural design of the hybrid sensor in (a) lateral, (b) top, (c) longitudinal, (d) perspective view.

3.2.2 Sensing Concept

In the proposed sensor, the gap between the fibers resulted in a predictable initial coupling power loss. Additionally, the deflection of the beam developed an angular misalignment between two fibers. This misalignment would lead to further power loss between fibers (Figure 3.4); therefore, the total loss of the power between fibers was due to both gap and angular misalignment.

The basic sensing concept behind this design was to measure the gap power loss by comparing the input power to the first fiber, P_i , with the output power of the second fiber, P_o . Nemoto and Makimoto [74] used geometrical optics principles and Gaussian distribution of the power spectrum on the cross section of an optical fiber to quantify the power loss due to coupling gap and misalignment between the two identical fibers. Gaussian distribution of the power spectrum is widely used by researchers as an acceptable approximation of the exact power spectrum distribution in optical fibers [74, 154–156]. Li *et al.* [154] enhanced the study conducted by Nemoto *et al.* by considering the parabolic propagation of light into space and introduced the coupling efficiency, η , defined as the logarithmic measure of the input power with respect to the output power. Recently, Ahmadi *et al.* [19] successfully applied the same method in prediction of the total power loss due to both gap and angular misalignment.

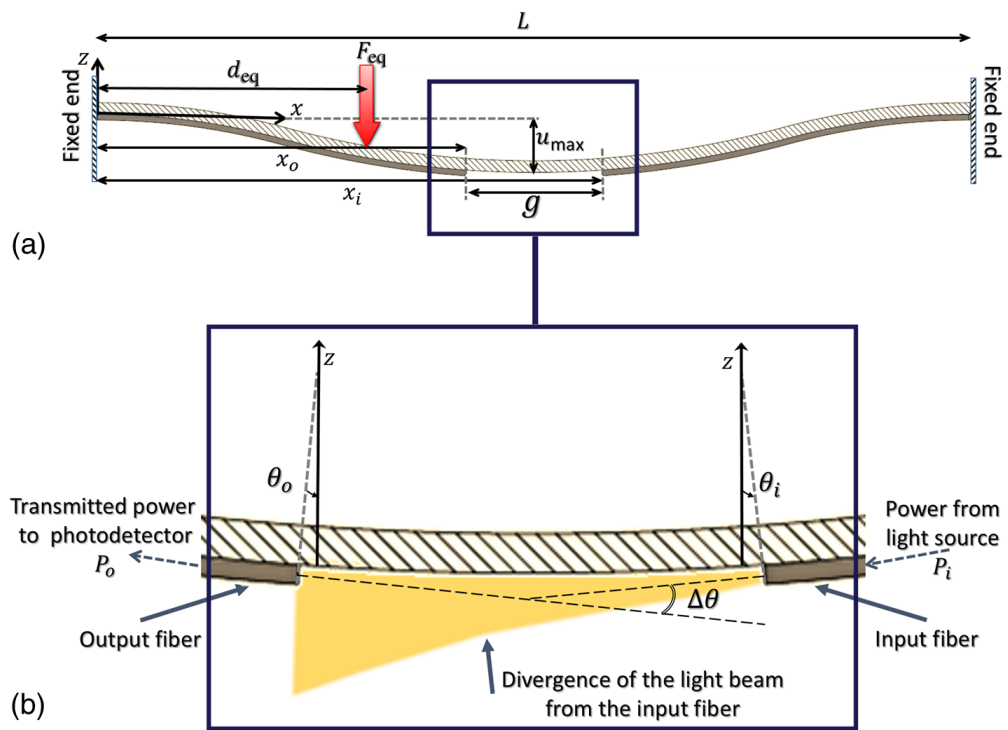


Figure 3.4: (a) Schematic view of the deformed configuration of the sensor beam and optical fibers, (b) detailed view of the gap between two optical fibers and formation of the angular misalignment, $\Delta\theta = |\theta_i| + |\theta_o|$ as a result of vertical deformation in the beam and movement of the fiber tips.

To determine the stiffness of the tissue, the maximum deformation resulting from the contact force was measured. This contact force is developed upon a sensor touching a tissue and causing a deflection in both tissue and sensor. As Figure 3.2 shows, the maximum deformation in the tissue is equal to the maximum deflection of the beam u_{max} . In this sensor, the total contact force was measured by the piezoresistive sensing elements. To measure the maximum deflection, a theoretical framework was used as described below.

In Figure 3.4, the distance between the fibers is represented by g , angular misalignment by $\Delta\theta$, total equivalent contact force by F_{eq} , and position of center of pressure by d_{eq} . In this framework, by using F_{eq} and d_{eq} , both distributed contact forces (large and flat tissues) and point contact forces (small and round tissues) are modeled. Because of the symmetry, the eccentricity and deflection of fibers in the y – *direction* was neglected (Figure 3.3 (d)). As the output voltage of the photodetector is a linear function of the transmitted power between fibers [19], the transmitted power (P_o) was obtained using the output voltage of the photodetector. The constant input power (P_i) was provided by a light source. Comparing output and input powers, the coupling efficiency (η) was calculated using Eq. 19, whereas Eq. 20 defines the coupling efficiency as a function of both axial gap and angular misalignment [74, 154]. As the gap (g) was assumed to remain constant throughout the deformation (small deformation assumption), the coupling efficiency was merely a function of angular misalignment $\Delta\theta$. Therefore, Eq. 20 was solved for $\Delta\theta$ to estimate the angular misalignment from the coupling efficiency.

$$P_o = \eta P_i, \quad (19)$$

$$\eta = 4 \frac{1}{B} e^{(-A \frac{C}{B})}, \quad (20)$$

$$A = 2 \left(\frac{\pi w n_0}{\lambda} \right)^2, \quad (21)$$

$$B = 4 + \left(\frac{g \lambda}{\pi n_0 w^2} \right)^2, \quad (22)$$

$$C = \left[2 + \left(\frac{g\lambda}{\pi n_0 w^2} \right)^2 \right] \sin^2 (\Delta\theta), \quad (23)$$

in which λ is the wavelength of the light and n_0 is the refractive index of the air. The Gaussian mode field radius of optical fibers, w , was calculated using;

$$w = a \left(0.65 + \frac{1.619}{H^{3/2}} + \frac{2.879}{H^6} \right), \quad (24)$$

where,

$$H = \frac{2\pi a}{\lambda} \sqrt{n_1^2 - n_2^2}, \quad (25)$$

in which a , n_1 , and n_2 were the radius of the core, refractive index of the core, and refractive index of the cladding of optical fibers, respectively. To calculate the deflection indicated in Figure 3.2, a composite beam problem consisted of both tissue materials, and a beam of the sensor was solved. Figure 3.4 represents a composite beam problem for finding the deflection of beam, u_z . The analytic solution for the displacement in this problem is provided in Eq. 26 [157]. By taking derivation of displacement u_z with respect to length x , the angular deformation $\theta(x)$ was obtained (Eq. 27). Furthermore, the angular misalignment $\Delta\theta$ was calculated by summation of absolute angular deformations at the tip of both fibers (Eq. 28).

$$u_z(x) = \begin{cases} \frac{F_{eq}(L-d_{eq})^2 x^2}{6E_c I_c L^3} [3d_{eq}(L-x) - (L-d_{eq})x] & x < d_{eq}, \\ \frac{F_{eq}d_{eq}^2 x^2}{6E_c I_c L^3} [3(L-d_{eq})(L-x) - d_{eq}x] & x \geq d_{eq}, \end{cases} \quad (26)$$

$$\theta(x) = \frac{du_z(x)}{dx} = \begin{cases} \frac{F_{eq}(L-d_{eq})^2 x}{2E_c I_c L^3} [2d_{eq}(L-x) - Lx] & x < d_{eq}, \\ \frac{F_{eq}d_{eq}^2 x}{2E_c I_c L^3} [2d_{eq}(L-x) + 2L^2 - 3Lx] & x \geq d_{eq}, \end{cases} \quad (27)$$

$$\Delta\theta = |\theta_i| + |\theta_o|, \quad (28)$$

$$E_c I_c = E_t I_t + E_b I_b, \quad (29)$$

where,

$$\theta_o = \theta(x_o), \quad (30)$$

$$\theta_i = \theta(x_i), \quad (31)$$

, where $x_o = \frac{L-g}{2}$ and $x_i = \frac{L+g}{2}$ in Eq. 30 and Eq. 31, respectively. Also, $E_c I_c$ is the flexural rigidity of the composite beam, $E_t I_t$ is the flexural rigidity of the tissue, and $E_b I_b$ is the flexural rigidity of the beam of sensor.

Introducing the angular misalignment $\Delta\theta$, from Eq. 20, and total contact force, F_{eq} , from measurement by piezoresistive sensing elements, to Eq. 28, the flexural rigidity of the composite beam, $E_c I_c$ was calculated. The deflection indicated in Figure 3.2 was calculated using Euler–Bernoulli beam theory. Solution of Eq. 27 for $\theta(x) = 0$ reveals the value of u_{max} (Eq. 32). As an angular misalignment of $\Delta\theta$ is developed in response to contact force between tissue and sensor, estimation of u_{max} is ensured in every test. Equation 33 defines the stiffness (K) as the ration of contact force (F_{eq}) to the maximum deflection of beam (u_{max}) derived from Eq. 32. The stiffness K is dependent on both the flexural rigidities of the sensor and the tissue; however, the contribution of the sensor is constant and the contribution of the tissue varies in different tissues. Therefore, as K is a function of only the stiffness of tissue, it was used for the purpose of tissue distinction.

$$u_{max} = \frac{2F_{eq}d_{eq}^3(L - d_{eq})^2}{3(E_t I_t + E_b I_b)(L + d_{eq})^2}, \quad (32)$$

$$K = \frac{F_{eq}}{u_{max}} = \frac{3(E_t I_t + E_b I_b)(L + d_{eq})^2}{2F_{eq}d_{eq}^3(L - d_{eq})^2}. \quad (33)$$

Depending on tissue type, d_{eq} and $E_c I_c$ possess a specific value when the sensor touches a tissue. These values are estimated in each test using Eqs. 26-31. In Eq. 33, d_{eq} and $E_c I_c$ depend only on the geometry and mechanical properties of the tissue and sensor.

3.3 Finite Element Modeling and Simulation

To model and predict the behavior of the sensor upon the application of an external force, or when contacting tissue, a 3-D model of the sensor was developed in CATIA V5 (6R2014, Dassault Systèmes, France) and imported into ANSYS Workbench v.17 (Ansys Inc., Pennsylvania). The size and dimension of the geometric model are shown in Figure 3.5. Fixed boundary conditions were applied to the sensor components. A frictionless contact condition was assumed between the sensor and the tissue phantoms.

An incompressible two-term Mooney–Rivlin (2MR) hyperelastic model was used for modeling the tissue phantoms. The 2MR hyperelastic model is well reported to successfully capture the mechanical properties of soft tissues, such as a cardiac wall, vessel wall, liver, skin, and bursae [158]. The constitutive equation of the 2MR hyperelastic material under uniaxial compression is provided in [159], as Eq. 34.

$$\sigma = 2 \left(C_{10} + \frac{L_0}{L} C_{01} \right) \left[\left(\frac{L_0}{L} \right)^2 - \frac{L}{L_0} \right] \quad (34)$$

in which σ is the Cauchy axial stress, C_{01} and C_{10} are the 2MR constitutive constants, L_0 is the uncompressed length, and L is the compressed length of the material sample. Three tissue phantom materials were synthesized using mouldable dual-component silicone rubber (Smooth On Co., Pennsylvania). Three shore hardnesses of 10-OO (extra soft), 30-OO (extra soft), and 20-A (soft) were obtained for tissues 1, 2 and 3, respectively. The constants for 2MR hyperelastic material model, C_{01} and C_{10} , were calculated for each tissue phantom as shown below.

A sample of each synthesized tissue phantom was tested during a uniaxial unconfined compression test. The mechanical tests were performed using a universal testing machine (Electroforce 3200, Bose Inc., Massachusetts). Then, the force–displacement data of each tissue phantom were used following the method reported in [149], and optimal model constants, C_{01} and C_{10} , were obtained. Figure 3.6 shows the nonlinear behavior of the softest tissue phantom (tissue 1) obtained during a monotonic compression test. The description, density, and mechanical properties for the constituents of the model are presented in Table 3.1. The model was analyzed under two different simulations.

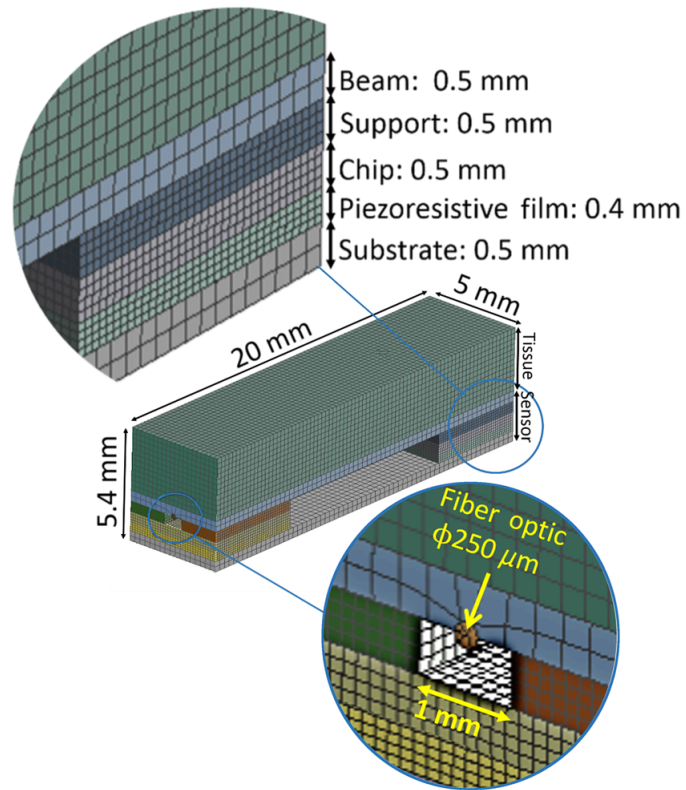


Figure 3.5: Mesh quality, geometric features, and dimensions of the sensor-tissue model.

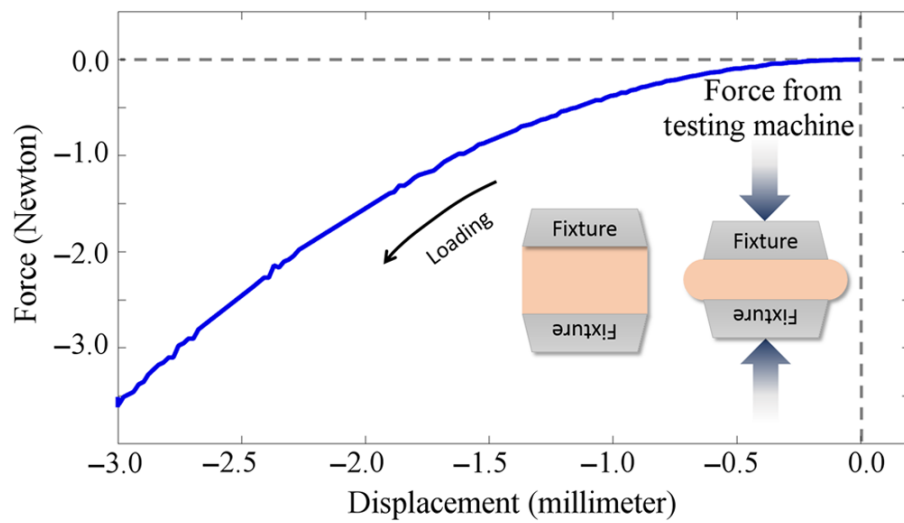


Figure 3.6: Force–displacement diagram of tissue phantom material made of Ecoflex® 00-10 silicone rubber (tissue 1). The nonlinear characteristic and large deformation are evident in the force–displacement relation.

Table 3.1: Material models used in finite element modeling of the sensor-tissue simulation.

| Material Model | Sensor Component | Material | Young's Modulus (GPa) | Poisson's Ratio | Density (kg/m ³) |
|----------------|------------------|--|-----------------------|-----------------|------------------------------|
| Linear Elastic | Structure | Silicon Wafer | 129.5 | 0.25 | 2330 |
| | Optical Fiber | - | 16.5 | 0.4 | 2500 |
| | Piezoresistor | Copper | 120 | 0.33 | 8960 |
| | | Mooney-Rivlin Constants | | | Density (kg/m ³) |
| | Tissue Phantom | Material | C_{10} (kPa) | C_{01} (kPa) | |
| Hyperelastic | Tissue 1 10-OO | Ecoflex [®] OO-10 silicone rubber | 27.147 | -25.776 | 1040 |
| | Tissue 2 30-OO | Ecoflex [®] OO-30 silicone rubber | 85.157 | -80.385 | 1070 |
| | Tissue 3 20-A | Dragon skin [®] 20A silicone rubber | 604.989 | -573.343 | 1080 |

3.3.1 Evaluation of Tissue Distinction (Simulation I)

As shown in Figure 3.7(a), the top surface of the tissue phantom, which was not in contact with the sensor, was subjected to a sinusoidal compressive force with an average amplitude of 1.3 N, at a frequency of 1 Hz. The analysis was repeated for three different tissue phantom materials. Meanwhile, the contact forces were extracted at the piezoresistive sensing elements and the relative angular misalignment between two fiber optics.

3.3.2 Evaluation of Hidden Mass Detection (Simulation II)

A spherical stainless steel inclusion, as a hidden mass, was modeled inside the tissue phantom at distance d on x-axis (Figure 3.7(b)). This method is frequently used by researchers to simulate the inclusion of a malignant tissue surrounded by normal tissue [84, 118, 149, 150, 160–162]. By this method, a sharp discontinuity in mechanical properties is incorporated to the model.

Sokhanvar *et al.* [44] have shown that the precision of the lump detection is decreased by increasing the stiffness of tissues; therefore, the hardest material model (tissue 3) was considered as being the worst-case scenario [44]. The tissue phantom was subjected to a sinusoidal compressive displacement at its superior surface with an average of 0.5 mm at a frequency of 1 Hz. The position of the hidden mass was changed from $d = 0$ mm to $d = 20$ mm (Figure 3.7). The simulation was repeated and the ration of force in the left piezoresistive sensor to the right sensor was estimated.

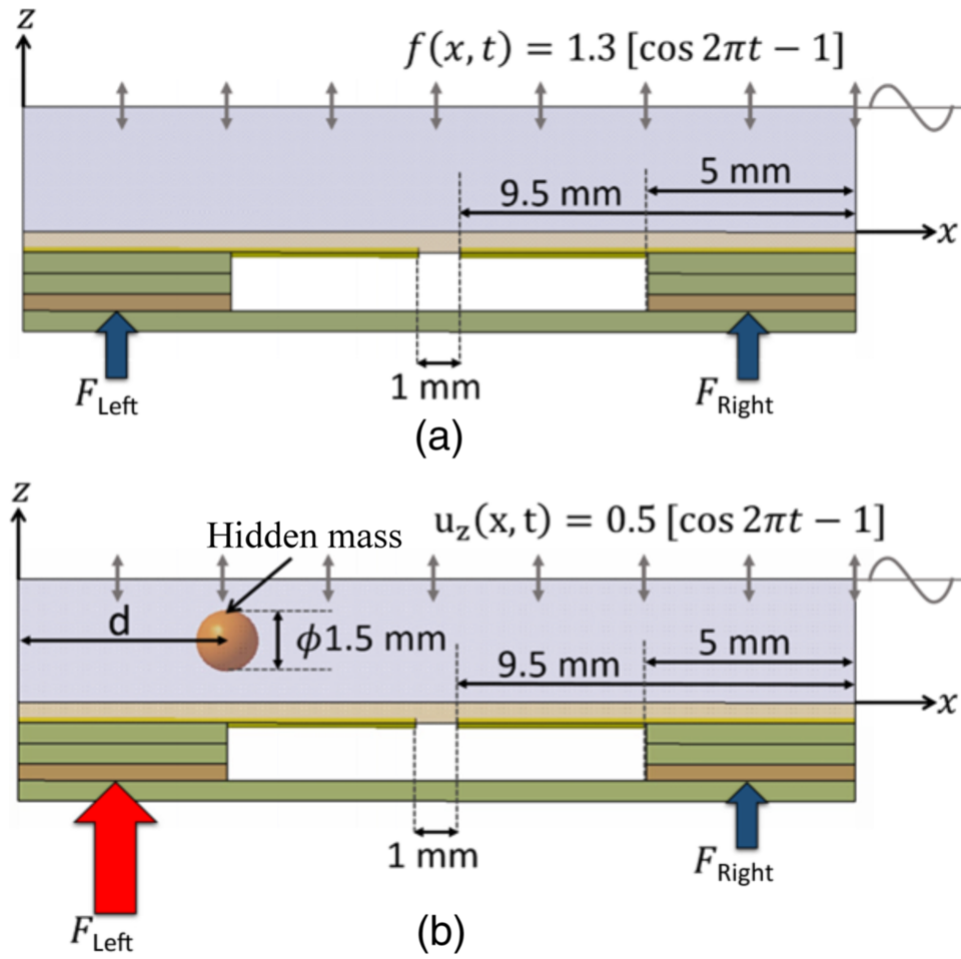


Figure 3.7: (a) Schematic loading on the tissue phantom and sensor in simulation I. $f(x, t)$ is the vertical compressive force applied on the top surface of the tissue phantom, (b) the tissue phantom with a hidden mass in simulation II. $u_z(x, t)$ is the displacement boundary condition at the top surface of the tissue phantom.

3.4 Microfabrication and Experimental Setup

The sensor was fabricated using micromachining technology. A V-groove was bulk micromachined on the bottom surface of the beam through an anisotropic wet etching process. The V-groove provided a foundation to integrate the optical fibers. Figure 3.8(a) shows a scanning electron microscopy (SEM) image taken from the V-groove and the integrated optical fiber in it. The smooth surface quality of the V-groove not only provided a smooth foundation on which to attach the fibers to the sensor but also led to the precise initial alignment of fibers.

Figure 3.8(b) shows the different structural components of the sensor before the final assembly. The silicon substrate, chips, and the supports were fabricated from an N-type $< 100 >$ silicon wafer with a thickness $500 \mu\text{m}$.

The substrate provides a rigid base to assemble the other components of the sensor. Two square parts of Linqstat film (piezoresistive element of required size) are sandwiched between two $200\text{-}\mu\text{m}$ thick copper electrodes (Figure 3.8(c)).

The assembled sensor was calibrated following the method introduced in [149]. A superluminescent diode light source (HP-371, Superlum Co., Ireland) with a central wavelength of 843 nm was connected to one fiber. The other fiber was connected to a photodetector with working wavelengths of 400 to 1100 nm (DET02AFC, Thorlabs Inc., New Jersey). The photodetector output voltage was recorded using LabVIEW software package (National Instruments Corp., Texas) and a data acquisition device (NI PCI-6225, National Instruments Corp., Texas).

The sensor and tissue phantom were assembled and secured between the fixtures of a universal testing machine (Electroforce 3200, Bose Inc., Massachusetts). The assemblies were subjected to cyclic compression testing conditions as described in simulation I and simulation II, while the force and displacement data were recorded. The schematic experimental system is represented in Figure 3.9.

3.5 Results and Discussion

To evaluate the performance of the proposed sensor in estimating the stiffness of the tissue, first a harmonic finite element analysis (FEA) was performed on the model of the sensor and phantom

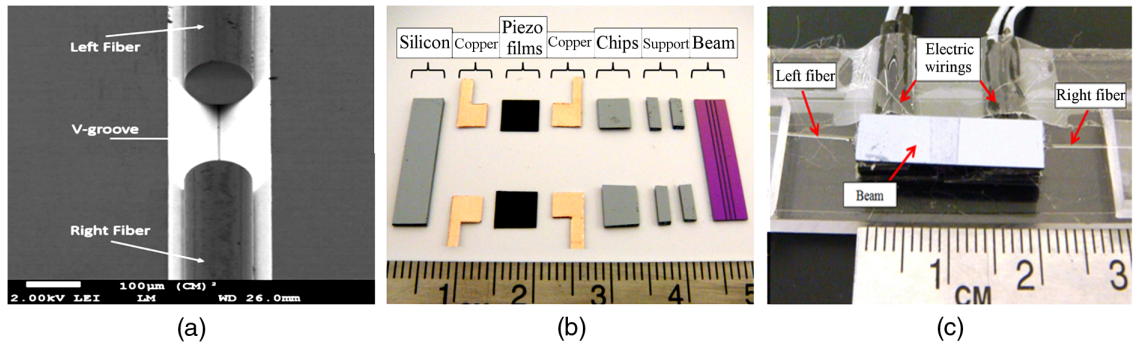


Figure 3.8: (a) SEM images of the V-groove on the lower surface of the sensor beam, (b) different structural components of the sensor, and (c) final assembled sensor.

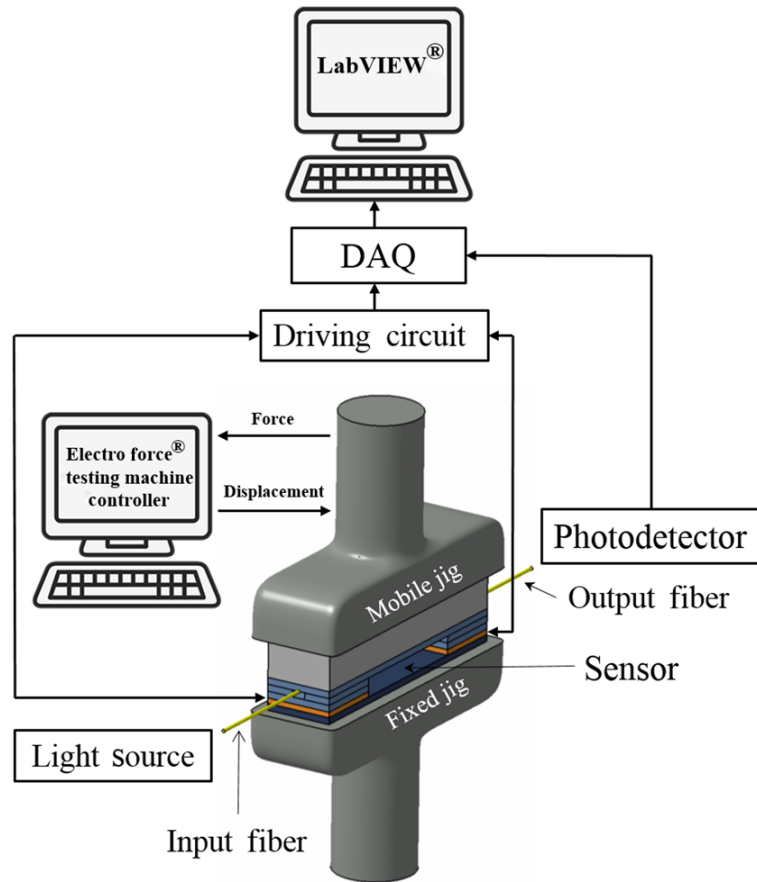


Figure 3.9: Schematic experimental setup for cyclic compression. The lower jig of the testing machine was fixed and equipped with a force sensor, while the upper jig was mobile and equipped with a displacement sensor.

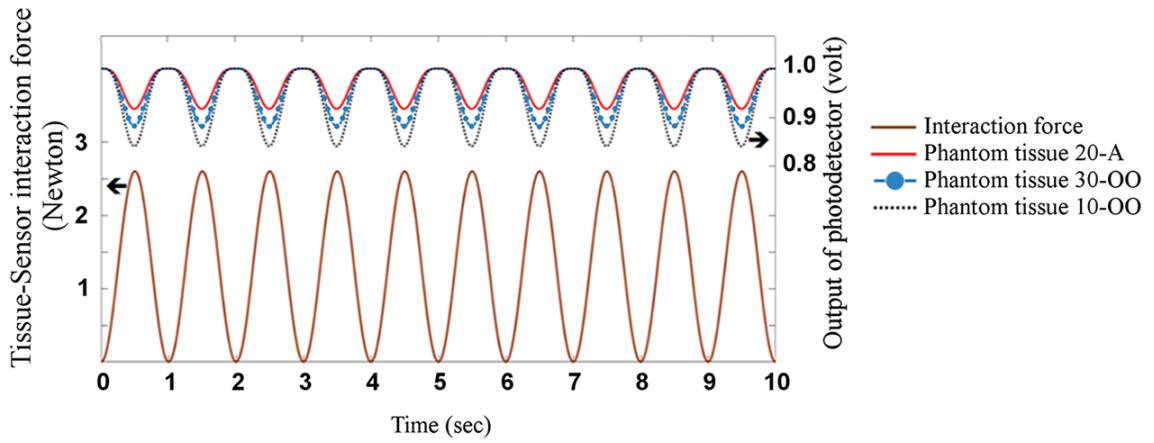
tissue (simulation I). By obtaining the angular misalignment of two optical fibers from FEA, the change in output voltage of the photodetector was estimated following the algorithm described in Section 3.2.2. To verify the simulations, a series of experiments were performed under the same conditions as those used during the simulation procedures.

Figure 3.10(a) shows the estimated values of the change in output voltage of the photodetector from an FEA and the measured changes in voltage from the experiments (Figure 3.10(b)) for three different tissue phantoms. The simulation results showed that the maximum total force transferred to the piezoelectric sensing elements was 2.6 N, whereas the experimentally measured force was 2.47 N. It indicates a 5% error in the sensor output that could be related to the calibration coefficient of the piezoresistive elements. Other studies have reported reliable force measurements with the same order of error [19]. As the range of change in the output voltage of the photodetector (Figure 3.10) is normalized with respect to its initial value, the graphs start from a unit value for both simulations and experiments.

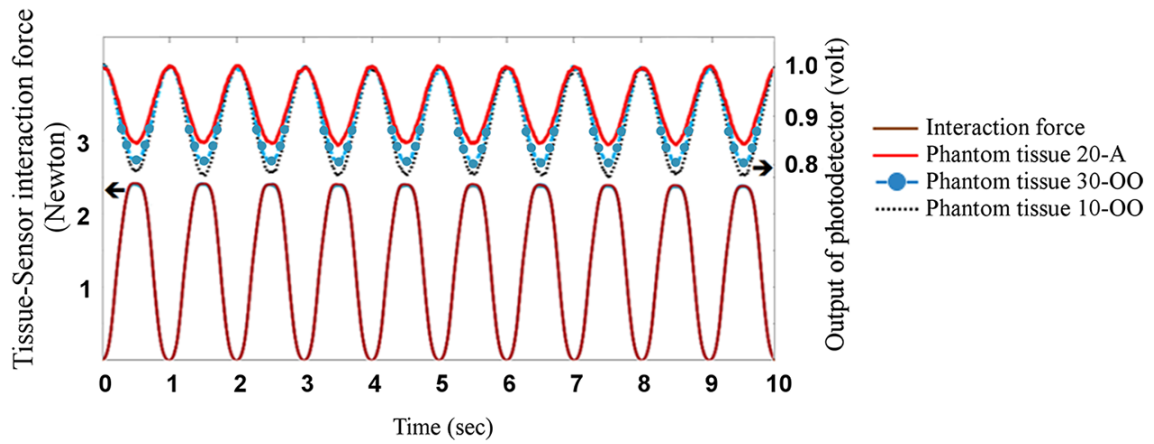
Because the output voltage of a photodetector is a linear function of the transmitted power, it is regulated by the misalignment of two optical fibers. Considering Eqs. 20 and 23, it is inferred that smaller misalignments, due to the harder material, lead to a smaller depreciation in the output voltage. The same trend was observed in simulations and confirmed by experiments. From Figure 3.10, it is evident that as the beam was being more deflected, the misalignment between the two optical fibers increased, and the transferred power decreased.

The stiffness was calculated by considering the total contact force of 2.6 N and introducing maximum deflection from Eqs. 32 to 33, for both simulations and experiments as shown in Table 3.2. Simulation results revealed that the smallest and largest decay in the output voltage corresponded to the hardest (tissue 3) and softest (tissue 1) phantoms, respectively. Despite a slight underestimation in the simulations, similar results for both decay in output voltage and tissue stiffness were obtained experimentally. The reason for the error could be attributed to the initial alignment of the optical fibers, erroneous physical constants, and residual errors of modeling in the material model and geometric model.

To test the capability of the sensor in finding the location of a hidden mass in the tissue phantom, the ratio of the forces in the left piezoresistive film with respect to the right piezoresistive film was



(a)



(b)

Figure 3.10: Estimated force between the tissue phantoms and the sensor (left axis) and the output voltage of photodetector (right axis) resulted from the: (a) simulation I, (b) experiments.

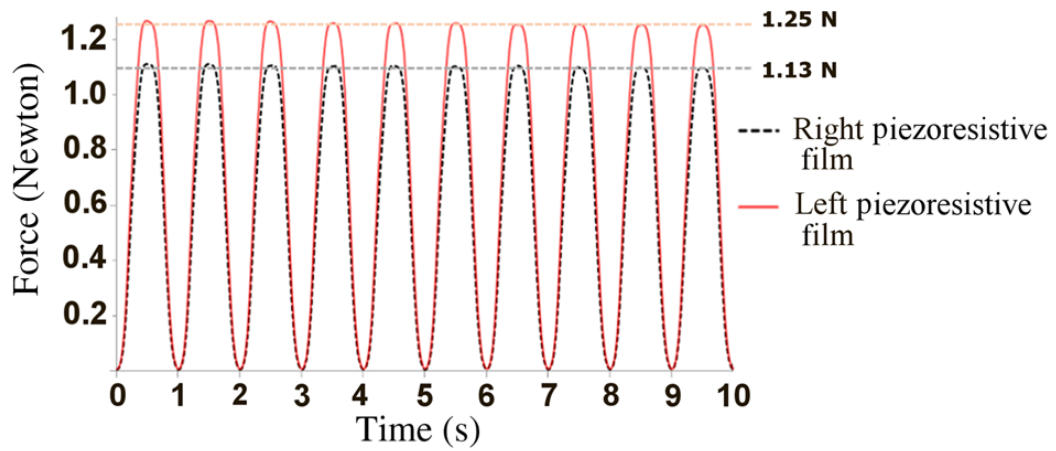
Table 3.2: Normalized maximum changes in the output voltage of photodetector and stiffness from simulation and measured in the experiment.

| Tissue Phantom (Shore hardness) | Stiffness K (N/mm) | | Difference (%) | Maximum Change in Output Voltage (%) | | |
|------------------------------------|--------------------|------------|----------------|---|------------|----------------|
| | Simulation | Experiment | | Simulation | Experiment | Difference (%) |
| Tissue 1 (10 OO) | 0.24 | 0.31 | +22.5 | 16.6 | 23.2 | +7.4 |
| Tissue 2 (30 OO) | 0.73 | 0.84 | +13.1 | 11.7 | 20 | +8.3 |
| Tissue 3 (20 A) | 1.46 | 1.66 | +12.0 | 8.1 | 14.4 | +6.3 |

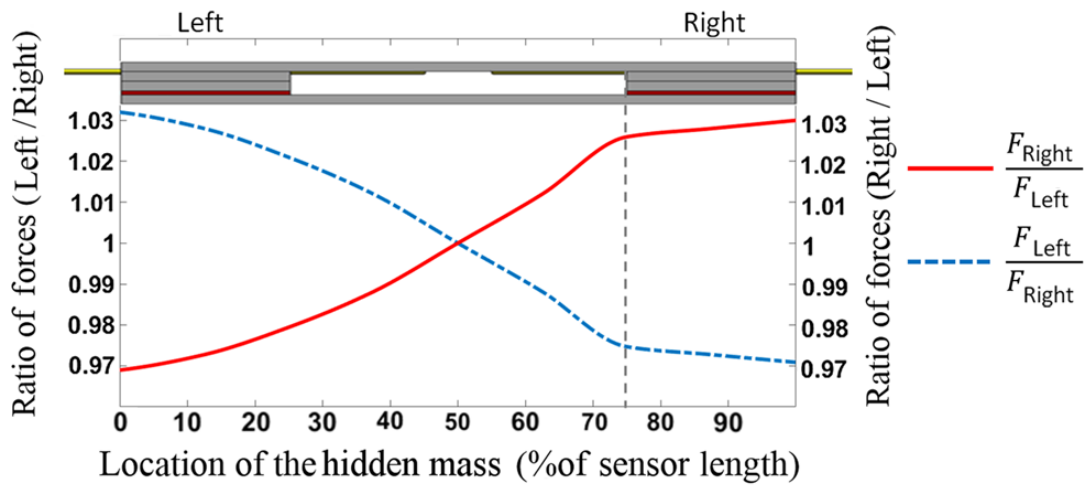
used. Figure 3.11 shows the variation of the force ratio versus the location of the mass on the longitudinal axis of the tissue phantom. In this regard, a harmonic compressive displacement was applied on the top surface of the tissue phantom, while a stainless steel ball was inside the tissue phantom simulating a hidden mass (Figure 3.7). Figure 3.11(a) shows the measured force at the left and right piezoresistive sensors, while the ball was located at $d = 5mm$ for tissue 3. The results revealed that the inclusion of the hidden mass in the tissue phantom led to unequal forces in the right and left piezoelectric films. This finding was in accordance with the simulation results, and the reason is due to the effect of hidden mass in shifting the center of pressure toward its location.

Figure 3.11(b) shows that as the location of the hidden mass changes toward either of the piezoresistive films, and the ratio of the forces deviates from unity. In other words, higher ratio in left to right force indicated that the mass was closer to the left film. The slope of this graph (sensitivity of the sensor to the position of hidden mass) decreases at about 75% of the length from left. The reason might be that when the mass is on the right side, due to the presence of the supports at the right side of the sensor, less change in the transmitted force to the sensor is observed. Due to the symmetry, the same phenomenon is observed for the ratio of force in the left sensor to the right (blue dashed line). This phenomenon can be calibrated by a bilinear or a nonlinear calibration rule. The same trend for the deflection in the beam in the presence of a hidden mass is reported by Ahmadi *et al.* [149].

According to Figure 3.11(b), as the location of the hidden mass moved from left to right, the ratio of forces deviated in a range of $\pm 3\%$ (1.03 and 0.97). The change in this ratio from the unit is proposed as that which is used as an indicator to locate the position of a hidden mass. The results represented in Figure 3.11(a) implied that the ratio of forces (left to right) was ~ 1.1 for $d = 5mm$. On the other hand, the simulations predicted the ratio of forces for the same case to be slightly < 1.03 (7% of error). This could prove one of the hypotheses of this study to use the ratio of forces as an indicator of the location of a hidden mass. As studied by Sokhanvar *et al.* [160], the factors that could affect the transmitted force from a specific tissue phantom to a contacting sensor are the lump size, magnitude of applied load/displacement, the stiffness of the lump, and the depth of the lump in the tissue.



(a)



(b)

Figure 3.11: (a) Variation of the force in left and right piezoresistive film with hidden mass located at $d = 5mm$, (b) variation of the ratio of forces as a function of the location of the hidden mass.

3.6 Conclusion

In this study, a hybrid optical fiber-based tactile sensor was proposed, and its capability of measuring the stiffness of the tissue was tested. In addition, the capacity of the proposed sensor in finding the location of a hidden mass was studied. In this hybrid design, the simplicity in integration, accuracy, repeatability in measurement, and linearity of response of piezoresistive sensors were used along with the biocompatibility and sensitivity of the optical fibers. In spite of the negligible discrepancy between simulated and experimental results, the response of the sensor that was subjected to dynamic loading condition was in fair agreement with the simulations and could support the main hypothesis of the hybrid design. In addition, the sensor showed high repeatability and negligible hysteresis under dynamic loading condition.

Utilization of a sensor with the capability of *in-situ* characterization of tissue is of high clinical value in robotic and MIS, where the tactile information to the surgeon is missing. Moreover, this sensor showed its capability in measuring the stiffness of an unknown tissue, which could be a uterus, vessel, nerve, lymphatic duct, etc. To investigate the clinical relevance of this sensor, one of the possible future directions could be to investigate its reliability and specificity for tissue classification. In addition, the performance of this sensor for measuring the stiffness and detecting hidden masses in heterogeneous phantom tissues is yet to be studied. In contrast to the piezoelectric sensors, the piezoresistive technology has no intrinsic limitation in measuring dynamic forces. This enables it to be utilized either in beating tissues (e.g., myocardial, vascular) or in static or quasistatic tissues (e.g., intestine, liver, prostate, kidney). Also, intrinsic scalability of the components, without compromising the sensing principles, makes the miniaturization feasible. Furthermore, the simplicity of its design (compared with array sensors) and straightforward working principle in finding the location of a hidden mass in a phantom tissue, together with its potential use in a broad field of other applications, increases its suitability for being mass produced.

However, in spite of the acceptable performance, the proposed sensor was neither MRI-compatible nor electrically-passive which limited its suitability for MIS applications such as cardiac surgery and neurosurgery. Therefore, optical-based sensors were selected in the continuation of this study for better compatibility with the usability and safety requirements pertinent to MIS applications.

Chapter 4

Optomechanical Modeling and Validation of a Distributed Bragg Reflector Force Sensor with Drift and Temperature Compensation

Distributed Bragg reflector fiber laser with the dual-polarization mode is commonly used as a sensing element in optical sensors. Lateral force on such a fiber induces birefringence and results in beating frequency generation in it. Also, the change in the magnitude of the lateral force is correlated to the shift in the beating frequency. This paper presents a multi-physics optomechanical model for a fiber laser force sensor based on the birefringence phenomenon. To this end, a theoretical model for the sensing principle was developed through employing the elastic beam theory, Hertzian contact mechanics, and optical birefringence principle. Based on the linearity of the developed optomechanical model to the lateral force and ambient temperature variation, a multi-linear regression calibration for the force sensor was proposed and experimentally validated. Also, the temperature-induced drift in the beating frequency was compensated through exponential adjustment. Moreover, the calibration results showed a relatively small sensitivity for temperature sensing with respect to

the external force (cross-talk). This phenomenon was predicted with the theoretical model. Verification of the calibration revealed a root-mean-square error of 0.12 °C and 0.04 N for temperature and force sensing, respectively. Furthermore, the validation study showed a root-mean-square error of 0.04 ± 0.03 N and zero hysteresis for the developed sensor. Moreover, the theoretical sensitivity to external force was similar to the experimental results. For future applications, the compliance of the sensor specifications with the requirements of three surgical procedures was confirmed through comparison with the available literature. This chapter is a result of an industrial collaboration with Optech CCTT, Montreal. The design, development, fabrication, experimentation, and data collection were performed by Optech CCTT.

4.1 Introduction

4.1.1 Background

Force sensor development for minimally invasive surgery (MIS) and robotic minimally invasive surgery (RMIS) has gained momentum in the last decade. Due to the small incision in MIS and RMIS, surgeons can not directly touch the patient's tissue, thus, have a limited tactile perception intraoperatively. Provision of tactile information to the surgeon, e.g., tool-tissue interaction forces is crucial for safe and precise manipulation of the surgical instruments [13, 163–165]. Studies have shown that tissue might be damaged by excessive handling force or slip through the instruments with inadequate grasping force [166].

The instrument–tissue interaction during MIS is associated with four main forces, i.e., rotational torque, manipulating force, grasping force, and palpation force [51]. Among the interaction forces, grasping force is the most difficult to measure, mainly because it occurs at the interaction surface of the tool and tissue and has a small amplitude, i.e., 0–2 N [21, 26].

Various sensors and sensing principles have been proposed for the intraoperative measurement of the grasping force [20, 21, 29], tissue deflection [122], and stiffness [29, 30, 84]. The most common sensing principles explored in the literature are piezoresistive [65, 67, 70], piezoelectric [64, 68, 71], capacitive [66, 69, 72], and optical principles [21, 25, 121, 122]. A comprehensive review of tactile sensing principles, their applications in MIS, and taxonomy of sensors can be found

in [27]. Also, the author has shown that the optical-fiber-based sensing is the most compatible principle with the physical and functional requirements of MIS procedures [27]. The main advantages of optical fiber-based sensors are the intrinsic biocompatibility, electromagnetic compatibility (EMC), electrical passivity, high resolution, and scalability. More specifically, optical force sensors work based on intensity, wavelength, phase, and polarity modulation phenomena [28, 32]. Among the optical fiber sensing principles, wavelength modulation-based sensors, e.g., fiber Bragg grating (FBG) sensors, exhibit higher measurement sensitivity in small force scale, i.e., 0–2 N, which is favorable in the case of grasping force of MIS.

Specifically, researchers have proposed FBG force sensors, since the longitudinal strain along an FBG is directly proportional to the axial force acting on it [167, 168]. FBG sensors are of small form-factor and can be miniaturized to fit at the tip of MIS tools. Furthermore, they are biocompatible, physically robust, disinfected, and inert to electromagnetic interference. Researchers have also accommodated multiple FBGs on a single fiber to measure multiple physical stimuli through simultaneous optical multiplexing, e.g., force, pressure, strain, and temperature, [169, 170]. FBG-based sensors are also capable of measuring temperature through the incurred thermal strain [171, 172]; thus, they have been proposed for MIS thermal therapy applications [22].

In this regard, Yu *et al.* [173] proposed a superstructure FBG–FPI (Fabry-Perot interferometry) sensor with an FBG component for temperature sensing and an FPI sensor for force measurement. However, the light intensity fluctuation and cumbersome manufacturing process were the major limitations of their proposed hybrid sensor. Yokohama *et al.* [22] proposed an FBG force sensor, later commercialized for cardiac ablation procedure, to provide surgeons with the information of the interaction force between the heart wall and catheter. The range of measurement in their study was 0–0.5 N, and their sensor exhibited a mean error of less than 1%. Müller *et al.* [112] designed an FBG-based force and torque sensor with six degrees-of-freedom for RMIS. Their sensor was capable of measuring three Cartesian components of force in the range of 0–10 N. Moreover, the resolution of their sensor was 100 ± 4 mN. Li *et al.* [121] presented a novel high sensitive FBG sensor to distinguish tissue abnormalities and localization in the MIS palpation procedure. Their proposed sensor could measure both static and dynamic forces. Their results showed sensor capability to detect the palpation force in the range of 0–5 N with a maximum relative error of 8.22%.

In order to compensate the thermal effects, James *et al.* [174] proposed to splice two FBGs with different cladding diameters and center Bragg wavelengths for simultaneous temperature and force measurement. The two FBGs were placed in the same thermal environment and showed the same response to the temperature variation, while longitudinal strain caused two sets of the wavelength-shift data. Although this method requires only a single broadband source and is immune to the light source fluctuation, fusion-splicing is a difficult fabrication process and results in splice loss and reduces the fiber strength.

The light source connected to FBG sensors must have a narrow bandwidth and be robust and stable. However, narrow-band laser sources are usually expensive and not suitable for embedded design. To alleviate this limitation, researchers have proposed to use integrated fiber lasers as active FBG sensors [175]. The active laser sources exhibit negligible temporal drift from their nominal wavelength, are robust in intensity, have a narrow bandwidth, and their laser output is composed of two orthogonal polarization modes [176]. Researchers have utilized coupled FBGs with active lasers for embedded temperature and force sensing applications [177–181]. Such sensors mainly work based on measuring the shift in the lasing wavelength for measuring temperature and the beating frequency of birefringence for measuring external force [175]. To couple an FBG with an active laser source, studies have proposed the Distributed Bragg Reflector (DBR) fiber laser sensors for embedded sensing (Figure 4.1(a)) [182]. With such a configuration measuring the DBR lasing wavelength and polarization beating frequency has been used for simultaneous measurement of temperature and external force, respectively, e.g., [173, 183, 184].

4.1.2 Rationale and Contributions

The main contribution of this study is proposing a contact mechanics-based analytical model for a simple-design and manufacturable DBR fiber laser force sensor. Furthermore, the proposed parameterized model facilitates the scalability of the sensing principle and is utile in future structural optimization studies. The proposed analytical model provides a theoretical framework to be used in custom-designing the proposed sensor for various conventional MIS and robotic applications where force and temperature measurement are necessary, e.g., [14, 163, 185]. For example, the range of grasping force in MIS general surgery is typically within 0–2 N [27] with a temperature range of

15–40 °C while MIS cardiac ablation intervention requires force measurement within the range of 0–0.3 N and temperature within the range of 35–60 °C [13, 27, 186]. In addition, the diameter of MIS instruments shall typically be less than 10 mm, to pass through MIS trocars, while their length varies for different applications, e.g., 45 mm for grasping retractor (Model no. 470318, Intuitive Surgical, CA, USA).

To the best of the author’s knowledge, this study is the first to propose a contact mechanics analytical model for a birefringence-based force sensor with DBR fiber laser suitable for MIS and RMIS applications.

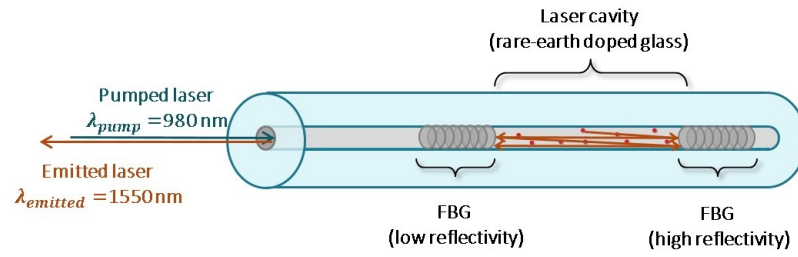
In the following, Section 4.2 presents the details of the sensing principle, structural design, analytical modeling, calibration, and experimental validation of the sensor. The results of the sensor performance and experimental validation are provided and discussed in Section 4.3. Finally, the main findings, contributions, limitations, and future directions are summarized in Section 4.4.

4.2 Materials and Methods

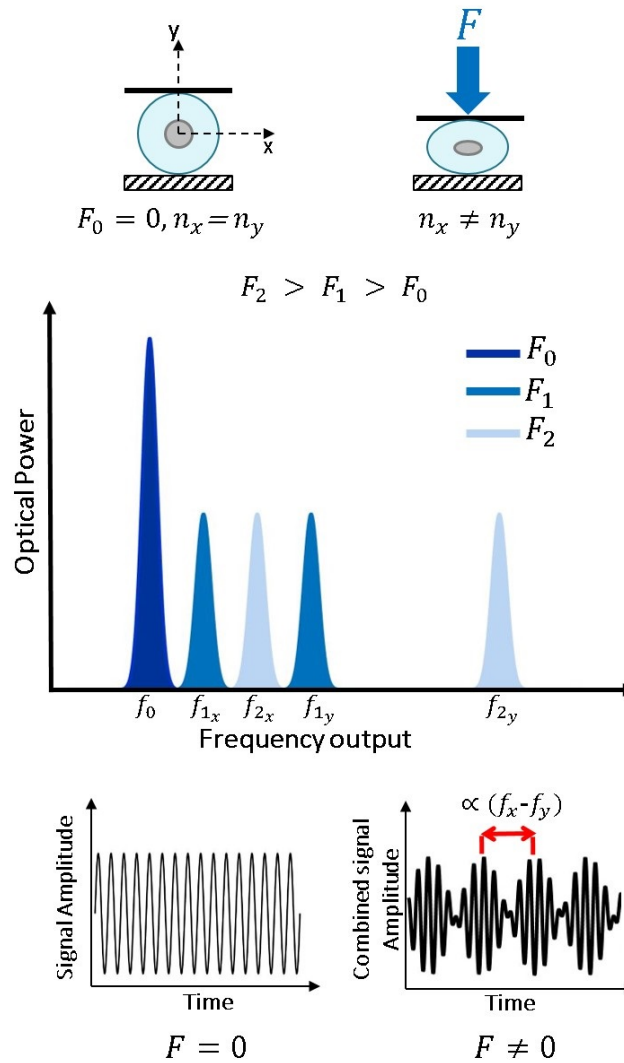
4.2.1 Sensing Principle

A DBR fiber laser is typically developed with a pair of Bragg gratings with matched wavelengths written in a rare-earth doped glass optical fiber [187]. With a low reflective FBG at the entrance and a high reflective FBG at the end, the laser cavity would act as a feedback frequency-selective mirror and would concentrate the lasing power at the output [182]. Figure 4.1(a) shows the lasing emission within the DBR fiber laser. The laser propagating in the DBR fiber laser oscillates in two polarization modes, known as x - and y - polarization, due to the fiber fabrication and grating inscription process [188, 189].

As shown in Figure 4.1(b), once a mechanical load is transversely applied on a fiber, the circular cross-section of the fiber tends to an oval shape [190]. Therefore and due to the elasto-optic effect, the refractive indices differ in the two orthogonal directions, i.e. x and y . This causes birefringence phenomena, which is identified by observing two peaks in the reflected spectrum of the laser [191, 192]. The frequency of the propagated DBR laser in the laser cavity, i.e., f_x and f_y , in x - and y -polarizations, is related to the directional refractive indices, n_x , and n_y , through the



(a)



(b)

Figure 4.1: (a) Narrow-band laser emission in a schematic DBR fiber laser, (b) birefringence phenomenon in a transversely loaded DBR fiber laser resulting in beating of the lasing frequency.

frequency–speed of light equation [193]:

$$f_x = N \frac{c}{2n_x L_c}, \quad (35)$$

$$f_y = M \frac{c}{2n_y L_c}, \quad (36)$$

where, L_c is the effective length of the fiber laser in contact with the load, and M and N are mode numbers, and c is the speed of light in vacuum. The beating frequency of DBR laser, i.e. Δf_b , is defined by Eq. 37 [194] and was measured in realtime with a high-speed interrogator and a spectrum analyzer.

$$\Delta f_b = f_x - f_y = \frac{cB}{n_0 \lambda_0}, \quad (37)$$

where, n_0 is the average refractive index seen by the two modes, λ_0 is the mean of lasing wavelengths and B is the birefringence when external lateral contact force $F_{contact}$ is applied to the length of the fiber L_c . Furthermore, B is linearly dependent on external force $F_{contact}$ and is defined by Eq. 38 [194]:

$$B = n_x - n_y = -\frac{n_0^3(p_{11} - p_{12})(1 + \nu_{fiber})F_{contact}}{L_c \pi r_{fiber} E_{fiber}}, \quad (38)$$

where, p_{11} and p_{12} are the components of the strain-optical tensor of the optical material, ν_{fiber} is Poisson's ratio, E_{fiber} is Young's modulus, and r_{fiber} is the radius of the fiber.

Also, temperature of the fiber changes with environmental temperature and aging. The aging effect is negligible in short shot applications; however, takes off exponentially if the laser is on for a relatively long period of time. The aging occurs mainly due to the accumulation of the internal heat generation caused by the photon-matter interaction inside the DBR fiber laser.

Temperature variation causes a longitudinal strain in the fiber; thus, changes the cavity length L_c and, consequently, shifts the beating frequency Δf_b . Using the Taylor expansion and partially derivating Eq. 37, the linearized effect of the temperature on the shift of beating frequency with respect to the temperature variation and longitudinal strain (caused by the external force F and through Poisson's effect) is obtained by Eq. 39 and Eq. 40, respectively [182].

$$\frac{\Delta f_b}{f_b} = \left(\frac{1}{B} \frac{dB}{dT} - (\alpha + \xi) \right) \Delta T, \quad (39)$$

where $\alpha=0.5 \times 10^{-6} \text{ K}^{-1}$ is the thermal expansion coefficient and $\xi=8.5 \times 10^{-6} \text{ K}^{-1}$ denotes the thermo-optic coefficient of the optical fiber [182].

$$\frac{\Delta f_b}{f_b} = \left(\frac{1}{B} \frac{dB}{d\epsilon} - (1 - p_e) \right) \Delta\epsilon, \quad (40)$$

where $p_e=0.22$ is the strain-optic coefficient for longitudinal strain [182] and according to Hooke's law:

$$\Delta\epsilon = \frac{L_c}{\pi r_{fiber}^2 E_{fiber}} \Delta F. \quad (41)$$

The summation of Eq. 39 and Eq. 40 gives the superposed effects of longitudinal strain $\Delta\epsilon$ and temperature ΔT on the beating frequency Δf_b . On the other hand, the DBR lasing wavelength would be shifted by both the longitudinal strain and temperature fluctuations, according to Eq. 42 [182]:

$$\frac{\Delta\lambda}{\lambda} = (1 - p_e)\Delta\epsilon + (\alpha + \xi)\Delta T. \quad (42)$$

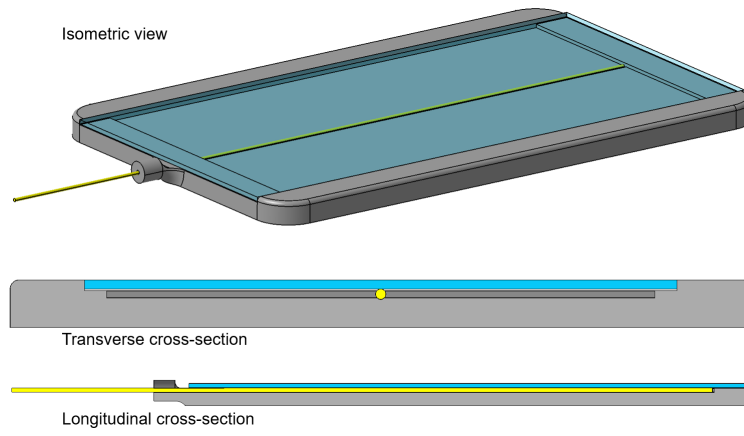
Therefore, given the linearity of Eq. 40 and Eq. 42 with respect to ΔT and ΔF , it was hypothesized that ΔT and ΔF could be determined by the realtime measurement of Δf_b and $\Delta\lambda$ and using a multi-linear model of the form:

$$\begin{pmatrix} \Delta f_b \\ \Delta\lambda \end{pmatrix} = \mathbf{C} \begin{pmatrix} \Delta F \\ \Delta T \end{pmatrix} = \begin{pmatrix} c_{11} & c_{12} \\ c_{21} & c_{22} \end{pmatrix} \begin{pmatrix} \Delta F \\ \Delta T \end{pmatrix}, \quad (43)$$

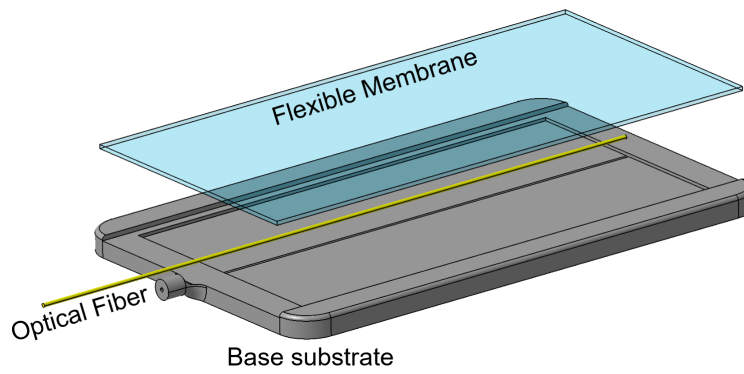
where, \mathbf{C} was a calibration coefficient matrix to be determined via experimental calibration.

4.2.2 Structural Design

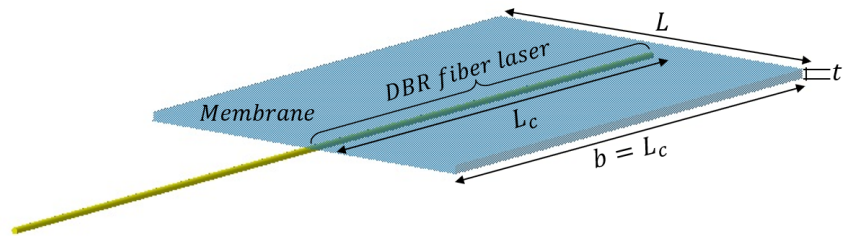
The sensor structure was designed in SolidWorks 3D V10 (Dassault Systemes S.A., France). Figure 4.2(a)–(c) illustrates the 3D design and its parametric configuration, respectively. The proposed sensor was composed of a flexible membrane fixed on a rectangular window of the detachable cap. This window and membrane were placed on top of the active part of the DBR fiber laser. The fiber was secured with glue at both ends on the substrate. In practice, a force on the membrane would be



(a)



(b)



(c)

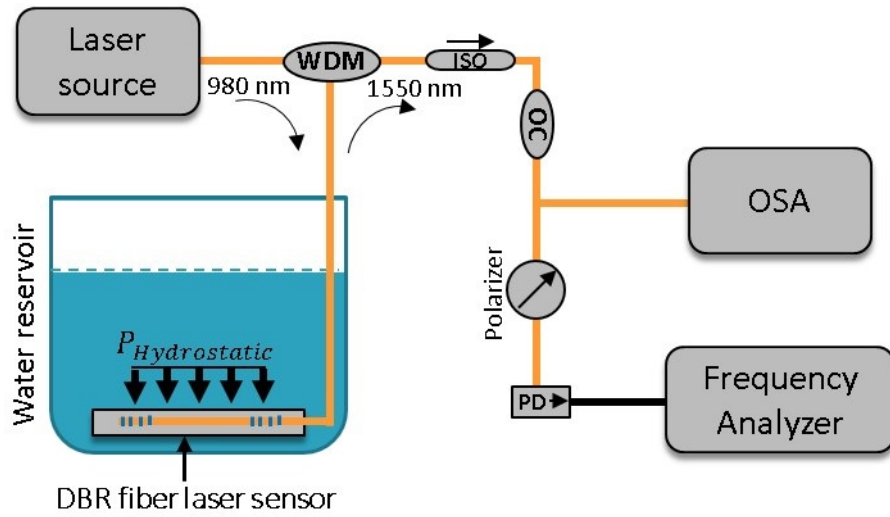
Figure 4.2: (a) Typical structure of DBR force sensors, (b) exploded view of the typical force sensor design, (c) parametric dimensions membrane and DBR fiber.

transferred to the DBR fiber laser, causing lateral strain and resulting in the birefringence. Also, the sensor would experience temperature variation in the working environment, causing a shift in the beating frequency and lasing wavelength. It was hypothesized that the temperature variation could be measured via monitoring both shift in lasing wavelength and beating frequency. Also, the lateral force could be measured via combined effects of temperature (obtained from FBG) and the shift in the beating frequency [182].

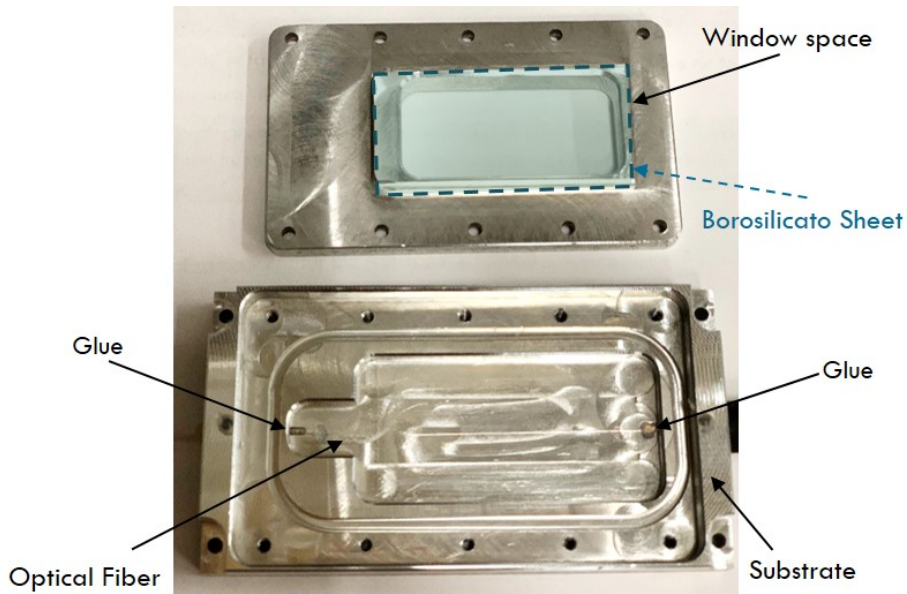
4.2.3 Optical Module and Experimental Setup

The DBR fiber laser was developed with a laser cavity made of gain fiber with FBG reflectors at two ends. Bragg gratings were inscribed using an ultraviolet (UV) laser beam with low and high reflectivity, as shown in Figure 4.1(a). During photo-inscription of the FBGs, the depth of reflectivity was monitored by observing through observing the fiber's transmission spectrum. The shape of the apodization was a standard Gaussian shape in order to eliminate side lobes of the FBG spectrum. As a design choice, it was empirically observed that a cavity length of 35 mm led to a single-mode light propagation within 1550 nm wavelength. Other studies have observed a similar single-mode propagation with other cavity lengths, e.g., 26 mm [187]. Figure 4.3(a) illustrates the schematic diagram of the experimental setup and the system components.

A laser source pumped 980-nm laser to the DBR fiber laser inside the sensor through a 980/1550 nm wavelength division multiplexer (WDM). The backward lasing emission of the DBR fiber laser was of a lasing wavelength of 1550 nm traveled back into the WDM and transferred to an isolator (ISO). The isolator prevented the laser beam from reflecting back into the sensor or the pump. Also, the output power of DBR laser was split into two using an optical coupler (OC) with 90%:10% splitting ratio. One output of the coupler (10%) was connected to an optical spectrum analyzer (OSA) (FBGA-S1525-1565-PA, Bayspec Inc., CA, USA) to monitor and measure the average lasing wavelength λ while the second output (90%) was passed through an in-line polarizer. The beating signal was detected by a biased photodetector (PD), (DET08CFC, Thorlabs Inc., NJ, USA) and its beating frequency f_b was measured using a frequency counter (53320A, Keysight Inc., CA, USA).



(a)



(b)

Figure 4.3: (a) Schematic diagram of the experimental setup and the system components, (b) fabricated sensor (courtesy of Optech CCTT).

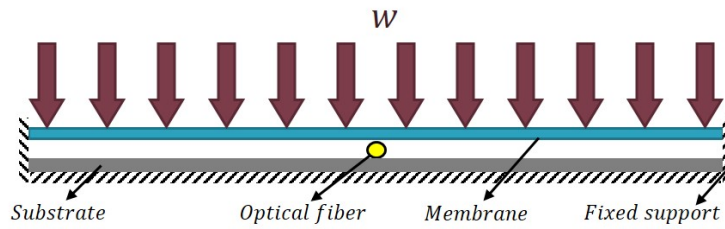
For calibration and validation tests, the sensor was submerged in a water reservoir to apply controllable hydrostatic pressure, and temperature. Meanwhile, the ground-truth (reference) temperature and pressure were simultaneously recorded using a pre-calibrated temperature sensor (1523, Fluke Corp., WA, USA) with a nominal resolution of 0.001 °C and a pre-calibrated pressure probe (FPI-HR, Fiso Technologies Inc., QC, Canada) with a nominal resolution of 0.025 psi, respectively. The hydrostatic pressure was translated to force by multiplying it with the top surface area of the membrane. Besides, the sensor structure, e.g., cap and substrate, were machined using a micro CNC machine out of Aluminum stock. Also, a sheet of Brosilicato with 200 μm thickness was used as the membrane and glued to cover the window on the upper fixture. The sealing and adhesion were achieved using a UV-adhesive. Figure 4.3(b) shows the fabricated sensor, attached membrane on the window space, and two fixed ends of the fiber.

4.2.4 Theoretical Modeling

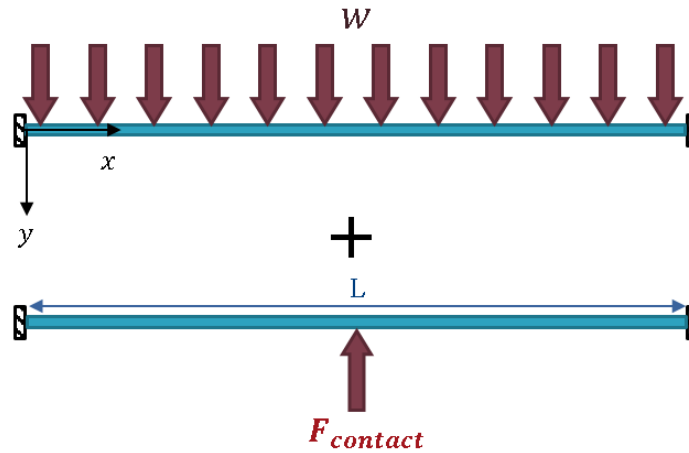
To model the interaction of the flexible membrane under an unknown external force, the mechanical model of the membrane and fiber and their interaction through their contact line was developed. To this end, initially, the membrane was modeled as a wide prismatic beam (constituting a shell). Afterward, the contact between the membrane and fiber was modeled, adopting a Hertzian contact model. In the end, the optomechanical model of the sensor was developed using the deflection, contact, and optical equations. In the following, the details of the theoretical modeling are presented.

Deflection of the Membrane

To obtain the deflection of the membrane under a given external force F , the membrane was modeled as a prismatic and wide Euler-Bernoulli beam. Figure 4.4 (a) illustrates the front view of the simplified mechanical model of the sensor and configuration of the fiber between the membrane and substrate. The boundary conditions of the membrane were assumed to be fixed-fixed at both ends. The optical fiber was assumed in initial stress-free contact with the bottom surface of the membrane at its mid-span, i.e., $x = \frac{L}{2}$. Also, the external loading was assumed as homogeneously distributed with the intensity of w per unit length on the top surface of the membrane. Furthermore, the effect of the thermal expansion of the membrane on the contact force was neglected, due to the small



(a)



(b)

Figure 4.4: (a) A simplified mechanical model of the membrane and optical fiber, (b) mechanical model of the membrane shows the superpositioning contact force and external force.

thickness of the membrane.

On the other hand, as explained in 4.2.2, the applied force results in deflection in y -direction of the membrane, which consequently applies a contact force on the optical fiber. The deflection-induced deformation of the cross-section of the optical fiber causes the birefringence due to the photo-elastic effect. The contact between the membrane and fiber was assumed to be a point of contact between two long cylinders. The radius of the top cylinder was assumed $R_1 = \infty$ to model the flat membrane, while the radius of the bottom cylinder was assumed $R_2 = 62.5 \mu\text{m}$ to model the optical fiber. Therefore, the membrane was loaded with the external load $F = wL$ on top and F_c at its mid-span from the bottom. Figure 4.4(b) depicts the full mechanical model of the membrane as the result of the superpositioning contact force and external force.

The principle of superposition denotes that:

$$Y_{total}(x) = Y_w(x) + Y_{contact}(x), \quad (44)$$

where, $Y_{total}(x)$ is the total deflection of the membrane, Y_w is the deflection due to the external distributed force, and $Y_{contact}$ is the deflection due to the contact force with the fiber. It should be noted that the contact force is always in the opposite direction to the external force. Therefore, the contact force tends to keep the membrane from deflecting at its mid-span.

From the Euler-Bernoulli beam solutions [195], $Y_w(x)$ and $Y_{contact}$ were obtained as:

$$Y_w(x) = \frac{wx^2}{24E_m I_m} (L - x)^2 \quad x \leq \frac{L}{2}, \quad (45)$$

$$Y_{contact}(x) = \frac{F_{contact}x^2}{48E_m I_m} (3L - 4x) \quad x \leq \frac{L}{2}, \quad (46)$$

where, E_m is the elastic modulus of the membrane and I_m is the second moment of area for the cross-section of beam and is calculated as $I_m = \frac{1}{12}bt^3$, where b and t are the breadth and the thickness of the membrane. Therefore, the total deformation of the membrane was formulated as:

$$Y_{total}(x) = \frac{wx^2}{24E_m I_m} (L - x)^2 - \frac{F_{contact}x^2}{48E_m I_m} (3L - 4x). \quad (47)$$

Contact force–Hertzian model

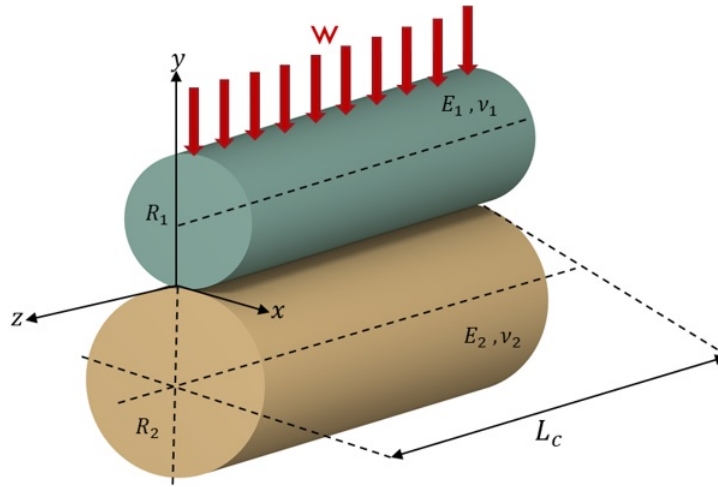
Figure 4.5 depicts two generalized cylinders in contact. According to the Hertzian contact theory, in such a contact interaction:

$$F_{contact} = \frac{\pi}{4} E^* L_c \delta, \quad (48)$$

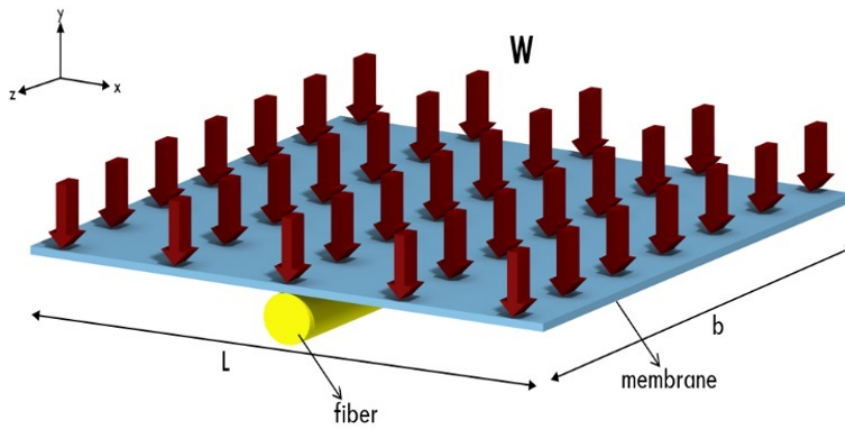
where, δ is the contact-induced indentation depth and E^* is the effective elastic modulus defined as:

$$\frac{1}{E^*} = \frac{1 - \nu_{fiber}}{E_{fiber}} + \frac{1 - \nu_m}{E_m}, \quad (49)$$

where, E_m , E_{fiber} are the elastic moduli of the top (membrane) and bottom (fiber) cylinders and ν_m and ν_{fiber} are their Poisson's ratios, respectively. Assuming $R_1 = \infty$ and $R_2 = 62.5 \mu\text{m}$,



(a)



(b)

Figure 4.5: (a) Generalized Hertzian contact configuration between two elastic cylinders, (b) schematic of the membrane and fiber in contact, dimensions are not to-the-scale.

the contact between the membrane (half-space) and optical fiber was modeled. Also, since the membrane and optical fiber are in initial contact, the total deflection of the membrane at the mid-span $Y_{total}(\frac{L}{2})$ was equal to the indentation depth of the fiber, i.e., δ .

Using Eq. 48, Eq. 47 was evaluated for $x = \frac{L}{2}$ to determine the contact force on the fiber:

$$Y_{total}(\frac{L}{2}) = Y_w(\frac{L}{2}) - Y_{contact}(\frac{L}{2}) \quad (50)$$

$$Y_{total}(\frac{L}{2}) = \frac{wL^4}{\pi E^* L_c L^3 + 768 E_m I_m}. \quad (51)$$

Since the deflection of the membrane at the mid-span, i.e., $Y_{total}(\frac{L}{2})$, is the same as the indentation depth of the fiber, i.e. δ :

$$F_{contact} = \frac{\pi}{4} E^* L_c \left(Y_{total}(\frac{L}{2}) \right), \quad (52)$$

$$F_{contact} = \frac{\pi}{8} E^* L_c \frac{wL^4}{\pi E^* L_c L^3 + 768 E_m I_m}. \quad (53)$$

As can be seen in the Eq. 53 the contact force applied on the fiber is linearly related to the force applied to the membrane. Specifications of the membrane and fiber are tabulated in Table 4.1.

Table 4.1: Specifications of the samples used in three-point bending tests (n=3) and material properties

| Parameter | E_m | E_{fiber} | ν_m | ν_{fiber} | L | $L_c = b$ | t |
|-----------|--------|-------------|---------|---------------|-------|-----------|-------------|
| Value | 44 GPa | 76 GPa | 0.3 | 0.17 | 15 mm | 35 mm | 200 μ m |

Elasticity of the Membrane

The membrane was made of Borosilicate glass. The elasticity (Young's modulus) of the membrane was obtained experimentally through applying a linear fitting on the force-displacement curve of three membrane samples. The samples were of rectangular shapes with $30 \times 20 \times 0.2$ mm size. Bose ElectroForceTM universal testing machine (UTM) was used for mechanical testing (Figure 4.6 (a)). The tests were performed in three-point bending mode under displacement-control with a rate of 1 mm.s⁻¹. Figure 4.6 (b) depicts the results of the three-point bending test. The linear fitting showed

the goodness of fit of $R^2=0.97$, which confirms the linear elastic behavior of the membrane. Elastic modulus of the membrane, E_m , was estimated through:

$$E_m = \frac{L_s^3 k}{4b_s t_s^3} \approx 44\text{GPa}, \quad (54)$$

where, $k = 1.22 \text{ N.mm}^{-1}$ was the slope of the linear part of the force-displacement curve, $L_s = 28.5 \text{ mm}$ was the length of the samples between the two rollers, $b_s = 20 \text{ mm}$ was the breadth of the samples, and $t_s = 0.2 \text{ mm}$ was the thickness of the samples.

Theoretical Beating Frequency

The theoretical beating frequency (Eq. 55) was obtained by eliminating $F_{contact}$ between Eq. 38 and Eq. 53 and substituting Eq. 38 in Eq. 37.

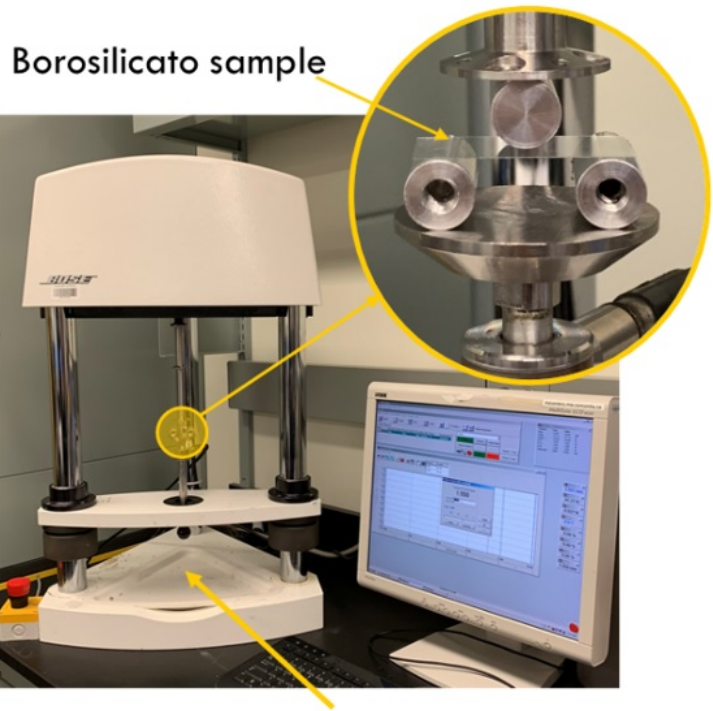
$$\Delta f_b = \frac{1}{8} \frac{cn_0^2(p_{12} - p_{11})(1 + \nu_{fiber})}{\lambda_0 L_c \pi r_{fiber} E_{fiber}} \frac{E^* L_c L^4}{E^* L_c L^3 + 768 E_m I_m} w. \quad (55)$$

By using the typical values of a silica fiber at a wavelength of $\lambda_0 = 1550 \text{ nm}$, $n_0 = 1.444$, $p_{11} = 0.12$ [196], $p_{12} = 0.27$ [196], $\nu_{fiber} = 0.17$, $E_{fiber} = 76 \text{ GPa}$, and the radius of optical fiber $r_{fiber} = 62.5 \mu\text{m}$, the relationship between the external force w and the beating frequency Δf_b was obtained. In terms of sensor characteristics, the rate of change of beating frequency with respect to the change in the external load, would determine the sensitivity of the sensor, S_w (Eq. 56).

$$f_b S_w = \frac{\partial \Delta f_b}{\partial w} = \frac{1}{8} \frac{cn_0^2(p_{12} - p_{11})(1 + \nu_{fiber})}{\lambda_0 L_c \pi r_{fiber} E_{fiber}} \times \frac{E^* L_c L^4}{E^* L_c L^3 + 768 E_m I_m}. \quad (56)$$

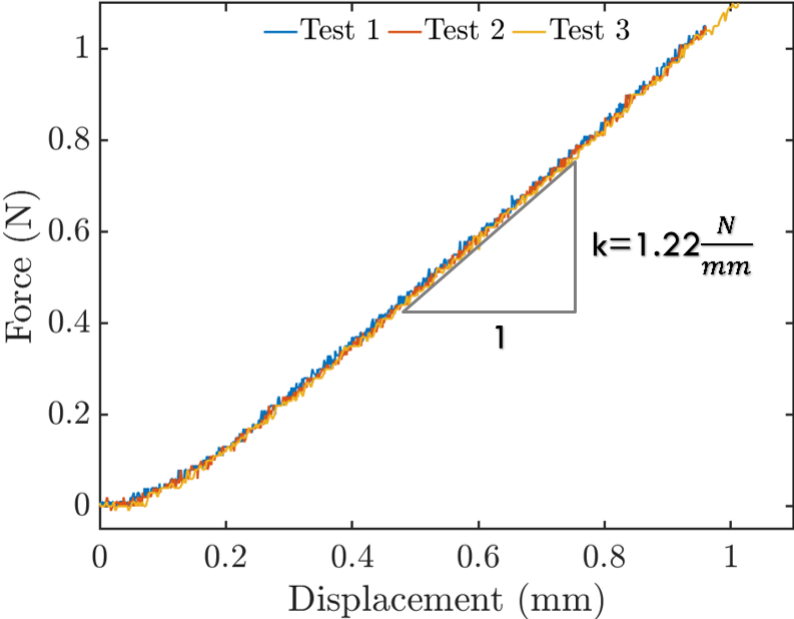
Eq. 56 shows that the sensitivity of the sensor can be tuned through selecting various combinations of laser wavelength λ_0 , size of the sensor, e.g., L_c , L , I_m , and mechanical properties of the membrane E_m . Also, increasing the temperature tends to increase the wavelength λ_0 , and unless compensated, will diminish the sensitivity.

It can be inferred that utilizing thin and soft membranes would decrease the term $E_m I_m$ and increase the sensitivity, however, it must be noted that a highly flexible or very thin membranes



Bose ElectroForce Universal testing machine

(a)



(b)

Figure 4.6: (a) Borosilicate sample under the compression test, (b) graph of force vs. displacement to calculate the module of elasticity of the Borosilicate or membrane.

would bend with large deformation, thus violate the linearity. Therefore, a trade-off must be kept between the sensitivity and flexural rigidity ($E_m I_m$) of the membrane. Table 4.1 summarizes the model parameters used in Eq. 55. Using the model parameters, the theoretical sensitivity of the sensor was determined to be $f_b S_w = 6.9 \frac{\text{MHz}}{\text{N}}$.

4.2.5 Calibration Protocol

To calibrate the sensor, two experiments were performed by Optech CCTT. In the first experiment, the reservoir was filled with hot water (34 °C) and left at the room temperature (23.4 °C) for 130 min for cooling to happen. The data acquisition was live while the water was cooling. During the cooling, the water level was constant; thus, the total force on the sensor was constant.

In the second experiment, the effect of the force on the sensor was studied. To this end, the reservoir was filled with water with room temperature, i.e., $T_{room} = 23.4$ °C. After the equilibrium achieved, the reservoir was flushed at a constant rate, resulting in a linear decrement of the total force on the sensor at room temperature. This type of loading was selected to simulate the situation where the entire sensor is in contact with soft tissue, and the contact pressure is distributed. With a given contact force, distributed contact makes the worst-case scenario as it incurs the least cross-sectional deformation along the optical fiber.

The acquired data during the calibration experiment was collected and randomly divided into training and verification datasets with a 70 : 30 percent ratio. After obtaining the calibration matrix from the training dataset, the calibration was verified by comparing the estimated ΔF and ΔT from $\Delta \lambda$ and Δf_b with their corresponding reference values in the verification dataset.

4.2.6 Sensor Validation

In order to validate the specifications of the sensor for practical applications, the accuracy, resolution, sensitivity, and drift performance of the sensor were studied. To this end, the sensor was fixed horizontally at the bottom of the water reservoir, and the reservoir was filled up to 300 mm of height. Afterward, the reservoir was drained gradually while its level was kept constant at 200 mm and 100 mm of height. Meanwhile, the outputs of the developed sensor and the reference sensors, i.e. Fiso and Fluke were recorded for further analysis. The experimentation and data collection of

this part was performed by Optech CCTT.

Accuracy

The accuracy of the sensor was quantified by calculating the root-mean-square error (RMSE) of the sensor measurements, i.e., temperature and force, with respect to the reference sensor(s):

$$RMSE_F = \sum_{i=1}^n \sqrt{\frac{(F_i^{Sensor} - F_i^{Fluke})^2}{n}}, \quad (57)$$

$$RMSE_T = \sum_{i=1}^n \sqrt{\frac{(T_i^{Sensor} - T_i^{Fluke})^2}{n}}, \quad (58)$$

where, n is the number of data points captured during the validation experiment.

Resolution

The resolution was defined as the smallest change in the temperature and force detected by the sensor. To this end, the data captured during the validation test were inspected numerically to find the smallest stepwise change in the output.

Sensitivity to Force

The sensitivity of the sensor for force was obtained by finding the rate of change in the beating frequency with respect to the external force. The experimental sensitivity was further compared with the theoretical sensitivity obtained from Eq. 56.

Aging-Drift

To capture the intrinsic drift caused by the aging of the DBR fiber laser, the system was kept turned ON while measuring the temperature with the Fluke sensor. Empirical studies have shown that aging causes a temporal exponential shift in the beating frequency with the form:

$$\delta f_b = k_1(1 - e^{-\frac{t}{\tau}}) + k_2t, \quad (59)$$

with k_1 , k_2 , and τ as the fitting parameters. The exponential part of δf_b is also known as the *burn-in* phase, and the linear portion is caused by the heat accumulation in the DBR fiber laser. The author speculate that the burn-in phase might be related to the initial thermal expansion of the cross-sectional area of the DBR fiber laser, which might happen non-homogeneously due to the presence of imperfections.

To characterize the aging phenomenon, the sensor was kept ON for 30 hours at the room temperature under no external force, while the data acquisition was performed.

4.3 Results and Discussion

4.3.1 Sensor Calibration

Effect of Temperature

Figure 4.7(a) shows the experimental data collected to detect the effects of temperature while the external force was kept constant. It can be seen that while the water was undergoing an exponential cooling, natural convective cooling, the lasing wavelength λ and the beating frequency f_b have changed exponentially with time. Qualitatively, the form of changes in the wavelength and beating frequency follow the form of changes in the temperature with positive and negative correlation, respectively.

Figure 4.7 (b) depicts the dependency of FBG wavelength and beating frequency to the temperature. The curves are fairly linear with the goodness of fits of $R_\lambda^2 = 99.99\%$ and $R_{f_b}^2 = 99.98\%$, respectively.

Effect of External Force

The second experiment was performed while the height of the water tank was steadily decreasing in the tank, while water was at the room temperature (23.4 °C). Figure 4.8(a) shows the experimental results. As can be seen, while the temperature was constant and the external force was decreasing linearly, the changes in the laser wavelength were negligible ($\frac{\Delta\lambda}{\lambda_0} = \pm 1.3 \times 10^{-6}$), however, the beating frequency followed the external force in a linear fashion. Figure 4.8(b) confirms the linear

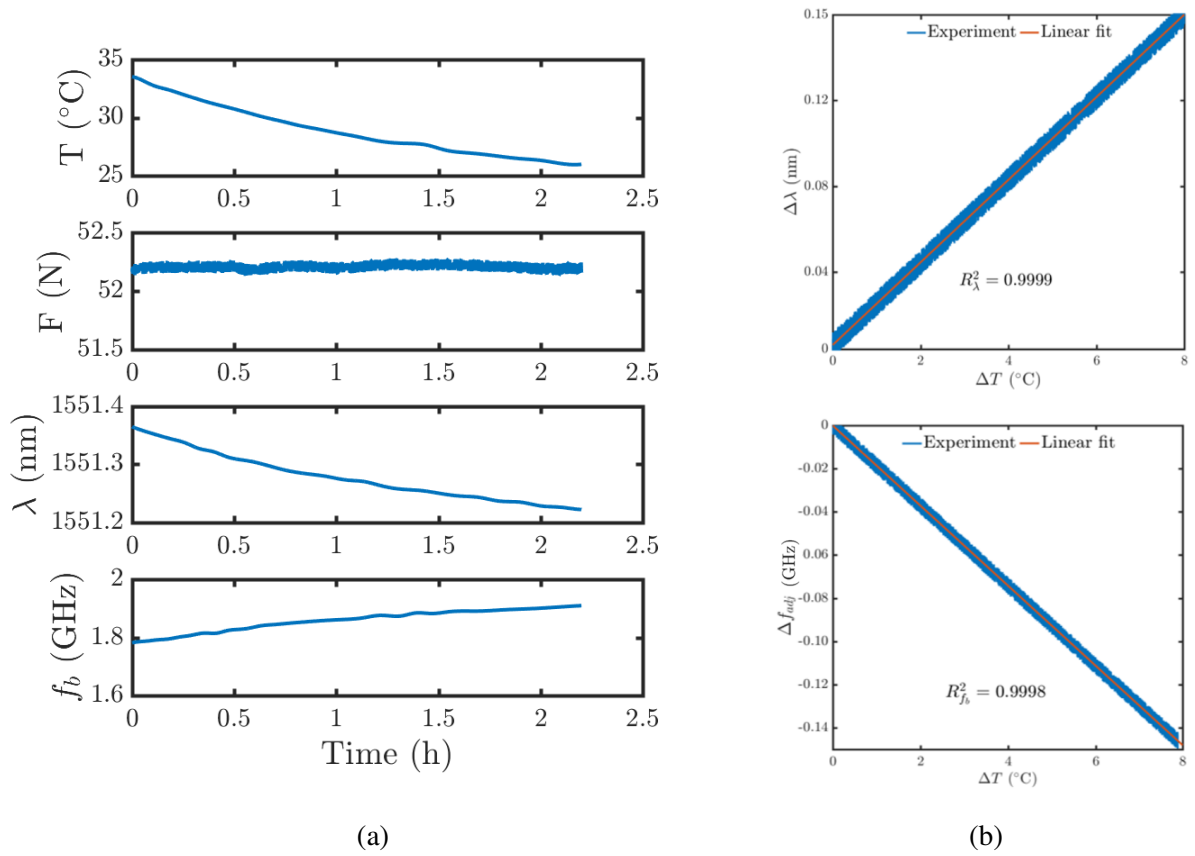


Figure 4.7: (a) Variation of the beating frequency f_b and lasing wavelength λ while the ambient temperature T changed, (b) linearity of changes in the beating frequency and lasing wavelength with temperature.

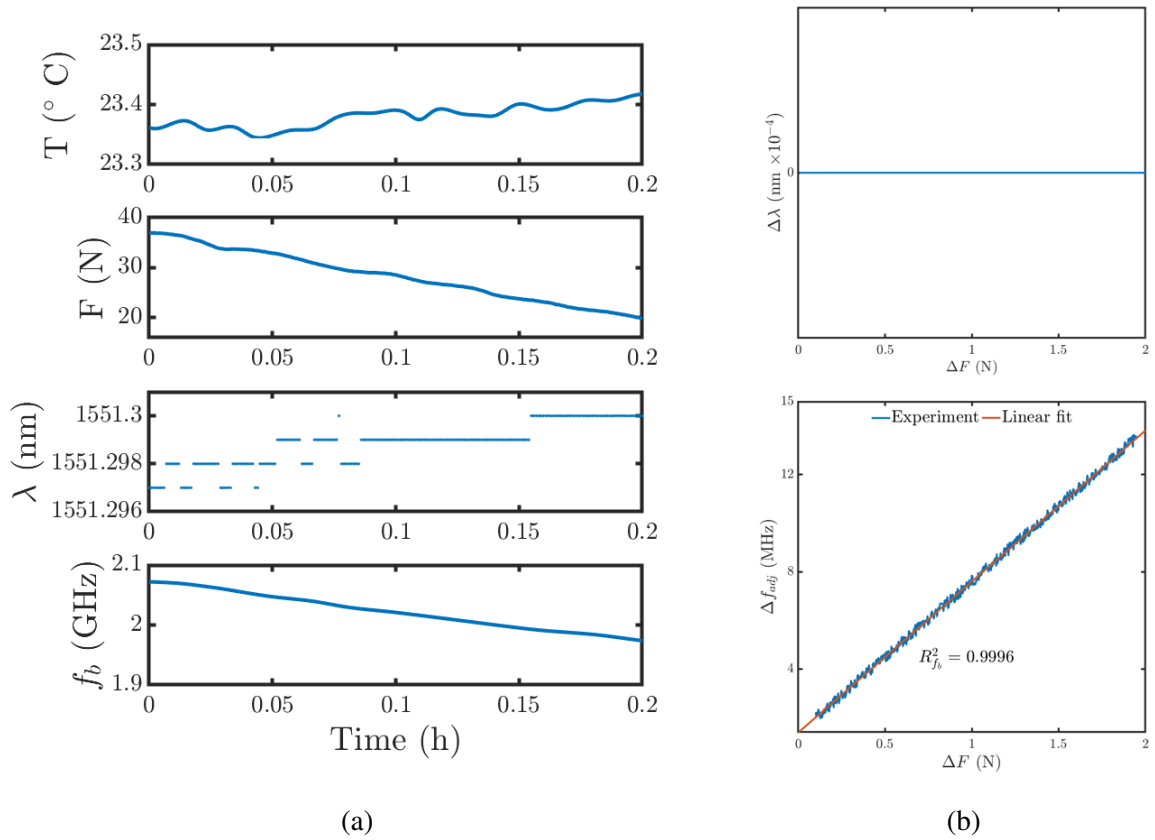


Figure 4.8: (a) Variation of the beating frequency f_b and lasing wavelength λ while the external force F changed, (b) insensitivity of the lasing wavelength and linearity of changes in the beating frequency to the external force.

relationship between the beating frequency f_b and external force with $R^2_{f_b} = 99.96\%$; however, the results showed a weak correlation between FBG wavelength and external force. More specifically, Figure 4.8(b) shows that for a change of 2 N in external force, the change in λ was zero.

Effect of Aging–drift

Figure 4.9 shows the changes in the beating frequency in the absence of external force acquired from the sensor in continuous operation over 30 hours. Using Eq. 59, the aging effect was modeled as:

$$\delta f_b = k_1(1 - e^{-\frac{t}{\tau}}) + k_2t. \quad (60)$$

Using a nonlinear least-square fitting revealed that $k_1 = 0.3605$, $k_2 = 0.006144$, and $\tau = 7.68$

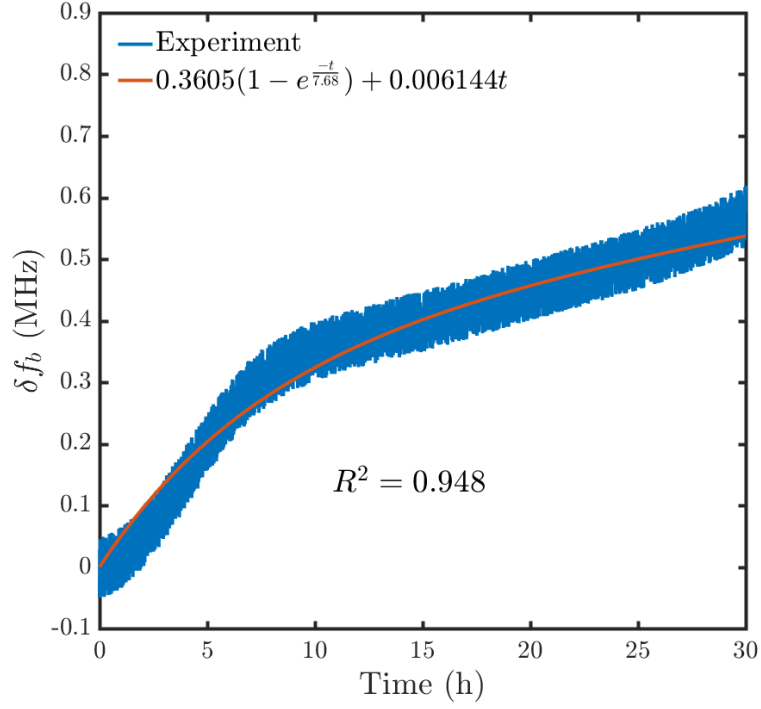


Figure 4.9: Evolution of intrinsic beating frequency over a long period of time for an Erbium-doped sample.

resulted in a goodness of fit of $R^2 = 94.8\%$ and RMSE of 0.02 MHz. The exhibited goodness of fit and RMSE showed a fairly accurate curve fitting within the measurement accuracy. Figure 4.9 compares the experimental results with the exponential model. The curve-fitting was performed in Matlab R2019b (Mathworks Inc., MA, USA). Therefore, in practice, the measured change in the beating frequency contains the effect of aging (with respect to t) and the effects of ambient temperature (with respect to ΔT). Thus, the following adjusted form of Δf_b was used in the calibration, i.e., Eq. 43.

$$\Delta f_{adj} = \Delta f_b + \delta f_b = \Delta f_b + k_1(1 - e^{-\frac{t}{\tau}}) + k_2t. \quad (61)$$

Multi-linear Regression

Multiple linear regression is commonly employed to find the relationship between two or more variables and the response variables by fitting a linear equation to the measurands [197]. Independent

variables, i.e., the lasing wavelength $\Delta\lambda$ and adjusted beating frequency Δf_{adj} previously obtained in Section 4.3.1 and Section 4.3.1 were used in a least-square multiple linear regression curve fitting and the calibration matrix \mathbf{C} was found as:

$$\mathbf{C} = \begin{pmatrix} 0.0065 & -0.0095 \\ -0.00015 & 0.0194 \end{pmatrix}. \quad (62)$$

The calibration formula (Eq. 63) for estimating external force and the temperature was obtained by multiplying both sides of Eq. 43 by \mathbf{C}^{-1} , where \mathbf{C}^{-1} was the inverse of \mathbf{C} :

$$\begin{pmatrix} \Delta F \\ \Delta T \end{pmatrix} = \mathbf{C}^{-1} \begin{pmatrix} \Delta f_{adj} \\ \Delta\lambda \end{pmatrix} = \begin{pmatrix} 155.6046 & 76.1981 \\ 1.2031 & 52.1356 \end{pmatrix} \begin{pmatrix} \Delta f_{adj} \\ \Delta\lambda \end{pmatrix}. \quad (63)$$

As can be seen in \mathbf{C} , the dependency of the temperature estimation on the Δf_{adj} is smaller than its dependency on $\Delta\lambda$. This implies that the longitudinal strain on the Bragg spacings caused by the external force is negligible compared to the strain caused by the temperature effects.

Verification

To verify the obtained calibration, T and F were reconstructed for the verification dataset using Eq. 63. Figure 4.10 depicts the fair agreement of the experimental data with the calibration output for the verification dataset. The goodness of fit for reconstructed temperature and force were $R^2 = 0.9998$ and $R^2 = 0.9965$, respectively. Also, the RMS-error between the reference values and reconstructed values were $0.12 \text{ }^\circ\text{C}$ and 0.04 N for temperature and force, respectively.

4.3.2 Validation

Figure 4.11(a) depicts the data obtained from the developed sensor and reference values for force. As can be seen in the graphs, the sensor output has a fair agreement with the reference values, i.e., from the Fiso sensor. The RMS-error of the sensor in this experiment was $0.04 \pm 0.03 \text{ N}$.

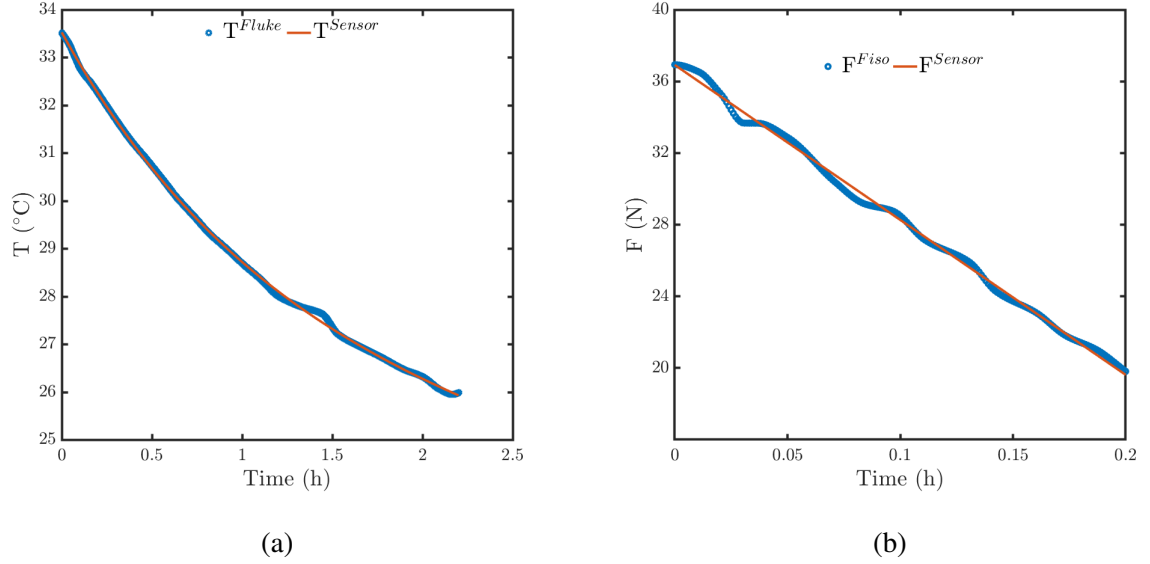
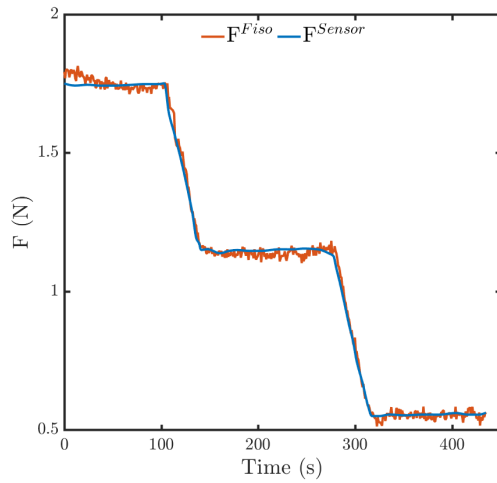


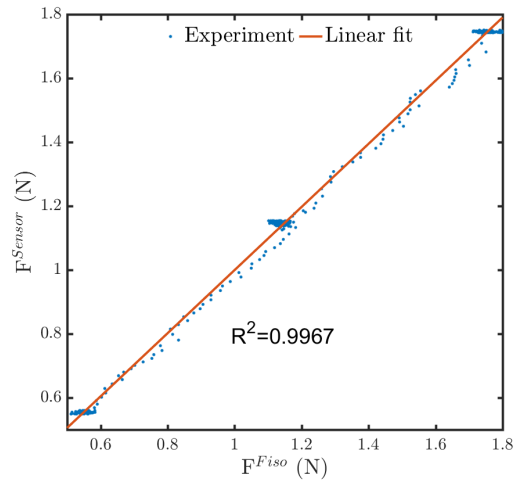
Figure 4.10: Verification of the multi-linear calibration through comparison of the experimental data with (a) the estimated temperature, (b) the estimated external force.

Also, Figure 4.11(b) confirms the linearity of the sensor output with the reference readings with $R^2 = 0.9967$. Furthermore, this figure shows no noticeable hysteresis in the sensor readings with respect to the reference value. Hysteresis in sensors is often present due to non-linear viscoelastic mechanical properties of the sensor structure or intrinsic hysteresis of the data acquisition system [27]. The absence of hysteresis in the developed sensor improves the accuracy and linearity of the sensor; thus, further contributes to its usability in dynamic environments, e.g., moving surgical instruments.

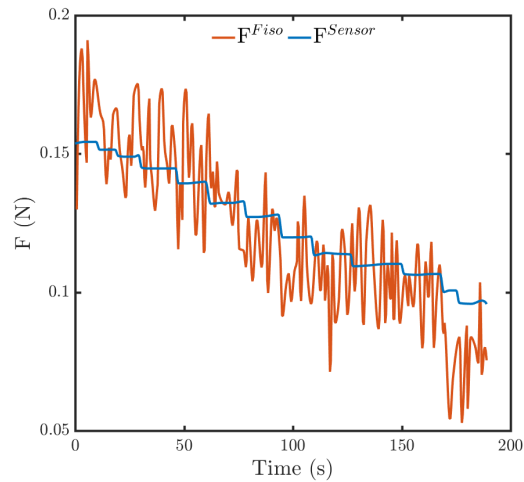
Moreover, Figure 4.11(c) shows an enlarged view of the recorded data for $0.1 \leq F \leq 0.15$ N. The numerical inspection showed that the average detectable change of force was 0.01 ± 0.006 N. It is noticeable that the developed sensor has more robust readings compared to the Fiso sensor used as the reference. Furthermore, the slope of Δf_{adj} with respect to ΔF in Figure 4.8 (b) determines the sensitivity of the sensor to force was $\Delta f_{adj} S_{\Delta F} = 6.5 \frac{MHz}{N}$. Comparing this finding with the theoretical sensitivity, i.e., $6.9 \frac{MHz}{N}$, (5.8% error) further validates the developed theoretical model.



(a)



(b)



(c)

Figure 4.11: (a) Raw pressure measurement of the calibrated sensor vs. the reference Fiso pressure prob, (b) linearity of the sensor output with the reference readings with $R^2 = 0.9967$, (c) enlarged view of the recorded data by the sensor and Fiso pressure probe.

4.3.3 Sensor Specifications

Table 4.2 summarizes the specifications of the proposed force sensor. Also, the requirements of three representative biomedical applications for force sensors are compared with the specifications of the developed sensor. The requirements were obtained from the literature, e.g., [13, 27].

Table 4.2: Specifications of the proposed sensor and comparison with the requirements of various minimally invasive surgeries [13, 27].

| Specification | Value | Requirement for application | | |
|-----------------------------|----------------|-----------------------------|---------|-----------------|
| | | MIS ¹ | Biopsy | CS ² |
| Range | 0–35 N | 0–5 N | 0–2 N | 0–2 N |
| Resolution | 0.01 ± 0.006 N | ±0.02 N | ±0.05 N | ±0.02 N |
| Accuracy (RMSE) | 0.04 ± 0.03 N | ±0.1 N | ±0.1 N | ±0.1 N |
| Hysteresis | 0% | ≤ 5% | ≤ 5% | ≤ 5% |
| Water-resistance | ✓ | ✓ | ✓ | ✓ |
| Thermal effect compensation | ✓ | ✓ | ✓ | ✓ |

¹ MIS: Minimally invasive surgery
² CS: Cardiac Surgery

Table 4.3: Comparison of the specifications of the proposed sensor with representative studies.

| Study | Application | Principle | Range (N) | Error (N or %) | Resolution (mN) |
|------------|-------------|-----------------|-----------|----------------|-----------------|
| [102] | Biopsy | FPI | 0–10 | 3.8% | 300 |
| [121] | MIS | FBG | 0–1 | 8.22% | 93 |
| [21] | MIS | LIM | 0–2 | 6% | 2 |
| This study | MIS | DBR fiber laser | 0-35 | 0.04N | 10 |

As the comparison shows, the proposed sensor fairly complies with the requirements of the representative applications. It is noteworthy that the output of the proposed sensor was more stable

than the readings from Fiso sensor. Therefore, the reported error includes the variations of the reference values. Nevertheless, the calculated RMS error is in compliance with the requirements of the representative MIS applications. In addition, Table 4.3 compares the specifications of the proposed sensor with representative optical sensors from the literature. As the comparison shows, the sensor specifications is comparable to the representative studies with significant superiority in the measurement range and accuracy (error).

4.4 Conclusion

In this study, a multi-physics optomechanical model was developed to relate the external force to the beating frequency in a DBR fiber laser force sensor. Utilization of the proposed analytical model and parameterized structure facilitates the optimization of the sensor structure in future studies.

The analytical model showed the linearity of the sensing principle with respect to the external force. As the theoretical model shows, the proposed sensing principle is intrinsically scalable. This property allows further miniaturization of the sensor while maintaining sensor sensitivity for desired applications, e.g., MIS and RMIS. Also, building upon the previous knowledge in the literature, showing the linearity of DBR wavelength to the temperature a multi-linear calibration form was adopted. In addition to that, to the best of author's knowledge, this was the first study to incorporate the temporal aging–drift in the calibration of DBR fiber laser sensor so that a one-time calibration could be sufficient for long time usage of the sensor in practice.

Furthermore, the verification of the calibration showed the fair linearity of the sensor and accuracy of the proposed multi-linear calibration model with drift compensation for the proposed sensor. Besides that, the validation study showed fair agreement between the analytical model, sensor estimations and reference sensors.

Another prominent finding of this study was that the readings of the developed sensor were more robust for temperature and force compared to the industrial reference sensors, i.e., Fluke and Fiso sensors. For future studies, researchers are encouraged to use a more accurate and robust pressure sensor as the variations of the reference values might affect the calculated error of the sensor.

Utilization of the optical sensing principles enables researchers to fabricate biocompatible sensors for medical applications. As representative applications, the specifications of the developed sensor were compared against the requirements stated for three biomedical applications in the literature, i.e. MIS, biopsy, and CS surgery. The comparison showed fair compatibility of the proposed sensor with the representative applications. However, the size of the developed sensor was not miniaturized, as this study was to provide a proof-of-concept.

For future studies, the proposed analytical model could be used for structural optimization of DBR fiber-laser-based sensors aiming for miniaturization. Another enhancement of this study could be to use a more compliant material, e.g., rubbers family, for the structure of the sensor. A more compliant sensor could be of use in sensor-integrated applications such as robotics and tactile sensing, e.g., [21]. That, however, would require a nonlinear calibration regulation, e.g., [21].

Although FBG-based sensors are very sensitive with high accuracy, the optical module fabrication and corresponding data acquisition systems are cumbersome and expensive. Thus, given that the proposed sensor would eventually be a single-patient disposable medical device, the integrated sensing system would be costly. In addition, this study showed that, even with a temporal drift compensation, the proposed sensor is more sensitive to the changes in the ambient temperature than the external force. Thus, in practice such sensitivity to temperature may be a source of inaccuracy. On the other hand, studies have shown that sensors based on the light intensity modulation require a rather simple data-acquisition system, are cost-effective, and are thermally stable. Therefore, in the next study an optical sensor with intensity modulation sensing principle was designed and validated for MIS applications. Intensity modulation-based sensors are typically less temperature dependent than FBG-based sensors.

Chapter 5

Miniaturized Optical Force Sensor for Minimally Invasive Surgery With Learning-Based Nonlinear Calibration

A simple and miniaturized optical tactile sensor for integrating with robotic and manual minimally invasive surgery graspers is proposed in this study. For better miniaturization, the sensing principle of constant-bending-radius light intensity modulation was replaced with a variable-bending-radius modulation principle, and the pertinent theoretical formulation was derived. Afterward, a finite element model of the sensor was optimized using response surface optimization technique. The optimized sensor design was 14.0 mm long, 1.8 mm wide and 4 mm high. Next, the sensor was prototyped using SLA 3D printing technique. Also, the sensor was calibrated using a rate-dependent learning-based support-vector-regression algorithm. Calibration was 96% linear with a goodness-of-fit of 93% and mean absolute error of 0.085 ± 0.096 N. Furthermore, the sensor was tested under cyclic triangular compression with a 3 sec pause between loading and unloading as well as manual grasping. Mean absolute error of 0.12 ± 0.08 N, the minimum force of 0.14 N, and repeatability of 0.07 N showed the acceptable performance of the proposed sensor for surgical applications. Moreover, the sensor showed the capability of working under combined dynamic and static loading conditions with low hysteresis, i.e., 0.057 N/cycle.

5.1 Introduction

5.1.1 Background

Minimally invasive surgery (MIS) has been one of the most evolutionary aspects of modern surgery. In this approach, the surgeon uses long and thin MIS devices which can fit through a 5–15 mm diameter insertion port. Compared to the conventional surgeries, MIS has proven advantages in terms of reducing blood loss and trauma, postoperative infection, recovery time, and patient's length-of-stay in hospital [198]. Figure 5.1 depicts a schematic MIS surgery, during which a surgeon accesses the patient's internal organs via small skin incisions.

Despite the advantages, clinical surveys have reported the compromised hand-eye coordination, loss of tactile information and, indirect access to the internal organs as the most critical limitations of MIS [5]. Therefore and to improve the accuracy, dexterity, and instrument control, robotic systems have been equipped with MIS devices to liaison between surgeon and patient [198].

In other words, MIS has facilitated the use of robots in surgery; while, the clinical needs in robotic surgery has further advanced the miniaturization and sensing capability of MIS devices [33, 34, 199]. Robot-assisted minimally invasive surgery (RMIS) has been successful in providing better intraoperative vision, reducing the surgeon's fatigue, and performing more precise surgeries. However, studies have reported the loss of a direct sense of touch and natural haptic feedback as the prime limitation of the state-of-the-art [3, 6, 8, 13, 200].

Loss of tactile feedback has been reported to result in excessive or insufficient grasping force. The excessive force would further cause a tissue laceration or trauma, while insufficient force would lead to the slippage of tissue and lengthening the procedure [166, 201]. For example, da Vinci robot (Intuitive Surgical Inc., CA, USA) as the most extensively used RMIS system [9], does not provide force or haptic feedback. Studies have shown that the tool–tissue interaction forces are significantly reduced by the provision of force feedback in RMIS procedures [13, 202–204].

5.1.2 Literature Review

Tool–tissue interaction force, stiffness of the tissue, location of the hidden lump, and grasping force of the surgical instrument are examples of human tactile cues during a surgery [9, 33, 199].

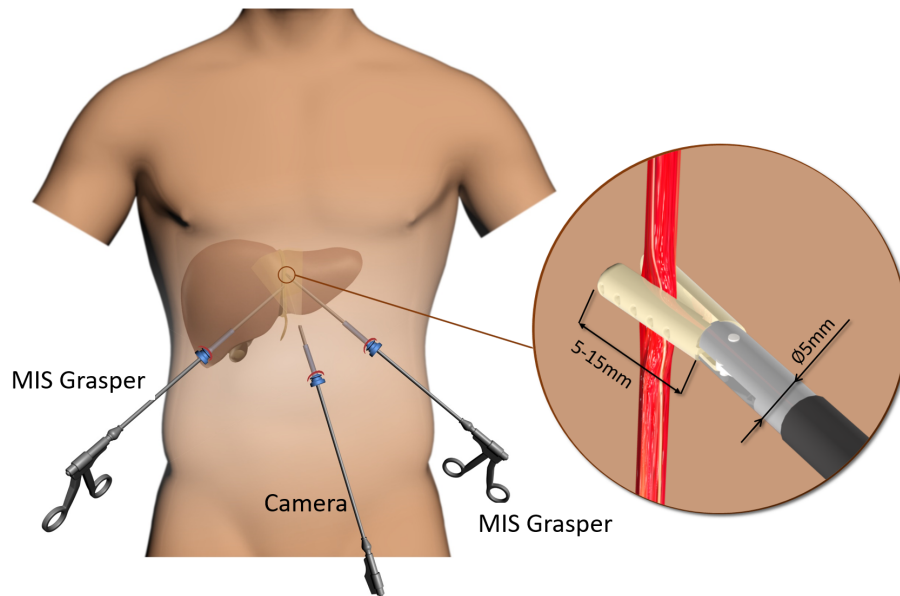


Figure 5.1: Schematic MIS surgery: surgeon operates on internal organs with using long and thin MIS instruments, while a camera is used and maneuvered to have a complete vision inside the body.

To answer the need for tactile feedback in MIS and RMIS, researchers have adopted sensorless and sensor-based approaches. Sensorless approaches mainly rely on mathematical modeling of tool–tissue interaction. The model is solved inversely in real-time to find the tool–tissue forces [13] and render the force feedback for the surgeon [164]. Such models rely on simplifying assumptions of material and contact models. Thus, they are more erroneous compared to the sensor-based methods. Also, the inverse solution of a model is usually computationally expensive, thus compromises the refresh-rate and fidelity of the feedback [13, 132]. Nevertheless, the sensorless approach is best adopted in surgical simulators and pre-operational planning, while the sensor-based approach is more used for intraoperative applications.

The developed sensors are required to be integrated with the MIS instruments or robotic end-effectors; thus, complying physical and functional requirements. Physical requirements attribute mainly to the shape, size, and material of a sensor, while the functional constraints relate to its compatibility and interaction with the bio-environment [22, 199]. Tactile sensors must be miniaturized sufficiently to fit in the limited space on the tip or body of MIS instruments. Nevertheless, the intended use of the sensor also affects the structural design and sensing principle of a sensor. For example, for the integration with a grasper, forceps, cutter, or a needle driver, the sensor must have a

thin and planar profile[205], while for integrating with a cardiac catheter, it must have a cylindrical shape [13, 30].

Also, biologic tissues demonstrate viscoelastic properties [143]; thus, the tool–tissue interaction force has both constant (holding) and changing (relaxation) components. Therefore, a tactile sensor intended for an MIS grasper must be capable of measuring both dynamic and static forces [13, 84].

Researchers have investigated various sensing principles for tactile sensors, e.g., piezoelectric, piezoresistive, capacitive, and optical [13, 16]. Sokhanvar *et al.* [44] proposed a smart endoscopic grasper equipped with an array of piezoelectric elements. Their grasper was capable of localizing and measuring the size of a hidden lump inside a tissue phantom. However, due to its piezoelectricity, their sensing element was only sensitive to dynamic forces. In continuation, Atieh *et al.* [206] postulated a piezoresistive tactile sensor. This sensor was capable of measuring static and dynamic contact force. Moreover, it was capable of identifying the relative hardness of different soft tissues. However, their sensor was bulky. Researchers have also proposed 4-DOF [66, 207] and 5-DOF [51] capacitive force/torque sensing system with micro-assembling multiple sensors. In these studies, prototypes were fabricated in a sequence of wire-cutting, micro-machining and, micro-assembly. Such manufacturing methods have complicated both the structure of sensors and the manufacturing process.

Nevertheless, capacitive sensors are likely to absorb thermal [208] and motion noises [209]. Researchers have indicated high precision, linearity, low hysteresis, direct force measurement, and scalability as the main characteristics of electrical sensors [14, 29, 38, 139–141, 210, 211]. However, these sensors are not magnetic resonance (MR)-compatible and electrically passive. Therefore, these sensors can not be used in the MR environment and minimally invasive cardiac and neurosurgery. Studies have shown that magnetism and bio-electricity impair the accuracy and reliability of electrical sensors [13, 212]. Nevertheless, piezoelectric sensors are not capable of under static force condition, intrinsically [44].

Alternatively, optical fiber sensors are biocompatible, MR-, and electrically passive [13]. Also, optical fiber-based sensors are scalable and have been developed in both micro and macro scales

[29, 112]. Optical fiber sensors mainly work based on three basic sensing principles of light intensity, wavelength, and phase modulation [78]. Fiber-brag-grating (FBG) and Fabry-Perrot interferometry (FPI)-based sensors are the most common techniques in wavelength and phase modulation principled, respectively.

In an early study, Fernandez *et al.* [213] developed an FBG sensor for a robot end-effector. Similarly, Yurkewich *et al.* [214] developed a force sensor for arthroscopic graspers. Their proposed solution was low-cost and incorporated 2-DOF tip force and 1-DOF grasping force sensing elements. Recently, Xue *et al.* [215] presented an innovative tension sensor based on FBG for estimating the grasping force of laparoscopic robot end-effectors. Similarly, Zarrin *et al.* [95] developed two sensorized needle-driver graspers for the MIS application. The FBG-based sensor in their study demonstrated an accuracy of 0.27 N in grasping and 0.3 N in axial measurements, respectively. Recently, Carotenuto *et al.* [216] used an FBG-based sensor on the epidural needle for intraoperative needle guidance. Their study demonstrated improved clinical outcomes compared to the conventional method.

In parallel, Liu *et al.* [115], developed a highly sensitive FPI-based miniaturized sensor for vitreoretinal microsurgery. Their proposed sensor met their design requirements, however its sensing principle was not scalable. Recently, Ulgen *et al.* [217], embedded an FPI sensor on a biopsy needle and demonstrated measurement resolution down to 0.1 N, for forces as high as 13 N. Despite the high accuracy and sensitivity, FBG and FPI-based sensors are not cheap and easy to use in medical applications [13, 78, 218]. Using such sensors mandates the utilization of an optical spectrum analyzer (OSA), sophisticated software to obtain the phase shift, and rigorous mathematical models to estimate the magnitude of a force. In addition to that, such sensors are temperature sensitive and lose accuracy in a varying-temperature environment like the human body. Also, since the infection control protocols and safety guidelines limit the life-cycle of a catheter to a single-patient use, FBG, and FPI sensors are relatively expensive to be used as single-patient-use in MIS applications [16].

Alternatively, the light intensity modulation (LIM) sensing principle provides unique advantages of being inexpensive, thermally-insensitive, simple design, and easy to implementable. Thanks to these features, LIM sensors are deemed suitable for developing single- and multi-DOF sensors for MIS applications[218]. In this regard, Ahmadi *et al.* proposed various MIS force and stiffness

sensors for MIS graspers based on the coupling and bending power loss [19, 84, 85, 118, 149].

In continuation, Bandari *et al.* [29] postulated a hybrid piezoresistive-optical sensor for force and stiffness measurement in MIS. In addition, their sensor was capable of localizing a hidden mass inside a tissue phantom. However, their sensor was bulky and not small enough to be integrable with an MIS grasper [84].

Literature review revealed that the bending LIM-based sensors have been mainly developed based on the constant bending radius (CBR) assumption. CBR condition was ensured in previous designs by using three or more relatively large cylinders for bending the fiber. The use of such cylinders was the main hurdle against the miniaturization of these sensors [19]. Eliminating the cylinders would lead to a slimmer sensor design; however, would also cause the sensor to demonstrate a non-linear behavior due to the variable bending radius (VBR) condition in the optical fiber [20]. To formulate the resulting nonlinearity, author have recently verified the proposed VBR-based sensing principle and have shown its feasibility through a series of experimental studies [20, 28, 219].

Kim *et al.* [51] have summarized the possible modes of loading on a robotic grasper as 1-DoF grasping force, 3-DoF manipulating force, 1-DoF rotational torque, and 1-DoF palpation force. The proposed sensor in this study was intended to measure the 1-DoF grasping force, which is applied perpendicular to the surface of the grasper jaws. In general, manipulating, rotational, and palpation forces are larger are directly transmitted to the hands of the surgeon through the body of the instrument. However, due to the lever mechanism design of MIS instruments, the grasping forces are scaled-down at the handles in the hands of the surgeon. Therefore, the indication of the proposed sensor was to measure and relay the level of the “grasping” force to the surgeon’s attention.

The present study was performed to propose, prototype, and investigate the performance of a miniaturized VBR LIM-based force sensor integrated with a mock surgical grasper. The structure of the sensor was miniaturized while optimizing its sensitivity. Afterward, the miniaturized sensor was prototyped using SLA 3D-printing technique. Next, the optical sensor was calibrated and verified using a machine learning algorithm, i.e., support-vector-regression (SVR). Furthermore, the sensor was integrated with a mock of to-the-scale MIS grasper and validated with a pre-calibrated 6-DOF sensor.

In the following, the sensor design and formulation of the sensing principle are explained in details, and the theoretical formulation is derived in Sec. 5.2. Details of the structural optimization and fabrication of the sensor are presented in Sec. 5.3 and Sec. 5.4, respectively. Also, methods used for calibration and verification are provided in Sec. 5.5, while Sec. 5.6 summarizes the methods and results of the sensor validation and performance analysis. Finally, Sec. 5.7 closes this article with concluding remarks.

5.2 Sensor Design and Modeling

In this section, the structural design of the sensor and grasper, and formulation of the sensing principle are provided.

5.2.1 Structural Design

Figure 5.2(a) illustrates the structural design of a mock surgical grasper with the proposed force sensor integrated with it. The sensor consisted of a flexible shell fixed at both ends on a substrate, i.e., the lower grasping arm of the grasper. The shell had a small semicircular indenter at the midspan of its bottom surface with a radius 0.5 mm. A single mode optical fiber was passed through the two substrates and under the indenter and was fixed (glued) to the substrate at both ends.

One end of the optical fiber was connected to a light source with a constant power. The other end of the fiber was coupled to a photodetector to capture the transmitted power. Utilization of a two-lever mechanism for transferring force from the handles of grasper to its grasping jaws has been a popular design concept for MIS graspers. Applying force on the shell would deflect it, and the indenter would bend the fiber and decrease its transmission efficiency [80]. Therefore it is hypothesized that by calibrating the power loss versus the force, a force-power relationship could be identified.

5.2.2 Sensing Principle

Researchers have investigated the bending power-loss in an optical fiber using the analytical framework postulated in [80]. It was assumed that the fiber undergoes a constant bending radius (CBR)

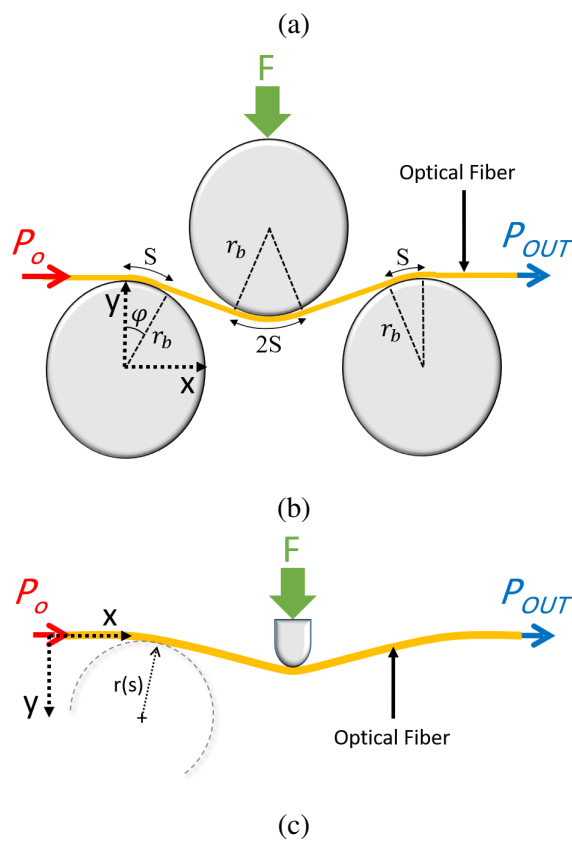
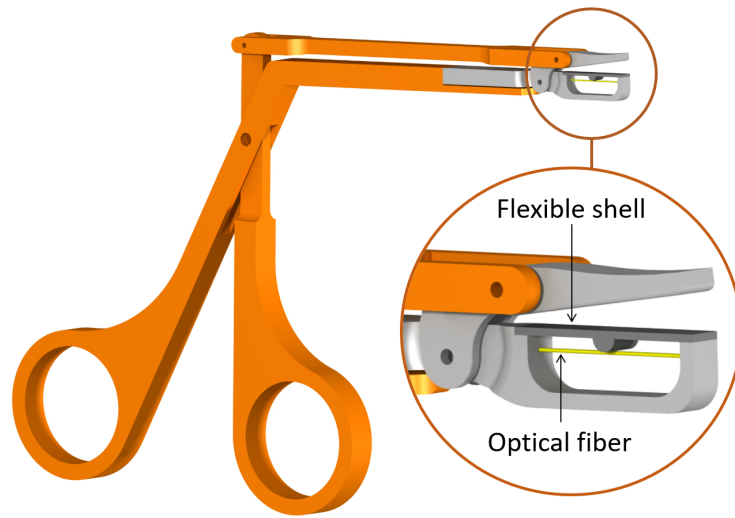


Figure 5.2: (a) 3D design of the sensor-embedded MIS grasper and mechanical model of an optical fiber as a beam in, (b) CBR, (c) VBR configurations.

deformation. Thus in practice, the optical fiber was passed through one mobile and two fixed cylinders, a.k.a. rollers, as indicated in Figure 5.2(b). As force F was applied on the mobile cylinder, the fiber would bend, and the output power P_{OUT} would decay. In order to maintain the CBR configuration, radii of indenter were required to be large enough. Therefore, the CBR requirement has limited the scale of miniaturization.

To alleviate this limitation, the VBR principle allowed for further miniaturization of the sensor. Figure 5.2(c) depicts the VBR condition. As depicted in Figure 5.2(b) during the bending, the input light power P_o was assumed transmitting through the optical fiber and decaying to P_{OUT} due to the bend. Eqs. 64–66 describe the transmitted power in the optical fiber under CBR configuration [80].

$$P_{OUT} = P_o e^{-\gamma S}, \quad (64)$$

$$S = r_b \varphi, \quad (65)$$

$$\gamma = c_o r(S)^{-\frac{1}{2}} e^{-c_1 r(S)}, \quad (66)$$

where, φ is the central angle of curvature, S is a quarter length of the total bent sections of the fiber, P_{OUT} is the output power at the end of the fiber, γ is the bending loss coefficient, and c_o and c_1 are optical fiber intrinsic properties. By its definition in [80], γ at an arbitrary point s along the fiber is a function of the bending radius $r(s)$ at that point. In the CBR condition $r(s)$ maintains a constant value equal to the radius of indenting cylinders.

By eliminating the cylinders, an optical fiber would behave as a Euler-Bernoulli beam with two fixed ends boundary condition. Therefore, $r(s)$ would no longer remain constant and would be a function of the distribution of internal shear force $V(s)$.

Assuming the fiber as a Euler-Bernoulli beam, Eq. 67 suggest that a unique center-span force F results in a unique distribution of internal bending moment $M(s)$ along the fiber. Furthermore, Eq. 68 states a hyperbolic relationship between the local radius of curvature, $r(s)$ and internal bending moment $M(s)$. Therefore, a unique power-loss value was expected from a unique external force, F .

$$M(s) = \int_0^s V(l)dl = F \left(\frac{L}{8} - \frac{s}{2} + \left\langle s - \frac{L}{2} \right\rangle \right), \quad (67)$$

where, $\langle \cdot \rangle$ denotes Macaulay's bracket. On the other hand, according to the beam theory for a slender beam:

$$r(s) = \frac{EI}{M(s)} = \frac{8F^{-1}EI}{L - 4s + \langle 8s - 4L \rangle}, \quad (68)$$

where EI is the flexural rigidity of fiber.

To derive the formulation of the power-loss for VBR conditions, S was substituted with the length parameter s in Eq. 64. Afterward, it was differentiated with respect to s and $d\gamma$ (Eq. 66) was substituted. Eq. 70 describes the infinitesimally small change in the power in a differential element of the fiber.

$$d\gamma = \left(-\frac{1}{2}c_0r(s)^{-\frac{3}{2}}e^{-c_1r(s)} - c_0c_1r(s)^{-\frac{1}{2}}e^{-c_1r(s)} \right) \frac{dr(s)}{ds} ds \quad (69)$$

$$dP_{\text{OUT}}(s) = -\gamma P_0 e^{-\gamma s} ds - s P_0 e^{-\gamma s} \times \left(-\frac{1}{2}c_0r(s)^{-\frac{3}{2}}e^{-c_1r(s)} - c_0c_1r(s)^{-\frac{1}{2}}e^{-c_1r(s)} \right) \frac{dr(s)}{ds} ds \quad (70)$$

As stated earlier, γ is a function of $r(s)$, therefore using the chain-rule, $dP(s)$ is a univariate function of s . By integrating the right-hand-side (RHS) of Eq. 70 over the length of the fiber, the power-loss was obtained as:

$$\Delta P_{\text{OUT}} = \int_0^L dP_{\text{OUT}} = P|_{s=L} - P_0 = P_0 D|_{s=L}, \quad (71)$$

where, $D(L)$ is the decay coefficient determining the output power received at the end of optical fiber.

$$D|_{s=L} = \int_0^L -\gamma e^{-\gamma s} ds - s e^{-\gamma s} \times \left(-\frac{1}{2}c_0r(s)^{-\frac{3}{2}}e^{-c_1r(s)} - c_0c_1r(s)^{-\frac{1}{2}}e^{-c_1r(s)} \right) \frac{dr(s)}{ds} ds. \quad (72)$$

Since \int_0^L is a definite integral, $D|_{s=L}$ would be a scalar depending on F , EI , and L . Since EI and L are constants in this sensor, $D(L)$ would only change by the changes in F . Moreover, the linearity of the photodetector with respect to its received light power was modeled as:

$$V_{\text{OUT}}(t) = kP_{\text{OUT}}(t), \quad (73)$$

thus,

$$V_{\text{OUT}}(0) = kP_{\text{OUT}}(0) = kP_{\circ}, \quad (74)$$

and,

$$\Delta V_{\text{OUT}}(t) = k\Delta P_{\text{OUT}}(t). \quad (75)$$

Since Eq. 73 is not zero at $t = 0$, Eq. 75 was divided by Eq. 74 to obtain:

$$\frac{\Delta V_{\text{OUT}}(t)}{V_{\circ}} = \frac{\Delta P_{\text{OUT}}(t)}{P_{\circ}} = D|_{s=L} \equiv g(F), \quad (76)$$

where, t is an arbitrary time instance, V_{\circ} is the initial voltage output of the photodetector before the deformation, and g is the expression relating F and $D|_{s=L}$. The left-hand-side of Eq. 76 is the relative change in voltage of photodetector (or percentage of change), while the right-hand-side is $g(F)$. Therefore, it was deduced that the relative change of V_{OUT} was independent of P_{\circ} and a unique relative change would be related to a unique external force F . As a result and with the discussion above, the relative change in voltage would be used as the optimization goal function and for calibration.

5.3 Structural Optimization

Structural optimization of the sensor was performed to minimize the dimensions of the sensor while maximizing its relative change of voltage at the end of the fiber. To this end, a parametric finite element model of the sensor was created and optimized to maximize $D|_{s=L}$ subjected to a set of feasibility and mechanical strength constraints. Details of the optimization procedures are described in this section.

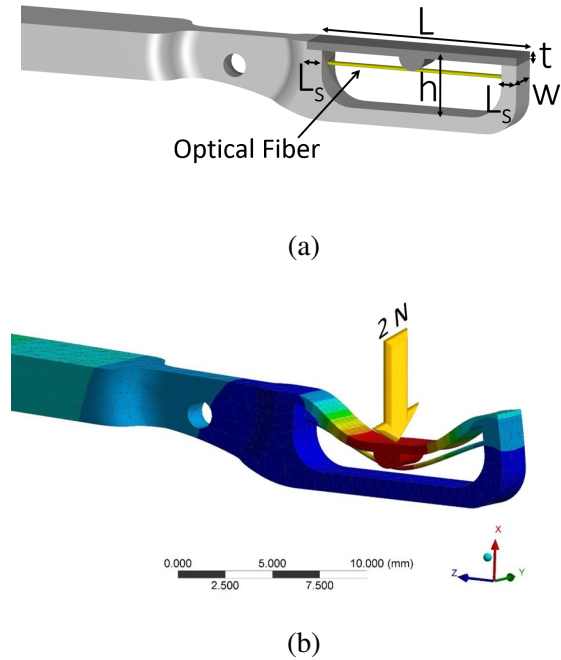


Figure 5.3: (a) Parametric geometry of the optical sensor, (b) deformation of the shell and optical fiber under a 2.0N force obtained from the finite element analysis.

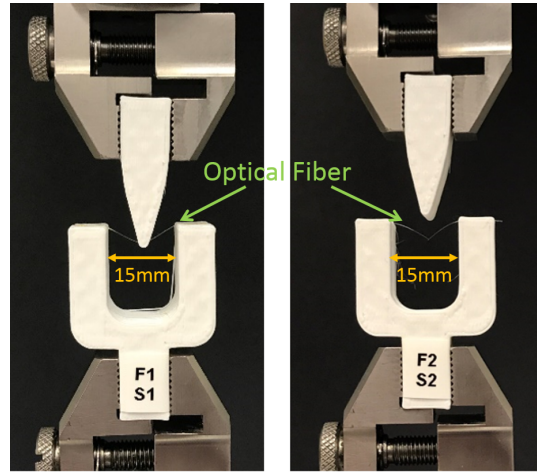
5.3.1 Optimization Parameters

Figure 5.3(a) depicts the parametric 3D design of the proposed sensor. The total length of shell L , length of its attachment to each side of the lower substrate, L_s , the thickness of the shell t , and width of the sensor (and grasper) w were selected as the optimization parameters determining the shape and size of the sensor. Height of the sensor, h was not considered in this optimization and was determined to clear the maximum feasible deflection of optical fiber and was set as 4 mm.

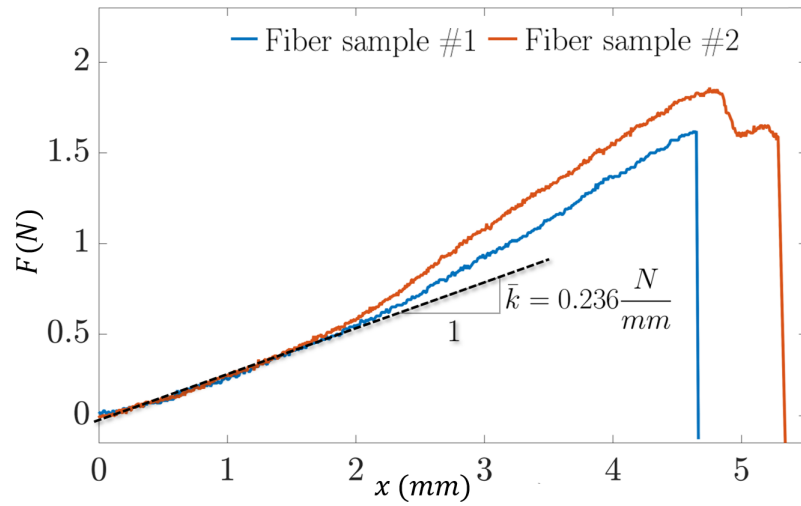
5.3.2 Feasible Range of Parameters and Constraints

Due to the limitations of SLA 3D-printing, the minimum feasible thickness t and substrate attachment L_s were set to 0.5 mm. Also, since the sensor must fit the commercially available graspers, length, and width of the sensor were limited to 5.0 – 15.0 mm and 1.5 – 2.5 mm, respectively.

Also, the feasibility study [20] showed that more deflection of the fiber would result in more power decay; however, more deflection would also increase the maximum strain along the fiber; thus, causing the breakage at a certain strain $\varepsilon_{\text{failure}}$.



(a)



(b)

Figure 5.4: (a) Optical fiber sample no.1 under bending test and sample no.2 after breakage, (b) force-displacement curve of the two optical fiber samples under bending tests.

Therefore to obtain the failure strain of the fiber, a series of bending tests were performed on two different samples of the fiber. The free length of each sample was 15 mm and was attached to the test jigs, as depicted in Figure 5.4(a). The tests were performed under a controlled displacement with a rate of 10 mm.min⁻¹. Figure 5.4(b) shows the force-displacement of two samples obtained from the bending tests. Each fiber demonstrated a linear force-displacement behavior below 2 mm of displacement. In displacements of more than 2 mm, the fibers showed nonlinear behavior mainly due to finite rotations of the fiber.

To obtain the failure strain of fibers, initially the average slope of the linear portion of curves was obtained, i.e., $\bar{k} = 0.236 \text{ Nmm}^{-1}$, i.e., slope of the dashed line in Figure 5.4(b). Using Eq. 77, the initial flexural rigidity $E_o I$ was estimated as 16.6 Nmm².

$$F = \bar{k}x = \frac{48E_o I}{L^3}x \quad (77)$$

According to [220], optical fibers with a silica core follows the following constitutive equation.

$$\sigma = \frac{\phi FL}{16I} = E_o (1 + \alpha\varepsilon) \varepsilon, \quad (78)$$

where, σ is the bending stress and α is a material heuristic equal to -3.2 for uncoated silica optical fibers and -1 for polymer coated fibers [220]. In this study since the utilized fiber was polymer coated (cladded), $\alpha = -1$ was considered. On the other hand, Awtar *et al.* [221] proposed and validated Eq. 79 for the force-displacement characteristic of a clamped-clamped Euler-Bernoulli beam.

$$F = \frac{E_o I}{L^2} (\beta_1 + \beta_2 \frac{\phi x}{L}) \frac{x}{L}. \quad (79)$$

Curve fitting revealed the fitting coefficients β_1 and β_2 as 48.5 and -445.7, respectively ($R^2 = 0.99$). Also $\phi = 0.250$ mm was the diameter of the fiber. Eliminating F between Eq. 78 and Eq. 79, the explicit strain-displacement relationship was found as:

$$\alpha\varepsilon^2 + \varepsilon - \frac{\phi}{16L^3} (\beta_1 L + \beta_2 x) x = 0. \quad (80)$$

Solving this equation revealed:

$$\varepsilon_{1,2} = \frac{-1 \pm \sqrt{1 + 4\frac{\phi}{16L^3} (\beta_1 L + \beta_2 x) x}}{2\alpha}. \quad (81)$$

Evaluating Eq. 81 for the average failure displacement, $x = 4.8$ mm, revealed two failure strains of $\varepsilon_{\text{failure}} = 0.069$ and $\varepsilon_{\text{failure}} = 0.931$. The first root was in accordance with the failure strain of optical fibers in the literature [220]; however, the second root was not admissible. To summarize, Table 5.1 presents the optimization constraints, initial dimensions and the obtained optimized geometrical parameters.

Table 5.1: Geometrical constraints and initial dimensions.

| Parameters | Constraints | Initial value | Optimized value |
|--|--|---------------|-----------------|
| L | 5.0mm < L < 15.0mm | 10.0mm | 14.0mm |
| L _s | 0.5mm < L _s < L/10 | 0.5mm | 0.8mm |
| w | 1.5mm < w < 2.5mm | 1.5mm | 1.8mm |
| t | 0.5mm < t < 2mm | 0.5mm | 0.5mm |
| Effective strain $\varepsilon_{\text{failure}}$ | $\varepsilon_{\text{failure}} < 0.069$ | - | 0.049 |

5.3.3 Material Models and Finite Element Analysis

In order to evaluate the goal function at various design points, a finite element (FE) model of the sensor with initial dimensions was developed in the ANSYS[®] software. The range of force on the top surface of the shell was 2.0 N to match the reported range in the literature [13, 118]. The contact between the indenter of shell and fiber was considered as frictionless and the shell was fixed to the substrates. The bottom part of the lower grasping arm was also fixed.

To obtain the deformation of the sensor under compression, the material properties of its components were identified as follows. The mechanical properties of shell/indenter were obtained by fitting a two-term Mooney-Rivlin hyperelastic model (Eq. 82) to the experimental stress-stretch

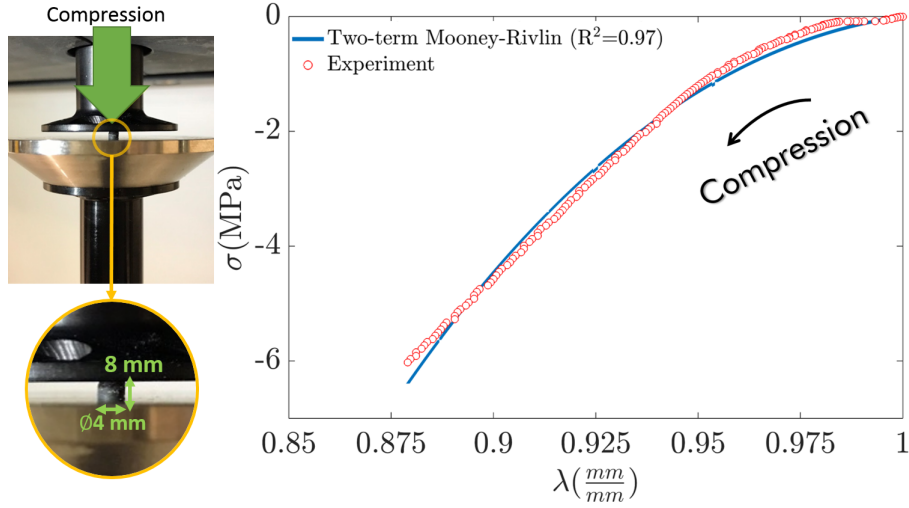


Figure 5.5: Stress-stretch characteristic curve of the flexible material under compression compared to the two-term Mooney-Rivlin fitting.

curve of a sample of flexible 3D printer material (Figure 5.5):

$$\sigma = k_0 \left(\lambda - \frac{1}{\lambda^2} \right) + k_1 \left(1 - \frac{1}{\lambda^3} \right), \quad (82)$$

where, σ was the engineering stress, λ was the stretch ratio, and k_0 and k_1 were the mechanical properties of the flexible material. The sample had a cylindrical shape with 4 mm diameter and 8mm height. The test was performed in compression under displacement-control with a rate of 1 mm.min⁻¹. The high goodness-of-fit, $R^2 = 0.97$ confirmed the validity of the material model used. A similar sample of the rigid 3D printer material used for substrate/support was also tested. The elastic modulus of substrate and support was obtained by fitting a line to the linear portion of its stress-strain curve. Material model and properties used in the finite element model are summarized in Table 5.2.

As discussed in Sec. 5.2.2, Eq. 72 shows the dependency between sensitivity, range, physical dimensions and mechanical properties of the sensor components. For the sensor to be functional up to a certain force level, e.g. 2 N, multiple feasible sets of length(L), width (W), and thickness (t) of the shell is possible. For each set of feasible dimensions the sensor exhibits a specific sensitivity (Eq. 72). Therefore, in this study, numerical optimization was used to obtain the most sensitive

sensor by structural optimization. The optimization goal function was to maximize the sensitivity of the sensor (Eq. 72), subjected to a series of feasible dimensional and strength of material constraints summarized in Table 5.1. The numerical parametric optimization was performed using the Response Surface Optimization (RSO) module of Ansys® 17 software (Ansys Inc., PA, USA). In the following details of optimization procedure are described.

Also, Figure 5.3(b) depicts the deformation of the sensor under a 2 N external force obtained from the finite element analysis and Table 5.3 summarizes the results of finite element optimization for five representative design points (out of 81).

Table 5.2: Material models and mechanical properties of the sensor components

| Component | Material model | Mechanical properties |
|--------------------|---------------------------------------|--|
| Shell/Indenter | Hyperelastic 2-terms Mooney-Rivlin | $k_o = -49.98$ $k_1 = 51.64$ |
| Substrate/Supports | Linear elastic | $E = 0.5 \text{ GPa}^*$ $\nu = 0.43^{**}$ |
| Optical fiber | Linear elastic | $E = 16.5 \text{ GPa}[222]$ $\nu = 0.2$ |

* : Elastic modulus,
** : Poisson's ratio.

5.4 Sensor Fabrication

Researchers have proposed various fabrication processes and materials for optical sensors to address the design requirements of MIS applications. Bandari *et al.* [29] used a micro-machining technique to fabricate their proposed sensor. Also, a wire EDM machine has been proposed for high-quality finishing processes [95]. However, EDM and micro-machining techniques are slow processes and are best suitable for planar objects.

In recent years, 3D printing has been widely used for medical prototyping. This technique

Table 5.3: Representative design parameters used in the RSO optimization and their corresponding goal function values.

| Design parameters (mm) | | | | Max. strain in optical fiber | Goal function (Sensitivity) |
|------------------------|----------------|------|-----|---------------------------------|--------------------------------|
| L | L _s | w | t | ϵ_{max} | $D(s) _{s=L}$ |
| 5 | 0.50 | 1.50 | 0.5 | 0.187 [∇] | 0.253 |
| 10 | 0.50 | 1.75 | 0.5 | 0.110 [∇] | 0.253 |
| 10 | 0.75 | 2.00 | 1.0 | 0.017 | 0.144 |
| 14 | 0.80 | 1.80 | 0.5 | 0.049 | 0.253 [◁] |
| 15 | 1.00 | 2.50 | 2.0 | 0.034 | 0.079 |

∇: violated the effective strain constraint,
◁: maximum goal function without violating the constraints.

offers simplicity, resolution, flexibility to design and non-metallic material which satisfies the MR-compatibility and electro-passivity. In this study, the components of the sensor were fabricated with a Form2 3D printer (Formlabs Inc., MA, USA) using flexible, clear, and white resins. After printing, the components were rinsed using 90% isopropyl alcohol (IPA) for washing any uncured resin residues. Figure 5.6(a) depicts a prototyped sensor integrated with a mock grasper.

5.5 Calibration and Validation

5.5.1 Experimental Setup

Figures 5.6(b) and 5.6(c) show the experimental setup for sensor calibration. A 635 nm laser source (TLS001, Thorlabs Inc., NJ, USA) was used as the light source. The output power of the laser source was set as 0.05 mW. Also, a single-mode 125 μm radius optical fiber was utilized. The fiber was passed through the sensor structure under the flexible shell and indenter and eventually was connected to a biased Silicon photodetector (DET100A, Thorlabs, NJ, USA).

The data-acquisition system (DAQ) used for recording the output voltage of photodetector was composed of an Arduino Mega2560 embedded-board and custom-developed interface software, developed in C++ and C#. Also, Bose ElectroForce[®] universal testing machine (UTM) was used

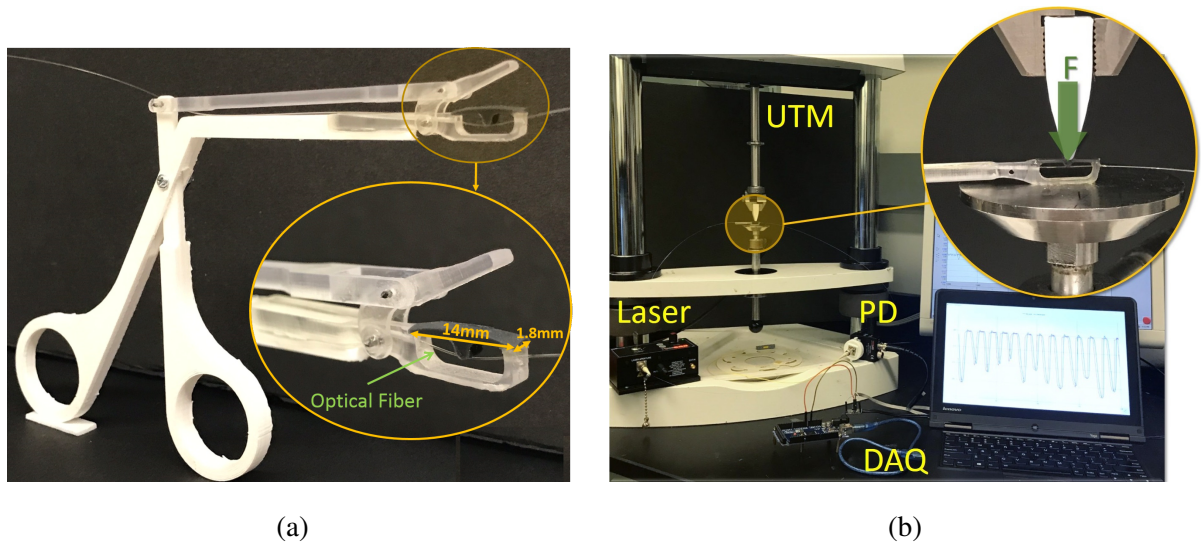


Figure 5.6: (a) Fabricated sensor and grasper with sensorized end-effector, (b) experimental setup for sensor calibration, (c) schematic system configuration.

to apply the displacement and record the reference force. After securing the sensor on the machine, a conical shape indenter was used to apply the deflection on at the mid-span of the shell. Data were recorded from the simultaneous measurement of the force by UTM and voltage with the DAQ, which were synchronized in. The sample-rate of UTM was 10 Hz and DAQ was 20 Hz; thus, the data from DAQ were down-sampled with the ratio of 1 : 2 to match the data from UTM.

5.5.2 Sensor Calibration

In order to calibrate the sensor for both dynamic and static loadings, two types of calibrating displacements were applied on the flexible shell: sinusoidal and triangular. Prior to each test, a pre-load of 1 mm was applied to remove the dead zone in the power output. The dead-zone has been known associated with the critical bending radius of the optical fiber [20, 219]. The findings of Sec. 5.3.1 confirmed that a force between 0 – 2 N would not result in fiber fracture. Therefore the range of displacement was adjusted in the run-time so that the force would not surpass 0 – 2 N. As suggested in the literature, the calibration displacements were applied with frequencies of 0.5, 1.0, and 2 Hz and for ten repetitions [13, 19]. Figure 5.7(a) and (b) depict the calibration force and voltage output of photodetector for sinusoidal and triangular displacements, respectively.

In order to find the independent calibration variables, a.k.a. training features, the relative change in voltage $\frac{\Delta V}{V_0}$ was selected (see Sec. 5.2.2 for the proof of independence from the initial condition). Also, since the flexible shell used in the proposed sensor was fabricated using a photopolymer, it intrinsically was a rate-dependent material [223]. Polymeric stereolithography (SLA) printed parts exhibit hysteresis, where higher force is needed to achieve a certain displacement in the loading compared to the unloading. Similarly, in the proposed sensor, hysteresis caused the shell-fiber contact force to be smaller in unloading ($\dot{V} > 0$) compared to loading ($\dot{V} < 0$). Because of the hysteresis, a non-rate-dependent calibration would not capture the differences in loading and unloading; therefore, the rate of change of voltage, \dot{V} was selected as the second calibration feature. A similar approach was reported in Yip *et al.* [87] to capture the hysteretic effects.

Due to multiple nonlinearities involved, e.g., rate-dependency, large deformation, and hysteresis, a learning-based nonlinear support vector regression (SVR) with Gaussian kernel was selected to perform the calibration. The SVR calibration function is expressed in Eq. 83.

$$F^* = \frac{\sum_{i=0}^m (w_i(X^*) F_i)}{\sum_{i=0}^m w_i(X^*)}, \quad (83)$$

where, m is the number of training data, and

$$w_i(X^*) = e^{-\frac{(X_i - X^*)^2}{2\psi^2}}, \quad (84)$$

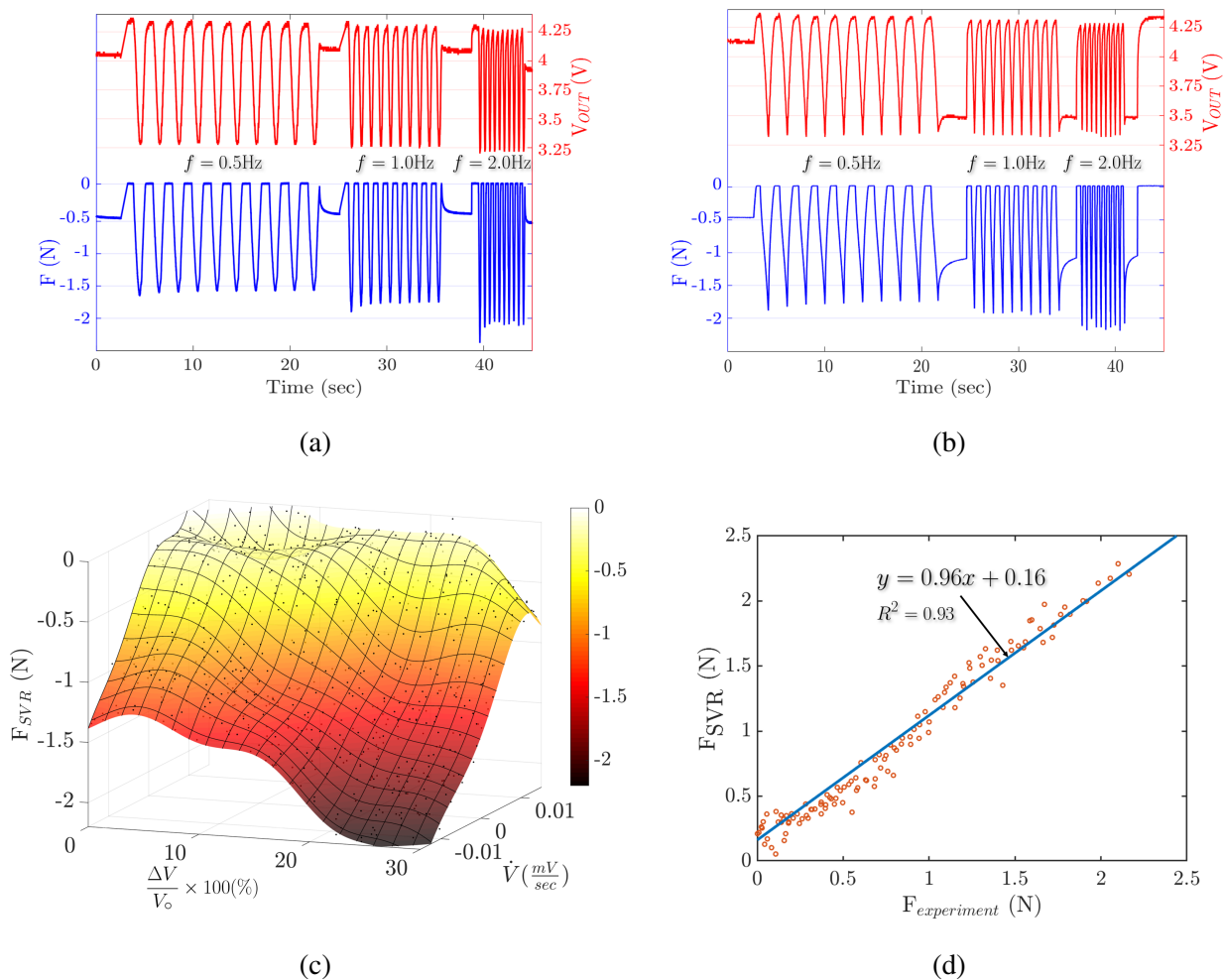


Figure 5.7: Force and the output voltage from the photodetector for (a) sinusoidal displacement, (b) triangular displacement, (c) response surface of SVR calibration over the working range of relative change of voltage and rate of change in voltage; black points indicate the training data used for calibration, (d) linearity of the SVR calibration.

is the i^{th} Gaussian coefficients for the i^{th} training point, ψ is the spread parameter determining the radius of influence of the training points, F^* is the test force obtained from the Bose ElectroForce[®] universal testing machine (UTM) and X is the features vector. Furthermore, i and \star indicate the iterator over all the training data. The spread parameter was selected $\psi = 100$ using the method suggested in [224] and features vector X was defined as:

$$X = \left(\frac{\Delta V}{V_0}, \dot{V} \right)^T. \quad (85)$$

The SVR training and validation were performed in Python 3.7.1 (scikit-learning 0.20.2) using a 30% : 70% testing-to-training ratio. Figure 5.7(c) depicts the response surface of SVR calibration over the working range of ΔV and \dot{V} . Also, Figure 5.7(d) depicts the linearity of the SVR calibration with respect to the test data. Table 5.4 summarizes the goodness-of-fit, R^2 , mean absolute error (MAE), and the linearity of SVR calibration compared to the test data.

Table 5.4: Performance of SVR regression calibration.

| Criteria | Indicator | Value |
|-----------------|--|------------------------------------|
| Goodness-of-fit | $(adj - R^2) \times 100$ | 93% |
| Linearity | $F_{SVR} = aF_{experiment} + b$ | $a = 0.96$ $b = 0.16 \text{ N}$ |
| MAE | $MAE = \frac{\sum_{i=0}^m F_i - F_i^* }{m}$ | $0.085 \pm 0.096 \text{ (N)}$ |

5.5.3 Experimental Validation

After calibrating the sensor, two experiments were performed to validate the results and assess its performance. To this end, an experimental setup was prepared as shown in Figure 5.8(a).

A 6-axis force/torque sensor (Mini45, ATI Industrial Automation, Inc., USA) was attached to a 3-axis desktop CNC machine using two custom-designed coupling pieces. A graphical user interface was developed in C# to control the CNC machine as well as for synchronous data acquisition from the optical sensor and ATI sensor.

In the first experiment, the sensor was attached on the top surface of the ATI sensor while a triangular compressive displacement from 0 – 2 mm was applied to it. The displacement was

repeated for 5 cycles at frequencies of 0.5, 1.0, and 2.0 Hz. There was a 0.3-second pause between loading and unloading, to assess the capability of the sensor in the detection of the viscoelastic stress relaxation (static measurement).

The performance of the sensor was evaluated by comparing the force measured by the ATI sensor and the force estimated by the SVR calibration. Figure 5.8(b) depicts force measured by ATI sensor versus force estimated by SVR calibration.

Furthermore, to evaluate the optical sensor performance in a more realistic condition, it was assembled with the mock grasper. Afterward, the two cylindrical attachments on the fixture for ATI sensor were squeezed manually using the sensor-embedded grasper. Such grasping resembles practical cases of grasping a vein, tendon, nerve in MIS. Figure 5.9(a) depicts the optical sensor grasping the experimental fixture and Figure 5.9(b) shows the force measurement by ATI versus the force estimated by SVR calibration.

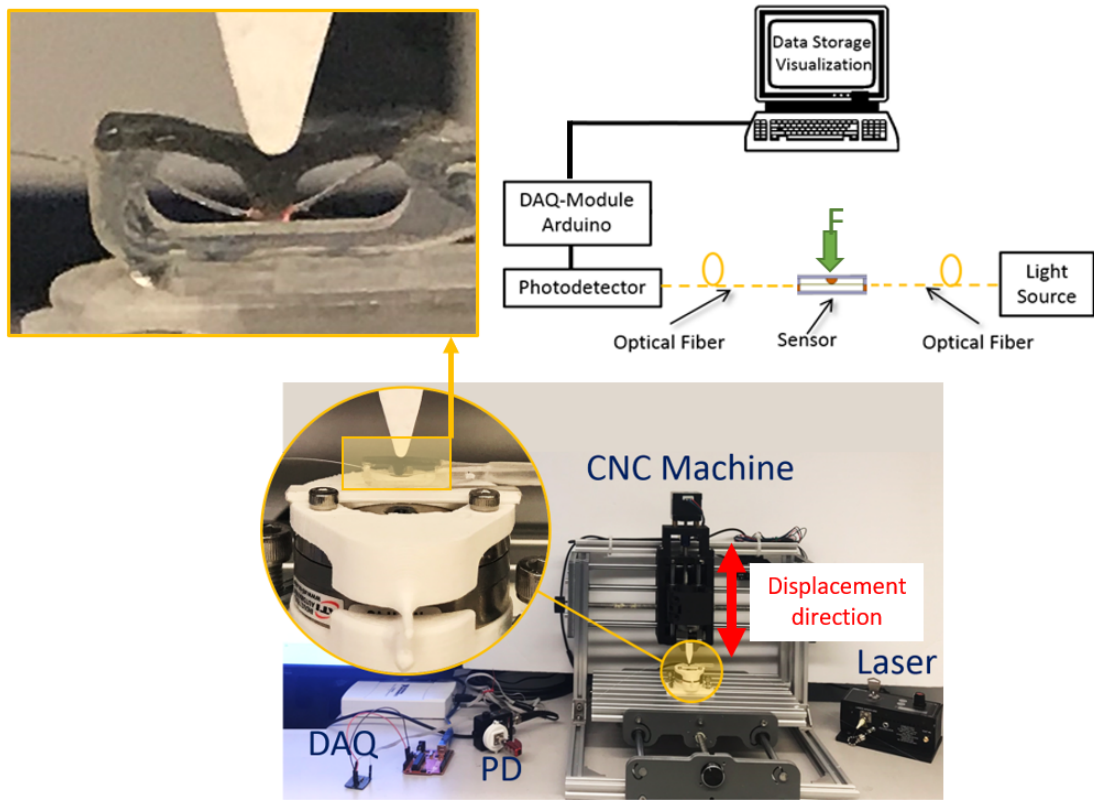
5.6 Performance Analysis

In order to evaluate the performance of the optical sensor, its accuracy, hysteresis, repeatability, and resolution were studied. As suggested in [95], mean absolute error (MAE) was calculated for accuracy, standard deviation of peak force for repeatability, and the average difference between consecutive force estimations for resolution.

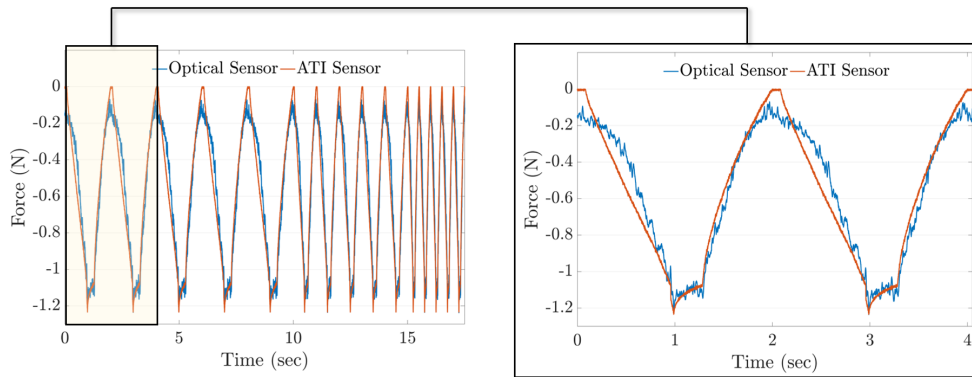
Table 5.5: Performance of the sensor in validation experiments.

| Criteria | Triangular test | Grasping test | Average |
|----------------------|-----------------|-----------------|-----------------|
| MAE (N) | 0.10 ± 0.08 | 0.13 ± 0.09 | 0.12 ± 0.08 |
| Resolution (N) | 0.02 | 0.02 | 0.02 |
| Min. Force (N) | 0.14 | 0.14 | 0.14 |
| Repeatability (N) | 0.07 | - | 0.07 |
| Hysteresis (N/cycle) | 0.057 | - | 0.057 |

As discussed earlier, due to the use of the flexible shell in this sensor, hysteresis is present in

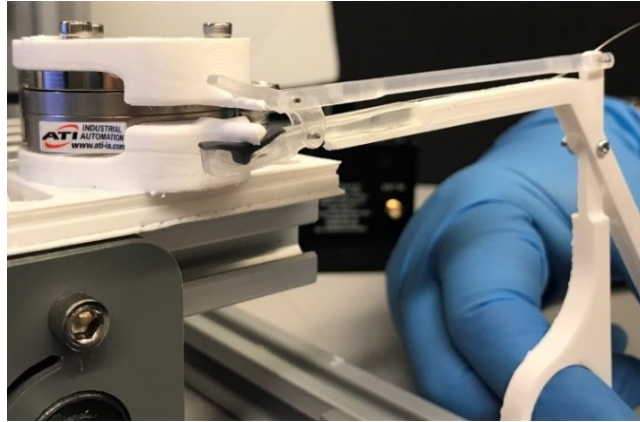


(a)

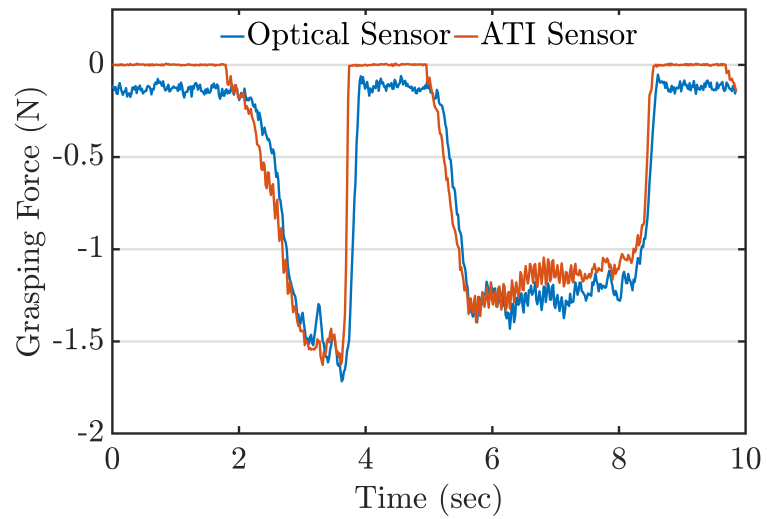


(b)

Figure 5.8: (a) Experimental setup for sensor performance assessment under cyclic triangular compression, (b) results of the force measured by the optical sensor compared to the ATI sensor.



(a)



(b)

Figure 5.9: (a) Optical sensor on a mock grasper squeezing the fixture installed on the ATI Mini45 force sensor, (b) results of the force measured by optical sensor compared to the ATI sensor.

its force-voltage characteristic. However, the rate-dependent calibration schema used in this study successfully captured and compensated for the hysteresis leading to accurate results. Therefore, for the hysteresis criterion, the difference between the demonstrated hysteresis and captured hysteresis by the SVR calibration was calculated. Figure 5.10(a) shows the force-voltage of the sensor with both ATI force and SVR estimations in triangular validation test. Thus, small values of this criterion would show a small difference between demonstrated and compensated hysteresis by the sensor.

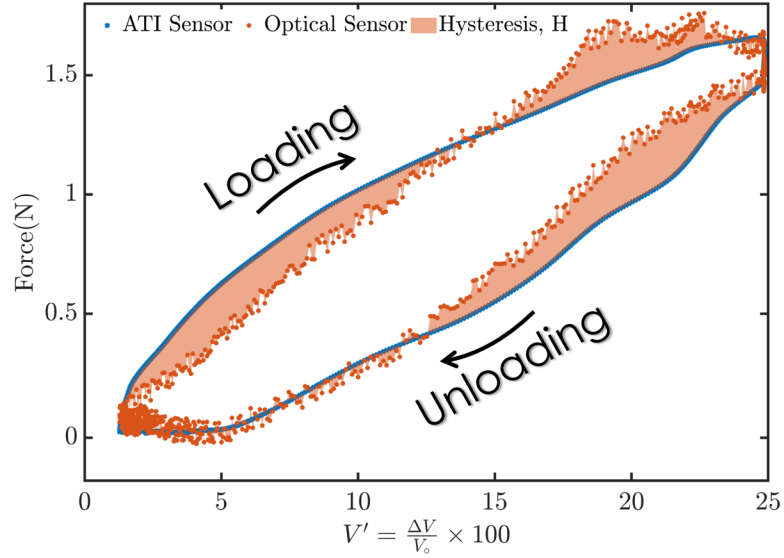
The hysteresis, H was calculated using the following definition:

$$H := \frac{1}{n} \left(\int_{\text{loading}} |F^{\text{ATI}} - F^{\text{SVR}}| dV' + \int_{\text{unloading}} |F^{\text{ATI}} - F^{\text{SVR}}| dV' \right), \quad (86)$$

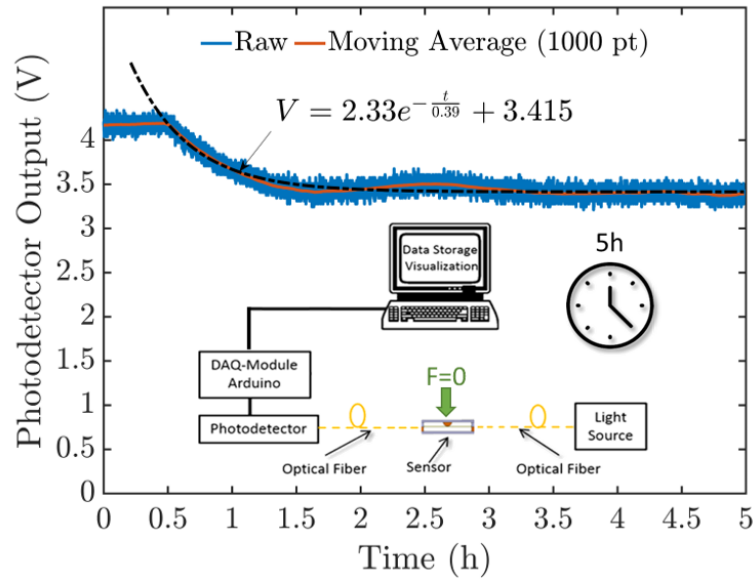
where, $n = 15$ indicates the number of loading-unloading cycles included in the calculations. Table 5.5 summarizes the performance criteria evaluated on the results of triangular and manual grasping tests. As indicated in the Table 5.5, the MAE was 0.12 N. This level of error shows better performance than results reported in [95] and lies in the acceptable region set in [13]. Also, the repeatability, minimum detectable force, and resolution were 0.07, 0.14 N, and 0.02 N, respectively. The obtained resolution also met the requirements suggested in [13, 29, 118] for tactile sensors in MIS and cardiovascular application. The evaluated hysteresis criteria (shaded area in Figure 5.10(a)) was 0.057 N/cycle which was less than the total mechanical hysteresis of the sensor (total area inside the blue loop in Figure 5.10(a)), i.e. 0.64 N/cycle. This finding also shows the fair success of the SVR calibration in capturing and compensating for the hysteresis effects.

In addition, Figure 5.8(b) between 0.9 – 1.2 sec and Figure 5.9(b) between 5.8 – 8.4 sec shows the capability of the sensor in capturing stress relaxation forces. As the displacement was kept constant in these two regions, the contact force dropped exponentially due to the nonlinear characteristics of the flexible shell. However, the sensor could fairly follow the decay. The findings confirm the capability of the sensor in working under both static and dynamic conditions.

In order to study the effect of the size and relative position of the tissue and the flexible shell on the accuracy of the sensor, three indenters were fabricated and using each three points on the flexible



(a)



(b)

Figure 5.10: (a) Force-voltage characteristic curve of the reference (blue) versus the estimated forces (red). Shaded area shows the hysteresis H , (b) drift and noise of the sensor in five hours with an exponential fit and moving average filtering.

shell were indented using the universal testing machine. The indenters were of an elliptical cross-section with 2, 4, and 8 mm major diameters. Each indenter was pushed under force control to reach 2 N. Table 5.6 compares the actual force and the estimated force by the sensor. The results showed that the average estimation error slightly increased by increasing the indenter size. Nevertheless, the average estimation error was 0.04 ± 0.05 N with the indenters at the center of the sensor (2% of range). Furthermore, the results showed no clear trend of error enhancement with moving the indenter to the left or right. To characterize the noise and drift, the sensor output voltage was recorded for five hours, while it was stationary on an optical table with zero external force. Figure 5.10(b) depicts the recorded voltage. The noise was defined as the average absolute difference between the recorded voltage and its moving average value (1000-point window). Also, the drift was characterized by the time-constant of the exponential fit to the decaying part of voltage.

The average noise was 0.028 ± 0.024 V, while the maximum absolute noise was 0.194 V (4.5% of the initial voltage) over the five hours. The time-constant of drift was 0.39 h (≈ 24 min). Also, the drift started after an initial 29 minutes of warm-up. Therefore in practical uses for more than 29 minutes, the system must be turned on 77 min (29 min (warm-up) + 2×24 min (95% stability)) earlier to stabilize. Another possibility is to reset the V_o each time the grasper is to grip a tissue. Since the sensor is calibrated based on the $\Delta V/V_o$, resetting the V_o would compensate for the drift-based change in the baseline voltage.

Table 5.6: Sensor outputs for 2 N reference force with three elliptical indenters with 2, 4, and 8 mm diameters at left, right and center of the sensor (Numbers in N).

| | | Location | | |
|-------------|------|---|--|---|
| | |  |  |  |
| Size | 2 mm | 1.98 ± 0.03 | 1.96 ± 0.07 | 1.91 ± 0.04 |
| | 4 mm | 2.02 ± 0.08 | 2.01 ± 0.09 | 2.00 ± 0.15 |
| | 8 mm | 2.04 ± 0.07 | 1.91 ± 0.06 | 2.05 ± 0.11 |
| Average (N) | | 2.01 ± 0.06 | 1.96 ± 0.05 | 1.99 ± 0.10 |

Table 5.7: Comparison of physical and functional requirements with the specifications of the proposed sensor.

| | Criterion | Requirement | Specification | Pass/Fail |
|-------------------|------------------|-------------------------|----------------------|------------------|
| Physical | Shape [205] | Layered | Layered | ✓ |
| | Size [225] | $5 \leq L \leq 15$ | 14 mm | ✓ |
| | | $5 \leq \phi \leq 8$ mm | 5 mm | ✓ |
| | Material | Biocompatible | Flexible Resin | × |
| | | | Clear Resin | × |
| | Safety | | White PLA | × |
| | | | MRI [19] | Non-magnetic |
| Electrical [19] | | | Electrical passive | ✓ |
| | | Laser [226] | Safe: IEC Class I | ✓ |
| Functional | Range [13] | 0–2.0 N | 0–2.0 N | ✓ |
| | Resolution [13] | 0.05 N | 0.02 N | ✓ |
| | Accuracy [13] | $\geq 95\%$ | $95 \pm 1\%$ | ✓ |

Although the prototyped sensor was designed for a force range of 0–2 N, the proposed optimization procedure, i.e., FEM and response surface optimization, allows for obtaining higher force ranges. As is suggested in the literature, the 2 N force range would be enough for grasping and holding delicate soft tissues such as nerves and veins; however, in specific MIS tasks such as needle handling and knot tying higher grasping forces (10–50 N) would be needed. In this regard, a possible improvement of this study in the future can be to utilize the same sensing principle for developing new configurations for more force demanding indications.

Besides, thanks to its simple and scalable structure, Cartesian and cylindrical arrays of this sensor can be assembled for sensing multiple forces, e.g., as suggested in [30]. Table 5.7 compares the requirements considered in this study with the specifications of the sensor. As shown in Table 5.7 the shape, size, safety, range, resolution, and accuracy requirements were met with the prototyped sensor. In this regard, the sensor was fairly accurate under combined dynamic and static testing conditions. The calibration and validation forces were within the range of force reported for MIS application and the sensor showed acceptable resolution. Also, the sensor was non-magnetic and

non-electric; thus would not interfere under MRI imaging (MRI-compatibility) and is electrically passive. Moreover, according to IEC-60825 classification [226], this sensor was laser-safe and would fall under *Class I* (laser sources with less than 0.39 mW power).

However, the material used in the prototyping of this sensor was not biocompatible. Nevertheless, there are biocompatible materials with similar mechanical properties in Formlabs' portfolio which could be utilized for the future works. Although the prototyped sensor was not sterile for the validation studies, thanks to its polymeric nature cold techniques, e.g. Ethylene Oxide (EtO), plasma, and gamma irradiation can be used for its sterility for the final usage.

Furthermore, due to the use of optical fiber in this sensor and dependency of the power loss to the bending of optical fiber, the proposed sensor is not suitable for being embedded at the multi-DoF wristed robotic manipulators. Multi-dimensional rotations of such wrists would cause extra bending in the optical fiber and lead to erroneous force measurements. Considering the comparison, author would conclude the proposed sensor fairly compatible with the requirements needed for MIS applications.

For further improvement of this study, an alternative array design is to be investigated for intra-operative measurement of the tissue stiffness. Another option would be to incorporate an encoder in the handle of the grasper, so both displacement and force data can be obtained for stiffness estimation. For the sensor to be fully usable at MIS, the outgoing end of the optical fiber needs to be cut and faced to an adjacent mirror configuring a retroreflecting design. Another option would be to use optical fibers with gold-coated ends to reflect the light on to the same fiber. Such a configuration, a.k.a. retroreflectance, necessitates using an optical circulator to isolate the reflecting light and direct it toward the photodetector [19]. Since in a retroreflection, light passes through the bent optical fiber twice, the power loss doubles and makes the sensing of small changes easier.

5.7 Conclusions

In this study, a novel miniaturized optical force sensor was proposed for integration at the end-effector of MIS and RMIS graspers. The sensor was designed based on a recently-proposed novel theoretical model for bending-based light intensity modulation. The theoretical framework of the

intensity modulation was fully explained and the suitability of intensity decay coefficient for force sensing was discussed.

Optimization of the proposed sensor was performed to obtain the smallest structure with the maximized sensitivity while avoiding breakage of the fiber. Afterward, the miniaturized sensor was fabricated using 3D printing technique. Also, the tactile sensor was calibrated using a learning-based technique, i.e., support-vector-regression (SVR). For calibration, the features vector was constructed with the relative change in voltage $\frac{\Delta V}{V_0}$ and the rate of change in voltage \dot{V} .

The simple structure of the sensor allows for versatile integration of the sensor into MIS graspers. Also, its optimized shape allows for fitting into a 5–8 mm MIS trocar. In addition, contact with blood and body fluids would not compromise the sensing principle; however, should be the need, its compact design allows for encapsulation of the entire lower grasping arm.

Considering the single degree-of-freedom nature of the proposed sensor, author would suggest a study to investigate the coupling effect of other loads in MIS, e.g., translation, rotation, palpation on the sensor measurements. Furthermore and as other alternatives to the SVR technique, researchers may investigate the performance of recurrent neural networks (RNN) and Gaussian process models (GPM) for the rate-dependent calibration, e.g. [227, 228].

The propose sensing principle and miniaturized structure paved the way to design and propose multi-DOF structure (array structure) for the sensors in future studies. However, one noticeable observation in the current study was that using photodetectors led to fluctuation and noise in the output. Besides, each optical fiber should be coupled to an individual photodetector which makes a cumbersome and expensive acquisition system in array structures. In addition, electrical leveling and synchronization of multiple photodetectors may be cumbersome and complicate the data-acquisition system. Therefore in the next study, an image-base data acquisition technique is proposed to facilitate using multiple optical fibers in array configuration by capturing the intensity loss of each fiber individually.

Chapter 6

Image-based Optical-fiber Force Sensor for Minimally Invasive Surgery with *ex-vivo* Validation

During minimally invasive surgery, surgeons insert specially-designed instruments through a small incision into the patient's body. Despite all the advantages of this procedure, surgeons do not have the natural force feedback in the surgery. Force feedback helps the surgeon to apply an appropriate force to avoid tissue damage. As a solution, this study was aimed at the *ex-vivo* validation of a proposed image-based optical force sensor with light intensity modulation principle. The sensor was to be integrated with conventional minimally invasive instruments and was working based on variable bending radius sensing principle. To this end, the sensor was integrated on the jaw of a custom-designed minimally invasive grasper and its performance was assessed *ex-vivo*. Furthermore, the light intensity measurement of this study was performed utilizing an image-based technique to avoid the complexities of using photodetectors. The sensor was calibrated using a rate-dependent learning-based support-vector-regression model, which showed an adjusted- R^2 of 94%. The results of the *ex-vivo* test on a freshly excised bovine muscle tissue showed fair agreement between sensor measurements and ground truth. Therefore, the proposed sensor was concluded as applicable for minimally invasive surgeries by comparing the minimum performance requirements

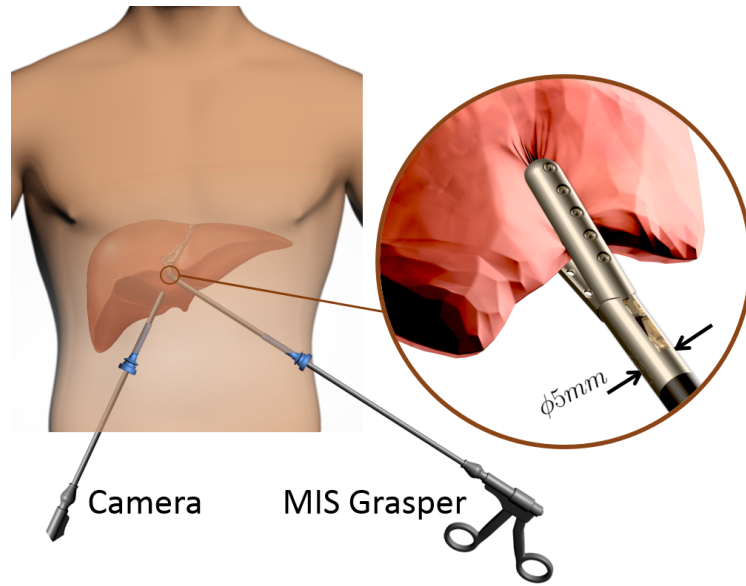


Figure 6.1: Schematic MIS procedure: the camera is used for the internal vision of the organs and grasper is used for holding and operating on the organs.

of force sensors for surgical applications.

6.1 Introduction

Within the last twenty years, minimally invasive surgery (MIS) approaches replaced conventional open surgery in many surgical procedures. MIS allows the surgeon to reach the internal anatomy through a small skin incision using 5-15 mm MIS instruments [1]. As a result, MIS reduces the anesthesia time, incision size, intraoperative blood loss, postoperative infection and trauma, and hospitalization time. Figure 6.1 depicts a schematic MIS procedure.

With the presence of robots in MIS, the accuracy and dexterity of manipulation of surgical instruments were considerably improved [8]. Furthermore, the surgeons' physical fatigue and ionizing radiation exposure have been decreased via robotic-assisted minimally invasive surgery (RMIS) [9]. Despite the outstanding advantages of MIS and RMIS, several noticeable limitations exist for surgeons due to indirect access to the operation site, including limited hand-eye coordination, restricted field of view and tool movements, and on top of all, lack of haptic perception [7]. To answer this need, researchers have proposed different force sensors to attach at the tip of surgical instruments

for measuring the tool-tissue interaction force. Studies have revealed that force feedback helps the surgeon to apply a just-enough force to grasp organs and avoid tissue damage [11]. The measured force can be relayed to a visual or tactile display system, e.g., [132, 163–165, 185], to be replicated for the surgeon.

It has been reported that the grasping force could be reduced by force feedback in da Vinci[®]-performed operation [202]. Therefore, a sensor to measure the force in RMIS can increase the efficiency of the surgery. The sensor must work under both static and dynamic conditions [13, 15]. Also, since the surgeons may operate in a magnetic resonance imaging (MRI) environment or do cardiovascular RMIS, the sensor must be MR-compatible and electrically-passive to avoid electromagnetic interference [17]. Furthermore, due to limited space on the MIS surgical instruments and small incision on the patient's body, sensors must be sufficiently miniaturized and scalable.

Optical sensing principles are favorable for biological and biomedical applications as their exhibit intrinsic precision, robustness, scalability, miniaturization, electromagnetic and biological compatibility, e.g., [229–232]. To this end, researchers have proposed various optical sensors to integrate at the MIS instruments. The author has reported a comprehensive review on such sensors in [27]. Xue *et al.* [215] and Zarin *et al.* [95] proposed fiber-bragg-grating (FBG)-based sensorized laparoscopic instruments for grasping and needle-driving purposes. Recently, Carotenuto *et al.* [216] equipped an epidural needle with an FBG-sensor and assessed sensor performance in a clinical study. Likewise, in a new study, Ulgen *et al.* [217] sensorized a biopsy needle with Fabry-Perrot interferometry (FPI)-based fiber optic force sensor and measured force up to 13 N.

Although FBG and FPI-based sensors are highly accurate, they are thermal-sensitive and require utilization of expensive and complicated interrogation systems [13, 27]. On the other hand, light intensity modulation (LIM)-based sensor are cheaper, simpler to design and scalable [27]. Various LIM-based force and stiffness sensors were introduced and designed by Ahmadi *et al.* [118, 149]. Also, Bandari *et al.* [29] proposed a hybrid piezoresistive-optical sensor for force and stiffness measurement in MIS applications.

In our previous studies, we proposed and experimentally validated a new LIM sensing principle, i.e., variable bending radius (VBR), which allowed for further miniaturization of MIS force sensors [21]. The proposed method not only decreased the size of the LIM-based sensor, but also increased

its sensitivity [20, 28]. Despite its favorable sensitivity and accuracy, the proposed sensor in [21], required utilization of a diode photodetector for measuring the transmitted optical power through the optical fiber. The photodetector measurements were prone to temporal drift without proper compensation, which could result in erroneous force measurement. Moreover, in case of array sensor, each fiber shall be coupled to an individual photodetector, and all the photodetectors shall be electrically leveled and synchronized [233]. Such synchrony and electrical leveling is cumbersome, especially with a high number of optical fibers, e.g., four fibers as proposed in [30].

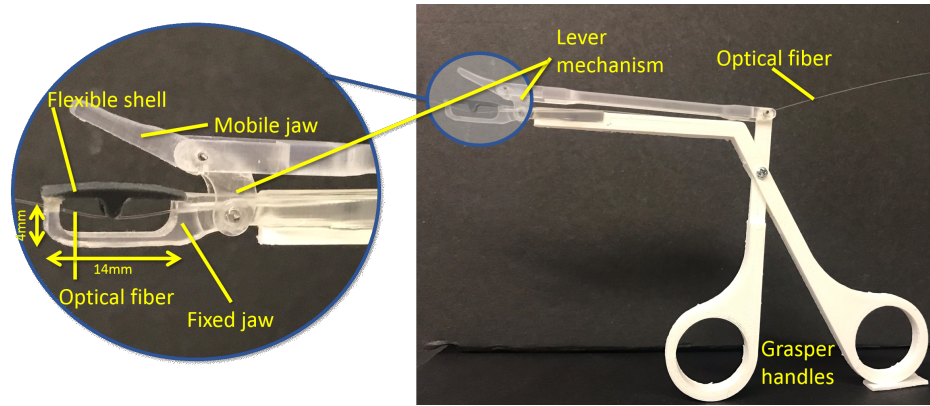
As an alternative to the use of photodetectors, in this study, an image-based force measurement technique is proposed and validated for the miniaturized VBR-based force sensor presented in [21]. The sensor was prototyped using SLA 3D printing method and was mounted on a custom-designed surgical grasper, equipped with a force-sensing resistor (FSR) for reference. An RGB-camera was calibrated to the light intensities and was used to measure the transmitting light through the optical fiber. Finally, the sensor was calibrated using a learning-based support-vector-regression technique and was used for multiple grasping tasks on a freshly excised bovine tissue.

In the following, section 6.2 provides the details of design and prototyping, experimental setup, image-based light intensity estimation, and sensor calibration. Afterward, *ex-vivo* validation procedure and the study results are discussed in section 6.3, followed by the concluding remarks in section 6.4.

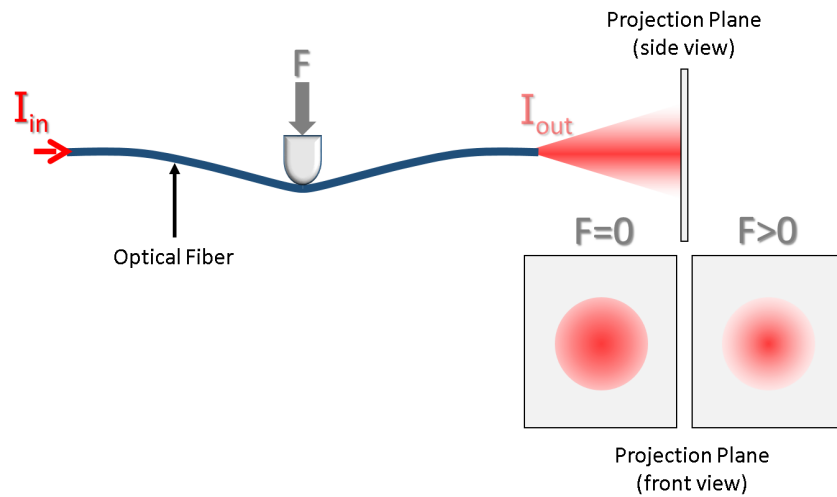
6.2 Material and Methods

6.2.1 Geometrical Design and Prototyping

Figure 6.2(a) depicts the geometry of the miniaturized sensor on the prototyped grasper. As depicted, the sensor has a flexible shell with a semi-circular indenter on the top of optical fiber. Upon any contact between the flexible shell and tissue, the shell bends downward and the semi-circular indenter applies a force F on the optical fiber. Figure 6.2(b) shows a schematic model of the optical fiber under an external contact force F . To reduce the risk of unwanted rotation or motion of the optical fiber, it was secured with glue in a confined channel through the body of the grasper. Moreover, the elastomeric flexible shell would to much extent damp the potential ambient low amplitude



(a)



(b)

Figure 6.2: (a) Prototyped force sensor embedded on the jaw of a typical MIS grasper, (b) schematic view of the transmitted light intensity on a projection plane while the optical fiber is under force.

vibrations. The details of the mathematical relationship between the transmitted light and contact force was rigorously derived in [21] and was validated experimentally in [20, 28].

As provided in [21], the relationship between the bending radius along the optical fiber $r(s)$ and percentage of the change in the transmitted intensity through the optical fiber is of the form:

$$\frac{\Delta I_{out}}{I_{in}} = - \int_0^L \gamma e^{-\gamma s} ds - \int_0^L s e^{-\gamma s} f(r(s)) \frac{d}{ds} r(s), \quad (87)$$

where, γ is an intrinsic optical property of the optical fiber, L is the length of the optical fiber, s is a dummy variable, and $f(r)$ is a nonlinear function relating the radius of curvature $r(s)$ to the

local rate of dissipation of light from optical fiber. In this study, an RGB camera was installed on a projection chamber, which provides a projection plane to capture the light spot. Once the magnitude of force F on the optical fiber increases, the intensity of the light spot on the projection plane decreases. The variations of the average light intensity were captured through real-time frame capturing with the camera. The sensor 3D printed with a Form2 SLA printer (Formlabs Inc., MA, USA) with flexible and transparent resins for the shell and grasper components, respectively.

In order to acquire the output light intensity I_{out} at the end of the optical fiber, photodetectors are commonly used. However, due to the above-mentioned limitations of the photodetectors, their measurements are prone to error, especially in long-term use, e.g., for hours during an MIS surgery. Therefore, in this study, an image-based intensity measurement system was developed. Applicability of such image-based technique has been validated in other studies, e.g. [26, 89].

6.2.2 Experimental Setup

Figure 6.3(a) shows the experimental setup set used for sensor calibration. The input light to the optical fiber was 0.05 mW, supplied by a 635-nm laser source (TLS001, Thorlabs Inc., NJ, USA). A single-mode 250- μm diameter optical fiber was used as the sensing media. As shown in figures 6.3(b) and 6.3(c), the fiber was terminated in an FC-PC connector, coupled to a matching port on a custom-designed projection chamber. Figure 6.3(b) shows the interior of the projection chamber with the top lid removed. The projection chamber was light-sealed with inter-connected walls and lid.

To have precise details in the prototype, the flexible membrane was 3D printed using a Form2 SLA printer and Formlabs flexible resin (80A resin, Formlabs Inc., MA, USA). The flexibility of the membrane was an essential requirement to make the bending of the underlying optical fiber possible. Moreover, to achieve a precise finished dimensions and details on the upper jaw and lower jaws of the grasper, these were printed with the same printer using the solid clear resin. The rigid body of the grasper was rapid prototyped using a Makerbot Replicator+ 3D printer (Makerbot Inc., NY, US) with white PLA filament. Similar to the body of the grasper, the projection chamber was 3D printed with the white PLA filament. The projection chamber was 100 mm long, 100 mm wide and 50 mm high (figure 6.3(b)). Although the materials used in this study are not biocompatible,

material providers, e.g., Formlabs Inc., MA, US, offer a variety of biocompatible flexible and solid materials for biomedical applications. For image-acquisition, a Logitech C920 (Logitech Inc., CA, USA) camera was installed on the projection chamber below the optical fiber port to the chamber. Such installation facilitated the light spot (on the opposite wall) be visible by the camera view. The image-acquisition and intensity estimation algorithm were developed in C++ (core) and data was recorded in a C# graphical user interface (GUI). The calibration tests were performed using a universal testing machine, UTM (ElectroForce[®] 3200, TA Instruments, DE, USA) (figure 6.3(a)).

6.2.3 Image-based Intensity Estimation

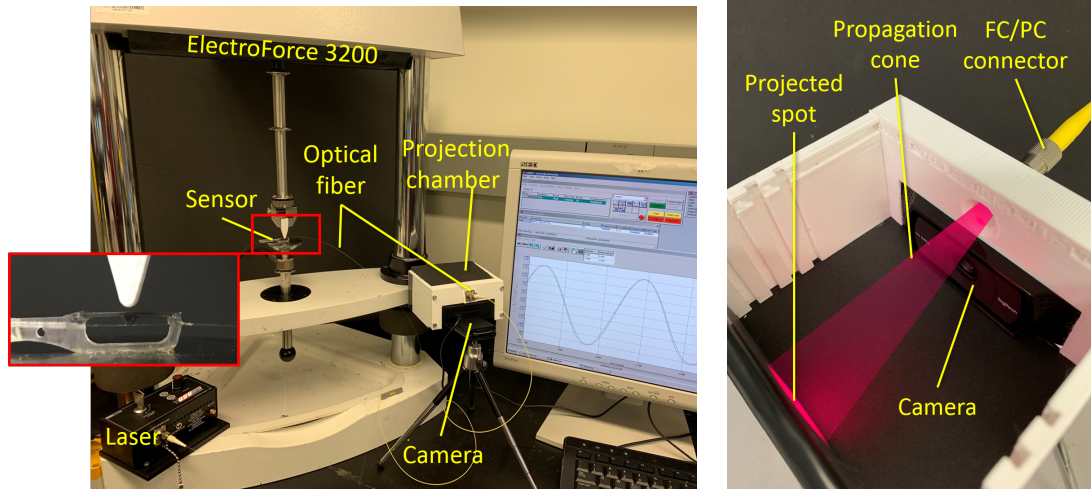
The frames obtained from the camera were of 640×480 pixels resolution, with 8-bit color depth. Since the frames were in red-green-blue (RGB) color-space, a greyscale to RGB mapping (Eq. 88) was performed on the images to obtain the greyscale image. The 8-bit color depth resulted in greyscale values in the range $[0, 255]$.

$$\sigma := \sigma_{ij} = \frac{1}{3}(R_{ij} + G_{ij} + B_{ij}), \quad (88)$$

where, i and j indicate the row and column of pixels in the image, σ is the greyscale value, and $R, G,$ and B indicate the red, green, and blue matrices (channels) of the RGB image. Afterward, a **Threshold** binary operation (Eq. 89) was applied to the greyscale image to find a binary mask μ , indicating the pixels where the intensities were above the threshold $\xi = 25$.

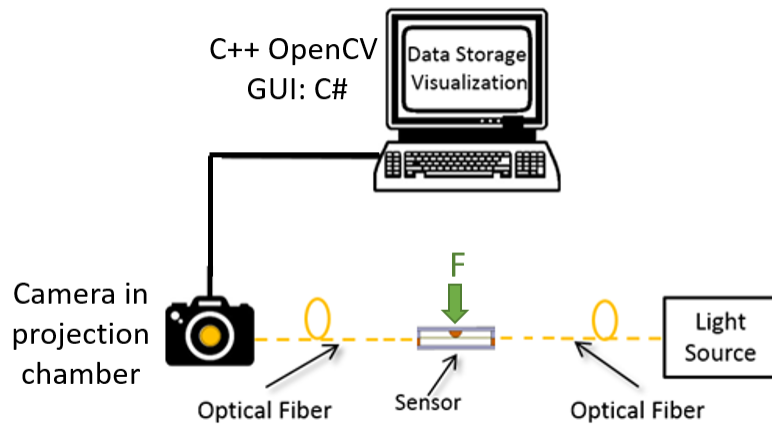
$$\mu := \mu_{ij} = \begin{cases} 0 & \text{if } \sigma_{ij} \leq \xi \\ 1 & \text{if } \sigma_{ij} > \xi \end{cases} \quad (89)$$

The threshold ξ was a heuristic and was experimentally set to a minimum value of $\xi = 25$, so that the binary mask would be all-zero, while the laser source was off. The reason for applying the thresholding was to obtain a true-dark image while the laser source is OFF. Theoretically, while the laser source is OFF, the image taken from the projection chamber shall be completely



(a)

(b)



(c)

Figure 6.3: (a) Experimental setup used for sensor calibration, (b) internal view of the projection chamber and camera with the top lid removed (propagation cone is overlaid on the image), (c) schematic system configuration.

dark, i.e., greyscale value of all the pixels be zero. However, due to the imperfections in the prototyping of the projections chamber and ambient light diffusion into the optical fiber, there existed non-zero greyscale values in the image with laser source OFF. Therefore, as a mitigation measure to set the zero state, multiple images were taken and analyzed offline to obtain the minimum greyscale threshold which robustly discard the light artifacts from the image. Figure 6.4 depicts a representative variation of the light intensity of the laser spot as the sinusoidal force was applied on the sensor.

To obtain the average intensity of the light spot, the average greyscale values, $\bar{\sigma}$, of each image frame were calculated in real-time using (Eq. 90).

$$\bar{\sigma} = (\boldsymbol{\mu} : \boldsymbol{\mu})^{-1} \boldsymbol{\sigma} : \boldsymbol{\mu}, \quad (90)$$

where, $(:)$ is the double-dot product operation defined as:

$$\boldsymbol{\sigma} : \boldsymbol{\mu} := \sum_{i=1}^{640} \sum_{j=1}^{480} \sigma_{ij} \mu_{ij}. \quad (91)$$

In practice, although no particular noise reduction filter, e.g., Gaussian blur filter, was used in this study, both the **Threshold** and greyscale averaging (Eq. 90) performed as high-pass filters on the images. Whereas, the thresholding would reduce the level of base noise present because of the ambient light diffusion to the chamber and optical fiber and the averaging would cancel potential spontaneous erroneous readings in the pixels of images.

6.2.4 Support-Vector-Regression (SVR) Calibration

For calibration, a sinusoidal force with a range of 0–2 N with 0.5, 1.0, and 2.0 Hz frequency was applied on the sensor. Due to the viscoelastic properties of the 3D printed materials, the intensity modulation within the sensor was dependent on the magnitude and the rate of force. A similar suggestion was made by Yip *et al.* [87] and was observed in [21]. As discussed by the author in [21], a rate-dependent SVR calibration can fairly compensate for the structural hysteresis present in the proposed sensor due to the use of viscoelastic flexible shell. Therefore, for the calibration

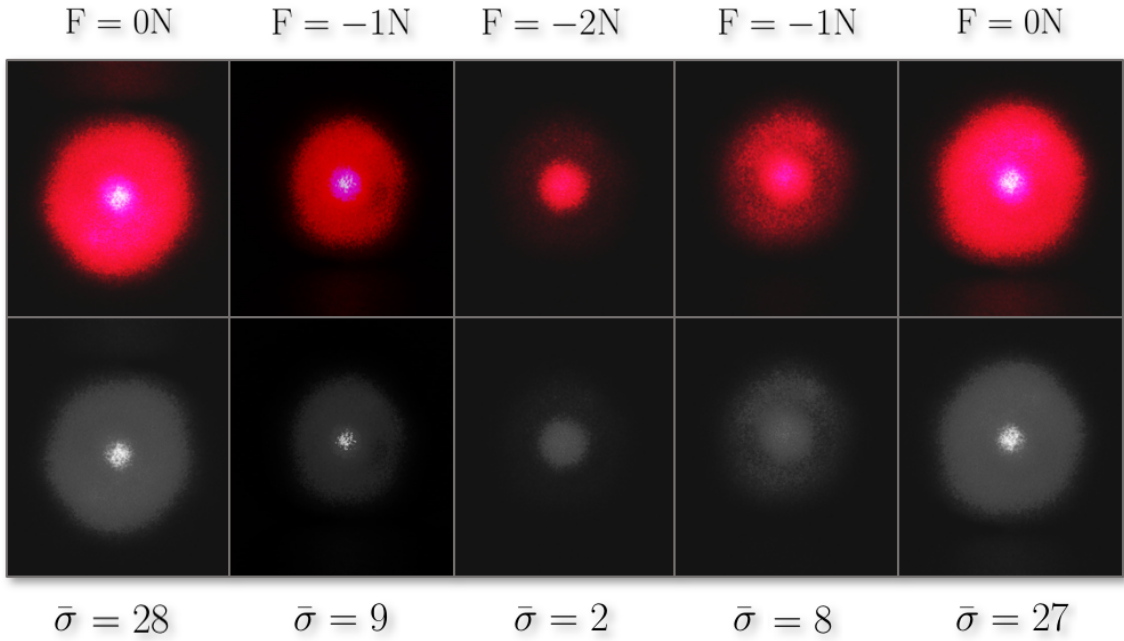


Figure 6.4: Variation of the light intensity of the laser spot on the projection plane captured by the camera.

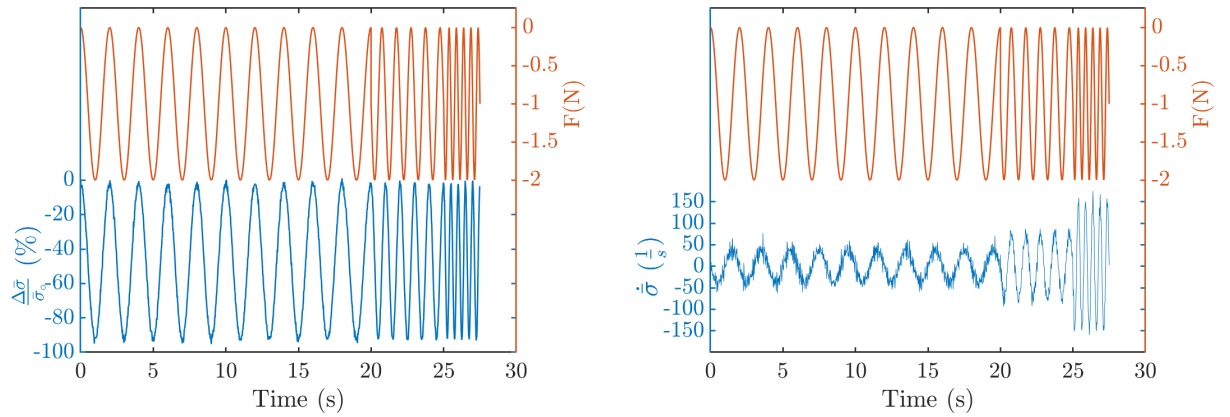
schema, a nonlinear rate-dependent learning-based (SVR) calibration was used. The general form of the calibration was:

$$F_{sensor} = f\left(\frac{\Delta\bar{\sigma}}{\bar{\sigma}_o}, \dot{\bar{\sigma}}\right), \quad (92)$$

where, F_{sensor} , is the estimated force by the sensor, f , represents the SVR calibration law, and $\frac{\Delta\bar{\sigma}}{\bar{\sigma}_o}$ and $\dot{\bar{\sigma}}$ are the relative change, and rate of change of the intensity in the images, respectively.

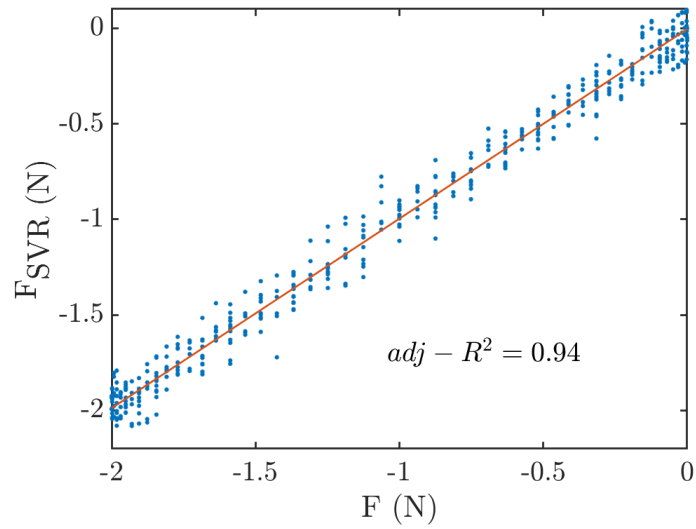
The SVR calibration model was trained with the training dataset obtained from the universal testing machine. The dataset was divided into training and verification with a ratio of 70:30 percent. The SVR training was performed in Matlab Machine Learning Toolbox (R2019b, Mathworks Inc., MA, USA). Figure 6.5(a) to 6.5(b) depicts the training data for the SVR calibration and figure 6.5(c) shows the linearity of the SVR-estimated forces with respect to the force recorded by the UTM machine (ground truth).

During the sinusoidal compression tests, the average greyscale value of the image taken by the camera decreased from 28 to 2 greyscale units for 0 to 2 N compressive force (Figure 6.4). The



(a)

(b)



(c)

Figure 6.5: Training data for the SVR calibration: (a) percentage of the change in the intensity of the laser spot, (b) temporal rate of change in the intensity, (c) comparison of the SVR-estimated force with respect to the reference force, F , recorded by UTM.

SVR-estimated forces showed an adjusted- $R^2 = 0.94$ with the ground truth with a root-mean-square (RMS-) error of 0.09 N (Figure 6.5(c)).

6.3 *Ex-vivo* Validation

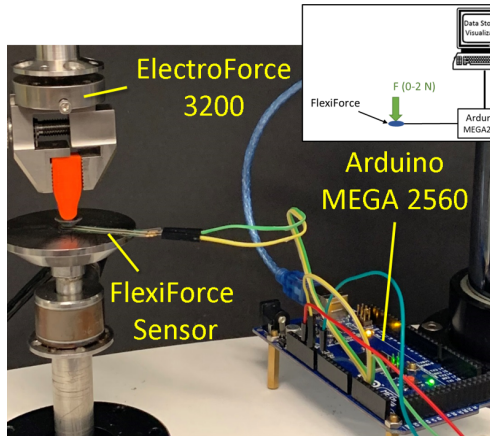
In order to further assess the performance of the proposed sensor in real surgical procedures, an *ex-vivo* test on freshly excised bovine muscle was performed. To provide a reference for the contact force between the jaws of the sensor and tissue, a FlexiForce (TekScan, MA, USA) was attached to the upper jaw of the grasper.

The FlexiForce was interfaced with an Arduino MEGA2560 with a sampling frequency of 50Hz and was calibrated using the universal testing machine (ElectroForce[®] 3200). Figure 6.6(a) shows the FlexiForce sensor and its data-acquisition system during the calibration test. Moreover, Figure 6.6(b) depicts the calibration curve of the FlexiForce sensor.

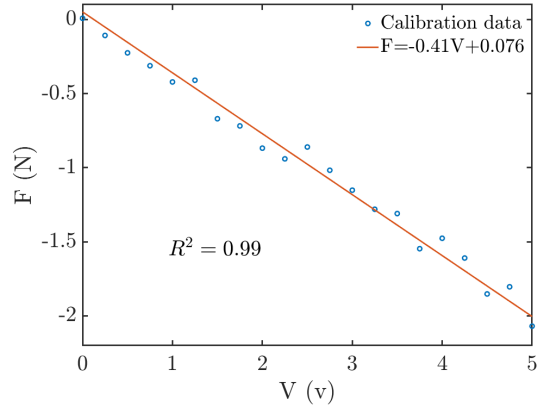
The tissue was manually squeezed using the sensor-embedded grasper, while the reference force was acquired. Meanwhile, the force was estimated by applying the SVR calibration to the light intensity, calculated by the image processing software. To assess the performance of the proposed image-based force estimation technique, the range, accuracy, and resolution of the sensor were characterized through measuring the minimum and maximum measured force, mean-absolute-error (MAE), and minimum detectable force of the sensor. Figure 6.6(c) shows the experimental setup for *ex-vivo* validation.

As depicted in Figure 6.6(d), the image-based force estimations showed a fair agreement with the ground truth. In the *ex-vivo* validation test, the minimum detectable force of the sensor was 0.14 N and the mean-absolute-error was 0.11 N. It is noteworthy that the SVR estimations showed no jitter and remained in fair synchrony with the FlexiForce readings. Figure 6.6(e) shows the schematic system configuration. Table 6.1 summarizes the performance metrics of the proposed force sensing system for the *ex-vivo* test.

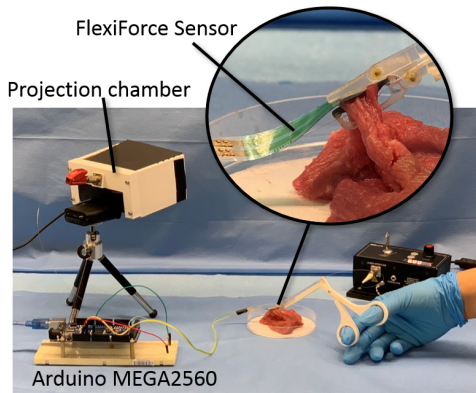
The frame-rate of the utilized camera was 30 Hz. Therefore, there was a delay of approximately 33 ms between two consecutive frames. On the other hand, the computational time of greyscale calculation and SVR force estimation was 8.4 ± 0.9 ms. Therefore, the proposed force estimation



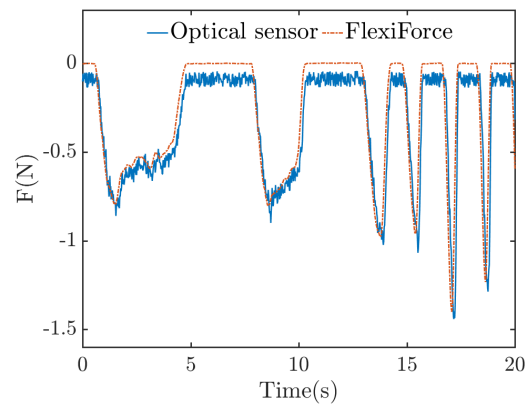
(a)



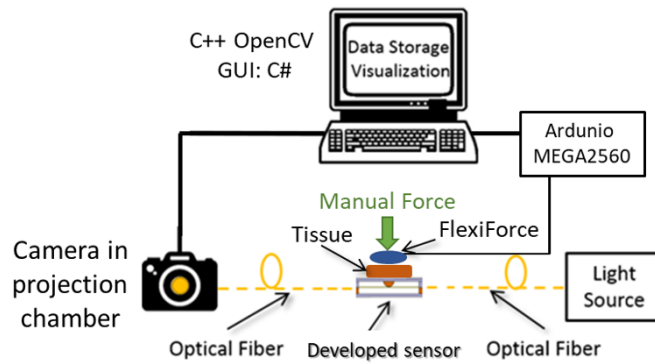
(b)



(c)



(d)



(e)

Figure 6.6: (a) FlexiForce sensor under calibration test, (b) force-voltage curve of FlexiForce sensor, (c) experimental setup for the *ex-vivo* validation test, (d) comparison of the force measured by the optical sensor versus the force measured by the calibrated FlexiForce sensor, (e) schematic system configuration.

Table 6.1: Performance metrics for the proposed image-based force sensing technique for the *ex-vivo* test in comparison with the literature.

| Study | Application | Range Min–Max (N) | Accuracy MAE (N) | Resolution (N) | Min. detectable Force (N) |
|------------|-------------|----------------------|---------------------|-------------------|------------------------------|
| [116] | MIS | 0–0.5 | 0.03 | 0.01 | 0 |
| [118] | MIS | 0–2 | 0.10 | 0.08 | 0 |
| [121] | Palpation | 0–5 | 0.40 | 0.093 | 0 |
| [13] | MIS | 0–2 | ≤ 0.10 | ≤ 0.05 | ≤ 0.2 |
| This study | MIS | 0.14–2 | 0.11 | 0.02 | 0.14 |

schema was capable of refreshing at a rate of up to 100 Hz, should the camera be replaced with a higher frequency camera. In the current configuration, the maximum refresh-rate of the force estimation was limited to the frame-rate of the camera, i.e., 30 Hz.

6.4 Conclusion

The objective of this study was to assess the performance of a proposed image-based light intensity modulation optical sensor for MIS applications. As indicated in [13], force sensors for MIS applications must show a minimum detectable force of 0.2 N, an average error of less than 0.1 N, and a resolution of 0.05 N. Therefore, considering the minimum detectable force of the proposed sensor, i.e., 0.14 N, MAE of 0.11 N, and resolution of 0.02 N, the author concludes that the proposed image-based sensing system, along with the employed learning-based calibration was applicable in MIS.

Furthermore, the utilization of the proposed image-based technique would further facilitate the employment of multiple optical fibers for array sensor designs, e.g., [30]. Moreover, the proposed system has favorably eliminated the need for electrical photodetectors. Although the LIM-based techniques, such as the proposed method, are theoretically insensitive to thermal fluctuations, the utilization of 37°C CO₂ or normal saline fluid during the MIS operations reduces the risk of thermal fluctuation during the operation of the proposed sensor. Therefore and in conjunction with the author’s experimental observations in thermally uncontrolled environment, the proposed sensor is

insensitive to ambient thermal fluctuations.

For future studies, it is recommended that the fiber be used in a retro-reflecting design, so that the transmitted light could be reflected back to the same fiber for ease of implementation. Such a retro-reflecting design would need the use of a mirror at the end of the fiber inside the sensor and an optical circulator to split the emitted and reflected light in the system. Furthermore, this study could be expanded to perform the *ex-vivo* experiments in an aqueous environment to study the effects of electrolytic interferences. Also, the robustness of the proposed sensor against the electromagnetic interference could be studied. Another improvement of this study would be to use metal 3D printing technique, especially with Titanium alloys, e.g., Ti ELI alloy, to prototype the body of the grasper. The use of such biocompatible materials would make the grasper sterilizable and disinfectible for real surgical application.

Furthermore, to improve the resolution of the proposed image-based force sensing, the color-depth and resolution of the image acquired by the camera can be increased. Whereas, for example, by increasing the color-depth to 16-bit the current greyscale resolution of $1/256$ will increase to $1/65536$. Similarly, increasing the resolution of the image from 640×480 to higher image resolutions will increase the number of pixels used in measuring the average greyscale values and finer changes in the greyscale values can be detected. However, both these improvement will increase the computational cost of the image processing and may adversely affect the real-time performance.

Chapter 7

Optical Fiber Array Sensor for Force Estimation and Localization in TAVI Procedure: Design, Modeling, Analysis and Validation

Transcatheter aortic valve implantation has shown superior clinical outcomes compared to open aortic valve replacement surgery. The loss of natural sense of touch, inherited from its minimally invasive nature, could lead to misplacement of the valve in the aortic annulus. In this study, a cylindrical optical fiber sensor is proposed to be integrated with valve delivery catheters. The proposed sensor works based on intensity modulation principle and is capable of measuring and localizing lateral force. The proposed sensor was constituted of an array of optical fibers embedded on a rigid substrate and covered by a flexible shell. The optical fibers were modeled as Euler-Bernoulli beams with both-end fixed boundary conditions. To study the sensing principle, a parametric finite element model of the sensor with lateral point loads was developed and the deflection of the optical fibers, as the determinant of light intensity modulation was analyzed. Moreover, the sensor was fabricated, and a set of experiments were performed to study the performance of the sensor in lateral force measurement and localization. The results showed that the transmitted light intensity decreased up

to 24% for an external force of 1 N. Also, the results showed the same trend between the simulation predictions and experimental results. The proposed sensor was sensitive to the magnitude and position of the external force which shows its capability for lateral force measurement and localization.

7.1 Introduction

Transcatheter procedures are among the most expanded areas in Minimally Invasive Surgeries (MIS). During such procedures, catheter-based techniques (CBT) are used to perform surgery or intervention on the heart and vasculature. A catheter is a thin flexible tube that is inserted into the patient's blood vessels and advanced towards an intraluminal anatomic site, e.g., coronary arteries, via small incisions on the femoral or radial artery or veins. Such procedures are performed for both diagnosis and treatment purposes [1]. Simultaneously, surgeons use x-ray fluoroscopy for real-time imaging and navigation of the catheter and surgical instruments. CBT procedures may also be performed under magnetic resonance (MR) imaging for navigation purposes [116], especially in neurovascular surgery. CBT is more favorable clinically in comparison with conventional open surgery. It has a shorter time of surgery, less anesthesia agent usage, and surgical trauma. In addition, blood loss, pain, tissue scar, hospitalization and recovery time is effectively reduced with CBT [7]. During the last decade, the CBT approach was adopted for cardiac valve replacement. Heart valve anomalies, e.g., aortic stenosis (AS), are among the most prevalent cardiac diseases in the senior population. Conventionally, AS has been treated through open-heart aortic valve replacement (AVR). Open AVR is associated with a mortality rate of up to 7% [87]. As an alternative, transcatheter aortic valve implantation (TAVI) has gained adoption as an MIS alternative to the AVR, especially for the elderly or patients with co-morbidity who may not tolerate long anesthesia time. TAVI technology has shown superior clinical outcomes compared to open AVR. However, it has limitations in terms of accurate placement of the valve within the heart. Constrained maneuverability of the valve during deployment, 2D projection and poor soft tissue contrast in X-ray fluoroscopy images, and lack of tactile feedback pollute the surgeon's perception of the position and the orientation of the valve which, often leads to misplacement of the valve. Inaccurate deployment of the artificial aortic valve could lead to regurgitation, stroke, insufficient coronary perfusion, cardiac

blockage and death [234]. The commercially available TAVI solutions, e.g., CoreValve (Medtronic Corp., Dublin, Ireland), and Sapien (Edwards Lifescience Corp., Irvine, CA), typically have 16-18 Fr diameter (1 Fr = $\frac{1}{3}$ mm and is pronounced as 'French'). However, there is no tactile sensor to assist surgeon for localization of the aortic annulus to deploy the prosthetic valve.

More specifically for TAVI and despite its advantages over AVR, its main technical limitation is the loss of natural tactile sensing. Loss of tactile feedback is shown to adversely affect the ability of surgeons in estimation of tool-tissue interaction force or tissue distinction [13, 14]. Consequently, surgeons are less situationally aware of the surgical site during TAVI procedures, which may result in risky surgical maneuvers and irreversible or catastrophic trauma to the patient. To provide tactile feedback during CBT procedures, researchers have investigated different tactile sensors to be mounted on CBT instruments and compensate for the lost tactile feedback [27, 235, 236]. Such tactile sensor shall be small enough to fit at the tip of these catheters, typically of 2–6 mm in diameter. In addition, these sensors shall be biocompatible, electrically-passive and MRI-compatible to be safe in the operation room and inside the patient's body [87, 237]. Also, these sensors shall work in both static and dynamic loading conditions while showing low hysteresis and non-linearity [85]. The output of such tactile sensors can be relayed to surgeons via visual feedback [163, 185, 186] or through tactile displays [164, 165]. The choice of the sensing principle for tactile sensors highly depends on the requirements of the surgical application. While the mentioned requirements are common, a complete set of functional and physical requirements for such tactile sensors is application dependent and some requirements may slightly vary among various surgical procedures [205]. The author have reported an exhaustive list of functional and physical requirements of tactile sensors for different MIS procedures in [27].

Among various sensing principles, e.g., electrical sensing and optical sensing, optical-based sensing principles exhibit the most compatibility with the MIS requirement [27]. Optical-based tactile sensors, mainly based on wavelength modulation, phase modulation, and light intensity modulation (LIM) [27]. The main component used in such tactile sensors structure is an optical fiber.

In recent years, various optical-fiber-sensors have been proposed to measure force, displacement, pressure, stiffness, and temperature to compensate for the loss of tactile feedback in MIS [27]. For example, Polygerinos *et al.* [238] proposed a LIM-based force sensor for cardiac catheters.

This sensor was suitable for cardiac catheterization to detect the catheter tip interaction force with the cardiac wall. The sensor had 3 mm diameter and could measure contact force in the range of 0-0.85 N. In another study, Polygerinos *et al.* [116] proposed a triaxial catheter-tip force sensor for the MRI-guided cardiac ablation procedure. They utilized a flexible structure with an integrated reflective surface was placed in front of the optical fibers. Applying the force on the catheter tip the distance and orientation of the reflector was changed and modulated the light intensity. The sensor showed high sensitivity and working range of 0.5 N along all three orthogonal axes. Also, Noh *et al.* [89] designed and proposed a small three-axis force sensor to measure the contact force during the cardiac ablation procedure. They coupled an optical fiber with a CCD camera and utilized an image processing technique to correlate the reflective intensity with external force on their sensor. However, their proposed multiple linear regression calibration had a noticeable error in comparison with the reference forces.

In another effort, Li *et al.* [239] proposed a novel 3D catheter distal force sensor for cardiac ablation using the wavelength modulation principle. They used fiber Bragg grating (FBG) in a force-sensitive flexure. They modeled 3-axis force components and temperature using the decoupling principle. A 3D printing technique with nonmagnetic material made sensor capable of working in both x-ray and MIR-guided cardiac ablation procedure. The sensor performance analysis showed linearity, repeatability, and hysteresis errors of less than 5%. Recently, Li *et al.* [240] developed a tri-axial FBG-based force sensor for enhanced force measurement in cardiac ablation procedures. The structure of their sensor was 3D printed with a force-sensitive fixture and consisted of five FBGs. Upon application of external force on the catheter tip, the strain-induced wavelength shift of FBGs was captured to calculate three components of the force. Also, to compensate for the thermal effect, they tested the sensor within a range of 25-50 °, with 5 ° intervals and showed below 6.5% temperature-induced error. The range of measured force was -0.8 to 0.8 N in the transversal plane of the catheter and 0-0.8 in its longitudinal direction with an average error of 23.28 mN (2.91%). *Ex-vivo* validation tests showed the performance and robustness of their sensor for detecting the tip contact force.

Our literature review on the sensorized catheters [27] showed that most of the tactile sensors proposed in the literature are intended for cardiac ablation procedures and are merely capable of

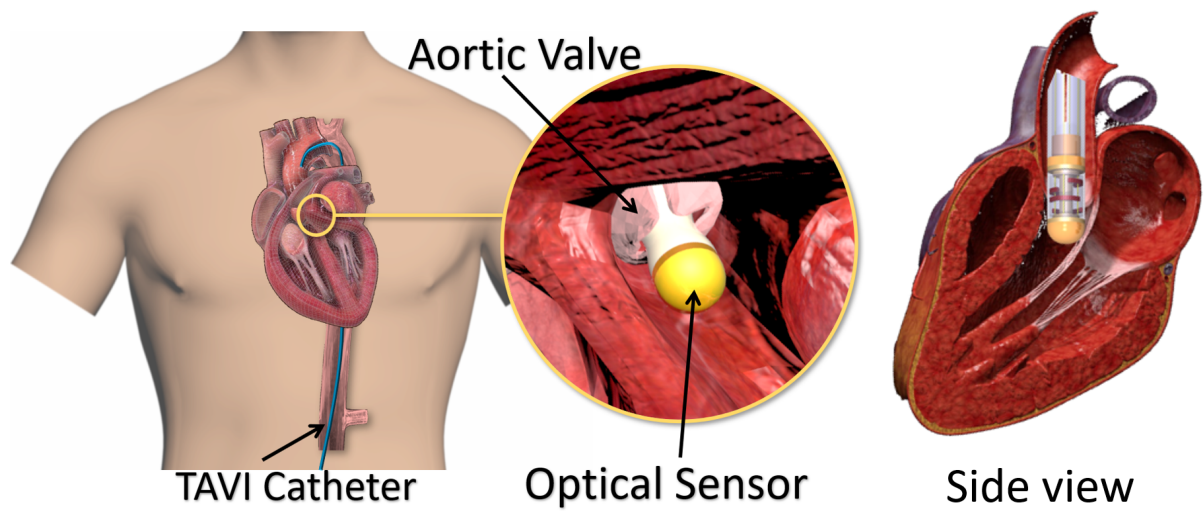


Figure 7.1: A schematic use-case of the proposed sensor for aortic valve localization (the figure is not to the scale)

measuring tip forces. Nevertheless, in cardiovascular CBT procedures, especially during TAVI, both the tip and side of the distal portion of the catheter are in contact with cardiac tissue. Moreover, to localize the aortic annulus, the sensor shall be able to measure the lateral contact forces. The reason is that, as shown in Figure 7.1, the leaflets of the aortic valve (connected to the aortic annulus) will press on the body of the sensor from the lateral direction. Given that during the pulsation, the leaflets open and close, a dynamic lateral contact force would generate between the sensor and the leaflets. Therefore, the sensor must be capable of measuring the lateral forces and localizing the forces to localize the leaflets (and annulus).

The motivation of this study was to propose an optical fiber-based sensor capable of measuring and localizing the lateral contact forces for integration with typical 18Fr TAVI catheter, also known as a delivery catheter. Thus, in this study, a conceptual optical fiber sensor based on the bending-based intensity modulation was proposed, simulated, and verified. The preliminary study of the conceptual design of the proposed sensor was first presented in [30]. The novelty of this work was in the ability of the sensor to measure the lateral contact forces between the valve leaflets connected to the annulus and the sensor surrounding area. This made the sensor capable of being used in TAVI procedures to locate the position of the annulus with respect to the sensor geometry.

Also, an optomechanical model was developed based on the optical fiber bending loss and deflection of the optical fiber as an Euler-Bernoulli beam. The simulation was performed using finite element analysis, which predicted the sensor behavior with various forces applied longitudinally and circumferentially. The results of the simulation were verified in an experimental study aiming at showing the feasibility of the proposed sensor. In the following, Section 7.2 describes the sensor design requirements and the proposed structural design specifications. Optomechanical modeling, sensing principle and simulation are described in Section 7.3. Section 7.4 summarizes the sensor fabrication, test setup, and validation protocol followed by result and discussion in Section 7.5. Finally, the concluding remarks are provided in Section 7.6.

7.2 Design Requirements and Structural Design

As the sensor was intended for TAVI applications for annulus localization, it should have the ability to measure the bending-based light intensity modulation in the optical fibers caused by lateral contact forces between the sensor and aortic valve leaflets. Also, the sensor had to be able to find the relative position of the annulus with respect to the sensor through localizing the contact forces. Moreover, the sensor should be capable of working under both dynamic and static conditions. In addition, the sensor should be small enough to be integrable at the tip of TAVI catheter and to move through vasculatures. Finally, the sensor needed to be biocompatible, electrically-passive and MRI-compatible. Figure 7.2(a) depicts the proposed sensor. To accommodate the size constraint, the outer diameter of the sensor was considered to be 6 mm. The sensor was cylindrical and was covered with a flexible shell on the outer circumference. The shell had four internal indenters to transfer external force from the shell to the optical fibers. The indenters were distributed at 20% increments along the length of the shell and were consecutively separated by 90° in the circumferential direction. Each indenter was of semi-circular shape with a radius of 0.5 mm and circumferential span of 120° . The flexible shell was mounted on a rigid substrate which, provided a base for the mounting of optical fibers. Four optical fibers were passed through the proximal end of the substrate and finished at its distal end. The distal end of the substrate could be internally coated by gold or silver, e.g., through the sputtering technique, to reflect the light back into each fiber for a retro-reflection

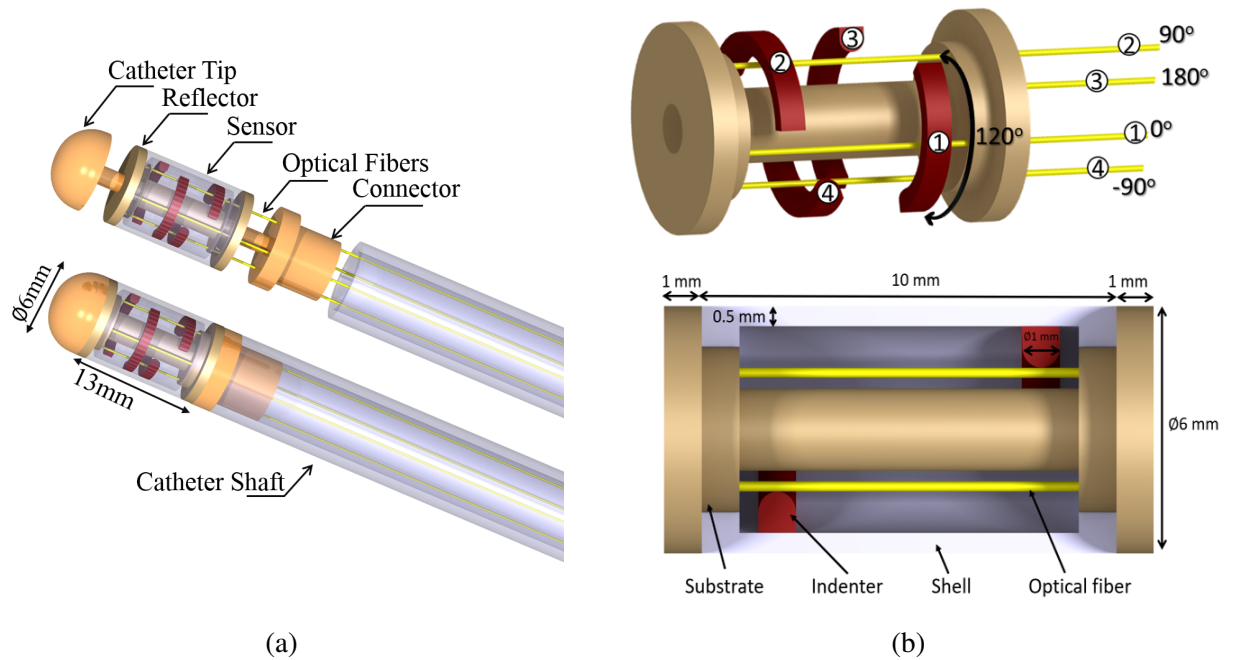


Figure 7.2: (a) Conceptual integration of the proposed sensor on a TAVI catheter, (b) cross-sectional view of the proposed sensor with the view of the flexible shell, indenters, substrate, and the optical fibers.

configuration. The cross-sectional view of the proposed sensor is shown in Figure 7.2(b).

With this design, upon application of a point (or distributed) contact force on the outer shell, contact forces were transmitted at different proportions to the optical fibers and consequently caused light intensity modulation in each fiber. With the proposed design, each optical fiber acted as an Euler-Bernoulli beam with circular cross-section fixed at both ends. The details of the geometric dimension are provided in Table 7.1.

7.3 Sensor Modeling

In this section, the details of the sensing principle formulation and finite element simulation of the proposed sensor are provided.

Table 7.1: Geometric dimensions and mechanical properties of the sensor used in the finite element study.

| | Dimensions | Value | Mechanical properties | Value |
|-----------------|----------------|----------|------------------------------|-----------------|
| Flexible shell | Outer diameter | 6 mm | Hyperelastic | $C_{01}=-24.49$ |
| | Length | 10 mm | Two-terms Mooney-Rivlin [21] | $C_{10}=25.82$ |
| | Thickness | 0.5 mm | | |
| Rigid Substrate | Tip diameter | 6 mm | Elastic modulus | 0.5 GPa |
| | Shaft diameter | 2 mm | Poisson's ratio | 0.43 |
| Optical fiber | Outer diameter | 0.250 mm | Elastic modulus | 16.5 GPa |
| | Free length | 8 mm | Poisson's ratio | 0.2 |

7.3.1 Sensing Principle

The use-case of the proposed sensor is in TAVI procedures. When the sensor is placed through the aortic valve (Figure 7.2(b)), the aortic leaflets open in the systolic phase and close in the diastolic phase of the heart cycle, thus, apply pulsatile contact forces perpendicular to the flexible shell. The pulsatile forces are transferred to the optical fibers and cause bending of the fibers. The relatively long-hanging span of the optical fibers and their relatively small flexural rigidity (EI) makes them quite sensitive to small contact forces from the indenters.

According to Gauthier *et al.* [80], Eqs. 93 and 94 express the relationship between the bending-based power-loss in an optical fiber with a constant radius of curvature is:

$$P(s) = P_0 e^{-\gamma s}, \quad (93)$$

$$s = r_b \theta, \quad (94)$$

where P_0 is the input power to the fiber, γ is an intrinsic optical constant of the fiber, r_b is the radius of circular indenters, s is the arc-length parameter along the fiber, θ is the central bending angle, and $P(s)$ is the output power from the fiber. Figure 7.3(a) shows the schematic of the constant bending radius principle. As the equations indicate, the output power (and intensity) from a bent optical

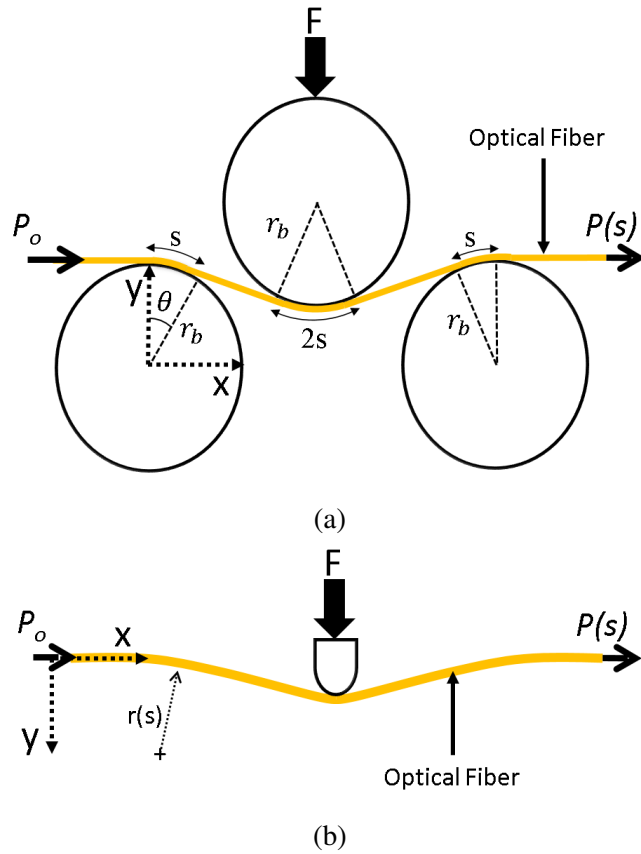


Figure 7.3: (a) Schematic of the constant bending radius principle, (b) schematic of the variable bending radius principle.

fiber, with a constant bending radius, depends on the total arc-length, optical properties of the fiber, and the bending angle.

In case an optical fiber is bent as an Euler-Bernoulli beam, the radius of curvature is not constant and varies with arc-length s . To accommodate that, the optical fiber was discretized into infinitesimally small elements which, are assumed to be of constant bending radius. Using a differential form of Eq. 93, and integration along s the total bending-based power-loss can be obtained. The author has previously reported the derivation of this principle, variable bending radius (VBR), verification and validation in [20, 21, 28]. Figure 7.3(b) illustrates the variable bending radius principle.

(Details of this derivation are provided in Section 5.2.2.

To perform the integration, the existence of an analytical description of r and θ , as functions of s is necessary. To obtain $r(s)$ and $\theta(s)$, the infinitesimal-strain form of Euler-Bernoulli theory was used. Each fiber was modeled as a finite-strain Euler-Bernoulli beam, depicted in Figure 7.4.

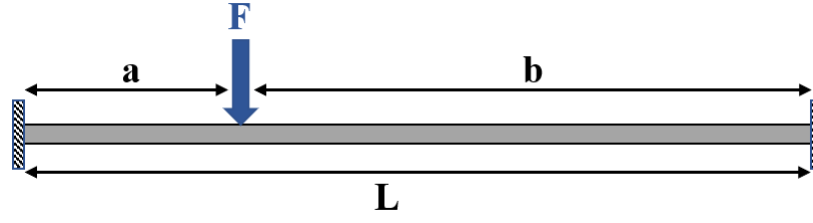


Figure 7.4: Simplified mechanical model of optical fibers in the proposed sensor with force F applied on it from the corresponding indenter.

Equation 95 is the governing equation of the Euler-Bernoulli beam subjected with an internal moment of $M(s)$ due to a lateral force F at a distance a from the left support. $M(s)$ for such a configuration is:

$$M(s) = \frac{EI}{r(s)} = \begin{cases} -\frac{ab^2}{L^2}F + P_1s & 0 < s \leq a \\ -P_1(s-a) - \frac{ab^2}{L^2}F + P_1s & a < s \leq L \end{cases}, \quad (95)$$

$$P_1 = \frac{b^2}{L^3}(3a+b)F, \quad (96)$$

$$r(s) = \frac{(1+y'^2)^{3/2}}{y''} \Rightarrow \text{with } y' \ll 1 \quad r(s) \approx \frac{1}{y''} \quad (97)$$

where $(\cdot)' = \frac{d}{ds}$ is a derivative operator, P_1 is the reaction force at the left support, and y is the deflection of the beam. As provided in Chapter 5.2.2, the substitution of Eqs. 95-97 in the differential form of Eqs. 93-94 and integrating over the length of optical fiber provides an analytical relationship relating the external force F to the output power P .

7.3.2 Finite Element Simulation

To calculate the deflection of the shell and fibers with respect to the applied force, a three-dimensional finite element model of the sensor was developed in ANSYS Workbench v.16 (Ansys Inc., PA, US). Geometrical dimensions and material properties of the sensor's structural components were assumed, as provided in Table 7.1. Since the 3D printed materials were used for sensor fabrication, the material properties of the components were characterized using method described in Section

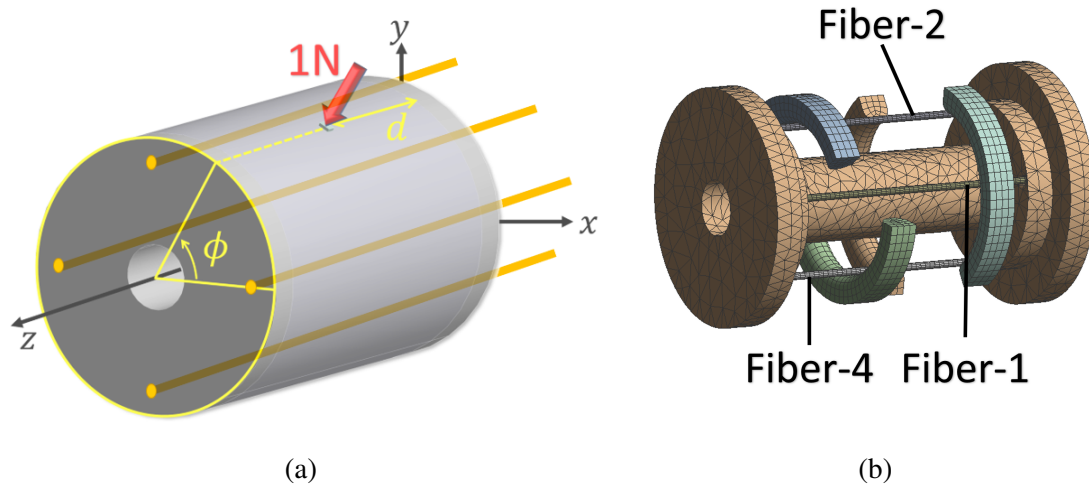


Figure 7.5: (a) Configuration of the external force on the flexible shell, (b) internal view of the meshed model used in the simulation.

5.3.3.

The contact between each fiber and its corresponding indenter was assumed as frictionless for the sake of simplicity. The embedded ends of each fiber into the substrate (1 mm at each end) were fixed (no rotation, and no displacement). Also, both end surfaces of the substrate were fixed. An external static force of 1 N magnitude was applied on the flexible shell. To facilitate the numerical stability and to avoid stress singularity (to the machine precision) the external force was applied on a rigid block (0.1x0.1 mm) attached to the external surface of the flexible shell. A total of 72 simulations were performed for various combinations of longitudinal (4 d -s) and circumferential position (18 ϕ -s) of the external force (and rigid block). Figure 7.5 shows the parametrized model and the meshed model with indenters. Table 7.2 shows the simulated geometric parameters and their values. The geometric model was meshed with quadratic brick and tetrahedron elements ($n \approx 27,000$). The solutions were performed using the static solver with large deformation effect enabled.

Table 7.2: Simulated geometric parameters and values used in finite element simulation.

| Parameter | Values |
|-----------|--|
| d | $(2 \ 4 \ 6 \ 8) \text{ mm}$ |
| ϕ | from -180° to 180° with 20° step-size |

Table 7.3: Maximum deflection of optical fibers when force is applied exactly on top of their corresponding indenters.

| Fiber no. | 1 | 2 | 3 | 4 |
|-------------------------|--------|--------|-------|-------|
| Maximum deflection (mm) | 0.0788 | 0.0788 | 0.136 | 0.136 |

The finite element model was solved for all possible combinations of parameters, i.e., (d, ϕ) -s. Figure 7.6 depicts the distribution of Von-Mises strain within the indenters, fibers, and membrane for a representative configuration when the external force was applied exactly on top of indenter-2. The maximum Von-Mises strain of the shell in the depicted simulation was approximately 0.06 which is beyond the finite strain limit of 0.002, thus confirms the assumption of finite strain.

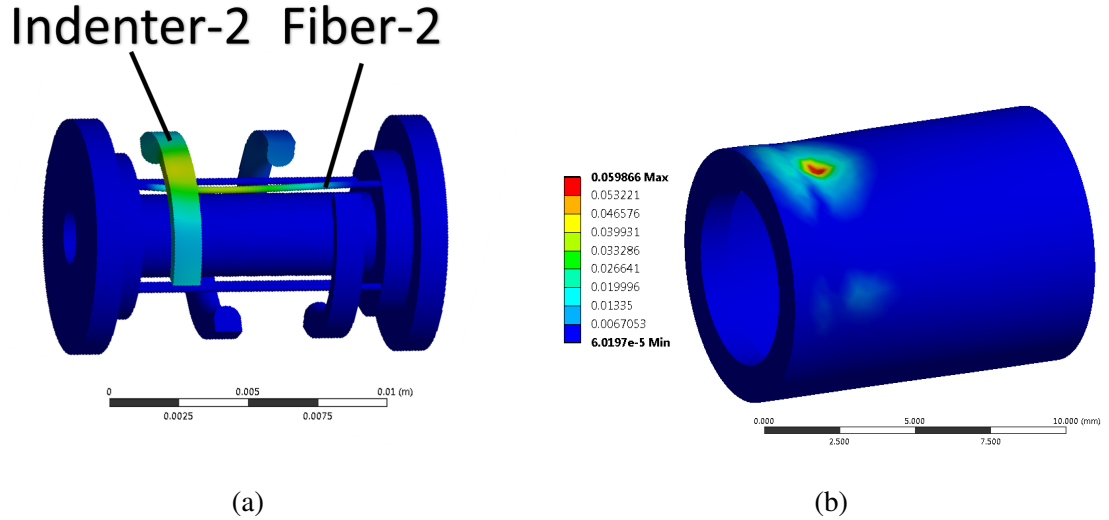


Figure 7.6: Distribution of Von-Mises strain for load-case $(d = 8, \phi = 90)$ in: (a) fiber-2 and indenter-2, and (b) the flexible shell.

Table 7.3 shows the maximum deflection of fibers in simulations. In all cases, the maximum deflection in each fiber was observed when the force was applied exactly on top of its corresponding indenter. The maximum deflection was observed in Fiber-3 and Fiber-4 with a value of 0.136 mm. The deflection to the free-length ratio for Fiber-3 and 4 at this deflection was $\frac{0.136}{8} = 0.017$. Since this ratio is less than 0.05, the typical linear limit threshold for Euler-Bernoulli beam [241], using the approximate definition of radius of curvature (Eq. 97) in the sensing principle formulation was justified.

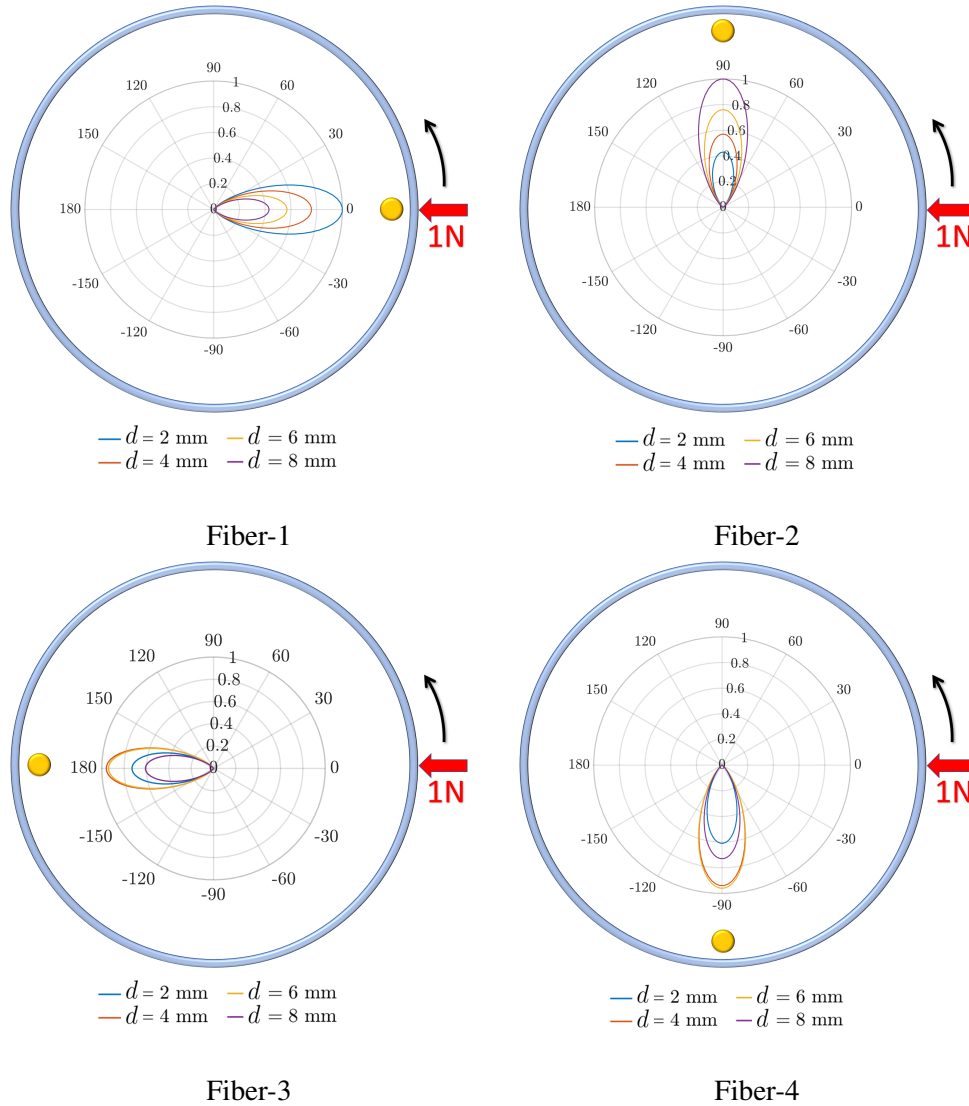


Figure 7.7: Normalized variation of the maximum deflection in each optical fiber with respect to the change in the longitudinal and circumferential positions of external force.

Another result of the simulations was the variation of the maximum deflection of the optical fibers with respect to the circumferential location of the external force. The maximum deflection of the optical fiber was used as an indicator of the intensity loss in each fiber. Figure 7.7 depicts the polar diagram of the normalized maximum deflection of each fiber. This figure shows the maximum deflection of each fiber with respect to the circumferential position of external force and for four different longitudinal positions of the external force. The results showed that each fiber underwent its maximum deflection while the external force was applied on top of its corresponding indenter. Also, in positions where the force was out of the circumferential span of each indenter, its contacting fiber was almost shielded from external force by the membrane. However, the 120° indenter span would provide a 30° overlap between two consecutive indenters which would help in transferring force to two optical fibers when the external force is applied at a ϕ between two fibers.

7.4 Validation Study

In order to validate the proposed sensor concept, a series of experiments were performed. To this end, initially, a prototype of the sensor was fabricated. After that, components of the sensor and optical fibers were assembled. The image-based intensity DAQ system which had been developed and validated earlier in chapter 6 was utilized in this study.

7.4.1 Sensor Fabrication

The components of the sensor were fabricated with 3D printing technology using a Form2 3D printer (Formlabs Inc., MA, USA). Formlabs clear resin was used to fabricate the sensor substrate. Also, for the flexible shell, Formlabs flexible resin was used. The indenters were printed at the bottom surface of the shell. This technique resulted in high spatial accuracy for indenter placement on the shell and eliminated the need for separate attachment and gluing. Figure 7.8 illustrates the sensor components and its assembled structure. The substrate facilitated passing four optical fibers with 90° angular separations, while each fiber was in contact with its corresponding indenter. However, since this study was a feasibility study and to reduce the complexity of data-acquisition, only a single fiber (Fiber-1) was assembled with the prototyped sensor.

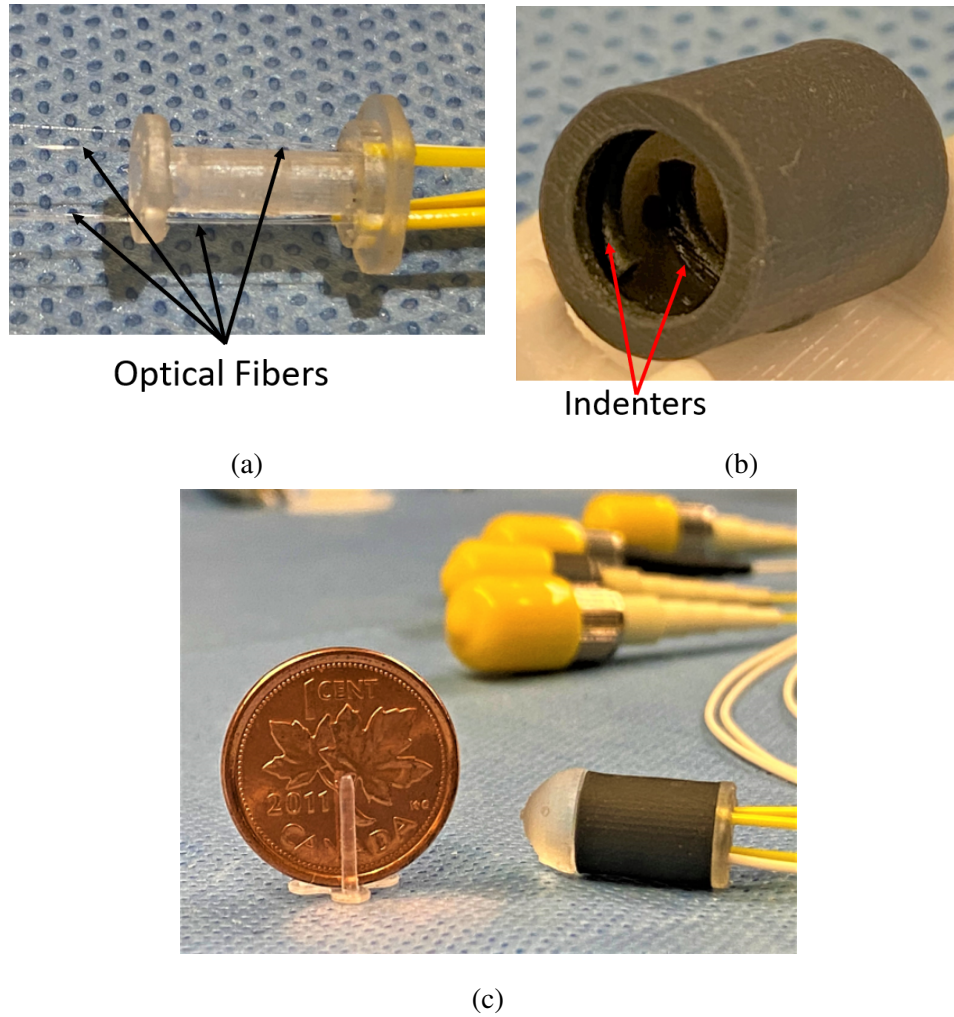


Figure 7.8: (a) 3D printed rigid substrate and four inserted optical fibers, (b) 3D printed shell and indenters on its bottom surface using Formlabs flexible resin, (c) assembled structure of the cylindrical sensor in comparison with a coin, the cap is attached to show final shape of the sensor with reflected surface suitable for TAVI procedure.

7.4.2 Experimental Setup and Validation Test

Figure 7.9(a) shows the experimental setup used for the sensor validation study. A laser source (OZ OPTIC, ON, CANADA) supplied an 635 nm laser beam at a power of 5 mW to a single mode 250 μm diameter optical fiber (S405-XP, Thorlabs, NJ). Since the sensor had a symmetric design and fibers were fixed in similar configurations, only one optical fiber was inserted to the fabricated sensor. As illustrated in Figure 7.9(a), the optical fiber was connected to an FC-PC connector attached to the projection chamber of the Camera, Logitech C920 (Logitech Inc., CA, USA)). Using the camera and image-based DAQ system would allow for using all the four fibers in future (with proper light isolation between the projected beams into the chamber).

The utilized image-based acquisition system and intensity measurement algorithms have previously been introduced in Chapter 6. For applying an external force, a universal testing machine (UTM) (ElectroForce[®] 3200, TA Instruments, DE, USA) was used. The sensor was located on a custom-designed holder which was adhered on the lower jaw of the UTM. A long thin indenter was installed on the upper and vertically movable fixture of the UTM to apply force on the sensor. For comparison, 1 N force was applied at a similar location as were considered in the finite element simulation. Meanwhile, the force was recorded through the UTM's interface software and light intensity (passed through Fiber-1) was captured with the developed light-intensity acquisition system. More specifically, the external force was a compressive sinusoidal force with a range of 0-1 N and frequencies of 0.5, 1.0, and 1.5 Hz. Such frequencies correspond to the heart's beat-per-minute (BPM) of 30, 60, and 90. The external force was applied on the sensor at longitudinal locations $d = (2, 4, 6, 8 \text{ mm})$ and at circumferential angles of $\phi = (-60^\circ, -40^\circ, -20^\circ, 0^\circ, 20^\circ, 40^\circ, 60^\circ)$ for each d .

Since only one optical fiber, i.e., Fiber-1, was studied in the experiments, the tests were done on circumferential span and length associated with indenter-1. Four representative images of the sensor under the test are provided in Figure 7.9(b). Also, Figure 7.9(c) shows the GUI of the image-based intensity acquisition graphical user interface developed in C# language.

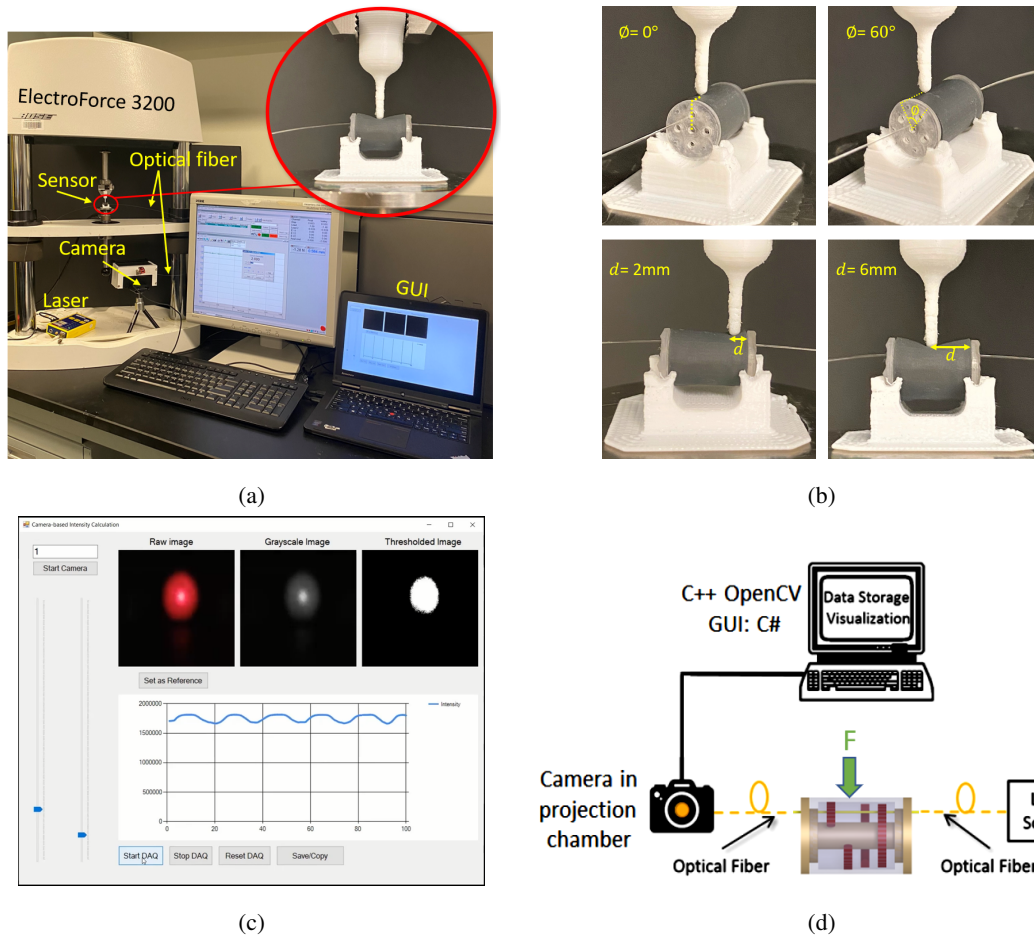


Figure 7.9: (a) Experimental setup, image-based DAQ, and fabricated sensor under the test, (b) the prototype sensor under various load-cases in the experimental study, (c) a representative view of the developed GUI software to record the intensity change in realtime, (d) schematic system configuration.

7.5 Results and Discussion

In the experiments a concentrated force, equal to the force used in simulation, was applied at different longitudinal and circumferential points on the flexible shell to investigate the light intensity modulation in Fiber-1. Figure 7.10(a) representatively shows variation of the light intensity measured by the sensor to the variation of the external force at various frequencies, i.e. 0.5, 1, 1.5 Hz, located at (2mm, 0°). The results showed that the light intensity for this load case decreased by 24% synchronously with the external force. Similar range of intensity loss have been observed in the validation tests on our previous VBR-based sensor reported in [21, 26].

The theoretical model of the sensor as well as the validation study performed in chapter 6 confirmed that the intensity in the optical fiber is monotonically decreasing with increasing the maximum deflection of the optical fiber. The same trend was observed in the experimental results in the current study. For comparing the trends, the variation of the normalized values of the maximum intensity loss in Fiber-1 in response to 1 N force was compared with its maximum deflection under the same force. The intensity losses were normalized with respect to the maximum observed intensity loss (from the experiment) and the deflection data were normalized with respect to the maximum deflection of Fiber-1 (from simulation). Figure 7.10(b) shows the comparison of the observed normalized intensity loss and maximum deflection of Fiber-1.

Also, to show the effect of changing the circumferential position of the external force on the intensity loss and comparison with the simulation, Figure 7.10(c) shows the polar diagram of the results of experiments and simulation.

The experimentally observed trends of changes in the intensity loss were in fair agreement with the simulations. Also, the results showed that both the circumferential and longitudinal positions of the external force affect the intensity loss. Furthermore, similar to the simulation results, the maximum intensity loss was observed by force located on top of the corresponding indenter of the Fiber-1. Figure 7.7(a) and Figure 7.10(c) showed a fair agreement between the observed trends in simulation and experiments. More specifically, Table 7.4 summarizes the observed variations in the intensity loss for 1 N force at various locations on the shell. Given the fact that the aortic annulus is of circular shape (or oval shape in pathologic conditions) the leaflets of the annulus will completely

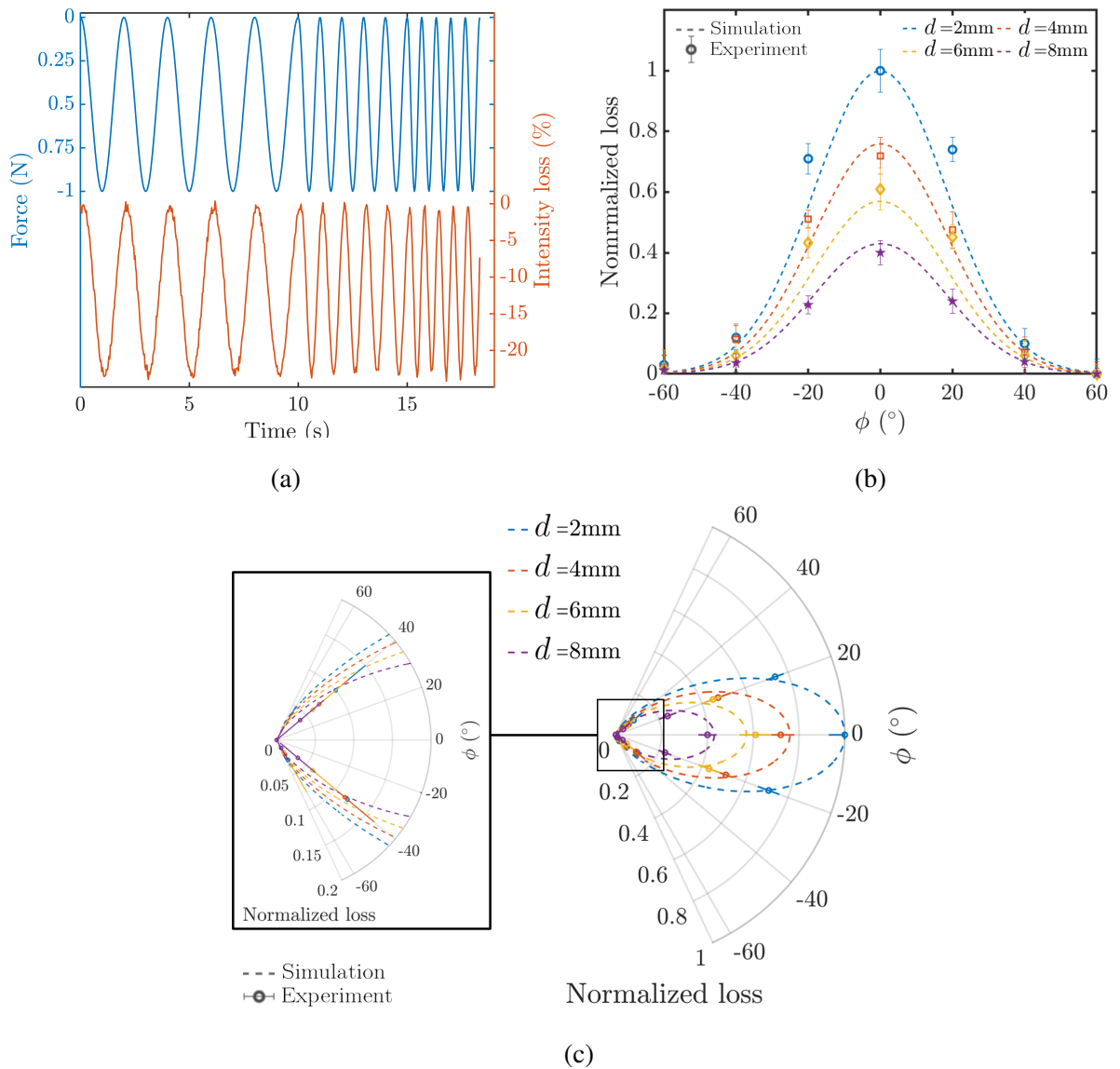


Figure 7.10: (a) Sensor response to 1 N concentrated force with frequencies 0.5, 1.0, and 1.5 Hz applied to the point (2mm,0°), and (b) comparison of the trends of change in the intensity loss of Fiber-1 with 1 N external force at various positions (Cartesian diagram), (c) comparison of the trends of change in the intensity loss of Fiber-1 with 1 N external force at various positions (polar diagram).

Table 7.4: Normalized intensity loss (in percentage of the maximum) in Fiber-1 with 1 N external force.

| ϕ | -60° | -40° | -20° | 0° | 20° | 40° | 60° |
|----------|------|-------|-------|---------------|-------|-------|------|
| $d=2$ mm | 3±3 | 12± 4 | 71± 5 | 100 (Maximum) | 74 ±4 | 10± 5 | 0± 5 |
| $d=4$ mm | 2± 4 | 11± 5 | 51± 3 | 72± 6 | 48 ±6 | 7± 5 | 0 ±4 |
| $d=6$ mm | 2± 6 | 6± 4 | 43± 5 | 61± 7 | 45 ±4 | 6 ±5 | 0 ±3 |
| $d=8$ mm | 1± 2 | 4± 3 | 23± 3 | 40± 4 | 24 ±4 | 4 ±4 | 0 ±2 |

surround the proposed sensor and push on the shell similar to a ring.

Therefore, the determination of the longitudinal position of the external force will be of higher clinical importance. In such a configuration, all the fibers will exhibit levels of intensity loss. With proper nonlinear calibration, i.e. learning-based rate-dependent methods, a mapping between states of the intensity loss in the four fibers and the position and magnitude of the external force can be obtained. Since in this experiment, only one fiber was utilized, obtaining such calibration was not possible. However, the feasibility of this form of calibration has previously been shown by the author, e.g., in Chapter 5 and Chapter 6. Post-processing showed that, as predicted from the simulation, the maximum intensity loss was observed with the external force on top of the indenter-1, i.e., $d = 2$ and $\phi = 0$. Also, the intensity loss decreased with increasing the distance of external force with the indenter both longitudinally and circumferentially.

Another finding was that as the external force moves away from the fiber in a circumferential direction its ability to deform the optical fiber (and causing the intensity loss) decreases more rapidly than when it moves along the sensor's longitudinal direction. Nevertheless, the existence of a 30° overlap between the consecutive indenters allows for capturing the effects of force with the next optical fiber in circumferential order as the external force departs from each fiber.

7.6 Conclusion

This study was a proof-of-concept to show the feasibility of an array force sensor based on variable bending radius light intensity modulation principle suitable for use in TAVI procedures. Initially, the theoretical sensing principle was derived to show the relationship with the deflection and radius

of curvature of the fibers and external force. Afterward, a finite element simulation was performed to study the variation of deflection in optical fibers of the sensor with the external force at various circumferential and longitudinal positions. The point load external force (1 N) was selected to simulate the worst-case scenario, whereas in real applications typically distributed forces along the surface of sensor will cause multiple-fiber deflections. Such a multiple fiber deflection (and its corresponding light intensity modulation) can be calibrated for accurate force measurement and localization.

Moreover, the numerical simulation approach was selected since the mechanical model involved complex geometry, material and geometric non-linearities (e.g., for the flexible shell), and contact mechanics, for which analytical solution was not available. The results of the simulation showed that the deflection of each fiber (thus, its light intensity modulation) is sensitive to both the circumferential and longitudinal position of the external force. Moreover, similar trend of intensity loss was observed in experiments with one fiber, i.e., Fiber-1.

The novelty of the proposed sensor was its potential capability to identify the lateral external force and its location with respect to the sensor. Thanks to the novel design and miniature structure, the proposed sensor can be integrated at the tip of commercially available cardiac catheters used in TAVI, either as an integral part or as an add-on feature.

In addition, the results of the performed tests verified the capability of the sensor to perform under dynamic loading conditions similar to the use-case in TAVI. Also, the proposed structure of the substrate allows for passing a separate optical fiber to be coupled with a flexible tip at the end of the sensor which can be used for normal tip force measurement, e.g., as proposed in [89]. This way, the sensor can be used as a miniaturized sensor with the ability to measure three spatial components of the tip forces as well as magnitude, longitudinal and circumferential positions of a lateral force (6 DoF sensor).

Moreover, the proposed shell-substrate design allows for proper isolation of the sensor to avoid blood penetration inside the shell. Also, since the proposed design does not employ ferromagnetic or electric components, it is MRI-compatible and electrically safe, which are of high usability importance. Another contribution of this study was utilizing SLA 3D printing technique to fabricate

flexible and rigid components with high spatial resolution. This technique facilitates fabricating delicate and complex structural components, should an optimized design (such as provided in Chapter 5) require. Besides, various providers, including Formlabs Inc., provide a wide range of biocompatible resins for SLA 3D printing which can be exploited to fabricate fully biocompatible sensors.

The proposed structure in this chapter is also adaptable with other sensing principles such as wavelength or phase modulation principles. For such adaptation, the optical fibers used in this sensor should be replaced with FBG or FPI fibers.

Chapter 8

Conclusion

8.1 Summary and Conclusions

This doctoral research was aimed at developing sensing principles and miniaturized sensors for MIS and RMIS applications, considering the functional and physical design requirements. In this thesis, different tactile sensors and distinct sensing principles and techniques were proposed, developed, and experimentally studied for compatibility with the requirements. The general framework followed in the studies of this research was first to propose a sensor structure and afterward to develop an optomechanical model for the sensor. Parameteric development of the optomechanical models allowed for structural miniaturization considering the sensitivity of the sensors as the objective function. As an example, such an optomechanical modeling framework was shown to be an appropriate approach for sensing principles other than bending-based intensity modulation, e.g., FBG-based sensors, in the collaborative study with an industrial partner. As discussed in detail within the chapters, all the developed sensors satisfied the physical and functional requirements for MIS applications.

More specifically, the new variable bending radius sensing principle, validated in this research, could significantly facilitate the miniaturization process of tactile sensors with bending-based intensity modulation. Also, the image-based intensity measurement system was utile, robust, and suitable for future researchers in using multi-fiber array sensor configurations. Moreover, the non-linear rate-dependent learning-based calibration schema used for the flexible sensors of this research

showed acceptable accuracy and repeatability for practical MIS and RMIS applications. Adopting such calibration schema would allow for further development of small and flexible tactile sensors by eliminating the concern of the effects of hysteresis or rate-dependency phenomena.

To summarize, in Chapter 2, a critical review of the proposed tactile sensors MIS applications along with a fundamental review of various sensing principles were provided. In Chapter 3, a hybrid tactile sensor based on the optical fiber coupling loss and piezoresistive sensing principles was modeled, simulated, and analyzed. The theoretical predictions showed fair agreement with the experimental data.

Chapter 4 was a collaborative study with an industrial partner for developing an optomechanical model for an FBG-based sensor with potential application in tactile sensing. To this end, an optomechanical model of their sensor was developed based on Hertzian contact mechanics and FBG sensing principle and was validated through a series of experiments. Also, a parametric relationship between external force and Bragg wavelength and beating frequency of the sensor was established. The parametric form of the developed optomechanical model would be suitable for miniaturizing the sensor structure while maintaining its sensitivity to force. The results of the preliminary study for this purpose were also included in this thesis. Moreover, to the best of my knowledge, this study was the first to propose an analytical form for accounting for the thermal and temporal aging-drift in calibration. Further development and miniaturization of this sensor can also be the subject of a future study.

In Chapter 5, a novel miniaturized optical-fiber-based sensor was developed and integrated at a rapid-prototyped typical MIS grasper. The proposed sensor was designed based on a novel optical fiber bending loss principle and optimized structurally to fit into 5-8 mm MIS trocar with maximized sensitivity. Using a learning-based non-linear calibration technique helped in accounting for the structural hysteresis of the sensor in both dynamic and static loading conditions. Furthermore, the proposed sensing principle was intrinsically inert to electromagnetic interference. The demonstrated feasibility of using 3D printed structure provides a ground for utilizing MRI-compatible and biocompatible materials in future studies.

In Chapter 6, an accurate and robust image-based light intensity estimation system was proposed for the tactile sensor developed in Chapter 5. This new intensity estimation system did not

have the complexities of using photodetectors, e.g., being bulky, exhibiting saturation at high intensities, and expensive. Besides, in the case of array sensor configurations, such a system is utile, whereas merely one projection chamber and camera can measure multiple light intensities with proper programming. Using a rate-dependent learning-based calibration model and *ex-vivo* test showed acceptable performance of the sensor for MIS applications. Hence, considering the single-degree of freedom of the proposed sensor in both recent chapters and validation of the image-based acquisition system, the sensor can be reconfigured as multi-axial sensing system in array design.

Chapter 7 proposed a novel bending-based sensor based on the VBR sensing principle. The study presented in this chapter showed the feasibility of using the proposed sensor for lateral force measurement and localization. This hypothesis was verified both theoretically and experimentally. In addition, utilization of the image-based intensity acquisition system facilitated simple sensor structure, especially for the future multi-fiber validation studies. The experimental validation of this study showed a fair agreement between the trends of changes in fiber intensity loss observed in experiments with the numerical model. It is noteworthy that the proposed cylindrical array sensor in this chapter is in fact a 2D expansion of the proposed 1D sensors in Chapter 5 and Chapter 6 that in a continuum builds upon its miniaturized structure, VBR sensing principle, and image-based intensity acquisition.

8.2 Future Studies

Some aspects of the developed sensors and sensing principles in this study can be further investigated in future studies. The following seven recommendations for future studies are provided:

- (1) In the present study, the proposed hybrid sensor was capable of estimating the softness of various tissues. For an extended study, a learning-base technique such as logistic regression models or neural network classifiers can be utilized and trained on data from tissues with known softness to enable the sensor to identify various tissues in real-time.
- (2) The investigated FBG-based sensor in this study can be further miniaturized using the proposed optomechanical model and by adopting the miniaturization method proposed in Chapter 5. One of the features to be noted is the active laser cavity length. This length sets a minimum for miniaturizing the length of the sensor; however, the breadth and height of this sensor can be miniaturized. Moreover, as the preliminary study (presented in the Appendix) showed, multi-fiber configuration for this sensor with a proper geometrical design will allow for increasing the range of measurements while maintaining the sensitivity at maximum.
- (3) In the proposed sensors in Chapter 5 and Chapter 6, the optical fiber was passed through the structure and connected to the photodetector or camera at the end of the sensor. An extension of this study to make it easier for clinical application is to use a retro-reflection technique. Such a configuration will allow the light to reflect on the same fiber; thus, the optical fiber can be terminated within the sensor without extending from its distal end.
- (4) The novel VBR sensing principle combined with the learning-based calibration, exhibited adequate sensitivity for MIS applications with a one-DoF sensing requirement. However, thanks to the small size of the optical fiber and micro-indenter, array configuration such as sensing units can be developed for multi-DoF sensing applications, e.g., in the RMIS instrument wrists.
- (5) Using an image-based technique for light intensity measurement can be further extended by using multiple colors (or invisible wavelengths) for each individual optical fiber in array configurations. Therefore, each color could be calibrated versus an individual measurand,

e.g., force and displacement, for simultaneous measurement of multiple physical variables. Using various colors also relieves the concern about optical isolation of the output of multiple fibers in the projection chamber, as through proper RGB color resolution, each color profile can be measured individually.

- (6) In addition to the proposed SVR calibration method, recurrent neural network (RNN) and Gaussian process model (GPM) can be used for the non-linear calibration of the proposed sensors. There is a compromise between accuracy and complexity of the methods, whereas SVRs provide a more accurate result with large training datasets, and RNN and GPM converge with relatively smaller datasets.
- (7) To evaluate the sensor performance in a clinical study, in-vivo tests can be investigated in the future. Besides, the materials used in such applications shall be biocompatible as a functional requirement mandated by ISO 10993. As the current study was a proof-of-concept, non-biocompatible materials were used for prototyping. Nevertheless, manufacturers, e.g., Form-lab Inc., MA, USA, offers a variety of biocompatible flexible, and solid resins for biomedical applications. Moreover, with the expansion of metal 3D printing services, especially on Titanium alloys, e.g., Ti ELI alloy, the body of the grasper and the sensing part can be manufactured using metal 3D printing techniques for more robustness and re-usability. The use of biocompatible materials would make the sensor sterilizable and disinfectable for surgical applications. Also, with proper surface treatment, metal surfaces of the graspers can act as a mirror further facilitating the retro-reflection configuration for optical fibers.

Bibliography

- [1] Ulrich Seibold, Bernhard Kübler, and Gerd Hirzinger. Prototype of instrument for minimally invasive surgery with 6-axis force sensing capability. In *ICRA*, volume 2005, pages 498–503, 2005.
- [2] J. Barry McKernan. Origin of laparoscopic cholecystectomy in the usa: personal experience. *World Journal of Surgery*, 23(4):332–333, 1999.
- [3] Feng WeiXing, Wang HuanRan, Guo ShuXiang, Wang KeJun, and Ye XiuFen. Design and experiments of a catheter side wall tactile sensor for minimum invasive surgery. In *2007 International Conference on Mechatronics and Automation*, pages 1073–1078. IEEE, 2007.
- [4] Frank Tendick, S Shankar Sastry, Ronald S Fearing, and Michael Cohn. Applications of micromechatronics in minimally invasive surgery. *IEEE/ASME transactions on mechatronics*, 3(1):34–42, 1998.
- [5] M Treat et al. A surgeon’s perspective on the difficulties of laparoscopic surgery. *Computer-integrated surgery*, pages 559–560, 1996.
- [6] Kentaro Totsu, Yoichi Haga, and Masayoshi Esashi. Ultra-miniature fiber-optic pressure sensor using white light interferometry. *Journal of Micromechanics and Microengineering*, 15(1):71, 2004.
- [7] Stefan Sauerland, Thomas Jaschinski, and Edmund AM Neugebauer. Laparoscopic versus open surgery for suspected appendicitis. *Cochrane Database of Systematic Reviews*, 10(10), 2010.

- [8] Allison M Okamura. Haptic feedback in robot-assisted minimally invasive surgery. *Current opinion in urology*, 19(1):102, 2009.
- [9] Sebastian Schostek, Marc O Schurr, and Gerhard F Buess. Review on aspects of artificial tactile feedback in laparoscopic surgery. *Medical engineering & physics*, 31(8):887–898, 2009.
- [10] Thomas Jaschinski, Christoph G Mosch, Michaela Eikermann, Edmund AM Neugebauer, and Stefan Sauerland. Laparoscopic versus open surgery for suspected appendicitis. *Cochrane Database of Systematic Reviews*, 11(11), 2018.
- [11] Dinesh Vyas and Sean Cronin. Peer review and surgical innovation: Robotic surgery and its hurdles. *American Journal of Robotic Surgery*, 2(1):39–44, 2015.
- [12] H Xin, JS Zelek, and H Carnahan. Laparoscopic surgery, perceptual limitations and force: A review. In *First Canadian student conference on biomedical computing*, volume 144, 2006.
- [13] Amir Hooshier, Siamak Najarian, and Javad Dargahi. Haptic telerobotic cardiovascular intervention: a review of approaches, methods, and future perspectives. *IEEE Reviews in Biomedical Engineering*, 13:32–50, 2020.
- [14] Amir Hooshier, Masoud Razban, Naghmeh M Bandari, and Javad Dargahi. Sensing principle for real-time characterization of viscoelasticity in the beating myocardial tissue. In *2017 IEEE International Conference on Computational Intelligence and Virtual Environments for Measurement Systems and Applications (CIVEMSA)*, pages 72–77. IEEE, 2017.
- [15] Jeffrey Stoll and Pierre Dupont. Force control for grasping soft tissue. In *Proceedings of the IEEE International Conference on Robotics and Automation, Orlando, FL, May*, pages 15–19, 2006.
- [16] Pinyo Puangmali, Kaspar Althoefer, Lakmal D Seneviratne, Declan Murphy, and Prokar Dasgupta. State-of-the-art in force and tactile sensing for minimally invasive surgery. *IEEE Sensors Journal*, 8(4):371–381, 2008.

- [17] Panagiotis Polygerinos, Dinusha Zbyszewski, Tobias Schaeffter, Reza Razavi, Lakmal D Seneviratne, and Kaspar Althoefer. Mri-compatible fiber-optic force sensors for catheterization procedures. *IEEE Sensors Journal*, 10(10):1598–1608, 2010.
- [18] AS Sezen, Rajesh Rajamani, D Morrow, Kenton R Kaufman, and Barry Kent Gilbert. An ultraminiature mems pressure sensor with high sensitivity for measurement of intramuscular pressure (imp) in patients with neuromuscular diseases. *Journal of Medical Devices*, 3(3):031006, 2009.
- [19] Roozbeh Ahmadi, Muthukumaran Packirisamy, and Javad Dargahi. High sensitive force sensing based on the optical fiber coupling loss. *Journal of Medical Devices*, 7(1):011001, 2013.
- [20] Naghmeh M Bandari, Amir Hooshair, Muthukumaran Packirisamy, and Javad Dargahi. Bending-based formulation of light intensity modulation for miniaturization of optical tactile sensors. In *Optical Sensors*, pages SeM2E–3. Optical Society of America, 2018.
- [21] Naghmeh Bandari, Javad Dargahi, and Muthukumaran Packirisamy. Miniaturized optical force sensor for minimally invasive surgery with learning-based nonlinear calibration. *IEEE Sensors Journal*, 20(7):3579–3592, 2020.
- [22] Katsuaki Yokoyama, Hiroshi Nakagawa, Dipen C Shah, Hendrik Lambert, Giovanni Leo, Nicolas Aeby, Atsushi Ikeda, Jan V Pitha, Tushar Sharma, Ralph Lazzara, et al. Novel contact force sensor incorporated in irrigated radiofrequency ablation catheter predicts lesion size and incidence of steam pop and thrombus. *Circulation: Arrhythmia and Electrophysiology*, 1(5):354–362, 2008.
- [23] Naghmeh Bandari, Javad Dargahi, and Muthukumaran Packirisamy. Optical fiber array sensor for force estimation and localization in tavi procedure: Design, modeling, analysis and validation. *IEEE Sensors*, Under-review, 2021.

- [24] Naghmeh Bandari, Patrick Orsini, Corbeil Jean-simon, Érick Jarry, Marie-maude de Denus Baillargeon, Maroun Massabki, Javad Dargahi, and Muthukumaran Packirisamy. Optomechanical modeling and validation of a distributed bragg reflector force sensor with drift and temperature compensation. *IEEE Sensors Journal*, 21(3):2929–2941, 2020.
- [25] Naghmeh Bandari, Javad Dargahi, and Muthukumaran Packirisamy. Image-based optical-fiber force sensor for minimally invasive surgery with ex-vivo validation. *Journal of the Electrochemical Society*, 167(12):127504, 2020.
- [26] Naghmeh Bandari, Javad Dargahi, and M Packirisamy. Camera-based optical-fiber tactile sensor for intraoperative grasping force measurement. In *237th ECS Meeting with the 18th International Meeting on Chemical Sensors (IMCS 2020)*. ECS, 2020.
- [27] Naghmeh Bandari, Javad Dargahi, and Muthukumaran Packirisamy. Tactile sensors for minimally invasive surgery: a review of the state-of-the-art, applications, and perspectives. *IEEE Access*, 8:7682–7708, 2020.
- [28] Naghmeh Bandari, Javad Dargahi, and Muthukumaran Packirisamy. Validation of a variable bending radius sensing principle for optical-fiber tactile sensors. In *2019 Photonics North (PN)*, pages 1–1. IEEE, 2019.
- [29] Naghmeh M Bandari, Roozbeh Ahmadi, Amir Hooshier, Javad Dargahi, and Muthukumaran Packirisamy. Hybrid piezoresistive-optical tactile sensor for simultaneous measurement of tissue stiffness and detection of tissue discontinuity in robot-assisted minimally invasive surgery. *Journal of biomedical optics*, 22(7):077002, 2017.
- [30] Naghmeh M Bandari, Amir Hooshier, Muthukumaran Packirisamy, and Javad Dargahi. Optical fiber array sensor for lateral and circumferential force measurement suitable for minimally invasive surgery: Design, modeling and analysis. In *Specialty Optical Fibers*, pages JT4A–44. Optical Society of America, 2016.
- [31] Stefano Stassi, Valentina Cauda, Giancarlo Canavese, and Candido Pirri. Flexible tactile sensing based on piezoresistive composites: A review. *Sensors*, 14(3):5296–5332, 2014.

- [32] Cheng Chi, Xuguang Sun, Ning Xue, Tong Li, and Chang Liu. Recent progress in technologies for tactile sensors. *Sensors*, 18(4):948, 2018.
- [33] Siamak Najarian, Javad Dargahi, and Ali Abouei Mehrizi. *Artificial tactile sensing in biomedical engineering*. McGraw Hill Professional, 2009.
- [34] Siamak Najarian, Javad Dargahi, Goldis Darbemamieh, and Siamak Hajizadeh Farkoush. *Mechatronics in medicine a biomedical engineering approach*. McGraw-Hill Professional, 2011.
- [35] Mitsutaka Tanimoto, Fumihito Arai, Toshio Fukuda, Hitoshi Iwata, Kouichi Itoigawa, Yasuhiro Gotoh, Masashi Hashimoto, and Makoto Negoro. Micro force sensor for intravascular neurosurgery and in vivo experiment. In *Proceedings MEMS 98. IEEE. Eleventh Annual International Workshop on Micro Electro Mechanical Systems. An Investigation of Micro Structures, Sensors, Actuators, Machines and Systems (Cat. No. 98CH36176*, pages 504–509. IEEE, 1998.
- [36] Javad Dargahi and Siamak Najarian. An endoscopic force-position sensor grasper with minimum sensors. *Canadian Journal of Electrical and Computer Engineering*, 28(3/4):155–161, 2003.
- [37] Chih-Hung King, Martin O Culjat, Miguel L Franco, James W Bisley, Gregory P Carman, Erik P Dutson, and Warren S Grundfest. A multielement tactile feedback system for robot-assisted minimally invasive surgery. *IEEE Transactions on Haptics*, 2(1):52–56, 2008.
- [38] Chih-Hung King, Martin O Culjat, Miguel L Franco, Catherine E Lewis, Erik P Dutson, Warren S Grundfest, and James W Bisley. Tactile feedback induces reduced grasping force in robot-assisted surgery. *IEEE transactions on haptics*, 2(2):103–110, 2009.
- [39] Yating Hu, Rakesh B Katragadda, Hongen Tu, Qinglong Zheng, Yuefa Li, and Yong Xu. Bioinspired 3-d tactile sensor for minimally invasive surgery. *Journal of microelectromechanical systems*, 19(6):1400–1408, 2010.

- [40] Kouros Zareinia, Yaser Maddahi, Liu Shi Gan, Ahmad Ghasemloonia, Sanju Lama, Taku Sugiyama, Fang Wei Yang, and Garnette R Sutherland. A force-sensing bipolar forceps to quantify tool–tissue interaction forces in microsurgery. *IEEE/ASME Transactions on Mechatronics*, 21(5):2365–2377, 2016.
- [41] Karsten Weiss and Heinz Woern. Tactile sensor system for an anthropomorphic robotic hand. In *Proceedings of IEEE International Conference on Manipulation and Grasping (IMG 2004), Kobe, Japan*, volume 1217, page 895901, 2004.
- [42] R Askeland Donald and P Pule Pradeep. The science and engineering of materials. *ÇeviriDr. M. Erdoğan*, 3, 1994.
- [43] Anders Eklund, Anders Bergh, and OA Lindahl. A catheter tactile sensor for measuring hardness of soft tissue: measurement in a silicone model and in an in vitro human prostate model. *Medical & biological engineering & computing*, 37(5):618–624, 1999.
- [44] Saeed Sokhanvar, Muthukumaran Packirisamy, and Javad Dargahi. Mems endoscopic tactile sensor: toward in-situ and in-vivo tissue softness characterization. *IEEE Sensors Journal*, 9(12):1679–1687, 2009.
- [45] Cheng-Hsin Chuang, Tsan-Hsiu Li, I-Chinms Chou, and Ying-Juimr Teng. Piezoelectric tactile sensor for submucosal tumor detection in endoscopy. *Sensors and Actuators A: Physical*, 244:299–309, 2016.
- [46] Shivani Sharma, Renato Aguilera, Jian Yu Rao, and James K Gimzewski. Piezoelectric needle sensor reveals mechanical heterogeneity in human thyroid tissue lesions. *Scientific Reports*, 9(1):9282, 2019.
- [47] Rebecca Smith-Bindman, Paulette Lebda, Vickie A Feldstein, Dorra Sellami, Ruth B Goldstein, Natasha Brasic, Chengshi Jin, and John Kornak. Risk of thyroid cancer based on thyroid ultrasound imaging characteristics: results of a population-based study. *JAMA internal medicine*, 173(19):1788–1795, 2013.

- [48] MEH Eltaib and JR Hewit. A tactile sensor for minimal access surgery applications. *IFAC Proceedings Volumes*, 33(26):505–508, 2000.
- [49] Peng Peng, Rajesh Rajamani, and Arthur G Erdman. Flexible tactile sensor for tissue elasticity measurements. *Journal of microelectromechanical systems*, 18(6):1226–1233, 2009.
- [50] Omeed H Paydar, Christopher R Wottawa, Richard E Fan, Erik P Dutson, Warren S Grundfest, Martin O Culjat, and Rob N Candler. Fabrication of a thin-film capacitive force sensor array for tactile feedback in robotic surgery. In *2012 Annual International Conference of the IEEE Engineering in Medicine and Biology Society*, pages 2355–2358. IEEE, 2012.
- [51] Uikyum Kim, Yong Bum Kim, Jinho So, Dong-Yeop Seok, and Hyouk Ryeol Choi. Sensorized surgical forceps for robotic-assisted minimally invasive surgery. *IEEE Transactions on Industrial Electronics*, 65(12):9604–9613, 2018.
- [52] Man Bok Hong and Yung-Ho Jo. Design of a novel 4-dof wrist-type surgical instrument with enhanced rigidity and dexterity. *IEEE/ASME Transactions on Mechatronics*, 19(2):500–511, 2013.
- [53] Javad Dargahi, Ash M. Parameswaran, and Shahram Payandeh. A micromachined piezoelectric tactile sensor for an endoscopic grasper-theory, fabrication and experiments. *Journal of microelectromechanical systems*, 9(3):329–335, 2000.
- [54] Nicholas Kattavenos, Brian Lawrenson, TG Frank, MS Pridham, RP Keatch, and Alfred Cuschieri. Force-sensitive tactile sensor for minimal access surgery. *Minimally Invasive Therapy & Allied Technologies*, 13(1):42–46, 2004.
- [55] Maria V Ottermo, Oyvind Stavadahl, and Tor Arne Johansen. Palpation instrument for augmented minimally invasive surgery. In *2004 IEEE/RSJ International Conference on Intelligent Robots and Systems (IROS)(IEEE Cat. No. 04CH37566)*, volume 4, pages 3960–3964. IEEE, 2004.
- [56] Mohammad A Qasaimeh, S Sokhanvar, J Dargahi, and M Kahrizi. A micro-tactile sensor

- for in situ tissue characterization in minimally invasive surgery. *Biomedical microdevices*, 10(6):823–837, 2008.
- [57] AL Trejos, RV Patel, MD Naish, AC Lyle, and CM Schlachta. A sensorized instrument for skills assessment and training in minimally invasive surgery. *Journal of Medical Devices*, 3(4):041002, 2009.
- [58] Ali Tavakoli Golpaygani, Siamak Najarian, and Mehdi Movahedi. Tactile sensor for robotic applications. In *World Congress on Medical Physics and Biomedical Engineering, September 7-12, 2009, Munich, Germany*, pages 2299–2302. Springer, 2009.
- [59] Ville Jalkanen. Hand-held resonance sensor for tissue stiffness measurements—a theoretical and experimental analysis. *Measurement science and technology*, 21(5):055801, 2010.
- [60] Masoud Kalantari, Mohammadreza Ramezanifard, Roozbeh Ahmadi, Javad Dargahi, and József Kövecses. A piezoresistive tactile sensor for tissue characterization during catheter-based cardiac surgery. *The International Journal of Medical Robotics and Computer Assisted Surgery*, 7(4):431–440, 2011.
- [61] Péter Baki, Gábor Székely, and Gábor Kósa. Miniature tri-axial force sensor for feedback in minimally invasive surgery. In *2012 4th IEEE RAS & EMBS International Conference on Biomedical Robotics and Biomechanics (BioRob)*, pages 805–810. IEEE, 2012.
- [62] Ali Talasaz and Rajni V Patel. Integration of force reflection with tactile sensing for minimally invasive robotics-assisted tumor localization. *IEEE Transactions on Haptics*, 6(2):217–228, 2012.
- [63] Jung-Hoon Hwang, Joon Ho Kwon, Tae-Keun Kim, and Daehie Hong. Design of simple structured tactile sensor for the minimally invasive robotic palpation. In *2013 IEEE/ASME International Conference on Advanced Intelligent Mechatronics*, pages 1296–1299. IEEE, 2013.
- [64] Junwoo Lee, Wook Choi, Yong Yoo, Kyo Hwang, Sang-Myung Lee, Sungchul Kang, Jinseok

- Kim, and Jeong Lee. A micro-fabricated force sensor using an all thin film piezoelectric active sensor. *Sensors*, 14(12):22199–22207, 2014.
- [65] Kun Li, Bo Pan, Juncheng Zhan, Wenpeng Gao, Yili Fu, and Shuguo Wang. Design and performance evaluation of a 3-axis force sensor for mis palpation. *Sensor Review*, 35(2):219–228, 2015.
- [66] Uiikum Kim, Dong-Hyuk Lee, Woon Jong Yoon, Blake Hannaford, and Hyouk Ryeol Choi. Force sensor integrated surgical forceps for minimally invasive robotic surgery. *IEEE Transactions on Robotics*, 31(5):1214–1224, 2015.
- [67] Markus Hessinger, Tobias Pilic, Roland Werthschützky, and Peter P Pott. Miniaturized force/torque sensor for in vivo measurements of tissue characteristics. In *2016 38th Annual International Conference of the IEEE Engineering in Medicine and Biology Society (EMBC)*, pages 2022–2025. IEEE, 2016.
- [68] Lei Zhang, Feng Ju, Yanfei Cao, Yaoyao Wang, and Bai Chen. A tactile sensor for measuring hardness of soft tissue with applications to minimally invasive surgery. *Sensors and Actuators A: Physical*, 266:197–204, 2017.
- [69] Uiikum Kim, Yong Bum Kim, Dong-Yeop Seok, Jinho So, and Hyouk Ryeol Choi. A surgical palpation probe with 6-axis force/torque sensing capability for minimally invasive surgery. *IEEE Transactions on Industrial Electronics*, 65(3):2755–2765, 2017.
- [70] János Radó, Csaba Dücső, Péter Földesy, Gábor Szebényi, Zbigniew Nawrat, Kamil Rohr, and Péter Fürjes. 3d force sensors for laparoscopic surgery tool. *Microsystem Technologies*, 24(1):519–525, 2018.
- [71] Feng Ju, Yaming Wang, Zhao Zhang, Yaoyao Wang, Yahui Yun, Hao Guo, and Bai Chen. A miniature piezoelectric spiral tactile sensor for tissue hardness palpation with catheter robot in minimally invasive surgery. *Smart Materials and Structures*, 2019.
- [72] Uiikum Kim, Yong Bum Kim, Dong-Yeop Seok, and Hyouk Ryeol Choi. S-surge: A

- portable surgical robot based on a novel mechanism with force-sensing capability for robotic surgery. In *Handbook of Robotic and Image-Guided Surgery*, pages 265–283. Elsevier, 2020.
- [73] Leland C Clark JR, Richard Wolf, Donald Granger, and Zena Taylor. Continuous recording of blood oxygen tensions by polarography. *Journal of applied physiology*, 6(3):189–193, 1953.
- [74] S Nemoto and T Makimoto. Analysis of splice loss in single-mode fibres using a gaussian field approximation. *Optical and Quantum Electronics*, 11(5):447–457, 1979.
- [75] Osamu Tohyama, Miki Kohashi, Keisuke Yamamoto, and Hirotaka Itoh. A fiber-optic silicon pressure sensor for ultra-thin catheters. *Sensors and Actuators A: Physical*, 54(1-3):622–625, 1996.
- [76] Michael L Polanyi and RM Hehir. New reflection oximeter. *Review of Scientific Instruments*, 31(4):401–403, 1960.
- [77] Peter L Frommer, John Ross Jr, Dean T Mason, James H Gault, and Eugene Braunwald. Clinical applications of an improved, rapidly responding fiberoptic catheter. *The American journal of cardiology*, 15(5):672–679, 1965.
- [78] J. A. C. Heijmans, L. K. Cheng, and Fokko Wieringa. Optical fiber sensors for medical applications—practical engineering considerations. In *4th European Conference of the International Federation for Medical and Biological Engineering*, pages 2330–2334. Springer, 2009.
- [79] Israel Gannot. Optical fibers and sensors for medical applications. In *Optical Fibers and Sensors for Medical Applications*, volume 4253, 2001.
- [80] Robert C. Gauthier and C. Ross. Theoretical and experimental considerations for a single-mode fiber-optic bend-type sensor. *Applied optics*, 36(25):6264–6273, 1997.
- [81] Nicholas Lagakos, JH Cole, and Joseph A Bucaro. Microbend fiber-optic sensor. *Applied optics*, 26(11):2171–2180, 1987.

- [82] Jose Brandao Faria. A theoretical analysis of the bifurcated fiber bundle displacement sensor. *IEEE Transactions on instrumentation and measurement*, 47(3):742–747, 1998.
- [83] Panagiotis Polygerinos, Lakmal D Seneviratne, and Kaspar Althoefer. Modeling of light intensity-modulated fiber-optic displacement sensors. *IEEE Transactions on Instrumentation and Measurement*, 60(4):1408–1415, 2010.
- [84] Roozbeh Ahmadi, Muthukumaran Packirisamy, Javad Dargahi, and Renzo Cecere. Discretely loaded beam-type optical fiber tactile sensor for tissue manipulation and palpation in minimally invasive robotic surgery. *IEEE Sensors Journal*, 12(1):22–32, 2012.
- [85] Roozbeh Ahmadi, Muthukumaran Packirisamy, and Javad Dargahi. Innovative optical microsystem for static and dynamic tissue diagnosis in minimally invasive surgical operations. *Journal of biomedical optics*, 17(8):0814161–0814168, 2012.
- [86] Borut Gersak and Z Sutlic. Aortic and mitral valve surgery on the beating heart is lowering cardiopulmonary bypass and aortic cross clamp time. *The Heart Surgery Forum*, 5(2):182–186, 2002.
- [87] Michael C Yip, Shelten G Yuen, and Robert D Howe. A robust uniaxial force sensor for minimally invasive surgery. *IEEE transactions on biomedical engineering*, 57(5):1008–1011, 2010.
- [88] Moustapha Atoui, Sampath Gunda, Dhanunjaya Lakkireddy, and Srijoy Mahapatra. Radiofrequency ablation to prevent sudden cardiac death. *Methodist DeBakey cardiovascular journal*, 11(2):121, 2015.
- [89] Yohan Noh, Hongbin Liu, Sina Sareh, D Chathuranga, Helge Wurdemann, Kawal Rhode, and Kaspar Althoefer. Image-based optical miniaturized three-axis force sensor for cardiac catheterization. *IEEE Sens. J*, 16:7924–7932, 2016.
- [90] K. O. Hill, Y. Fujii, Derwyn C. Johnson, and B. S. Kawasaki. Photosensitivity in optical fiber waveguides: Application to reflection filter fabrication. *Applied physics letters*, 32(10):647–649, 1978.

- [91] G. Meltz, W. W. Morey, and W. H. Glenn. Formation of bragg gratings in optical fibers by a transverse holographic method. *Optics letters*, 14(15):823–825, 1989.
- [92] Yong-Lae Park, Santhi Elayaperumal, Bruce Daniel, Seok Chang Ryu, Mihye Shin, Joan Savall, Richard J Black, Behzad Moslehi, and Mark R Cutkosky. Real-time estimation of 3-d needle shape and deflection for mri-guided interventions. *IEEE/ASME Transactions On Mechatronics*, 15(6):906–915, 2010.
- [93] Thomas Lehmann, Mahdi Tavakoli, Nawaid Usmani, and Ronald Sloboda. Force-sensor-based estimation of needle tip deflection in brachytherapy. *Journal of Sensors*, 2013, 2013.
- [94] Thomas Lehmann, Ronald Sloboda, Nawaid Usmani, and Mahdi Tavakoli. Model-based needle steering in soft tissue via lateral needle actuation. *IEEE Robotics and Automation Letters*, 3(4):3930–3936, 2018.
- [95] Pouya Soltani Zarrin, Abelardo Escoto, Ran Xu, Rajni V Patel, Michael D Naish, and Ana Luisa Trejos. Development of a 2-dof sensorized surgical grasper for grasping and axial force measurements. *IEEE Sensors Journal*, 18(7):2816–2826, 2018.
- [96] Pouya Soltani Zarrin, Abelardo Escoto, Ran Xu, Rajni V Patel, Michael D Naish, and Ana Luisa Trejos. Development of an optical fiber-based sensor for grasping and axial force sensing. In *2017 IEEE International Conference on Robotics and Automation (ICRA)*, pages 939–944. IEEE, 2017.
- [97] Fabrizio Taffoni, Domenico Formica, Paola Saccomandi, Giovanni Pino, and Emiliano Schena. Optical fiber-based mr-compatible sensors for medical applications: An overview. *Sensors*, 13(10):14105–14120, 2013.
- [98] Hao Su, Michael Zervas, Gregory A Cole, Cosme Furlong, and Gregory S Fischer. Real-time mri-guided needle placement robot with integrated fiber optic force sensing. In *2011 IEEE International Conference on Robotics and Automation*, pages 1583–1588. IEEE, 2011.
- [99] Md Islam, Muhammad Ali, Man-Hong Lai, Kok-Sing Lim, and Harith Ahmad. Chronology

- of fabry-perot interferometer fiber-optic sensors and their applications: a review. *Sensors*, 14(4):7451–7488, 2014.
- [100] Byeong Ha Lee, Young Ho Kim, Kwan Seob Park, Joo Beom Eom, Myoung Jin Kim, Byung Sup Rho, and Hae Young Choi. Interferometric fiber optic sensors. *sensors*, 12(3):2467–2486, 2012.
- [101] Tarun Kumar Gangopadhyay. Prospects for fibre bragg gratings and fabry-perot interferometers in fibre-optic vibration sensing. *Sensors and Actuators A: Physical*, 113(1):20–38, 2004.
- [102] Weijian Shang, Hao Su, Gang Li, Cosme Furlong, and Gregory S Fischer. A fabry-perot interferometry based mri-compatible miniature uniaxial force sensor for percutaneous needle placement. In *SENSORS, 2013 IEEE*, pages 1–4. IEEE, 2013.
- [103] Hao Su, Diana C Cardona, Weijian Shang, Alexander Camilo, Gregory A Cole, D Caleb Rucker, Robert J Webster, and Gregory S Fischer. A mri-guided concentric tube continuum robot with piezoelectric actuation: a feasibility study. In *2012 IEEE International Conference on Robotics and Automation*, pages 1939–1945. IEEE, 2012.
- [104] Zonglai Mo and Weiliang Xu. Temperature-compensated optical fiber force sensing at the tip of a surgical needle. *IEEE Sensors Journal*, 16(24):8936–8943, 2016.
- [105] Zengling Ran, Yunjiang Rao, Jian Zhang, Zhiwei Liu, and Bing Xu. A miniature fiber-optic refractive-index sensor based on laser-machined fabry–perot interferometer tip. *Journal of Lightwave Technology*, 27(23):5426–5429, 2009.
- [106] Yun-Jiang Rao, Ming Deng, De-Wen Duan, Xiao-Chen Yang, Tao Zhu, and Guang-Hua Cheng. Micro fabry-perot interferometers in silica fibers machined by femtosecond laser. *Optics express*, 15(21):14123–14128, 2007.
- [107] Venkata R. Machavaram, Rod A. Badcock, and Gerard F. Fernando. Fabrication of intrinsic fibre fabry–perot sensors in silica fibres using hydrofluoric acid etching. *Sensors and Actuators A: Physical*, 138(1):248–260, 2007.

- [108] David J Webb, MW Hathaway, David A Jackson, S Jones, Lin Zhang, and Ian Bennion. First in-vivo trials of a fiber bragg grating based temperature profiling system. *Journal of biomedical optics*, 5(1):45–51, 2000.
- [109] Mitsunori Tada, Shinsuke Sasaki, and Tsukasa Ogasawara. Development of an optical 2-axis force sensor usable in mri environments. In *Sensors, 2002. Proceedings of IEEE*, volume 2, pages 984–989. IEEE, 2002.
- [110] Dominique Chapuis, Roger Gassert, Laurent Sache, Etienne Burdet, and Hannes Bleuler. Design of a simple mri/fmri compatible force/torque sensor. In *Intelligent Robots and Systems, 2004.(IROS 2004). Proceedings. 2004 IEEE/RSJ International Conference on*, volume 3, pages 2593–2599. IEEE, 2004.
- [111] Hao Su and Gregory S Fischer. A 3-axis optical force/torque sensor for prostate needle placement in magnetic resonance imaging environments. In *2009 IEEE International Conference on Technologies for Practical Robot Applications*, pages 5–9. IEEE, 2009.
- [112] Mathias Stefan Müller, Lars Hoffmann, Thorbjörn Christopher Buck, and Alexander Walter Koch. Fiber bragg grating-based force-torque sensor with six degrees of freedom. *International Journal of Optomechatronics*, 3(3):201–214, 2009.
- [113] Panagiotis Polygerinos, Tobias Schaeffter, Lakmal Seneviratne, and Kaspar Althoefer. A fibre-optic catheter-tip force sensor with mri compatibility: A feasibility study. In *2009 Annual International Conference of the IEEE Engineering in Medicine and Biology Society*, pages 1501–1054. IEEE, 2009.
- [114] Samuel B Kesner and Robert D Howe. Design principles for rapid prototyping forces sensors using 3-d printing. *IEEE/ASME Transactions on mechatronics*, 16(5):866–870, 2011.
- [115] Xuan Liu, Iulian I Iordachita, Xingchi He, Russell H Taylor, and Jin U Kang. Miniature fiber-optic force sensor based on low-coherence fabry-pérot interferometry for vitreoretinal microsurgery. *Biomedical optics express*, 3(5):1062–1076, 2012.

- [116] Panagiotis Polygerinos, Lakmal D Seneviratne, Reza Razavi, Tobias Schaeffter, and Kaspar Althoefer. Triaxial catheter-tip force sensor for mri-guided cardiac procedures. *IEEE/ASME Transactions on mechatronics*, 18(1):386–396, 2013.
- [117] Santhi Elayaperumal, Jung Hwa Bae, Bruce L Daniel, and Mark R Cutkosky. Detection of membrane puncture with haptic feedback using a tip-force sensing needle. In *2014 IEEE/RSJ International Conference on Intelligent Robots and Systems*, pages 3975–3981. IEEE, 2014.
- [118] Roozbeh Ahmadi, Siamak Arbatani, Muthukumaran Packirisamy, and Javad Dargahi. Micro-optical force distribution sensing suitable for lump/artery detection. *Biomedical microdevices*, 17(1):1–12, 2015.
- [119] Zonglai Mo, Weiliang Xu, and Neil Broderick. A fabry-perot optical fiber force sensor based on intensity modulation for needle tip force sensing. In *2015 6th International Conference on Automation, Robotics and Applications (ICARA)*, pages 376–380. IEEE, 2015.
- [120] Yi Qiu, Yahui Wang, Yiqing Xu, Namas Chandra, James Haorah, Basil Hubbi, Bryan J Pfister, and Xuan Liu. Quantitative optical coherence elastography based on fiber-optic probe for in situ measurement of tissue mechanical properties. *Biomedical optics express*, 7(2):688–700, 2016.
- [121] Tianliang Li, Chaoyang Shi, and Hongliang Ren. A high-sensitivity tactile sensor array based on fiber bragg grating sensing for tissue palpation in minimally invasive surgery. *IEEE/ASME Transactions on Mechatronics*, 23(5):2306–2315, 2018.
- [122] Indika B Wanninayake. Miniaturised optical fibre based palpations instrument for minimally invasive surgery. In *Journal of Physics: Conference Series*, volume 1151, page 012014. IOP Publishing, 2019.
- [123] Daniele Tosi, Edoardo Gino Macchi, Giovanni Braschi, Alfredo Cigada, Mario Gallati, Sandro Rossi, Sven Poeggel, Gabriel Leen, and Elfed Lewis. Fiber-optic combined fpi/fbg sensors for monitoring of radiofrequency thermal ablation of liver tumors: ex vivo experiments. *Applied optics*, 53(10):2136–2144, 2014.

- [124] Thomas Köhler, Sven Haase, Sebastian Bauer, Jakob Wasza, Thomas Kilgus, Lena Maier-Hein, Hubertus Feußner, and Joachim Hornegger. Tof meets rgb: novel multi-sensor super-resolution for hybrid 3-d endoscopy. In *International Conference on Medical Image Computing and Computer-Assisted Intervention*, pages 139–146. Springer, 2013.
- [125] Marcel Fajkus, Jan Nedoma, Radek Martinek, Vladimir Vasinek, Homer Nazeran, and Petr Siska. A non-invasive multichannel hybrid fiber-optic sensor system for vital sign monitoring. *Sensors*, 17(1):111, 2017.
- [126] Kozo Konishi, Masahiko Nakamoto, Yoshihiro Kakeji, Kazuo Tanoue, Hirofumi Kawanaka, Shohei Yamaguchi, Satoshi Ieiri, Yoshinobu Sato, Yoshihiko Maehara, Shinichi Tamura, et al. A real-time navigation system for laparoscopic surgery based on three-dimensional ultrasound using magneto-optic hybrid tracking configuration. *International Journal of Computer Assisted Radiology and Surgery*, 2(1):1–10, 2007.
- [127] Uddhav Bhattarai and Ali T Alouani. Hybrid navigation information system for minimally invasive surgery: Offline sensors registration. In *Science and Information Conference*, pages 205–219. Springer, 2019.
- [128] Mohd Saiful Dzulkefly Zan, Mohamed M Elgaud, and Ahmad Ashrif A Bakar. Coding the optical pulse in tdm-fbg sensors with hybrid simplex-and golay codes for snr improvement. In *2019 24th OptoElectronics and Communications Conference (OECC) and 2019 International Conference on Photonics in Switching and Computing (PSC)*, pages 1–3. IEEE, 2019.
- [129] Brian D Hoffman, David Q Larkin, Giuseppe Maria Prisco, Guanghua G Zhang, and Rajesh Kumar. Methods and system for performing 3-d tool tracking by fusion of sensor and/or camera derived data during minimally invasive robotic surgery, Aug ” 15” 2019. US Patent App. 16/396,125.
- [130] Thomas George Thuruthel, Benjamin Shih, Cecilia Laschi, and Michael Thomas Tolley. Soft robot perception using embedded soft sensors and recurrent neural networks. *Science Robotics*, 4(26):eaav1488, 2019.

- [131] Zhen Guo, Chen Xing, Changjian Ke, Keyuan Yang, and Deming Liu. 3d shape sensing utilizing sbs in multi-core fiber. In *2019 Optical Fiber Communications Conference and Exhibition (OFC)*, pages 1–3. IEEE, 2019.
- [132] Mohammad Jolaei, Amir Hooshidar, and Javad Dargahi. Displacement-based model for estimation of contact force between rfa catheter and atrial tissue with ex-vivo validation. In *2019 IEEE International Symposium on Robotic and Sensors Environments (ROSE)*, pages 1–7. IEEE, 2019.
- [133] Ruoyu Wang, Shiheng Wang, Erdong Xiao, Kshitij Jindal, Wenzhen Yuan, and Chen Feng. Real-time soft robot 3d proprioception via deep vision-based sensing. *arXiv preprint arXiv:1904.03820*, 2019.
- [134] Tiago Leal Ghezzi and Oly Campos Corleta. 30 years of robotic surgery. *World journal of surgery*, pages 1–8, 2016.
- [135] BL Davies, SJ Harris, WJ Lin, RD Hibberd, R Middleton, and JC Cobb. Active compliance in robotic surgery—the use of force control as a dynamic constraint. *Proceedings of the Institution of Mechanical Engineers, Part H: Journal of Engineering in Medicine*, 211(4):285–292, 1997.
- [136] Ali Üneri, Marcin A Balicki, James Handa, Peter Gehlbach, Russell H Taylor, and Iulian Iordachita. New steady-hand eye robot with micro-force sensing for vitreoretinal surgery. In *Biomedical Robotics and Biomechatronics (BioRob), 2010 3rd IEEE RAS and EMBS International Conference on*, pages 814–819. IEEE, 2010.
- [137] Christos Bergeles and Guang-Zhong Yang. From passive tool holders to microsurgeons: safer, smaller, smarter surgical robots. *IEEE Transactions on Biomedical Engineering*, 61(5):1565–1576, 2013.
- [138] Harsh Singh, Ramin Sedaghati, and Javad Dargahi. Experimental and finite element analysis of an endoscopic tooth-like tactile sensor. In *SENSORS, 2003 IEEE*, volume 1, pages 259–264. IEEE, 2003.

- [139] Javad Dargahi and Siamak Najarian. Theoretical and experimental analysis of a piezoelectric tactile sensor for use in endoscopic surgery. *Sensor Review*, 2004.
- [140] Anish S Naidu, Rajni V Patel, and Michael D Naish. Low-cost disposable tactile sensors for palpation in minimally invasive surgery. *IEEE/ASME Transactions on Mechatronics*, 22(1):127–137, 2016.
- [141] Dariush Nazarynasab, Farzam Farahmand, Alireza Mirbagheri, and Elnaz Afshari. A novel laparoscopic grasper with two parallel jaws capable of extracting the mechanical behaviour of soft tissues. *Journal of medical engineering & technology*, 41(5):339–345, 2017.
- [142] Gerhard A Holzapfel. On large strain viscoelasticity: continuum formulation and finite element applications to elastomeric structures. *International Journal for Numerical Methods in Engineering*, 39(22):3903–3926, 1996.
- [143] Yuan-cheng Fung. *Biomechanics: mechanical properties of living tissues*. Springer Science & Business Media, 2013.
- [144] Kiyoyuki Chinzei, Ron Kikinis, and Ferenc A Jolesz. Mr compatibility of mechatronic devices: Design criteria. In *International Conference on Medical Image Computing and Computer-Assisted Intervention*, pages 1020–1030. Springer, 1999.
- [145] Yong S Lee and Kensall D Wise. A batch-fabricated silicon capacitive pressure transducer with low temperature sensitivity. *IEEE transactions on electron devices*, 29(1):42–48, 1982.
- [146] Mark H Lee and Howard R Nicholls. Review article tactile sensing for mechatronics—a state of the art survey. *Mechatronics*, 9(1):1–31, 1999.
- [147] Kiyoyuki Chinzei, Karol Miller, et al. Towards mri guided surgical manipulator. *Medical science monitor*, 7(1):153–163, 2001.
- [148] Israel Gannot. Optical fibers and sensors for medical applications ii. In *Optical Fibers and Sensors for Medical Applications II*, volume 4616, 2002.

- [149] Roozbeh Ahmadi, Siamak Arbatani, Jayan Ozhikandathil, Muthukumaran Packirisamy, and Javad Dargahi. A multi-purpose optical microsystem for static and dynamic tactile sensing. *Sensors and Actuators A: Physical*, 235:37–47, 2015.
- [150] Saeed Sokhanvar, Mohammadreza Ramezanifard, Javad Dargahi, and Muthukumaran Packirisamy. Graphical rendering of localized lumps for mis applications. *Journal of Medical Devices*, 1(3):217–224, 2007.
- [151] Simon Phipps, Tao HJ Yang, Fouad K Habib, Robert Lewis Reuben, and S Alan McNeill. Measurement of tissue mechanical characteristics to distinguish between benign and malignant prostatic disease. *Urology*, 66(2):447–450, 2005.
- [152] Thomas A Krouskop, Thomas M Wheeler, Faouzi Kallel, Brian S Garra, and Timothy Hall. Elastic moduli of breast and prostate tissues under compression. *Ultrasonic imaging*, 20(4):260–274, 1998.
- [153] Christopher Walter, Lindsey Crawford, Melinda Lai, Joseph A Toonen, Yuan Pan, Shelly Sakiyama-Elbert, David H Gutmann, and Amit Pathak. Increased tissue stiffness in tumors from mice with neurofibromatosis-1 optic glioma. *Biophysical journal*, 112(8):1535–1538, 2017.
- [154] Juhui Li, Qingxin Zhang, and Aiqun Liu. Advanced fiber optical switches using deep riefabrication. *Sensors and Actuators A: physical*, 102(3):286–295, 2003.
- [155] Pinyo Puangmali, Kaspar Althoefer, and Lakmal D Seneviratne. Mathematical modeling of intensity-modulated bent-tip optical fiber displacement sensors. *IEEE transactions on Instrumentation and Measurement*, 59(2):283–291, 2009.
- [156] Govind P Agrawal. *Nonlinear fiber optics*. Springer, 2000.
- [157] Ferdinand Beer. *Mechanics of materials*. McGraw-Hill, 2015.
- [158] Francois Peyraut, Christine Renaud, Nadia Labed, and Zhi-Qiang Feng. Modeling of biological tissues with anisotropic hyperelastic laws-theoretical study and finite element analysis. *Comptes Rendus Mécanique*, 337(2):101–106, 2009.

- [159] Ronald S. Rivlin. Large elastic deformations of isotropic materials iv. further developments of the general theory. *Philosophical Transactions of the Royal Society of London. Series A, Mathematical and Physical Sciences*, 241(835):379–397, 1948.
- [160] Saeed Sokhanvar, Javad Dargahi, and Muthukumaran Packirisamy. Hyperelastic modelling and parametric study of soft tissue embedded lump for mis applications. *The International Journal of Medical Robotics and Computer Assisted Surgery*, 4(3):232–241, 2008.
- [161] Xiaodan Jia, Rui Li, Mandayam A Srinivasan, and Edward H Adelson. Lump detection with a gelsight sensor. In *2013 World Haptics Conference (WHC)*, pages 175–179. IEEE, 2013.
- [162] James C Gwilliam, Zachary Pezzementi, Erica Jantho, Allison M Okamura, and Steven Hsiao. Human vs. robotic tactile sensing: Detecting lumps in soft tissue. In *2010 IEEE Haptics Symposium*, pages 21–28. IEEE, 2010.
- [163] Amir Hooshier, Naghmeh M Bandari, and Javad Dargahi. Image-based estimation of contact forces on catheters for robot-assisted cardiovascular intervention. In *Proc. Hamlyn Symp. Med. Robot.*, pages 119–120, 2018.
- [164] Amir Hooshier, Ali Alkhalaf, and Javad Dargahi. Development and assessment of a stiffness display system for minimally invasive surgery based on smart magneto-rheological elastomers. *Materials Science and Engineering: C*, 108:110409, 2020.
- [165] Ali Alkhalaf, Amir Hooshier, and Javad Dargahi. Composite magnetorheological elastomers for tactile displays: Enhanced mreeffect through bi-layer composition. *Composites Part B: Engineering*, page 107888, 2020.
- [166] Christopher R Wagner, Nicholas Stylopoulos, Patrick G Jackson, and Robert D Howe. The benefit of force feedback in surgery: Examination of blunt dissection. *Presence: teleoperators and virtual environments*, 16(3):252–262, 2007.
- [167] Chaoyang Shi, Tianliang Li, and Hongliang Ren. A millinewton resolution fiber bragg grating-based catheter two-dimensional distal force sensor for cardiac catheterization. *IEEE Sensors Journal*, 18(4):1539–1546, 2017.

- [168] Chaoyang Shi, Ming Li, Changhu Lv, Jianmin Li, and Shuxin Wang. A high-sensitivity fiber bragg grating-based distal force sensor for laparoscopic surgery. *IEEE Sensors Journal*, 20(5):2467–2475, 2019.
- [169] Abdulfatah AG Abushagur, Norhana Arsad, Mamun Ibne Reaz, and A Bakar. Advances in bio-tactile sensors for minimally invasive surgery using the fibre bragg grating force sensor technique: A survey. *Sensors*, 14(4):6633–6665, 2014.
- [170] Qiaokang Liang, Kunlin Zou, Jianyong Long, Jing Jin, Dan Zhang, Gianmarc Coppola, Wei Sun, Yaonan Wang, and Yunjian Ge. Multi-component fbg-based force sensing systems by comparison with other sensing technologies: A review. *IEEE Sensors Journal*, 18(18):7345–7357, 2018.
- [171] Oliver Hadeler, Morten Ibsen, and Michalis N. Zervas. Distributed-feedback fiber laser sensor for simultaneous strain and temperature measurements operating in the radio-frequency domain. *Applied optics*, 40(19):3169–3175, 2001.
- [172] Yi Jiang, Vladislav Reimer, Tobias Schossig, Martin Angelmahr, and Wolfgang Schade. Fiber optical multifunctional human-machine interface for motion capture, temperature, and contact force monitoring. *Optics and Lasers in Engineering*, 128:106018, 2020.
- [173] Xueke Yu, Ningfang Song, and Jingming Song. A novel method for simultaneous measurement of temperature and strain based on efpi/fbg. *Optics Communications*, 459:125020, 2020.
- [174] Stephen W. James, Michael L. Dockney, and Ralph P. Tatam. Simultaneous independent temperature and strain measurement using in-fibre bragg grating sensors. *Electronics Letters*, 32(12):1133–1134, 1996.
- [175] Marek Dobosz and Mariusz Kozuchowski. Overview of the laser-wavelength measurement methods. *Optics and Lasers in Engineering*, 98:107–117, 2017.
- [176] Kenny P. Koo and Alan D. Kersey. Fibre laser sensor with ultrahigh strain resolution using interferometric interrogation. *Electronics Letters*, 31(14):1180–1182, 1995.

- [177] Manuel Silva-López, William N MacPherson, Cheng Li, Andrew J Moore, James S Barton, Julian DC Jones, Donghui Zhao, Lin Zhang, and Ian Bennion. Transverse load and orientation measurement with multicore fiber bragg gratings. *Applied optics*, 44(32):6890–6897, 2005.
- [178] Andrea Rosales-García, Iván Cruz-Torres, and Juan Hernández-Cordero. Fiber lasers with hybrid birefringence resonators. *Optics and lasers in engineering*, 44(10):1027–1038, 2006.
- [179] Kuikui Guo, Jun He, Gaixia Xu, and Yiping Wang. Dual-polarization distributed feedback fiber laser sensor based on femtosecond laser-inscribed in-fiber stressors for simultaneous strain and temperature measurements. *IEEE Access*, 8:97823–97829, 2020.
- [180] Yu Tang, Muguang Wang, Jing Zhang, Naihan Zhang, Yan Li, Qi Ding, Beilei Wu, Yan Liu, and Guofang Fan. Curvature and temperature sensing based on a dual-frequency oeo using cascaded tcfbg-fp and smfbg-fp cavities. *Optics & Laser Technology*, 131:106442, 2020.
- [181] Yao-Jen Chang, Chien-Hung Yeh, and Chi-Wai Chow. Reliability of stable fiber bragg grating sensor system for monitoring temperature and strain individually. *Measurement Science and Technology*, 30(10):105108, 2019.
- [182] Li-Yang Shao, Xinyong Dong, A Ping Zhang, Hwa-Yaw Tam, and Sailing He. High-resolution strain and temperature sensor based on distributed bragg reflector fiber laser. *IEEE Photonics Technology Letters*, 19(20):1598–1600, 2007.
- [183] Frantisek Urban, Jaroslav Kadlec, Radek Vlach, and Radek Kuchta. Design of a pressure sensor based on optical fiber bragg grating lateral deformation. *Sensors*, 10(12):11212–11225, 2010.
- [184] Rachaen Huq. Fiber bragg gratings (fbg) for force sensing in biomechanics applications. Master’s thesis, Dalhousie University, 2019.
- [185] Mohammad Jolaei, Amir Hooshier, Javad Dargahi, and Muthukumaran Packirisamy. Toward task autonomy in robotic cardiac ablation: Learning-based kinematic control of soft tendon-driven catheters. *Soft Robotics*, pages In-Press, 2020.

- [186] Mohammad Jolaei, Amir Hooshier, Amir Sayadi, Javad Dargahi, and Muthukumaran Packirisamy. Sensor-free force control of tendon-driven ablation catheters through position control and contact modeling. In *2020 42nd Annual International Conference of the IEEE Engineering in Medicine & Biology Society (EMBC)*, pages 5248–5251. IEEE, 2020.
- [187] Tuan Guo, Allan CL Wong, Wei-Sheng Liu, Bai-Ou Guan, Chao Lu, and Hwa-Yaw Tam. Beat-frequency adjustable er 3+-doped dbr fiber laser for ultrasound detection. *Optics express*, 19(3):2485–2492, 2011.
- [188] Scott C Rashleigh. Characterization and performance of polarization-preserving fibers. In *Optical Fiber Communication Conference*, page ME1. Optical Society of America, 1984.
- [189] Turan Erdogan and Victor Mizrahi. Characterization of uv-induced birefringence in photo-sensitive ge-doped silica optical fibers. *JOSA B*, 11(10):2100–2105, 1994.
- [190] Peter D Gianino and Bernard Bendow. Calculations of stress-induced changes in the transverse refractive-index profile of optical fibers. *Applied optics*, 20(3):430–434, 1981.
- [191] Rachid Gafsi and Mahmoud A El-Sherif. Analysis of induced-birefringence effects on fiber bragg gratings. *Optical Fiber Technology*, 6(3):299–323, 2000.
- [192] Luigi Fazzi, Aydin Rajabzadeh, Alberto Milazzo, and Roger M Groves. Analysis of fbg reflection spectra under uniform and non-uniform transverse loads. In *Sensors and Smart Structures Technologies for Civil, Mechanical, and Aerospace Systems 2019*, volume 10970, page 109701X. International Society for Optics and Photonics, 2019.
- [193] JT Kringlebotn, WH Loh, and RI Laming. Polarimetric er 3+-doped fiber distributed-feedback laser sensor for differential pressure and force measurements. *Optics letters*, 21(22):1869–1871, 1996.
- [194] Yang Zhang, Bai-Ou Guan, and Hwa-Yaw Tam. Characteristics of the distributed bragg reflector fiber laser sensor for lateral force measurement. *Optics Communications*, 281(18):4619–4622, 2008.

- [195] Russell Charles Hibbeler and SC Fan. *Statics and mechanics of materials*, volume 2. Prentice Hall Upper Saddle River, 2004.
- [196] Fanqi Kong, Wangzhe Li, and Jianping Yao. Transverse load sensing based on a dual-frequency optoelectronic oscillator. *Optics letters*, 38(14):2611–2613, 2013.
- [197] Laura L Nathans, Frederick L Oswald, and Kim Nimon. Interpreting multiple linear regression: A guidebook of variable importance. *Practical Assessment, Research, and Evaluation*, 17(1):9, 2012.
- [198] Paula Gomes. *Medical robotics: Minimally invasive surgery*. Elsevier, 2012.
- [199] Javad Dargahi, Saeed Sokhanvar, Siamak Najarian, and Siamak Arbatani. *Tactile Sensing and Displays: Haptic Feedback for Minimally Invasive Surgery and Robotics*. John Wiley & Sons, 2012.
- [200] Stefan Sauerland, Rolf Lefering, EA Neugebauer, et al. Laparoscopic versus open surgery for suspected appendicitis. *Cochrane Database Syst Rev*, 4(4), 2004.
- [201] Christopher R Wagner, Robert D Howe, and Nicholas Stylopoulos. The role of force feedback in surgery: analysis of blunt dissection. In *haptics*, page 73. IEEE, 2002.
- [202] Allison M Okamura. Methods for haptic feedback in teleoperated robot-assisted surgery. *Industrial Robot: An International Journal*, 31(6):499–508, 2004.
- [203] Ahmad Abiri, Jake Pensa, Anna Tao, Ji Ma, Yen-Yi Juo, Syed J Askari, James Bisley, Jacob Rosen, Erik P Dutson, and Warren S Grundfest. Multi-modal haptic feedback for grip force reduction in robotic surgery. *Scientific reports*, 9(1):5016, 2019.
- [204] Evelien M Overtoom, Tim Horeman, Frank-Willem Jansen, Jenny Dankelman, and Henk WR Schreuder. Haptic feedback, force feedback, and force-sensing in simulation training for laparoscopy: A systematic overview. *Journal of surgical education*, 76(1):242–261, 2019.
- [205] Jelizaveta Konstantinova, Allen Jiang, Kaspar Althoefer, Prokar Dasgupta, and Thrishantha Nanayakkara. Implementation of tactile sensing for palpation in robot-assisted minimally invasive surgery: A review. *IEEE Sensors Journal*, 14(8):2490–2501, 2014.

- [206] Ahmad Atieh, Roozbeh Ahmadi, Masoud Kalantari, Javad Dargahi, and Muthukumaran Packirisamy. A piezoresistive based tactile sensor for use in minimally invasive surgery. In *2011 IEEE 37th Annual Northeast Bioengineering Conference (NEBEC)*, pages 1–2. IEEE, 2011.
- [207] Dong-Hyuk Lee, Uikyum Kim, Tauseef Gulrez, Woon Jong Yoon, Blake Hannaford, and Hyouk Ryeol Choi. A laparoscopic grasping tool with force sensing capability. *IEEE/ASME Transactions on Mechatronics*, 21(1):130–141, 2016.
- [208] Thomas B Gabrielson. Mechanical-thermal noise in micromachined acoustic and vibration sensors. *IEEE transactions on Electron Devices*, 40(5):903–909, 1993.
- [209] Haluk Kulah, Junseok Chae, Navid Yazdi, and Khalil Najafi. Noise analysis and characterization of a sigma-delta capacitive microaccelerometer. *IEEE journal of solid-state circuits*, 41(2):352–361, 2006.
- [210] Mahdi Tavakoli, Arash Aziminejad, Ranji V. Patel, and Mehrdad Moallem. Multi-sensory force/deformation cues for stiffness characterization in soft-tissue palpation. In *Engineering in Medicine and Biology Society, 2006. EMBS'06. 28th Annual International Conference of the IEEE*, pages 837–840. IEEE, 2006.
- [211] Amir Molaie, Amir Hooshier, Vahid Karamzadeh, Ebrahim Abedloo, and Javad Dargahi. Pretensioned structures as multi axis force sensors. In *2017 5th RSI International Conference on Robotics and Mechatronics (ICRoM)*, pages 416–420. IEEE, 2017.
- [212] Shelten G Yuen, Michael C Yip, Nikolay V Vasilyev, Douglas P Perrin, J Pedro, and Robert D Howe. Robotic force stabilization for beating heart intracardiac surgery. In *International Conference on Medical Image Computing and Computer-Assisted Intervention*, pages 26–33. Springer, 2009.
- [213] Alberto Fernandez Fernandez, Francis Berghmans, Benoit Brichard, Patrice Mégret, Marc Decréton, Michel Blondel, and Alain Delchambre. Multi-component force sensor based on multiplexed fibre bragg grating strain sensors. *Measurement science and technology*, 12(7):810, 2001.

- [214] Daniel S Yurkewich, Abelardo Escoto, Ana Luisa Trejos, Marie-Eve LeBel, Rajni V Patel, and Michael D Naish. Low-cost force-sensing arthroscopic tool using threaded fiber bragg grating sensors. In *5th IEEE RAS/EMBS International Conference on Biomedical Robotics and Biomechatronics*, pages 28–33. IEEE, 2014.
- [215] Renfeng Xue, Bingyin Ren, Jiaqing Huang, Zhiyuan Yan, and Zhijiang Du. Design and evaluation of fbg-based tension sensor in laparoscope surgical robots. *Sensors*, 18(7):2067, 2018.
- [216] Benito Carotenuto, Armando Ricciardi, Alberto Micco, Ezio Amorizzo, Marco Mercieri, Antonello Cutolo, and Andrea Cusano. Optical fiber technology enables smart needles for epidurals: an in-vivo swine study. *Biomedical optics express*, 10(3):1351–1364, 2019.
- [217] Nurettin Okan Ulgen, Dogangun Uzun, and Ozgur Kocaturk. Phantom study of a fiber optic force sensor design for biopsy needles under mri. *Biomedical optics express*, 10(1):242–251, 2019.
- [218] Paulo Roriz, Orlando Frazão, António B Lobo-Ribeiro, José L Santos, and José A Simões. Review of fiber-optic pressure sensors for biomedical and biomechanical applications. *Journal of biomedical optics*, 18(5):050903–050903, 2013.
- [219] Naghmeh M. Bandari, Javad Dargahi, and Muthukumaran Packirisamy. Force sensor for robotic graspers in minimally invasive surgery. In *ICME 2018: International Conference on Mechanical Engineering, Montreal, Canada, (May 24-25, 2018)*, volume 4, page 2257. World Academy of Science, Engineering and Technology, 2017.
- [220] Paul E. Klingsporn. Characterization of optical fiber strength under applied tensile stress and bending stress. Technical report, Kansas City Plant (KCP), Kansas City, MO (United States), 2011.
- [221] Shorya Awtar. *Synthesis and analysis of parallel kinematic XY flexure mechanisms*. PhD thesis, Massachusetts Institute of Technology, 2003.

- [222] Paulo Antunes, Fátima Domingues, Marco Granada, and Paulo André. Mechanical properties of optical fibers. In *Selected topics on optical fiber technology*. IntechOpen, 2012.
- [223] Se Song, Min Park, Jung Lee, and Ji Yun. A study on the rheological and mechanical properties of photo-curable ceramic/polymer composites with different silane coupling agents for 3d printing technology. *Nanomaterials*, 8(2):93, 2018.
- [224] Wenjian Wang, Zongben Xu, Weizhen Lu, and Xiaoyun Zhang. Determination of the spread parameter in the gaussian kernel for classification and regression. *Neurocomputing*, 55(3-4):643–663, 2003.
- [225] Da vinci xi system first access accessories. (Date last accessed 14-10-2019).
- [226] International Electrotechnical Commission et al. Safety of laser products – part 1: Equipment classification, requirements and user’s guide. Standard, International Electrotechnical Commission, Geneva, CH, 1 2001.
- [227] Krzysztof Czuszyński, Jacek Rumiński, and Alicja Kwaśniewska. Gesture recognition with the linear optical sensor and recurrent neural networks. *IEEE Sensors Journal*, 18(13):5429–5438, 2018.
- [228] Janne MJ Huttunen, Leo Kärkkäinen, and Harri Lindholm. Pulse transit time estimation of aortic pulse wave velocity and blood pressure using machine learning and simulated training data. *PLoS computational biology*, 15(8):e1007259, 2019.
- [229] Ahmad Sohrabi Kashani, Simona Badilescu, Alisa Piekny, and Muthukumaran Packirisamy. Perspective—bio-nano-interaction in treatment and management of cancer. *Journal of the Electrochemical Society*, 166(9):B3007, 2018.
- [230] Jayan Ozhikandathil and Muthukumaran Packirisamy. Monolithically integrated optical microfluidic chip by single step lithography and etching for detection of fluorophore tagged recombinant bovine somatotropin (rbst). *Journal of The Electrochemical Society*, 161(2):B3155, 2014.

- [231] Eric M Hofferber, Joseph A Stapleton, and Nicole M Iverson. Single walled carbon nanotubes as optical sensors for biological applications. *Journal of The Electrochemical Society*, 167(3):037530, 2020.
- [232] Duraichelvan Raju, Srinivas Bathini, Simona Badilescu, Rodney J Ouellette, Anirban Ghosh, and Muthukumaran Packirisamy. Study of detection and capture of exosomes by using the morphologies of ex situ and in situ nanostructures. *Journal of The Electrochemical Society*, 166(9):B3001, 2018.
- [233] Ravinder Kour, Sandeep Arya, Sonali Verma, Anoop Singh, Prerna Mahajan, and Ajit Khosla. Recent advances and challenges in indium gallium nitride (inxga1-xn) materials for solid state lighting. *ECS Journal of Solid State Science and Technology*, 9(1):015011, 2019.
- [234] Jean-Bernard Masson, Jan Kovac, Gerhard Schuler, Jian Ye, Anson Cheung, Samir Kapadia, Murat E Tuzcu, Susheel Kodali, Martin B Leon, and John G Webb. Transcatheter aortic valve implantation: review of the nature, management, and avoidance of procedural complications. *JACC: Cardiovascular Interventions*, 2(9):811–820, 2009.
- [235] Giuseppe Andrea Fontanelli, Luca Rosario Buonocore, Fanny Ficuciello, Luigi Villani, and Bruno Siciliano. An external force sensing system for minimally invasive robotic surgery. *IEEE/ASME Transactions on Mechatronics*, 25(3):1543–1554, 2020.
- [236] Nitish Kumar, Jackson Wirekoh, Samir Saba, Cameron N Riviere, and Yong-Lae Park. Soft miniaturized actuation and sensing units for dynamic force control of cardiac ablation catheters. *Soft Robotics*, 2020.
- [237] Dogangun Uzun, Okan Ulgen, and Ozgur Kocaturk. Optical force sensor with enhanced resolution for mri guided biopsy. *IEEE Sensors Journal*, 2020.
- [238] Panagiotis Polygerinos, Asghar Ataollahi, Tobias Schaeffter, Reza Razavi, Lakmal D Seneviratne, and Kaspar Althoefer. Mri-compatible intensity-modulated force sensor for cardiac catheterization procedures. *IEEE Transactions on biomedical engineering*, 58(3):721–726, 2011.

- [239] Tianliang Li, Chaoyang Shi, and Hongliang Ren. Three-dimensional catheter distal force sensing for cardiac ablation based on fiber bragg grating. *IEEE/ASME Transactions on Mechatronics*, 23(5):2316–2327, 2018.
- [240] Tianliang Li, Anqi Pan, and Hongliang Ren. A high-resolution tri-axial catheter-tip force sensor with miniature flexure and suspended optical fibers. *IEEE Transactions on Industrial Electronics*, 2019.
- [241] Merhyle Franklin Spotts, Terry E Shoup, and Lee Emrey Hornberger. *Design of machine elements*. Pearson Education, 2006.

Appendix A

A.1 Bending-based Formulation of Light Intensity Modulation for Miniaturization of Optical Tactile Sensors

In recent studies, various force sensor based on light-intensity-modulation (LIM) principle were proposed and tested for MIS applications (Figure A.1(a)) [80, 84]. In these studies cylindrical indenters were used as the means to bend the optical fiber in a constant bending radius (CBR) deflection. The idea of using CBR deflection has been investigated thoroughly and formulated. Figure A.1(b) depicts the CBR deflection of an optical fiber schematically. Due to the simple analytical solution of power loss in a CBR deflected fiber (Eqs. 98- 100), it is a preferred design choice; however, to achieve CBR deflection, it is necessary to use large-enough cylindrical elements to bend the fiber. This has been a major limitation in miniaturization of optical tactile sensors.

$$P_1(4S) = P_o e^{-4\gamma S}, \quad (98)$$

$$S = r_b \varphi, \quad (99)$$

$$\gamma = k_o r_b^{-\frac{1}{2}} e^{-k_1 r_b}, \quad (100)$$

where, P_1 , P_o , r_b and φ are output power, input power, radius of indenter cylinders, and central angle of the bent portions of fiber, while k_o , and k_1 are two intrinsic fiber properties. In the present study, a miniature LIM-based force sensor is designed by removing the cylindrical indenting parts. Figure A.2(a) illustrates the structural design of the proposed layered force sensor. A flexible shell

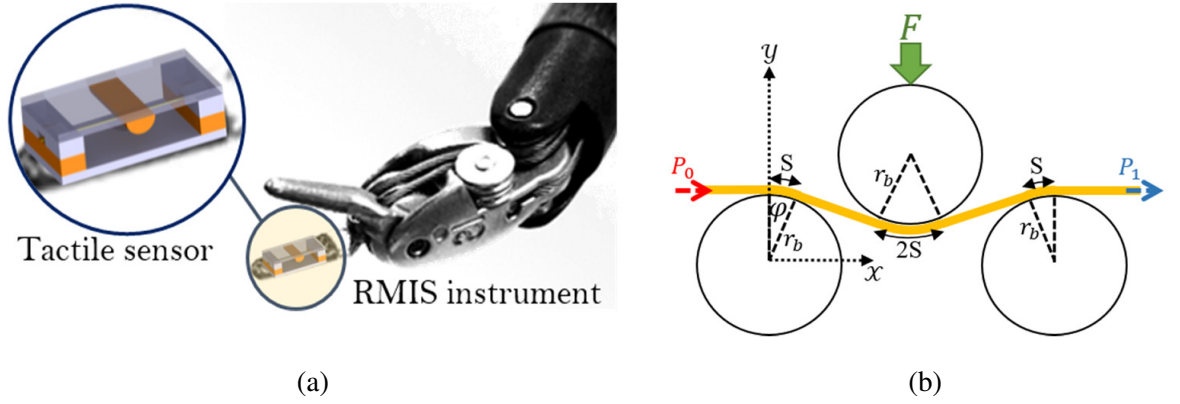


Figure A.1: (a) Conceptual integration of tactile sensor on an RMIS instrument (EndoWristTM-da VinciTM Surgical System, Intuitive Surgical Inc., Sunnyvale, CA), (b) mechanical model of an optical fiber as a beam and its shape in a single radius bending configuration.

(Mooney-Rivlin Silicon rubber) was used as a bending beam. This beam acts as a Euler-Bernoulli beam (slenderness=0.1) with fixed-fixed boundary condition. A single mode optical fiber was fixed at two supports of the substrate ends that the indenter is in contact with the indenter. To obtain the displacement of fiber under force on the beam, the finite element analysis (FEA) of the sensor was performed considering distributed force F , 0.8 N, over the top surface of the flexible shell. The resulting deflection of the optical fiber was used to calculate the light intensity modulation and output power (Figure A.2(b)). Since the cylindrical elements are removed in this design, CBR condition was no longer valid and Eq. 98 was differentiated and modified to apt with the general VBR deflection of the beam. The output power was estimated using (Eqs. 101- 102).

$$dP(S) = -\gamma P_o e^{-\gamma s} ds - s P_o e^{-\gamma s}, \quad (101)$$

$$\gamma = k_o r(s)^{-\frac{1}{2}} e^{-k_1 r(s)}, \quad (102)$$

Where, $r(s)$ is the variable bending radius along the fiber, and s is the length parameter. Parameters $k_o=0.00275$, and $k_1=155$, were identified using a 2 mm compression bending test under CBR condition (Figure A.3(a)). A fiber under both constant- and variable-bending radius (VBR) was subjected to bending. A compression bending displacement of 2mm with rate of $0.1 \text{ mm} \cdot \text{sec}^{-1}$ was applied in both cases. The theoretical and experimental power loss were compared for CBR and VBR.

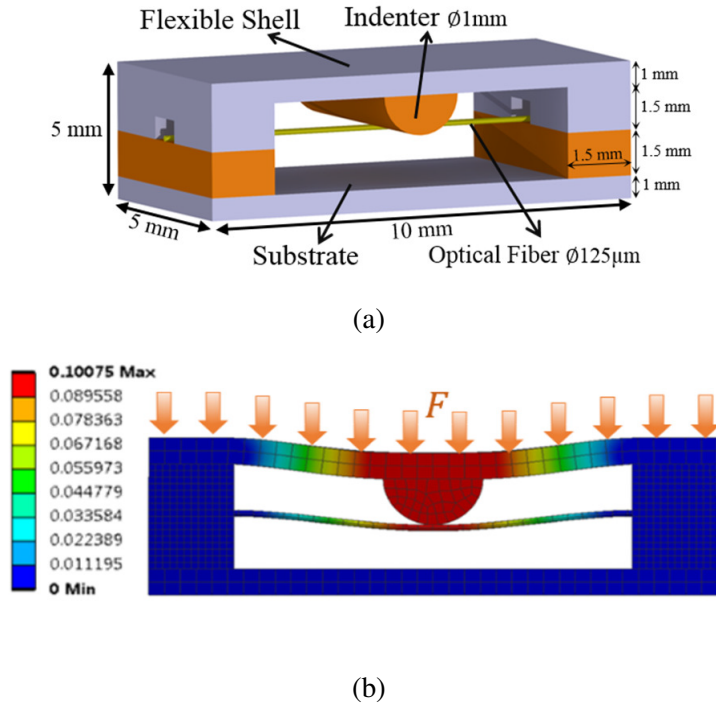
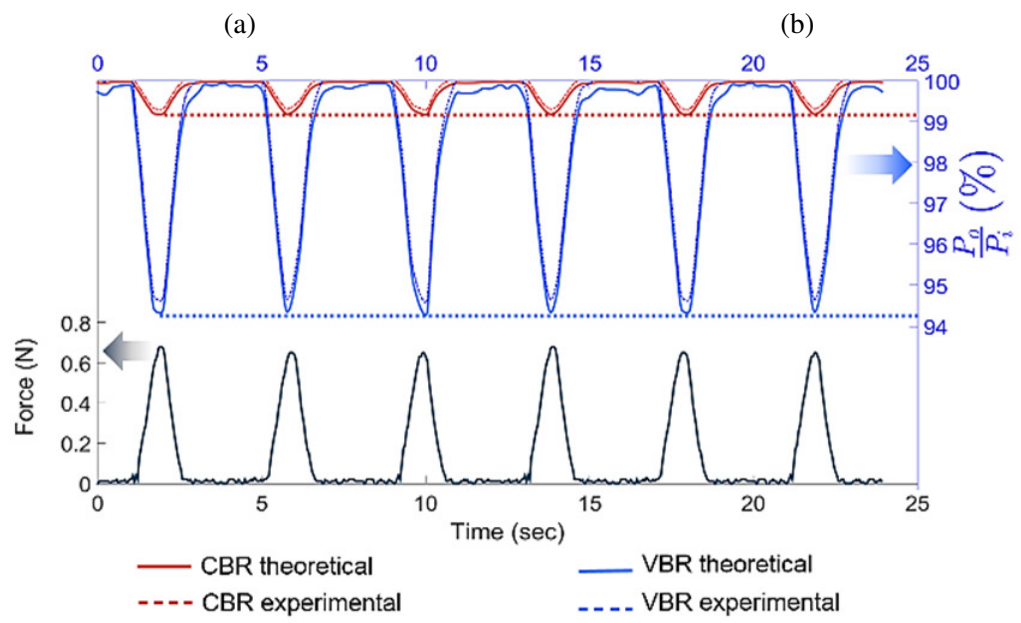
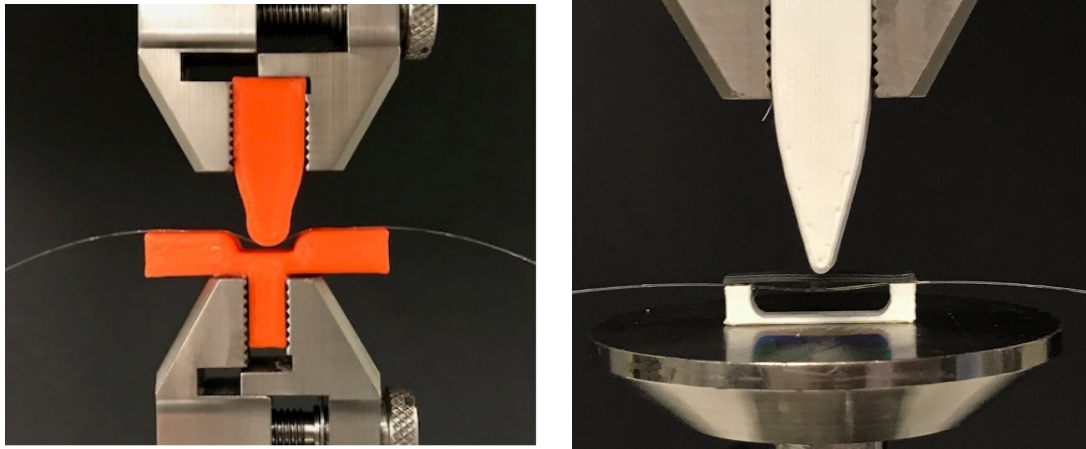


Figure A.2: (a) Structure of the proposed planar tactile sensor, (b) distribution of internal forces in the sensor (FEA).

The FEA revealed that a bending force of 0.8 N would be needed to cause a deflection of 2mm in the fiber. This finding was later confirmed by the experimental results (Figure A.3(b)). Since the sensor was designed with 1.5 mm vertical space for bending below the fiber, 2 mm would serve as the worst-case-scenario for this design. The power loss predicted by Eq. 98- and Eq. 101 were in fair agreement with experimental measurements for both VBR and CBR (RMS Error < 5%) (Figure A.3(b)). The maximum power loss for CBR and VBR due to 2 mm of bending displacement were approximately 1% and 5.6%, respectively. The power loss observed in VBR was significantly larger than CBR (460% higher). The reason might be due to the second negative term in Eq. 101, where due to the non-constant radius of curvature along the fiber, term $d\gamma$ is non-zero and adds-up in the integration over the length of the fiber resulting in larger power loss in the fiber. Further analysis showed that by reducing the radius of indenters and tending to a point load bending condition the contribution of the second negative term in Eq. 101 prevails that of the first term. However, that would adversely affect the sensing range of the sensor. Therefore, there should be an optimum level of radius for the indenter by which both the desired range and sensitivity of a sensor is satisfied.



(c)

Figure A.3: Experimental setup for deflecting optical fiber under (a) CBR, (b) VBR conditions, (c) bending force, theoretical prediction and experimentally measured power loss in the proposed sensor.

A.2 Validation of the Variable Bending Radius Sensing Principle

Optical-fiber-based force sensors mainly work based on the light intensity modulation (LIM) principle. Researchers have modeled the bending power-loss in an optical fiber with the constant-bending-radius (CBR) assumption (Figure A.4(a)). Recently, a new LIM sensing principle with a variable-bending-radius (VBR) configuration was postulated in (Figure A.4(b)). VBR configuration led to the design of a miniaturized LIM-based force sensor with simpler manufacturing. This study was performed for numerical and experimental validation of the proposed sensing principle.

The analytical framework, relating the power decay in a bent optical fiber to the external force acting on it was previously postulated in A.1. Eqs. 98- 102 describe the transmitted power in the optical fiber through its length under CBR and VBR configuration, respectively. Considering a Euler-Bemoulli beam model for the optical fiber and integrating the differential of power decay over the length of the fiber, the power-loss was obtained as a function of the radius of curvature, $r(s)$. Since the radius of curvature is a function of the unknown center-span force F , the force was estimated using an inverse solution Eq. 103.

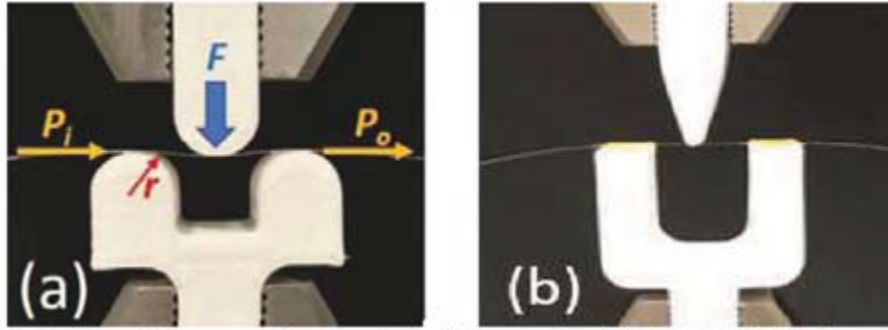


Figure A.4: Bending test of an optical fiber under (a) CBR, (b) VBR configuration.

$$\frac{EI}{M(s)} = r(s) = \frac{1}{\int_0^s F(s)ds}, \quad (103)$$

For the validation, deflected shape of the fiber under a compressive bending displacement of 5 mm was obtained using Eq. 103. The deflected shape was introduced in BeamProp software, and the power-loss was predicted using the beam propagation method (BPM). Furthermore, 12 identical fiber samples were mechanically tested under half-sinusoidal compression down to 5 mm

at a frequency of 0.35 Hz (CBR, $n=6$ and VBR, $n=6$) while the power-loss was recorded (Figure A.4). Also, using the force and deflection from the experiments, the power-losses were theoretically estimated using Eqs. 98-101 were compared with the experimental values.

Numerical simulations in BeamProp predicted a terminal power-loss of 1% and 8% for CBR and VBR, respectively. Theoretical prediction and experimental measurements both showed 1% power-loss for CBR, while it was predicted 5.4% and measured 5.6% for VBR. There was a fair agreement for the power-loss in both CBR and VBR (Figure A.5).

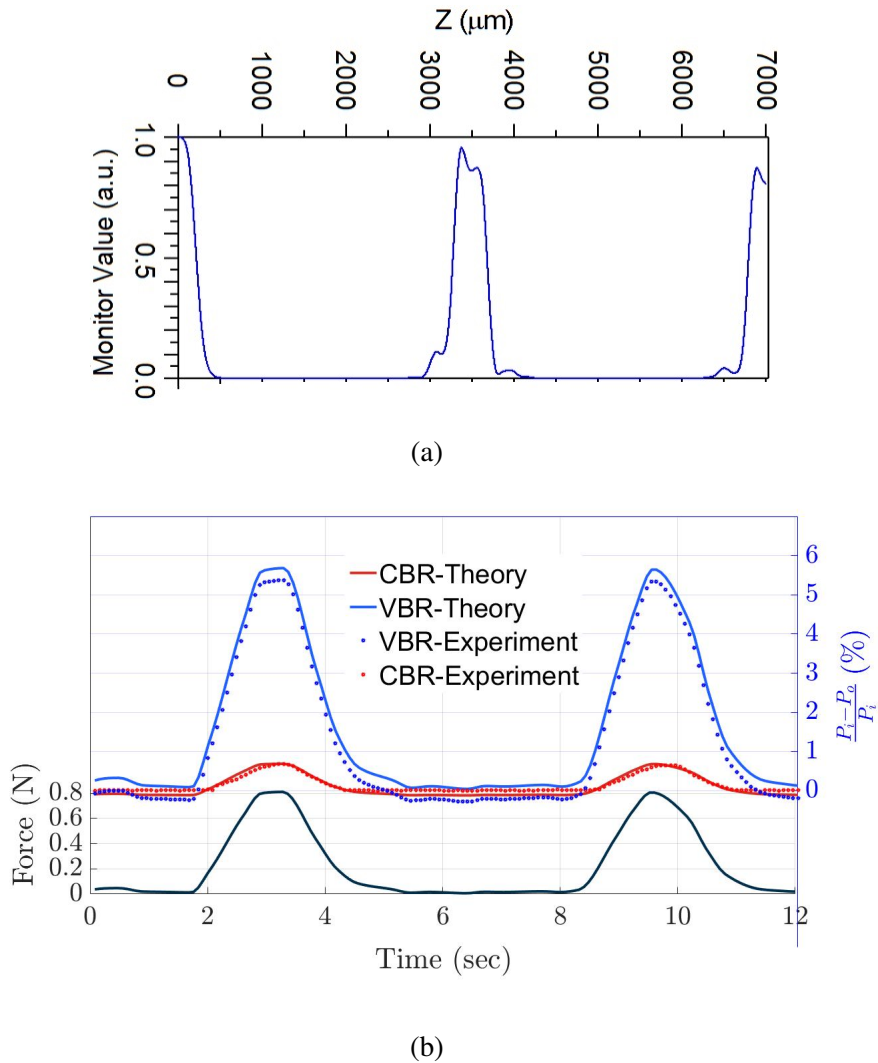


Figure A.5: (a) Result of the power-loss in VBR simulation, (b) theoretical prediction vs. experimentally power-loss in the for VBR and CBR.

A.3 Fabrication and Experimental Setup Preparation for Light Intensity Measurement

A.3.1 3D Printing Fabrication

The sensors fabrication was done using SLA technology by means of a *Form2* 3D printer available at the Optical-BioMEMS Lab, Concordia University (Figure A.6). The namely spatial resolution of this printer is 25 micrometers with its regular resin and 50 micrometers with its flexible resin. Examples of a planar and a cylindrical sensor fabricated and a 3D printed model of aortic arch and valve are shown in Figure A.7.

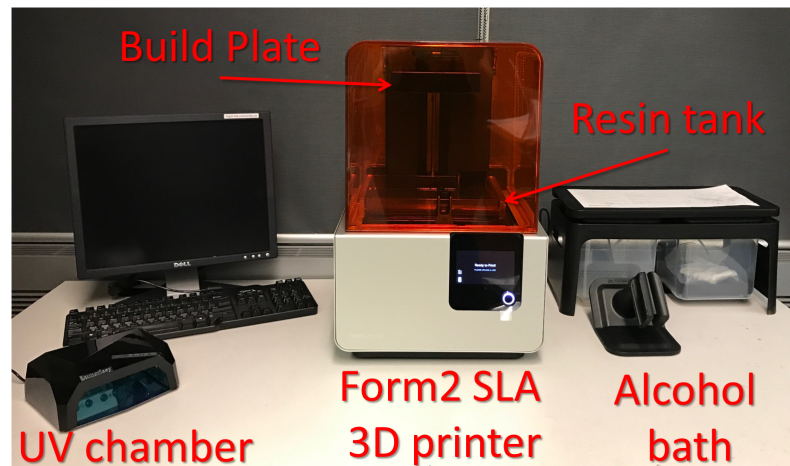


Figure A.6: Form2 3D printer working based SLA technology

As per its documentations, Formlabs flexible resin simulates an 80A shore hardness rubber. This resin makes parts that can bend and compress conveniently. However, the shore hardness of this material as well as its hyperelastic mechanical properties, i.e. C_0 and C_1 were to be determined in each printed sample. Form2 printer uses UV photopolymeric resins which mandates post-rinsing with alcohol (isopropyl alcohol, 90% IPA) finished by a UV post-cure for elimination of resin residues. Material characterization for the materials printed are performed after the alcohol and UV treatment.

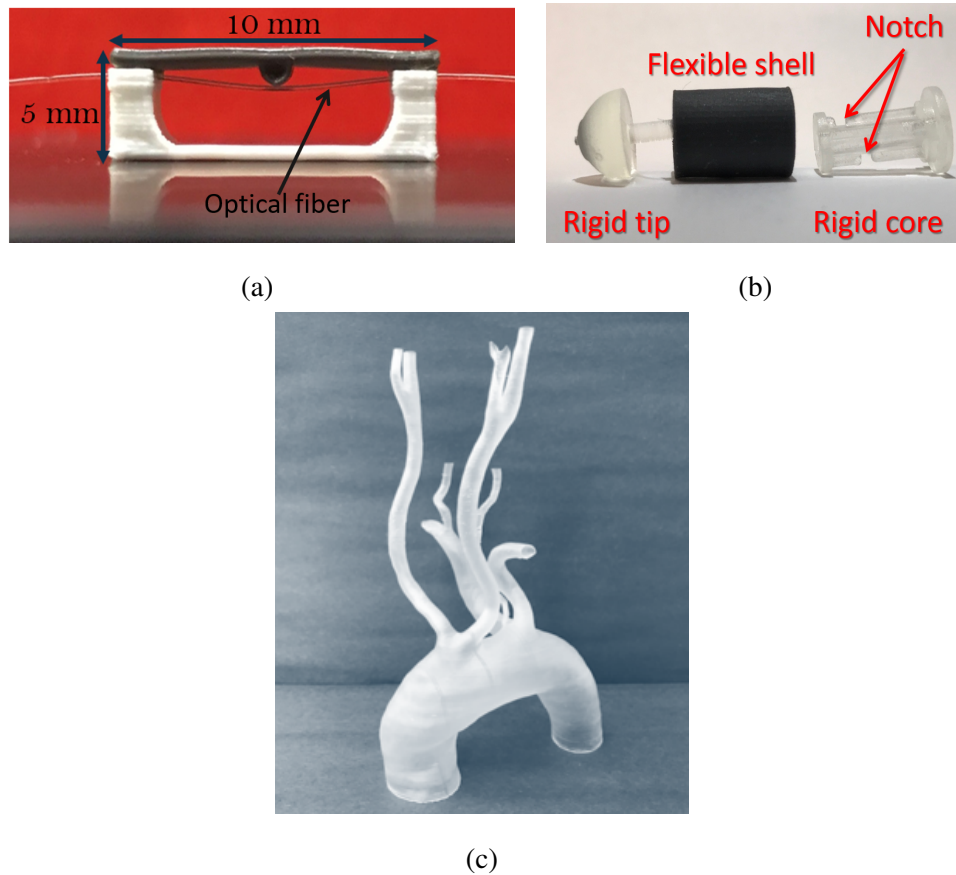


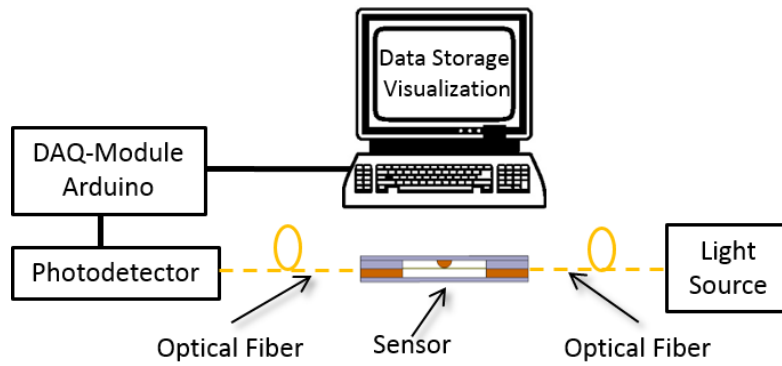
Figure A.7: (a) Fabricated Robotic surgery planar sensor, (b) fabricated valvuloplasty and annuloplasty cylindrical sensor, (c) 3D printed model of aortic arch and valve.

A.3.2 Experimental Setup

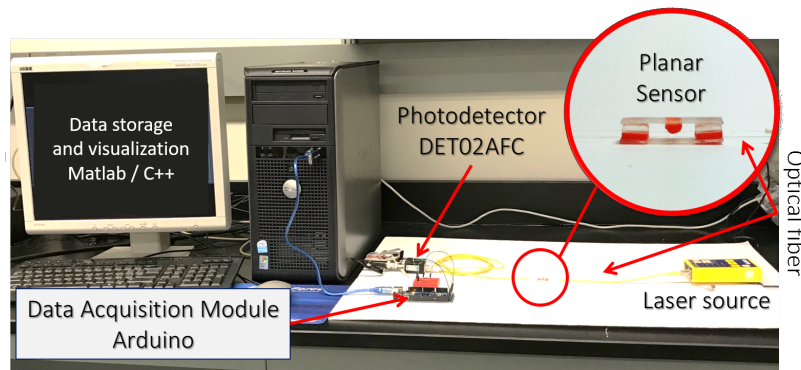
The experimental setup with photodetector is depicted in Figure A.8. The optical fibers are single-mode with 250 micrometer diameter (Thorlabs, NJ, US). The laser light source (Thorlabs Inc., NJ, US) generates 800 nanometers laser beam at a power of 5 milliWatts. The fiber passes through the sensor and enters a DET02AFC Silicon photo-detector (Thorlabs Inc., NJ, US). The DET02AFC photodetectors were used for the proof-of-concept of sensing principles.

Alternatively, to monitor the light intensity in multiple fibers of a sensor in real-time, a CCD camera with a maximum resolution of 1250×1000 pixels and magnification factor of 200 were used (Figure A.9). The image processing was implemented using OpenCV open-source library in C++ language.

Utilization of CCD camera in measuring light intensity in optical fiber is a quite new approach



(a)



(b)

Figure A.8: (a) Schematic diagram of the experimental setup, (b) experimental setup implemented for data acquisition using an Arduino embedded board and a photodetector.

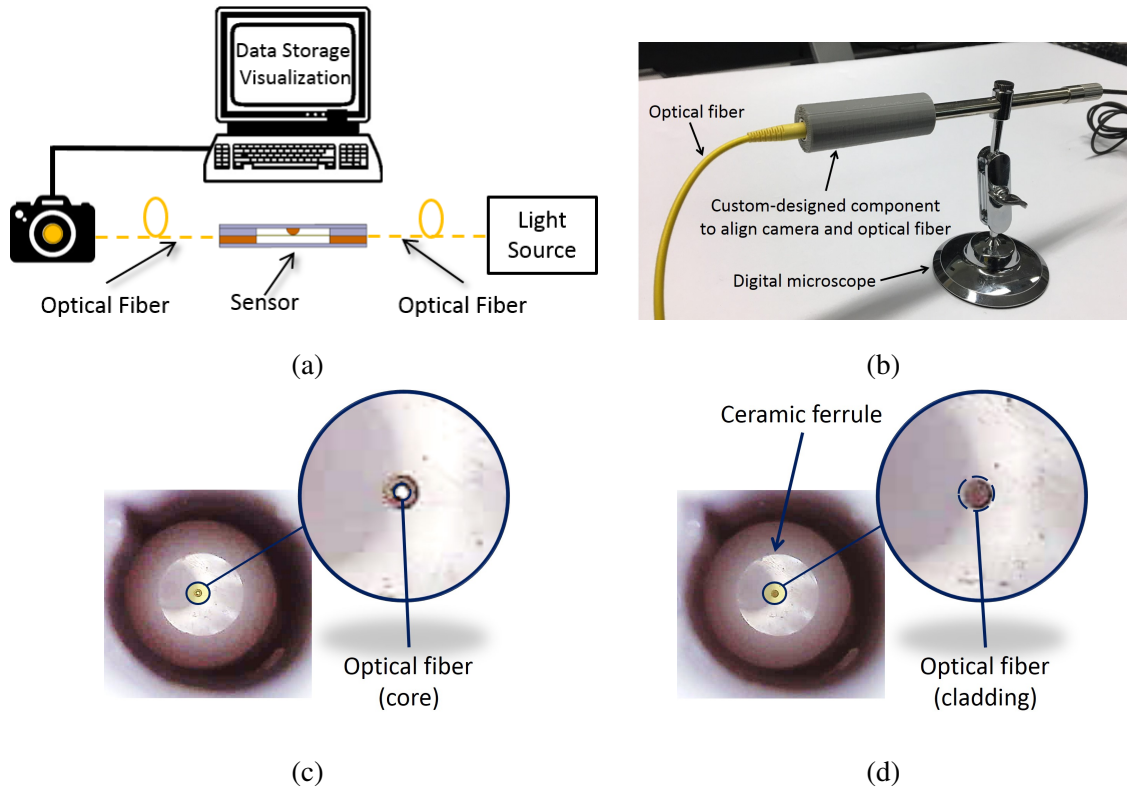


Figure A.9: (a) Schematic diagram of the experimental setup implemented for data acquisition using an CCD camera, (b) digital USB microscope with 200X magnification equipped with a 1250x1000 pixel camera used for optical fiber light intensity measurement, a custom-designed component is used to align camera and optical fiber, while (c) optical fiber is connected to the light source, (d) optical fiber is disconnected from the light source.

in this field. Noh *et al.* [89] reported using a CCD camera with multiple regions of interests (ROI) for the reflective loss principle in a proposed sensorized ablation catheter.

A.4 Finite Element Analysis for Non-linear Deflection and Optimization of DBR Fiber Laser Sensor

Figure A.10 depicts the maximum deflection of the membrane under pressure. The diameter of the optical fiber used in the system was 0.125 mm. From the graph, it was observed that the membrane deflected more than the fiber's diameter which is not practically feasible. In other words, in the pressure higher than the 0.75 atm or deflection more than 0.125 mm, the membrane touches the substrate and lies on the base on left and right sides of the fiber. This unwanted contact with

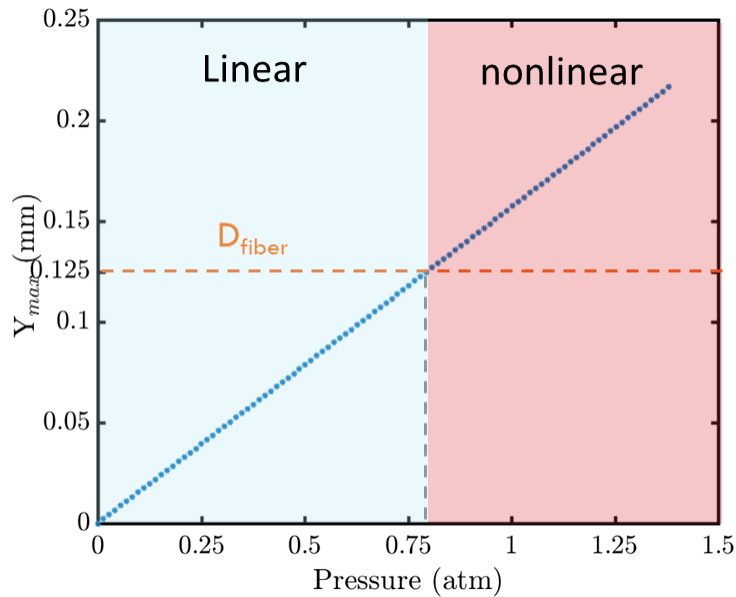


Figure A.10: Maximum deflection of the membrane at connection point with the optical fiber versus the pressure.

the substrate is a nonlinearity which is not accounted in the linear analytical model of DBR fiber laser sensor in Section 4.2.4. Linear and nonlinear regions are shown in Figure A.10 with two shaded areas. As a result, it is noted that system works linearly as long as the membrane has an optimal thickness or elastic modulus that does not touch the substrate under pressure. To obtain the minimum thickness and elastic modulus which keep the sensor in linear region a finite element

parametric study over various thicknesses and elastic moduli was performed.

A.4.1 Finite Element Analysis

To model and predict the behavior of the sensor upon the application of external pressure, or when contact happens, a 3D model of the sensor was developed in SolidWorks and imported into ANSYS Workbench v.17 (Ansys Inc., Pennsylvania). The 3D geometrical model is shown in Figure A.11(a). To simplify and reduce the time of finite element analysis, the 2D structure of the front view of the sensor was evaluated in Ansys Workbench, as illustrated in Figure A.11(b).

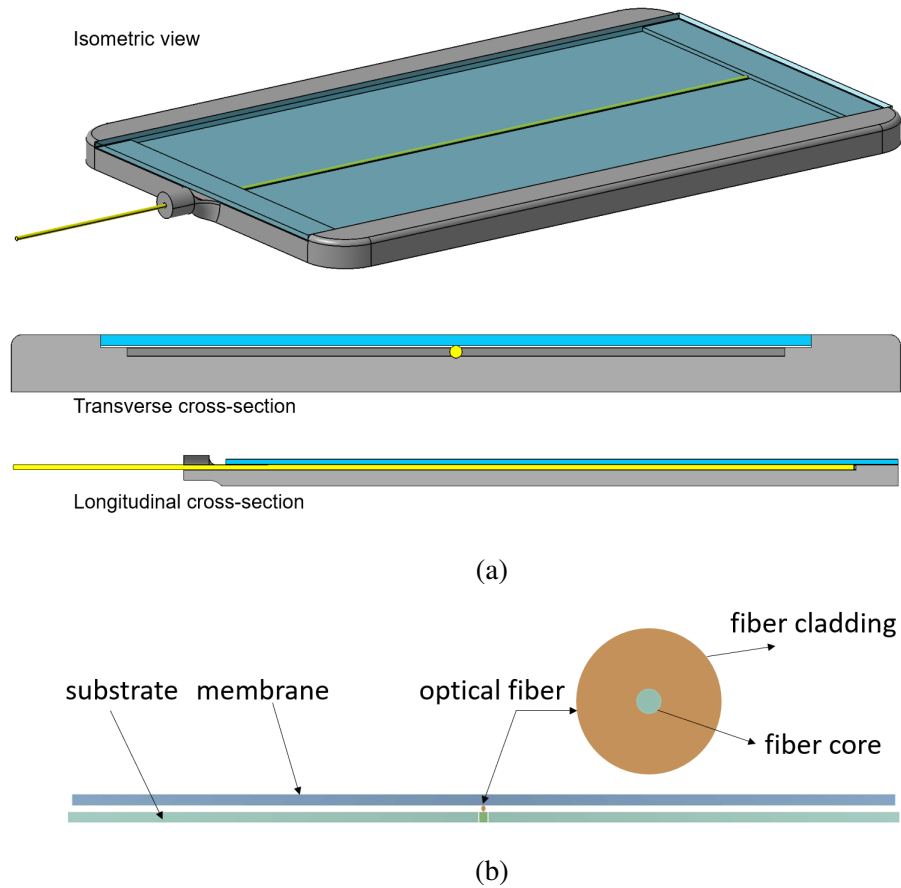


Figure A.11: (a) 3D geometrical model of the DBR sensor, (b) 2D structure of the front view of the sensor finite element analysis

Fixed boundary conditions were applied to the sensor components. A frictionless contact condition was assumed between the membrane and the optical fiber. Also, the contact between the

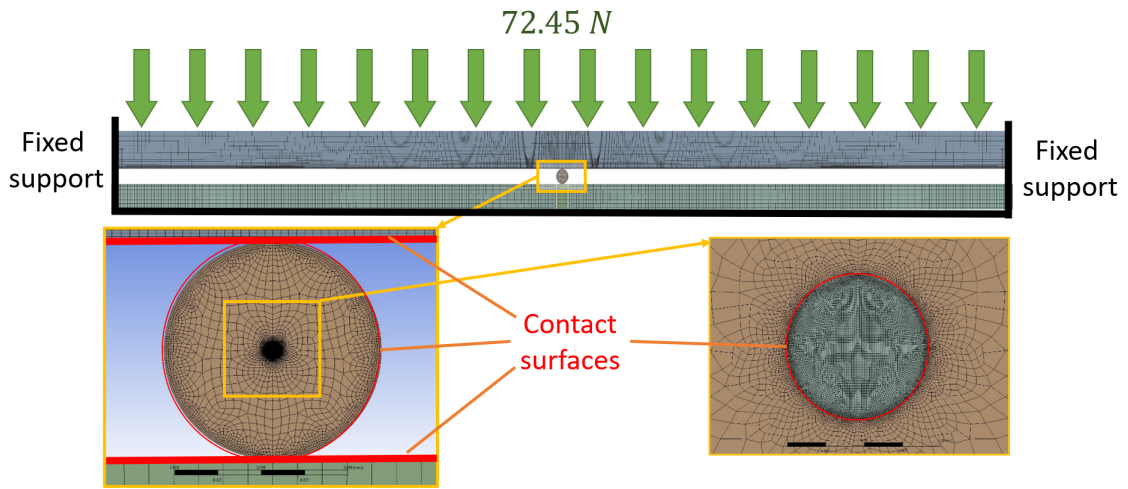


Figure A.12: Mesh quality, geometric features, and the max distributed transverse force per unit length on the membrane.

membrane and substrate was assumed to be frictionless when they touch each other in higher pressure. Figure A.12 shows the mesh quality, geometric features, and the maximum magnitude of the distributed transverse force per unit length resulted by the pressure on the membrane. This force was increased linearly according to the pressure of 0 to 1.5 atm.

The material properties of the sensor components and their dimensions are tabulated in Table A.1.

Table A.1: Material properties of the sensor components and their dimensions

| | Material | E (GPa) | Poisson's ratio | Length (mm) | Depth (mm) | Thickness (mm) | Diameter (mm) |
|-----------|----------|---------|-----------------|-------------|------------|----------------|---------------|
| Substrate | Aluminum | 68.9 | 0.33 | 15 | 35 | 2 | - |
| Membrane | — | 60-400 | 0.3 | 15 | 35 | 0.1-0.5 | - |
| Cladding | Silica | 76 | 0.17 | - | 35 | - | 0.125 |
| Core | Silica | 76 | 0.17 | - | 35 | - | 0.800 |

A.4.2 Parametric Response Surface

To find the thickness and elastic modulus of the membrane, which keeps the sensor in the linear region, the results of finite element model were afterward used in the Response Surface Optimization (RSO) module of Ansys. The model was solved for 50 design points, i.e. combinations of different elastic modulus and thickness inside the feasible range of all constraint shown in Table A.1. The

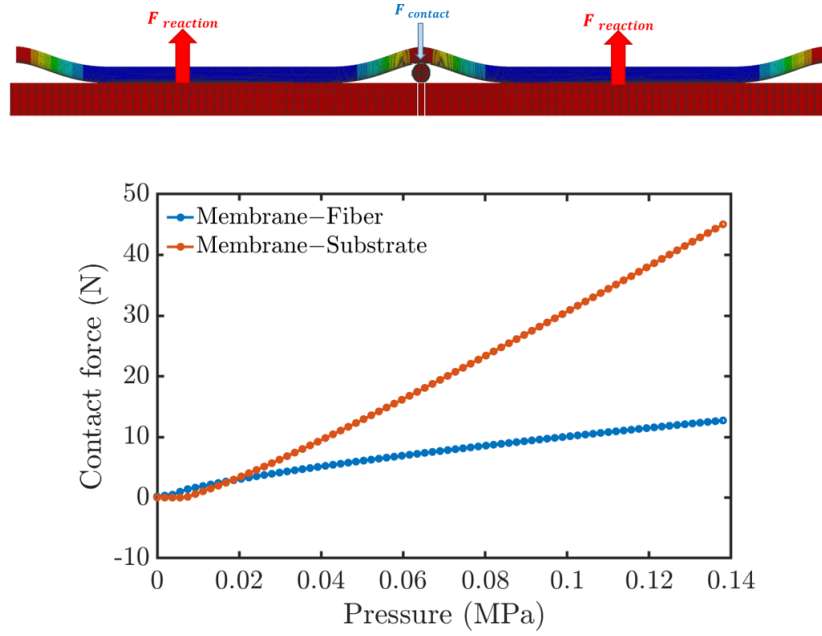


Figure A.13: Shape of the membrane under the distributed force and finite element results of the reaction force on the optical fiber (blue line) and substrate (red line) versus the pressure, membrane with 0.1 mm thickness and elastic modulus 63 GPa.

reaction force on the optical fiber in the y -direction, the interaction force between the membrane and substrate and maximum deflection of the membrane were obtained as the output of the optimization. To keep the sensor in the linear phase the deflection of the membrane should be limited in less than the diameter of the optical fiber. In addition, the interaction force between the membrane and the substrate should stay at 0 N. The reaction force obtained by FEM is considered as the $F_{contact}$ in the analytical model. In Section 4.2.4, it was proved that the magnitude of this force is linearly related to the beating frequency (Eq. 104). Figures A.13 - A.15 demonstrate how the thickness changes the reaction force on the fiber and interaction between the membrane and substrate while the elastic modulus of the membrane is constant as 63 GPa.

$$\Delta f_b = f_x - f_y = \frac{cB}{n_0\lambda_0}, B = \frac{n_0^3(p_{11} - p_{12})(1 + \nu_{fiber})F_{contact}}{L_c\pi r_{fiber}E_{fiber}}, \quad (104)$$

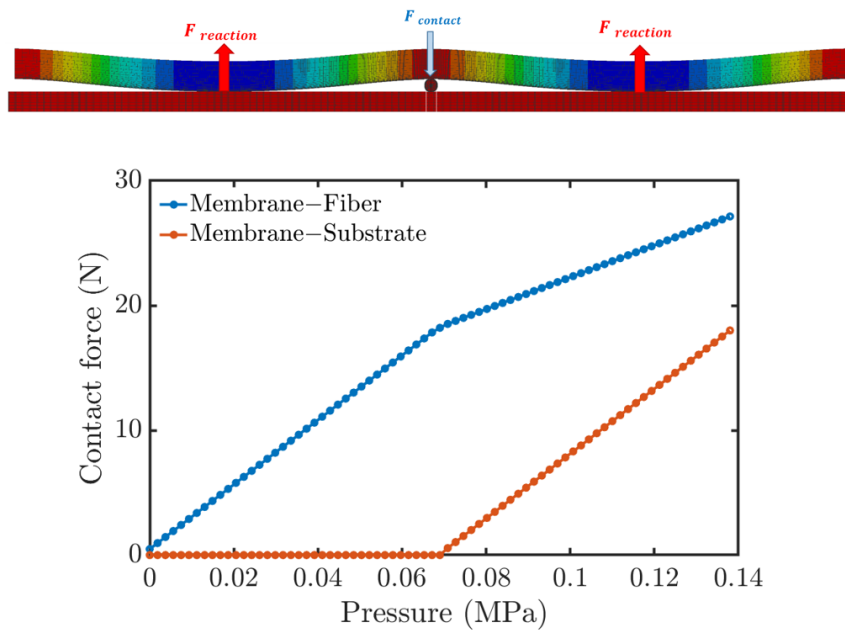


Figure A.14: Shape of the membrane under the distributed force and finite element results of the reaction force on the optical fiber (blue line) and substrate (red line) versus the pressure, membrane with 0.3 mm thickness and elastic modulus 63 GPa.

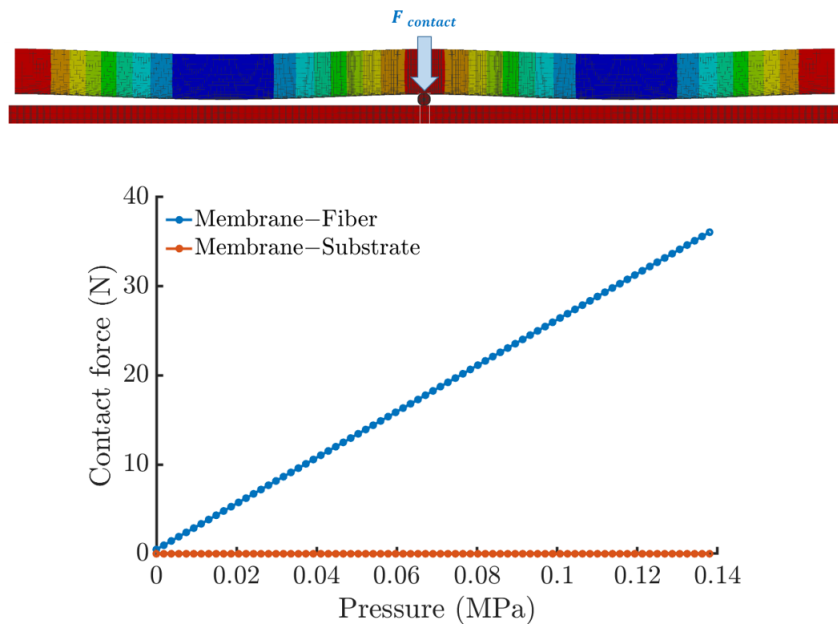


Figure A.15: Shape of the membrane under the distributed force and finite element results of the reaction force on the optical fiber (blue line) and substrate (red line) versus the pressure, membrane with 0.5 mm thickness and elastic modulus 63 GPa.

A.4.3 Parametric Study Results

The finite element study was done for all study points in the optimization process. The reaction force on the optical fiber was obtained to use as a reference to check sensors linearity and accuracy. Also, the reaction force was required to calculate the beating frequency in the analytical model. Figure A.16 revealed that the reaction force on the optical fiber versus the different module of elasticity and various thicknesses. Results showed that the maximum reaction force happens when the membrane does not touch the substrate.

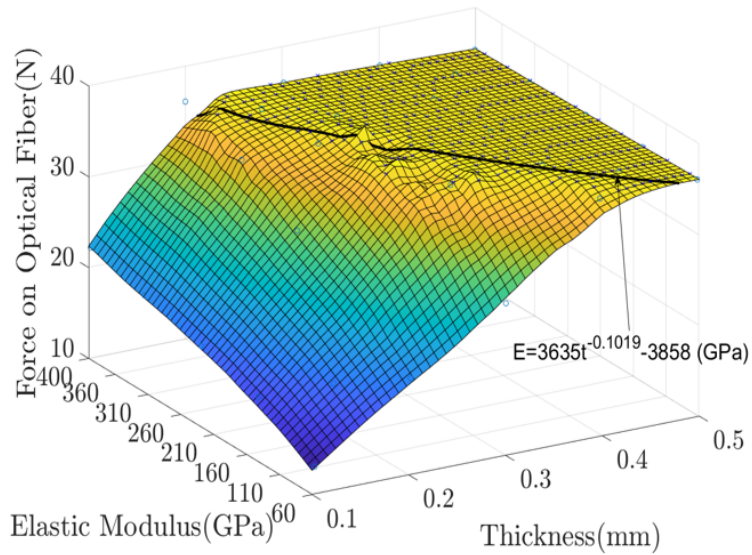


Figure A.16: Reaction force on the optical fiber versus the different module of elasticity and various thicknesses.

Equation $E = 3635t^{-0.1019} - 3858$ defines a relationship between the module of elasticity and the thickness. This line shows the minimum E and t to have a linear sensing system. In elasticity and thickness less than this line, the membrane will touch the substrate and system will behave nonlinearly. In addition to that, the reaction force on the optical fiber used to calculate the beating frequency through Eq. 104. The graph in Figure A.17 shows the beating frequency with respect to different E and t .

The sensor sensitivity with different thickness design and material is defined as the ratio between the output signal and measured property. Therefore since this sensor measures pressure and has a beating frequency output, the sensitivity is value with the units [GHz/atm]. Figure A.18 depicts the

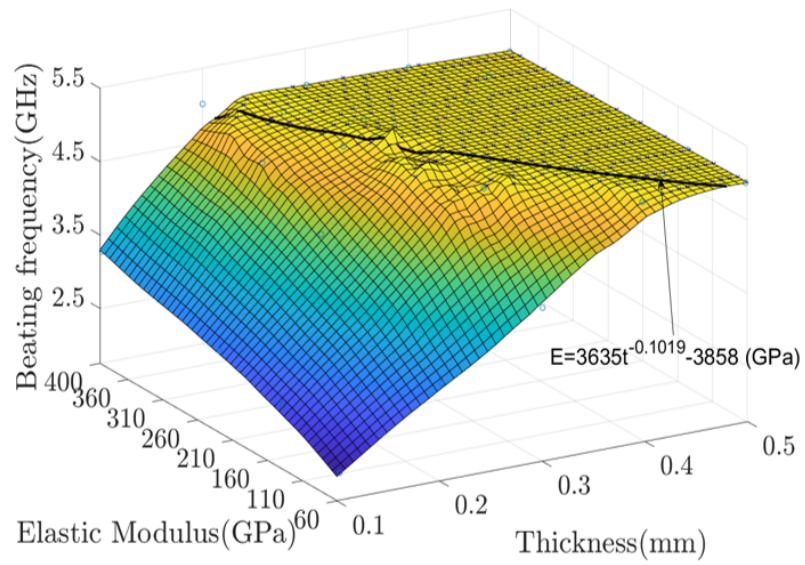


Figure A.17: Beating frequency with respect to different E and t

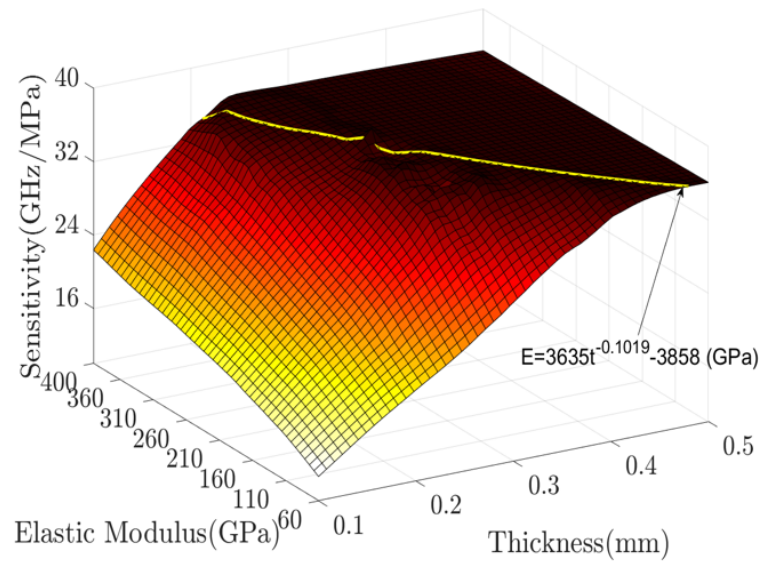


Figure A.18: Sensor sensitivity with respect E and t.

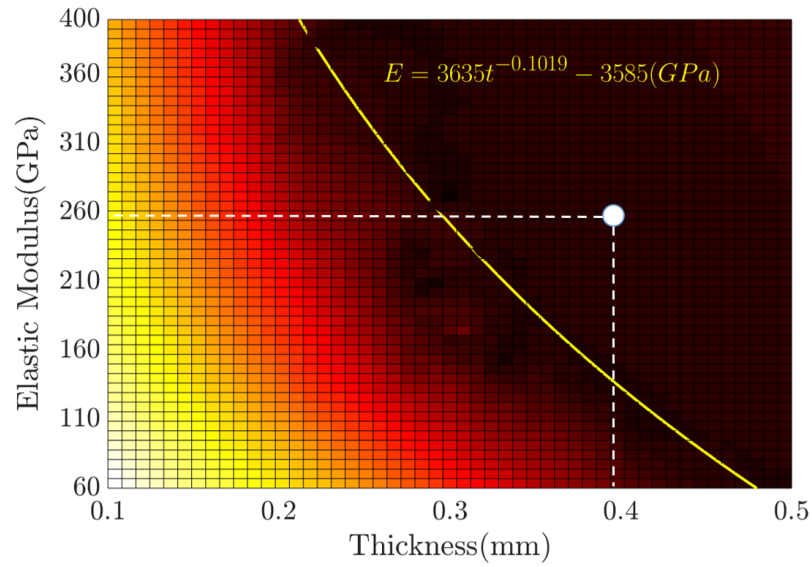


Figure A.19: Various elastic modulus versus the different thicknesses, the line shows minimum acceptable E and t to keep the system linear

sensor sensitivity with respect E and t.

To conclude the results of the parametric study, it is noticeable that there is a design criteria to have a linear system. As previously mentioned, the equation between elasticity and thickness shows the minimum feasible E and t to keep the system linear at the pressure of 0 to 1.5 atm. In other words, in the range of modulus of elasticity in this study, the membrane thickness should be more than 0.2mm as can be seen in Figure A.19.

A.5 Feasibility Study of a Novel Force Sensor with Three DBR Fibers

A.5.1 Finite Element Analysis

The previous design showed that in the higher pressure, membrane would touch the substrate and reduced the beating frequency range of measurement. To tackle this issue and have the chance of more range of measurement, the various design was recommended for the feasibility study. One possible structure for the sensor was using two extra fibers in two sides of the main one. In this way, it is expected that in the high-pressure membrane will touch the new fibers instead of substrate. As a result, these fibers will be considered as a new sensing component to record the pressure. To this

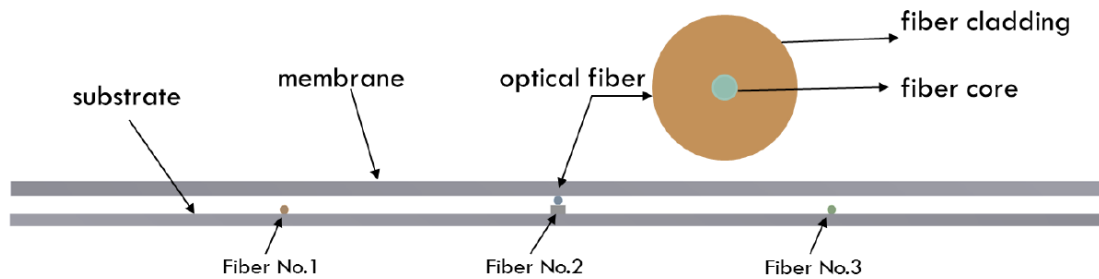


Figure A.20: 2D front view of the sensor structure with three optical fibers.

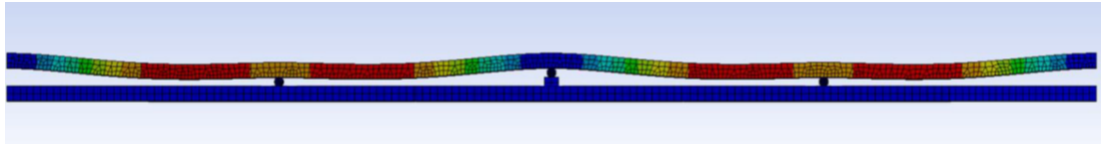
end, a new 2D scheme of the proposed structure was imported into the Ansys. Evaluating the finite element analysis proved the idea. Figure 27 shows the 2D front view of the proposed structure.

A.5.2 Simulation

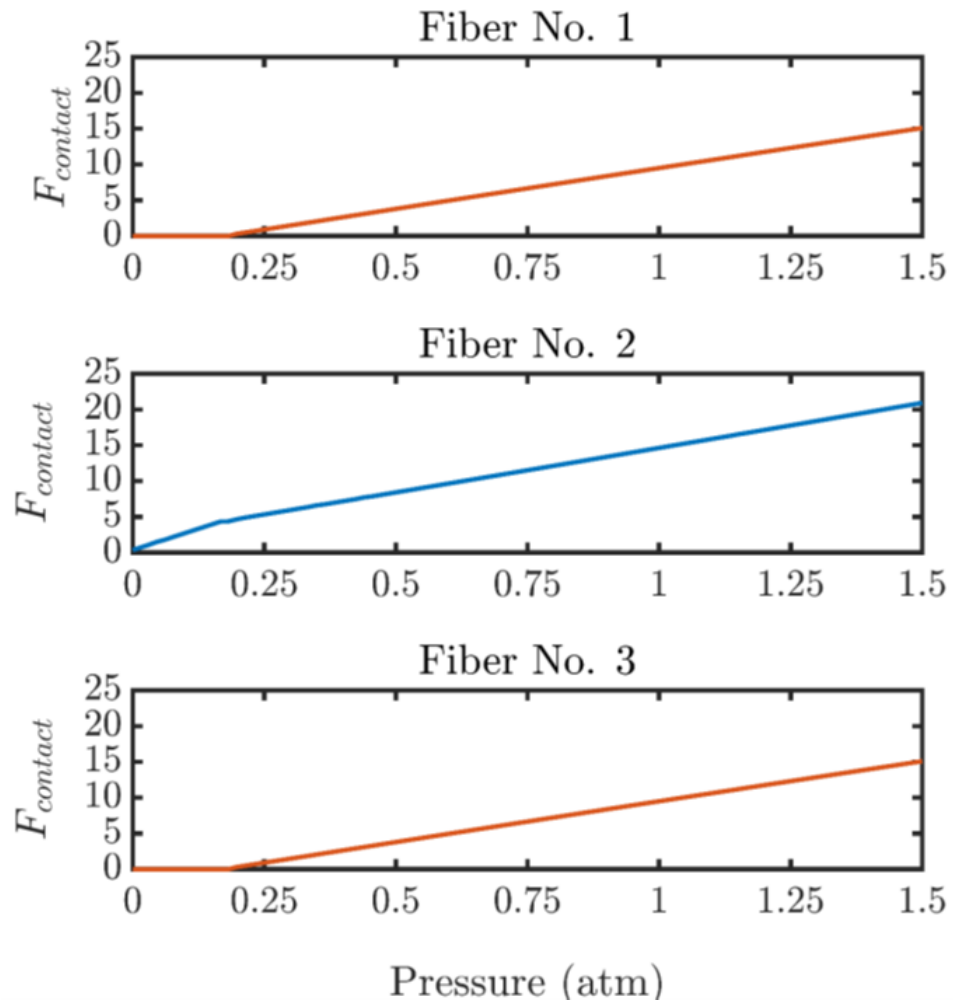
The boundary conditions which applied to the sensor components were like the Section A.4.1. Also, the contact between the membrane and fiber No.1, No.3 and substrate were assumed to be frictionless while they touch each other in higher pressure. A distributed transverse force per unit length resulted by the pressure range 0-1.5 atm was applied on the membrane surface. This force was increased linearly from zero to 72 N in 100 sec. Reaction forces on each fiber were recorded to check the proportion of the total force on the fibers. Also, the maximum deflection of the membrane was studied to check the system linearity. Figure A.21(a) illustrates the deflected membrane while is in contact with the all three fibers.

The graphs of reaction forces versus the pressure for each fiber is drawn in Figure A.21(b). It can be seen that after force 5 N the reaction force on the fiber No.1 and No.3 has been started and causes the deflection on these fibers and beating frequency indeed. Therefore, like the previous design fiber No.2 is the first component under the pressure then two other fibers will detect the pressure.

The graph shows that the membrane applied force up to 15 N on the two sides optical fibers instead of lying on the substrate. Therefore, having an analytical model to measure the reaction force on the two end supports and superposition of the three reaction forces on the fibers can conclude the total force on the sensor.



(a)



(b)

Figure A.21: (a) Deflected membrane while is in contact with all three fibers, (b) reaction forces versus the pressure for fibers No.1, No.2, and No.3.